SYNTHESIS AND CHARACTERIZATIONS OF ANODE MATERIALS FOR LITHIUM ION BATTERY

A THESIS

Submitted in partial fulfilment of the requirements for the award of the degree

of

DOCTOR OF PHILOSOPHY

in

METALLURGICAL AND MATERIALS ENGINEERING

by

KULDEEP SINGH RANA

M.G. CENTRAL LIBRARY
ACC No. G21269
Date 25/4/12
I.I.T. ROORKEE

DEPARTMENT OF METALLURGICAL AND MATERIALS ENGINEERING
INDIAN INSTITUTE OF TECHNOLOGY ROORKEE
ROORKEE-247 667 (INDIA)

SEPTEMBER, 2010

©INDIAN INSTITUTE OF TECHNOLOGY ROORKEE, ROORKEE, 2010
ALL RIGHTS RESERVED

INDIAN INSTITUTE OF TECHNOLOGY ROORKEE
ROORKEE

CANDIDATE'S DECLARATION

I hereby certify that the work which is being presented in the thesis entitled **SYNTHESIS AND CHARACTERIZATIONS OF ANODE MATERIALS FOR LITHIUM ION BATTERY** in partial fulfillment of the requirements for the award of the degree of Doctor of Philosophy and submitted in the Department of Metallurgical and Materials Engineering of the Indian Institute of Technology Roorkee, Roorkee is an authentic record of my own work carried out during a period from January, 2005 to September, 2010 under the supervision of Dr. Anjan Sil, Professor, Department of Metallurgical and Materials Engineering, Indian Institute of Technology Roorkee, Roorkee.

The matter presented in the thesis has not been submitted by me for the award of any other degree of this or any other Institute.

(KULDEEP SINGH RANA)

This is to certify that the above statement made by the candidate is correct to the best of my knowledge.

(Anjan Sil)
Supervisor

Date: 30/9/2010

The Ph.D. Viva-Voice Examination of Mr. **KULDEEP SINGH RANA**, Research Scholar, has been held on _____

Signature of Supervisor

Signature of External Examiner

ABSTRACT

To meet the increasing global demands for energy and allow for the depletion of fossil fuel supplies in the coming years, alternate clean energy sources, which do not depend on conventional energy sources must be developed. To use renewable sources effectively, reliable ways of storing energy are needed. One alternative energy storage technology that has already taken off in a big way is the rechargeable lithium-ion battery. This technology has become a commercial reality through the efforts of the Sony Corporation and others, and is used widely today in portable computer and telecommunications devices, which is also receiving considerable attention in applications for electric vehicles, especially as these devices are becoming smaller and more efficient. Demand and competition are driving the quest for higher storage capacity, longer operating times, faster recharging times, and other performance optimizations. The three primary functional components for lithium ion battery are the anode, cathode and electrolyte, for all of which a variety of materials may be used. Steady progress has been made by using improved materials for the anode, cathode, electrolyte and the interfaces between them. The cathode used is generally one of three materials viz. an oxide layered structure, such as $LiCoO_2$, polyanion based oxide, $LiFePO_4$ type, or a spinel structure, such as $LiMn_2O_4$. Electrolyte used in lithium ion batteries consists of lithium salts, such as $LiPF_6$, $LiBF_4$, or $LiClO_4$ dissolved in an organic solvent, namely ethylene carbonate and di-ethyl carbonate. A liquid electrolyte conducts the Li ions, which are acting as carriers between the cathode and the anode when current is passed through an external circuit. Typical conductivity of liquid electrolyte at room temperature (i.e. 20 °C) is in the range of 10 mS/cm. The choice of material for the anode, cathode, and electrolyte depends on the voltage, capacity, life and safety of lithium ion battery can change dramatically.

Various anode materials such as transition metal oxides (MoO_2, WO_3), and chalcogenides (Li_xMVO_4, M = Co, Zn, Ni), polymers (Polyacetylene, Polythiophene), lithium alloys (Li-Al, Li-Si, Li-Sn, Li-Bi, Li-Pb, Li-Sb, etc) and carbon based (graphite, MCMB, disordered carbon) materials have been proposed for lithium ion batteries. However, the carbon based materials are

used for commercial lithium ion batteries. These materials have (i) higher specific charge capacity and negative redox potential than most of the metal, oxides, chalcogenides and polymers, and (ii) dimensional stability and better cyclic performance than other anode materials proposed. The insertion of lithium into carbonaceous materials is known as intercalation. The lithium intercalation sites in carbonaceous materials strongly depend upon the crystallinity, the microstructure and morphology of host materials. Thus, the kinds of carbon determine the current/voltage characteristics of electrochemical intercalation reaction and risk of solvent co-intercalation. Carbons those are capable of reversible lithium intercalation are of two types one graphitic having layered structure and other nongraphitic with number of structural defects. Intercalation in graphitic carbon is the stepwise formation of periodic array of unoccupied layer gaps at low concentration of guest species. The second types are non-graphitic carbon consisting of carbon atoms mainly arranged in planar hexagonal network but without far reaching crystallographic order in *c*-direction. The non-graphitic carbon can store more lithium than graphitic one. The charge/discharge profile of non-graphitic materials differs considerably from graphitic carbons. Various attempts have been made to improve the carbon based host materials. Ball milling of graphite, doping of hetro-atoms in graphite lattice (B, N) and composites of carbon with elements that can make alloy with lithium (such as Si, Sn etc) were some of the attempts.

Nanostructured materials have attracted great interest in recent years because of their unusual mechanical, electrical and optical properties endowed by confining the dimensions of such materials. These materials are becoming increasingly important for electrochemical energy storage devices. There are several potential advantages associated with the development of materials with electrodes made with nanomaterials for lithium batteries. The advantage of using nanomaterials are better accommodation of the strain of lithium insertion/removal, improved cycle life, higher electrode/electrolyte contact area leading to higher charge/discharge rates, short path lengths for electron and Li^+ transports. Carbon nanotubes (CNTs) are a candidate material for use in lithium ion batteries due to their unique set of electrochemical and mechanical properties. Several years after the discovery of CNTs by Iijima, Nalimova *et al* studied lithium vapor interactions with MWCNTs. Subsequently Che *et al* and Frackowiak *et al* measured the electrochemical properties. Since then, there have been numerous reports evaluating the use of

CNTs in lithium ion batteries. Lithium ion capacity in CNTs results from effective diffusion of lithium ions into stable sites located on the nanotube surface and/or inside individual nanotubes through end cap or sidewall openings. In addition, lithium ion intercalation can occur between the MWCNT layers (entering through lattice defects or open nanotube ends) or in the interstitial sites of close packed SWCNT bundles (the 2-dimensional triangular lattice arising from van der Waals attractions between nanotube sidewalls). In addition to Li_xC capacity, there are calculations, which propose a curvature induced lithium condensation inside the core of the nanotubes. These results show a linear dependence with diameter that could improve the capacity further for CNTs having larger diameter.

This PhD thesis aims at exploring and investigating different form of carbon (bulk as well nanostructure) based anode materials for lithium ion batteries. A systematic study has been performed including synthesis of materials, structural characterization, fabrication of cell and electrochemical testing. The work in the thesis has been divided into following seven chapters.

Chapter 1 presents a brief overview on energy requirements, history of battery development, working principle and components used in lithium ion battery. This chapter also introduces various advantages of lithium ion battery over other rechargeable batteries available.

Chapter 2 presents a literature review on lithium-ion batteries and their electrode materials. The basic concept of rechargeable batteries and lithium ion batteries are discussed. The properties and present status of the cathode materials for lithium ion batteries are summarized. These include $LiCoO_2$, $LiNiO_2$, $LiMn_2O_4$, $LiFePO_4$, and their transition metal doped derivative compounds. The detailed survey on anode materials for lithium-ion batteries has been conducted. The advantages, disadvantages, and challenges of carbon based anode materials are discussed in details. The alloy based and metal oxide anode materials are discussed briefly. Finally, a brief description about electrolytes used in lithium-ion battery system has been made.

Chapter 3 contains the experimental details. The experimental procedure and techniques including for materials synthesis have been described. The carbon nanostructures were synthesized by chemical vapor deposition (CVD) of acetylene gas using catalyst of transition metal oxide compound containing lithium. The boron doping in graphite has been done by conventional solid-state synthesis method. The Si-graphite system has been prepared by using

planetary ball mill. The graphite powder has been ground for different time periods in liquid medium (methanol) by using planetary ball-mill to induce size and morphology change in the powder. The morphology of the synthesized materials has been examined under field emission scanning electron microscope (FE-SEM) (FEI QUANTA 200 F) and simultaneous elemental analysis of the powders was also carried out using energy dispersive X-ray analysis (EDX). The carbon nanostructured samples were also examined by transmission electron microscopy (TEM) (FEI Technai G2-20-S-Twin microscope) at an operating voltage of 200 KV. X-ray diffraction (XRD) studies of the sample have been conducted using X-ray diffractometer (Bruker AXS, D8 advance). Raman spectra of the all synthesized carbonaceous materials have been recorded by Raman spectrometer (Renishaw-system 1000 B). For electrochemical measurements, teflon cells have been assembled in Ar-filled glove box (MBRAUN-MB 200G) having oxygen and moisture level below 0.1 ppm. The cell was tested at 20 °C using computer-controlled cycler (Arbin BT 200) at constant current of 100 μA in a voltage range 0.05 and 2.5V.

The results and discussion of the present work have been divided in chapter 4, chapter 5 and chapter 6.

Chapter 4 presents the synthesis and structural characteristics of catalysts powder, substrate (anodized alumina) and CNTs. The electrochemical performances in lithium ion cell of two types of carbon nanostructures i.e. tubes (CNTs) and ribbons (CNRs) synthesized with different catalysts have been studied. The effect of temperature on synthesis of CNTs shows that quality of tubes synthesized at higher temperature (650) has better graphitization compared to those synthesized at lower temperature (580 °C). Different types of carbon nanostructure viz. straight, coils, ribbon and waved morphologies have been observed for different novel catalysts ($LiNiCoO_2$, $LiFePO_4$, $LiCu_{0.5}Zn_{0.5}O$, $LiMn_2O_4$ and $LiMn_{1.8}Fe_{0.2}O_4$) used in this study.

The structural study of synthesized CNTs / CNRs have been carried out by XRD, Raman spectroscopy, FE-SEM and TEM. The results of CNTs synthesized with different catalysts have been analyzed and compared. The electrochemical behavior of the MWCNTs synthesized using $LiNi_{0.5}Co_{0.5}O_2$ catalyst and carbon nanoribbon grown with $LiFePO_4$ catalyst have been studied as anode in a lithium ion cell. The reversible capacity and coulombic efficiency of cell using CNTs as anode have been estimated and are found to be higher than that observed in MWCNTs grown over conventional catalysts such as iron, cobalt and nickel. The anode performance of purified

carbon nanoribbons has been studied and the reversible lithium intercalation capacity has been found to be about 345 mAh/g. The coulombic efficiency has been stabilized at approximately 98 % from the fifth cycle. The electrochemical behavior of such CNRs shows better reversible capacity and higher coulombic efficiency compared to graphite and CNTs synthesized using conventional catalyst. Such improvement in electrochemical behavior of these carbon nanostructures is related to their structural properties.

Chapter 5 has been divided into two parts. In the first part, the results of boron doped graphite have been analyzed and discussed. The second part consists of results and discussion of ball milled graphite material.

Structure and electrochemical performance of boron doped graphite samples have been studied comparatively. The different boron content (1, 3 & 5 wt %) enhances the growth of crystallite size expressed by the parameters $L_{c(002)}$ and $L_{a(110)}$ determined from XRD patterns of pure and boron doped graphite samples. The decrease in d-value of (002) peak of graphite has been observed in boron doped graphite samples. The new band in Raman spectra appears at 1620 cm^{-1}, not observed for pure graphite material. The shift in E_{2g2} band at 1578 cm^{-1} has been observed, which represents the change in electronic structure of graphite due to boron doping. The electrochemical performances of the doped materials show better reversible capacity compared to pure graphite. The coulombic efficiency of all boron doped graphite samples attains up to 98 % which then remains constant. However the coulombic efficiency of pure graphite sample is about 92% after 2nd cycles.

Graphite-silicon mixtures with 1, 5, 10 and 15 wt% Si, have been prepared in liquid medium using planetary ball mill and heat treating at 1200 °C. The XRD results show the formation of SiC which increases with the increase in Si content. The XRD results also show that the disorderness in graphite structure increases with increase in Si content. The Raman spectra of the of two compositions i.e. 1 and 15 wt % Si mixed graphite show the disorderness increases with increasing Si-content as calculated by intensity ratio of D to G-band. Raman spectra are in agreement with the XRD results. The electrochemical behavior of these two compositions has been studied. The first discharge capacity, coulombic efficiency and capacity retention of anode having 1 wt% Si are found better than that of 15 wt% Si-graphite material.

Chapter 6 presents the results of ball-milled graphite and anode of the same material tested in Li-ion cell. The powder has been ground in liquid medium (methanol) for different time periods of (8, 16, 24, 32 and 80 hours) using planetary ball-mill in order to reduce the grain size as well as increase the disorderness in the graphite lattice. The effect of mechanical grinding on morphology and electrochemical performance of graphite powder with respect to lithium insertion was studied. The powders after milling have been characterized by XRD, FE-SEM, TEM, TGA, Raman Spectra and anode performance has been studied by using it in lithium ion cell. The XRD results show that the relative intensity of (002) Bragg peak diminishes with increasing milling time, which implies that mechanical grinding, generates an increasing amount of unorganized (disordered) carbon). Raman spectra of ball-milled graphite show that the intensity and full width at half maximum (FWHM) of D-band increases with milling time. These results indicate that the Raman spectra are consistent with XRD results. The microstructure and morphology of milled graphite have been analyzed by FE-SEM and TEM. The grain size of milled powder decreases with longer milling time. The electrochemical study shows that charge capacity of powder milled for 80 hours is higher compared to powder milled for 24 and 32 hours. However, the slope of discharge profile becomes sharper/steeper for longer milling time. The increase in charge capacity of powder milled for longer time has been related to lower particle size and formation of new sites (voids and cavities) for lithium insertions. All the results are analyzed and discussed in details.

Chapter 7 presents the major conclusions of the present study and future scope of work.

A. **Patent : Kuldeep Rana**, Anjan Sil and S.Ray, "An improved high energy density silicon-graphite anode material and method for preparation thereof". *(Filed: CINIITR000 100003, dated 23.02.2010)*

B. Papers in Referred Journals

[1] **Kuldeep Rana,** Anjan Sil and S. Ray, "Synthesis of ribbon type carbon nanostructure using $LiFePO_4$ catalyst and their electrochemical performance", *Materials Research Bulletin 44 (2009) 2155–2159.*

[2] **Kuldeep Rana,** Anjan Sil and S.Ray, "Modification of the Structure of Multi-walled Carbon Nanotubes by choice of catalyst and their Electro-chemical Behaviour", *Materials Chemistry and Physics 120 (2010) 484-489.*

[3] **Kuldeep Rana**, Anjan Sil and S.Ray, "Synthesis and characterization of carbon nanotubes by using catalyst $LiNi_{0.5}Co_{0.5}O_2$ on anodized alumina substrate", *Advanced Materials research 67 (2009) 197-202.*

C. Manuscripts under preparation

[1] Kuldeep Rana, Anjan Sil, S. Ray, Structural modification in boron doped graphite and its electrochemical studies.

[2] Kuldeep Rana, Anjan Sil, S. Ray, Structural and magnetic properties of carbon nanoribbon.

[3] Different shapes of carbon nanostructure synthesize by novel catalysts.

[4] Ball-milled graphite as anode material for lithium ion battery.

D. Conference

[1] **Kuldeep Rana,** Anjan Sil and S. Ray, "Synthesis and characterization of bromine intercalated graphite material", Proceedings of the 54 th **DAE** Solid State Physics Symposium (accepted).

[2] **Kuldeep Rana**, Anjan Sil and S. Ray, "Synthesis and characterization of Mg doped Manganese oxide system and its lithiation", Proceedings of the 53rd **DAE** Solid State Physics Symposium volume53 (2008) page no.1279.

[3] **Kuldeep Rana**, Anjan Sil and S. Ray, "Synthesis of lithium doped carbon nanotubes and their structural and electrochemical characterization", International Conference on Nanomaterials and Devices : processing and application, 11-13 december 2008, pp.66.

[4] **Kuldeep Rana**, Anjan Sil, and S. Ray, "Effect of mechanical grinding on graphite powder characteristics", PSSARA-2006: Workshop on Emerging Trends in Power Source Systems for Aerospace and Related Applications, 6-8 October, A-11, pp.6,2006, RCI, Hyderabad.

[5] **Kuldeep Rana**, Amrish Panwar, Yogesh Sharma, Anjan Sil and S. Ray, "Synthesis and characterization of $(MnO_2)_{1-x}(MgO)_x$ cathode base material", PSSARA-2006: Workshop on Emerging Trends in Power Source Systems for Aerospace and Related Applications, 6-8 October, A-12, pp.7, 2006, RCI, Hyderabad.

A journey is easier when you travel together. Interdependence is certainly more valuable than independence. This thesis is the result of five years of work whereby I have been accompanied and supported by many people. It is a pleasant aspect that I have now the opportunity to express my gratitude for all of them.

I would like to express my gratitude to all those who gave me the possibility to complete this thesis. It is my great privilege and pleasure to record my heartiest thanks and deep sense of gratitude to my supervisor **Dr. Anjan Sil,** for his valuable guidance and untiring efforts throughout the tenure of this work. His timely help, constructive criticism, positive attitude, painstaking efforts, humanistic and warm personal approaches enabled me to compile the thesis in its present form. I also express my sincere gratitude and indebtedness for his invaluable guidance, cooperation, encouragement and providing all possible assistance to complete this work. His painstaking efforts in going through the manuscript, giving good suggestions for its improvement are gratefully acknowledged. I also express my sincere gratitude and indebtedness to **Dr. Subrata Ray,** for his invaluable guidance, cooperation, encouragement and providing all possible assistance to complete this work. He has been my inspiration and constant driving force when targets appeared to be difficult to achieve during the course of my PhD work. His painstaking efforts in going through the manuscript, giving good suggestions for its improvement are gratefully acknowledged.

I also express my sincere gratitude to Professor **Samar Basu** for providing me the excellent facilities for battery testing at IIT Kharagpur. I am very much thankful to him for helping me in every respect during my stay at IIT Kharagpur, this work was not possible without his suggestions and guidance.

I am deeply indebted to Dr. S.K. Nath, Professor and Head of the Department of Metallurgical and Materials Engineering (MMED), Indian Institute of Technology Roorkee (IITR), for his help and providing the excellent facilities in the department for the research work. I wish to also record my gratitude to Dr. Satya Prakash, Dr. V.K. Tiwari and Dr. P.S. Misra, Professors and former Heads of MMED and the Head, Institute Instrumentation Centre (IIC), for

their co-operation in providing excellent facilities during the entire course of my experimental work. I am also thankful to all the faculty members of the MMED.

I am very much thankful to Mr. Vijay kumar Sharma, Ajeet Pandey and Vinay Pratap Singh and Nigamanand Ojha, friends from IIT Roorkee, who helped me a lot during thesis submission. I wish to place on record my sincere thanks to the technical and administrative staff of the Department of Metallurgical and Materials Engineering. My five years stay in IIT Roorkee was made pleasant due to my association with several friends and colleagues. I appreciate each one of them for their moral support and camaraderie, which helped to keep things in perspective. My sincere thanks are due to Dr. Amrish Panwar, Dr. Suresh Rana (kandi), Miss Priti Singh, Mr Gurpreet singh, Dr. Sandeep Bansal, Deepak Sharma, Dr. Rishi Asthana, Ms. Vineeta Rawat, Dr. Araya, Dr. K P Singh, Mr. Kuntal Maiti, Dr. Komal Dave, Mr. Triloki Panth, Vivekanand. The inspiration, support, cooperation and patience, which I have received from friends outside IIT Roorkee, specially Ms. Neelam Rawat (Neelu) who has been with me every moment of time, Mrs. Rashmi Rawat, Kuldeep Panwar, Ashutosh Gaur, Anant, Bhagwati Prasad, Sandeep Majumdar, Prabhakar Sati, are beyond the scope of any acknowledgement, yet I would express my heartfelt gratitude to them.

At this time, I cannot help but remember my late father Mr. M.S. Rana with reverence and great admiration that had left no stone unturned for my sake, I humbly dedicate this thesis to my father. I feel a deep sense of gratitude for my mother Mrs. Sakuntala Devi Rana who formed part of my vision and taught me the good things that really matter in life and do whatever best, she could do for me. I am also grateful to all my family members for their kind co-operation and help during the entire duration of this work, especially to brothers Pradeep, Sandeep and sister in law Mrs. Lalita Rana. Above all, I am highly indebted to the almighty God, who blessed me with spiritual support and fortitude at each and every stage of my work.

(KULDEEP RANA)

Date:

Roorkee

LIST OF TABLES

Table No.	Title	Page No.
2.1	Characteristics of representative negative electrode materials for lithium batteries.	14
3.1	Diameter obtained by anodization of aluminum in different electrolytes.	53
4.1.	The pore diameter obtained by using different electrolyte bath.	88
4.2.	Raman spectral parameters of carbon nanotubes synthesized with different catalysts.	111
5.1	Crystallite size of graphite and boron-doped graphite calculated from XRD patterns.	126
5.2	Raman spectral parameters obtained after curve fitting experimental spectra using Lorentzian bands (G, D, D′).	129
5.3	Raman spectroscopic parameters obtained after curve fitting experimental spectra using Lorentzian bands (G, D).	142
6.1	Raman spectroscopic parameters obtained after curve fitting experimental spectra using Lorentzian bands (G, D).	159
6.2	First discharge, charge and irreversible capacity of unmilled and milled graphite powders for 24, 32 and 80 hours.	160

LIST OF FIGURES

Figure No.	Title	Page No.
2.1	Energy density of different types of secondary batteries.	7
2.2	Schematic diagram of battery and its operation	10
2.3	Anode Materials for Li-ion Battery	15
2.4	Different types of carbon (a) Soft carbon (b) hard carbon and (c) graphite.	19
2.5	(a) Structure of hexagonal graphite showing ABAB... stacking (b) Rhombohedral graphite showing ABCABC... stacking	20
2.6	Lithium intercalated compounds (stage 1 yellow and stage 2 blue) synthesized in our lab.	21
2.7	(a) Structure of LiC_6 showing the AA layer stacking (b) simplified representation (c) Perpendicular view of LiC_6 and (d) LiC_2	22
2.8	(a) Staging phenomena during intercalation of graphite constant current curve and (b) schematic voltametric curve.	23
2.9	Typical schematic charge/discharge profile of graphite for first (a) and second (b) cycle.	24
2.10	Schematic drawing of some mechanisms for reversible lithium storage in high specific charge carbonaceous materials as proposed.	27
2.11	Different structures of MWCNTs. Top-left: cross-section of a MWCNT, Top-right: Symmetrical or non-symmetrical cone shaped end caps of MWNTs. Bottom-left: a SWCNT with a diameter of 1 or 2 nm. Bottom-right: A MWCNT with defects.	34
2.12	Schematic representations of the CNTs synthesizing apparatus	36
2.13	The two growth modes of filamentous carbon	38
2.14	Schematic view of the nucleation of a cap and a SWNT. (a) Hydrocarbon decomposition. (b) Carbon diffusion in the surface layer. (c) Super-saturation of the surface and formation of the cap.	39

(d) Growth of a SWNT

3.1	Schematic flow diagram of experimental work out	48
3.2	The detailed steps for the formation of the compounds by solid state reaction method.	49
3.3	The detailed steps for the synthesis of the studied materials by sol-gel method.	51
3.4	SEM image of well-ordered nanopore arrays (a) top view (b) side view.	52
3.5	Schematic of two-step anodization process.	53
3.6	Ball-mill (planetary ball-mill) used for milling of graphite powder.	55
3.7	Chemical vapor deposition setup.	57
3.8	Schematic diagram of DTA setup.	59
3.9	Schematic diagram of X-ray Diffractometer, in which θ is a glancing angle and 2θ is a diffraction angle.	60
3.10	Various components used in Raman Spectrometer.	64
3.11	Different geometry of study of sample in Raman spectrometer.	65
3.12	A schematic diagram of electron interaction with a thin specimen	67
3.13	Schematic diagram of Scanning electron microscope.	68
3.14	Schematic diagram of transmission electron microscope in image mode.	70
3.15	Schematic diagram showing the geometry of diffraction pattern formation.	73
3.16	Different steps used for cell-fabrication.	75
3.17	Schematic diagram of cell used for electrochemical testing.	75
4.1	FE-SEM micrograph of catalysts particles of (a) $LiMn_2O_4$ (b) $LiMn_{1.8}Fe_{0.2}O_4$ (c) $LiCu_{0.5}Zn_{0.5}O_2$ (d) $LiFePO_4$ (e) $LiCo_{0.5}Ni_{0.5}O_2$	79
4.2	Typical current density-time curves for anodization process under constant-voltage mode at a voltage of 40 V and in a 3-wt% oxalic acid bath, maintained at 25 °C.	82
4.3	(a) Pure aluminum sample as-received (b) FE-SEM micrograph of the unpolished surface and (c) surface showing electro polished area	83

4.4	FE-SEM micrograph of AAO image obtained with H_3PO_4 solution carried out for 60 minutes at 100 V (a) pore structure all over the sample (b) FFT image as inset (c) separate boundaries between pores and (d) frequency histogram of distribution of pore diameter.	85
4.5	FE-SEM micrograph of AAO image obtained with oxalic acid electrolyte carried out at 40 V for 60 minutes (a) regular pore structure, (b) regular pore structure with separate boundaries (c) at higher magnification and (d) frequency histogram of distribution of pore diameter.	86
4.6	FE-SEM micrograph of AAO image obtained with H_2SO_4 solution carried out at 24 V for 60 minutes (a) pores distributed all over sample (b)at magnification 1,20,000X (c) at magnification 2,40,000X and(d) frequency histogram of distribution of pore diameter.	87
4.7	(a) Top view of substrate deposited with catalyst particle (b) EDX spectrum of deposited catalyst particle (c) growth of carbon nanostructure from catalyst (d) and anodized alumna as self-catalyst.	89
4.8	FE-SEM image of CNTs grown by catalytic decomposition of acetylene gas over $LiNi_{0.5}Co_{0.5}O_2$ at 580 °C (a & b) and at 650°C (c & d).	91
4.9	TEM micrograph of CNTs synthesized at 650 °C by catalytic decomposition of acetylene gas over $LiNi_{0.5}Co_{0.5}O_2$, (a) Morphology of tubes and (b) large inner diameter of tube with SAD pattern as inset.	92
4.10	XRD patterns of CNTs, synthesized by catalytic decomposition of acetylene gas over $LiNi_{0.5}Co_{0.5}O_2$ at (a) 580 °C and (b) 650 °C.	93
4.11	Raman spectra of CNTs synthesized by catalytic decomposition of acetylene gas over $LiNi_{0.5}Co_{0.5}O_2$, at (a) 580 °C and (b) 650 °C.	93
4.12	Elemental analysis by EDX of CNTs synthesized by catalytic decomposition of acetylene gas over $LiNi_{0.5}Co_{0.5}O_2$.	95
4.13	FE-SEM image of CNTs grown at 650 °C by catalytic	96

decomposition of acetylene gas over $LiNi_{0.5}Co_{0.5}O_2$, (a) curving morphology, (b) straight morphology, (c) coiled morphology and (d) coiled CNTs at higher magnification.

4.14 TEM micrographs of CNTs showing inner channel in (a) SAD pattern in (b) and helix morphologies both in (c) and (d) synthesized by catalytic decomposition of acetylene gas over $LiNi_{0.5}Co_{0.5}O_2$. **97**

4.15 FE-SEM micrographs (a) shows high yield (b) CNRs at magnification X 4 K, (b) at X 16 K (d) and growth of CNRs starts from catalyst shown by red mark. **99**

4.16 (a) TEM micrographs show ribbon type structure (b) at higher magnification and inset showing the SAD pattern of CNRs and **(c)** growth of CNRs from catalyst as shown inside a by square boundaries. **100**

4.17 FE-SEM micrograph of CNTs grown with a mixture of lithium Zn and Cu oxide catalyst shows wavy structure and (a) shows the higher yield (b, c & d) at different magnifications shows the most of the tubes have wavy structure. **102**

4.18 TEM micrographs of CNRs synthesized with a mixture of lithium Zn and Cu oxide catalyst (a) wavy structure (b) wavy structure at higher magnification(c) bamboo type morphology (d) SAD pattern showing the polycrystalline nature of CNTs. **103**

4.19 FE-SEM micrographs of CNBs (a) carbon nanoparticles joined together (b) shows the high yield (c) SAD pattern show the amorphous nature of these CNB (d) TEM image shows the cluster of CNBs. **105**

4.20 FE-SEM micrographs of CNTs grown with $LiMn_{1.8}Fe_{0.2}O_4$ catalyst (a & b) showing high yield (c) catalyst particles is shown at tip of CNTs (tip growth mode) (d) CNTs at different magnification and different area. **106**

4.21 TEM micrographs of CNTs growth using catalyst $LiMn_{1.8}Fe_{0.2}O_4$ Bamboo like structure **(b)** large inner diameter as compared to wall **107**

thickness **(c)** SAD pattern as inset **(d)** agglomerated tubes.

4.22 XRD patterns of CNTs, synthesized by catalytic decomposition of acetylene gas over (a)$LiNi_{0.5}Co_{0.5}O_2$ (b)$LiFePO_4$ (c)$LiCu_{0.5}Zn_{0.5}O$ (d)$LiMn_2O_4$ and (e) $LiMn_{1.8}Fe_{0.2}O_4$ **109**

4.23 Raman spectra of CNTs, synthesized by catalytic decomposition of acetylene gas over (a) $LiNi_{0.5}Co_{0.5}O_2$ (b) $LiFePO_4$ (c) $LiCu_{0.5}Zn_{0.5}O$ (d) $LiMn_2O_4$ and (e) $LiMn_{1.8}Fe_{0.2}O_4$. **112**

4.24 Typical first charge-discharge profile of a cell Li / $LiPF_6$ (in EC:DEC) / electrode of CNTs synthesized by catalytic decomposition of acetylene gas over $LiNi_{0.5}Co_{0.5}O_2$, in terms of the voltage of the electrode containing CNTs measured against the lithium metal foil. **114**

4.25 Discharge profile measured against lithium foil for 2nd to 11th cycle, indicating capacity-fading behavior with number of cycles for electrode of CNTs synthesized by catalytic decomposition of acetylene gas over $LiNi_{0.5}Co_{0.5}O_2$. **116**

4.26 Variation of coulombic efficiency with number of cycles in cells with electrode made of CNTs synthesized by catalytic decomposition of acetylene gas over $LiNi_{0.5}Co_{0.5}O_2$. **117**

4.27 Typical first charge-discharge profile of a cell Li / $LiPF_6$ (in EC:DEC) / electrode of CNRs **118**

4.28 Discharge profiles measured against lithium foil for 2nd to 14th cycles, and inset showing variation of columbic efficiency with number of cycles in cells with electrode made of CNRs **119**

5.1 FE-SEM micrographs of (a) undoped graphite and doped graphite with (b) 1 wt %, (c) 3 wt%, (d) 5 wt % of boron. **125**

5.2 x-ray diffraction patterns of graphite and graphite doped with boron of 1 wt%, 3 wt% and 5 wt %. **126**

5.3 First order Raman spectra of pure graphite and boron-doped graphite: (a) $C_{1.0}B_{0.0}$ (b) $C_{0.99}B_{0.01}$ (c) $C_{0.97}B_{0.03}$ and (d) $C_{0.95}B_{0.05}$. **128**

5.4 Charge capacity and potentials during first discharging/charging **130**

cycles of (a) undoped graphite, (b) $B_{0.01}C_{0.99}$, (c) $B_{0.03}C_{0.97}$ and (d) $B_{0.05}C_{0.95}$ samples.

5.5 Discharge profiles against lithium metal foil for all cycles studied from second cycle for the samples of (a) undoped graphite, (b) $B_{0.01}C_{0.99}$, (c) $B_{0.03}C_{0.97}$ and (d) $B_{0.05}C_{0.95}$ 131

5.6 Plot of cycle efficiency and cycle number in the pure graphite and boron-doped samples. 132

5.7 Thermo gravimeteric analysis of unmilled graphite powder and milled Si-graphite powder. 135

5.8 EDX spectra off (a) Si 1wt% (b) Si 5 wt % (c) Si 10 wt % and (d) Si 15 wt % mixed graphite powder. 136

5.9 FE-SEM images of (a) pure graphite, (b) Si 1wt%, (c) Si 5 wt%, (d) Si 10 wt% and (e) Si 15 wt% mixed graphite powder. 137

5.10 EDX mapping of Si-graphite mixture prepared by ball-milling of (a) Si 1wt% (b) Si 15 wt % mixed graphite. 138

5.11 XRD pattern of (a) pure graphite, (b) 1 wt% Si, (c) 5 wt % Si, (d) 10 wt % Si and (e) 15 wt % Si mixed graphite powders ball milled for 5 hours and heat treated at 1200 °C. 139

5.12 The effect of Si content in graphite powder on (a) (002) peak intensity and (b) FWHM of (002) and (101). 140

5.13 Raman Spectra of (a) Pure graphite (b) Si 1wt% (c) Si 10 wt% and (d) Si 15 wt% mixed graphite. 141

5.14 Charge capacity and potentials during first discharging/charging cycles of (a) pure graphite, and the graphite samples containing (b) Si 1 wt% (c) Si-15 wt%. 143

5.15 Discharge profile of (a) for Si-1 wt% (b) Si 15 % and (c) cycling behavior of both compositions. 145

6.1 XRD pattern of ball-milled graphite for pure graphite and milled for different time 0h, 8h, 16h, 24h, 32h and 80 h. 150

6.2 The effect of milling time on (002) Bragg peak of graphite and inset showing the variation in intensity of same peak with milling time 151

6.3	FE-SEM micrographs of ball-milled graphite for different time period of (a) 0 h (b) 8 h (c) 16 h (d) 24h (e) 32 h and (f) 80 h.	**152**
6.4	(a) Variation of particle size with milling time and (b) Increase of iron content with milling time.	**153**
6.5	TEM micrograph of ball milled graphite for 80-hours (a) plates like structure (b) SAD pattern (C) morphology at higher magnification (d) agglomeration of milled powder.	**155**
6.6	TGA analysis of unmilled and ball-milled graphite powders in liquid medium for different time periods in planetary ball-mill.	**156**
6.7	Raman spectra of (a) unmilled graphite powder (b) milled graphite powder for 32 hours and (c) milled graphite powder for 80 hours.	**158**
6.8	First charge and discharge capacity of (a) unmilled graphite and graphite milled in liquid medium using planetary ball-mill for (b) 24 hours (c) 32 hours (d) 80 hours.	**161**
6.9	The discharge behavior from 2nd cycle onward of (a) milled graphite (b) 24 hours milled graphite (c) 32 hours milled graphite and (d) 80 hours milled graphite powder in liquid medium using planetary ball-mill.	**163**
6.10	The coulombic efficiency of (a) milled graphite (b) 24 hours milled graphite (c) 32 hours milled graphite & (d) 80 hours milled graphite powder in liquid medium using planetary ball-mill.	**164**

CONTENTS

	Page No.
Candidate's Declaration	**i**
Abstract	**iii**
List of publications	**ix**
Acknowledgement	**xi**
List of tables	**xiii**
List of figures	**xv**
Contents	**xxiii**
Chapter-1: INTRODUCTION	**1-5**
Chapter-2: LITERATURE REVIEW	**7-45**
2.1 INTRODUCTION OF LITHIUM-ION BATTERY	**7**
2.2 HISTORICAL DEVELOPMENT OF LITHIUM-ION BATTERY	**8**
2.3 WORKING PRINCIPLE OF LITHIUM-ION BATTERY	**9**
2.4 CATHODE MATERIALS FOR LITHIUM-ION BATTERY	**11**
2.4.1 Lithium Cobalt Oxides	**11**
2.4.2 Lithium Nickel Oxides	**12**
2.4.3 Layered $LiMnO_2$	**12**
2.4.4 Spinel Lithium Manganese Oxides	**13**
2.4.5 Olivine $LiFePO_4$	**13**
2.5 ANODE MATERIALS FOR LITHIUM-ION BATTERIES	**14**
2.5.1 Lithium Alloys as Negative Insertion Electrode Materials	**15**
2.5.2 Silicon-Carbon Based Anode Materials for Lithium-ion Battery	**17**
2.5.3 Carbon Based Insertion Electrode (Anode) Materials	**18**
2.5.3.1 Structure of Graphitic carbon	**19**
2.5.3.2 Electrochemical Li Storage in Graphite Carbon	**21**
2.5.3.3 Stage Formation by Lithium Intercalation	**23**
2.5.3.4 Reversible and Irreversible Capacity	**24**

2.5.4. Non-graphitic Carbon as Anode Materials of Lithium-Ion Battery 25
2.5.5 Modified Carbon as Anode Materials 28
2.5.5.1 Oxidation of Graphite 28
2.5.5.2 Coating by Polymers 29
2.5.5.3 *Carbon Host Containing Heteroatom as Anode Materials* 29
2.5.6. Ball-Milled Graphite as Anode Materials for Li-ion Battery 31
2.5.7 Carbon Nanotubes as Anode Materials for Li-ion Battery 33
2.5.7.1 Synthesis Methods 35
2.5.7.2 Chemical Vapour Deposition (CVD) Method 35
2.5.7.3 Growth Mechanism of Carbon Nanotubes 37
2.5.7.4. Catalyst Used for Growth of CNTs 39
2.5.7.5. Electrochemical Storage of Lithium into CNTs 40
2.5.7.6. Electrochemical Storage of Lithium into MWCNTs 41
2.5.7.7 Electrochemical Storage of Lithium into SWCNTs 42
2.6 ELECTROLYTE FOR LITHIUM-ION BATTERIES 43

CHAPTER- 3: EXPERIMENTAL TECHNIQUES 47-76
3.1 INTRODUCTION 47
3.2 SAMPLE PREPARATION 48
3.2.1 Solid State Reaction Method 48
3.2.2 Sol-gel Method 50
3.2.3 Synthesis of Anodic Alumina Templates 52
3.2.4 Ball-Milling 54
3.2.5 Chemical Vapor Deposition (CVD) 56
3.3 THERMAL ANALYSIS 58
3.3.1 Thermal Gravimetric Analysis (TGA) 58
3.3.2 Differential Thermal Analysis 58
3.3.2.1 Instrumentation 59
3.4 X-RAY DIFFRACTION (XRD) 59
3.4.1 Indexing of X-ray Diffraction Patterns 60
3.4.2 Crystallite Size Determination 62

3.5 RAMAN SPECTROSCOPY 63
3.5.1 Basic Principle 63
3.5.2 Instrumentation 64
3.6 FIELD EMISSION SCANNING ELECTRON MICROSCOPE (FE-SEM) 66
3.6.1 Principle of Field Emission Scanning Electron Microscopy 66
3.6.2 Working of FE-SEM 68
3.7 TRANSMISSION ELECTRON MICROSCOPE 69
3.7.1 Principle of Transmission Electron Microscopy 69
3.7.2 Imaging Mode Methods 70
3.7.2.1 *Bright field* 70
3.7.2.2 *Diffraction contrast* 71
3.7.2.3 *Diffraction* 71
3.7.3 Sample Preparation 72
3.7.4. Indexing of Polycrystalline Diffraction Rings 73
3.8. ELECTROCHEMICAL MEASUREMENTS 74
3.8.1 Electrode Preparation 74
3.8.2 Cell Fabrication 74
3.8.3 Electrochemical Testing 75
CHAPTER-4: STRUCTURURAL AND ELECTROCHEMICAL BEHAVIOR OF CARBON NANOSTRUCTURES 77-121
4.1 INTRODUCTION 77
4.2 CATALYST PARTICLES USED 78
4.3 ANODIZATION 81
4.4. EFFECT OF ACID BATH USED FOR ANODIZATION 82
4.5 DEPOSITION OF CATALYST PARTICLES ON SUBSTRATE 88
4.6 CATALYTIC GROWTH of CNTs BY CVD 89
4.6.1 Effect of Temperature on Structure of CNTs 90
4.6.2 Effect of Catalytic Particles on Structure and Morphology of CNTs 94
4.6.3 Morphology of CNTs 95
4.6.3.1 CNTs grown with $LiNi_{0.5}Co_{0.5}O_2$ Catalyst 95
4.6.3.2 CNTs grown with $LiFePO_4$ Catalyst 98

4.6.3.3 CNTs grown with Mixture of Lithium Zinc and Cu Oxide Compound ($LiCu_{0.5}Zn_{0.5}O$) **101**
4.6.3.4 CNTs grown with $LiMn_2O_4$ Catalyst **104**
4.6.3.5 CNTs grown with $LiMn_{1.8}Fe_{0.2}O_4$ Catalyst **106**
4.6.4 XRD Results **108**
4.6.5 Raman Spectra **110**
4.6.6 Electrochemical Measurements **113**
4.6.6.1 Electrochemical Behavior of CNTs Grown With $LiNi_{0.5}Co_{0.5}O_2$ **113**
4.6.6.2 Electrochemical Behavior of CNTs Grown With $LiFePO_4$ **117**
4.7 SUMMARY **120**

CHAPTER-5: STRUCTURAL AND ELECTROCHEMICAL BEHAVIOR OF CARBON HOST CONTAINING HETEROATOMS (B, Si) AS ANODE MATERIALS **123-147**
5.1 INTRODUCTION **123**
5.2 STRUCTURAL AND ELECTROCHEMICAL PROPERTIES OF BORON DOPED GRAPHITE ANODE IN Li-ion CELL **124**
5.2.1 Microstructural Studies **124**
5.2.2 x-ray Diffraction **125**
5.2.3 Raman Spectroscopy **127**
5.2.4 Electrochemical Behavior of Boron-doped Graphite **129**
5.3 BALL MILLED GRAPHITE-SILICON BASED ANODE MATERIALS FOR LITHIUM-ION BATTERY **134**
5.3.1 Thermal Studies **134**
5.3.2 Microstructure/Morphology Analysis **135**
5.3.3 x-ray Diffraction Analysis **139**
5.3.4 Raman Spectroscopy **141**
5.3.5 Electrochemical Behavior **142**
5.4 SUMMARY **146**

CHAPTER-6: BALL-MILLED GRAPHITE AS ANODE MATERIAL **149-166**

FOR LITHIUM-ION BATTERY
6.1. INTRODUCTION 149
6.2. XRD RESULTS 150
6.3. MICROSTRUCTURAL STUDIES 152
6.3.1. FE-SEM Results 152
6.3.2. TEM Results 154
6.4. THERMAL ANALYSIS 155
6.5. RAMAN SPECTRA 157
6.6. ELECTRCHEMICAL MEASUREMENTS 159
6.7 SUMMARY 165

CHAPTER-7: CONCLUSIONS AND SUGGESTIONS FOR FUTURE WORK 167-172
7.1 STUDIES ON THE CARBON NANOSTRUCTURES 167
7.2 GRAPHITE MATERIALS WITH HETEROATOM (B, Si) 169
7.3 BALL-MILLED GRAPHITE AS ANODE MATERIALS FOR LITHIUM-ION BATTERY 171
7.4 SUGGESTIONS FOR FUTURE WORK 172

REFERNCES 173-195

INTRODUCTION

One of the great challenges of this century is the conversion and storage of energy, which led the scientists to develop the new alternate energy sources. The current rate of fossil fuel usage will lead to an energy crisis in future. In response to energy requirement in modern society, there is rapid development of research in energy conversion and storage devices such as batteries, super capacitors and fuel cells. Lithium ion batteries are one of the great successes of modern materials electrochemistry.

Lithium ion battery is one of the energy storage devices in which lithium ions are transported between anode and cathode due to their potential difference. During the discharge process of battery lithium ions move from the anode to the cathode, while in charging the lithium ions move from the cathode to anode.

Lithium ion batteries are commonly used as energy source in various consumer electronics devcies. Such batteries can be formed in a wide variety of shapes and sizes so as to fit into different portable electronic devices. The key advantage of using lithium ion chemistry is higher voltage than other secondary batteries (such as lead acid, nickel metal hydride and nickel-cadmium). They also do not suffer from the memory effect and have a low self-discharge rate (approximately 5 % per month) compared with other secondary batteries (30 % per month). Most of the applications of lithium ion batteries are in consumer electronics. They are capable of delivering high energy density and are considered potential energy sources for defense, automotive and aerospace applications.

The main working components of lithium ion battery are the anode, cathode and electrolyte. There are varieties of materials used for these three different components of lithium ion battery. Commercially, the most popular materials for anode are different type of carbons like hard carbon, soft carbon, mesocarbon microbeads and highly oriented pyrolytic graphite. The cathode is generally any one of three different type of materials, a layered (lithium cobalt oxide), olivine type (lithium iron phosphate) or spinel structure (lithium manganese oxide). The characteristic of battery such as

voltage, capacity, life and safety can change dramatically depending on the choice of materials for anode cathode and electrolyte.

M.S. Whittingham first proposed lithium battery in 1970s, in which TiS_2 was used as cathode and lithium metal as the anode. Such battery can be charged only once, which is known as primary battery. In this battery, lithium metal acts as anode, which poses severe safety issue that may cause an explosion. To overcome this problem lithium ion battery were developed, in which the anode is made of material containing lithium ions. Lithium ion batteries (secondary type) came into reality when Bell Labs developed a workable graphite anode alternative to lithium metal. However, the ground-breaking research has been carried out by a research group led by John Goodenough. Sony released the first commercial lithium ion battery in 1991. The cell used consists of layered oxide material specifically lithium cobalt oxide. These batteries revolutionized the market of consumer electronics.

The three components of lithium ion battery that participate in electrochemical reactions are the anode, cathode and electrolyte. Lithium can migrate in and out of anode and cathode material. The process of lithium moving into the anode or cathode is referred to as insertion (or intercalation), and the reverse process in which lithium moves out of anode or cathode is referred to as extraction (or deintercalation). The liquid electrolyte in lithium ion batteries consist of lithium salts ($LiPF_6$, $LiBF_4$, or $LiCLO_4$) dissolves in organic solvents (ethyl carbonate, di-ethyl carbonate or ether). The liquid electrolyte conducts lithium ions, which acts as a carrier between the cathode and anode when a battery passes an electric current through an external circuit. However, the organic solvents are easily decomposed on anode during charging and form a solid electrolyte interphase (SEI) which is electrically insulating and lithium ion conducting.

The performance of the lithium ion battery depends intimately on the properties of their materials. Since the birth of lithium ion secondary battery, the research on anode material has been a focus. So far a lot of anode materials have been investigated including graphitic carbon, amorphous carbon, transition metal oxide, chalcogenides, nitride, tin oxides and the alloys of aluminum, silicon and tin. Earlier lithium battery used anode of transition metal oxide (WO_2, MoO_2) but these materials have low specific capacity and low cell voltage. Polymer based anode materials such as polyacetylene and polythiophene have also been suggested, however they suffer from poor stability. The replacement of metallic lithium by lithium alloys have also been

investigated. A.N. Dey demonstrated the feasibility of electrochemical formation of lithium alloys in liquid electrolyte. Lithium can form alloy with different metal such as Al, Si, Sn, Pb, In, Bi, Sb, Ag, etc. The metals, which form alloys by electrochemical process is partially reversible and having low voltage compared to lithium as anode, provides a higher capacity than that of conventional graphite. However, the accommodation of lithium in large quantity accompanied by large volume change in host metal. Such structural changes are common to alloying reactions. There have been lot of efforts to improve the electrode integrity. Among them, the active/inactive concept has been adopted to eliminate such a large volume change during alloying/de-alloying reactions. These reactions involve mixing of two materials, one reacting with lithium (active) whereas other materials act as an inactive buffer. This concept has been tried out through various systems such as Sn-Fe-C, Sn-Mn-C and Si-C. The Si-C nanocomposites have attracted considerable interest because these materials show high capacity of the order of 1000 mAh/g for more than 100 cycles. The improvement achieved by using above concept is that the anode materials avoid cracking and hence maintaining better conduction path for lithium ion transportation.

Presently, carbon based anode materials are being used in commercially available rechargeable lithium ion batteries. These anode exhibits higher specific charge and more negative redox potential than majority of the other anode materials reported. The carbon materials also show better dimensional stability and better cycling performance than lithium alloys. Due to electrochemical reduction of the carbon lithium ions reversibly intercalate into the carbon through electrolyte and form lithium intercalation compound Li_xC_n, The site for lithium interaction in carbon host strongly depends on the crystallinity, the microstructure and morphology of the carbonaceous materials. Thus, a different type of carbon determines the electrochemical characteristics and amount of SEI formation and hence solvent intercalation. The carbon materials, which can intercalate lithium reversibly, are classified graphitic and nongraphitic carbon. In graphitic carbon, the intercalation occurs only at pristine surfaces. Through basal plane intercalation is possible at defects sites only. The general feature of intercalation into graphite is the stepwise formation of a periodic array of unoccupied layer gaps at low concentrations of lithium ions called stage formation. The staging phenomenon is a thermodynamic phenomenon, which is related to energy required to expand the van der Waals gap between two graphene layers and repulsive interaction between guest ions. Due to staging phenomenon, a potential plateau can be

seen in first discharge profile of graphitic carbon based electrode. However in non-graphitic carbon interaction starts at about 1.2 V vs Li/Li^+, and the curve slop without distinguishable plateaus. This behavior is consequence of the disordered structure providing electronically and geometrically nonequivalent sites, whereas for particular intercalation stage in crystalline graphite the sites are equivalent. The carbon materials synthesized at low temperature from 500 to 1000 °C show a very high reversible capacity of 400 to 2000 mAh/g. A number of models have been suggested for such large capacity for example, (i) formation of lithium multilayer on graphene sheets (ii) accommodation of lithium at the zig-zag and arm chair faces between two adjacent crystallite and (iii) possibility of LiC_2 formation etc.

The electrochemical behaviour of carbon-based material also can be improved by changing its electronic structure by doping electron donar or acceptor element in graphite lattice. Boron is one of the electron acceptor have been used to improve the electrochemical performance of graphite. The prominent phenomena of boron-doping in carbon materials is that the boron atom can be subsitutionally incorporated into graphite layers. The boron doping in carbon, enhanced graphitization and modified electronic properties of host materials. Boron doped graphite prepared by CVD showed the significantly increased reversible capacity than by pure carbon materials.

Nanostructured materials have attracted great interest in recent years because of the unusual properties. There are several advantages of nanomaterials based electrode for lithium batteries. The main advantages are better accommodation of the strain of lithium insertion/removal, better cycle life, and higher electrode/electrolyte contact area leading to higher charge/discharge rates, short path length for electronic conductivity and short path length for lithium ion transport. However, using nanomaterials as electrode there are some disadvantages such as an increase in undesirable electrode electrolyte reaction due to high surface area leading to self-discharge and synthesis of nanomaterials is too complex. With the above advantage and disadvantages in mind effort have been devoted to synthesize nanomaterials for electrode of lithium ion battery. Carbon based nanomaterials are usually graphitic or amorphous; they show some unique properties including potential use as anode materials of lithium ion batteries. Slightly graphitized MWCNTs show a high specific capacity of 640 mAh/g, because of doping of lithium into micrpores, edge sites and surfaces of graphite layers. In contrast, well-graphitized MWCNTs show a lower capacity of 282 mAh/g during the first charge. The oxidized CNTs show a first discharge capacity of 660 mAh/g. Lithium

can also reversibly intercalate into SWCNTs. and the reversible capacities can range from 460 mAh/g to 1000 mAh/g after introduction of defects by ball milling. Different type of CNTs displays very interesting properties as anode materials.

Although lithium ion battery has a high-energy storage capability, they still cannot meet the requirements for large-scale energy storage and electrical vehicle applications. On the other hand, global market of rechargeable batteries is growing fast due to increasing mobile communication and portable electronics. The electrochemical performance of lithium ion batteries is mainly determined by physical, chemical and structural properties of anode and cathode materials used in battery system. The PhD thesis aims to explore and investigate the different form of carbon (bulk as well as nanostructure, carbon with heteroatom and ball milled graphite) based anode materials for lithium ion batteries with improved electrochemical behavior. A systematic study has been performed including synthesis of materials, structural characterization, fabrication of cell and electrochemical testing.

LITERATURE REVIEW

2.1 INTRODUCTION OF LITHIUM ION BATTERY

Lithium-ion batteries have the highest energy density among all rechargeable battery systems. These batteries are widely used as power sources for modern consumer electronics such as camcorders, laptop, cellular phones, field generator and many other portable devices. Moreover, lithium-ion batteries offer high energy density, flexibility, lightweight in design, and have longer service life as compared to other battery systems. Large-scale lithium-ion batteries are prime contenders as power sources for electrical vehicles (EVs) and load-leveling applications. The fuel cell (Mathur et al., 2007) also may be the future energy source but it is not useful for portable applications. Figure 2.1 shows comparison of the energy densities of the different types of rechargeable batteries.

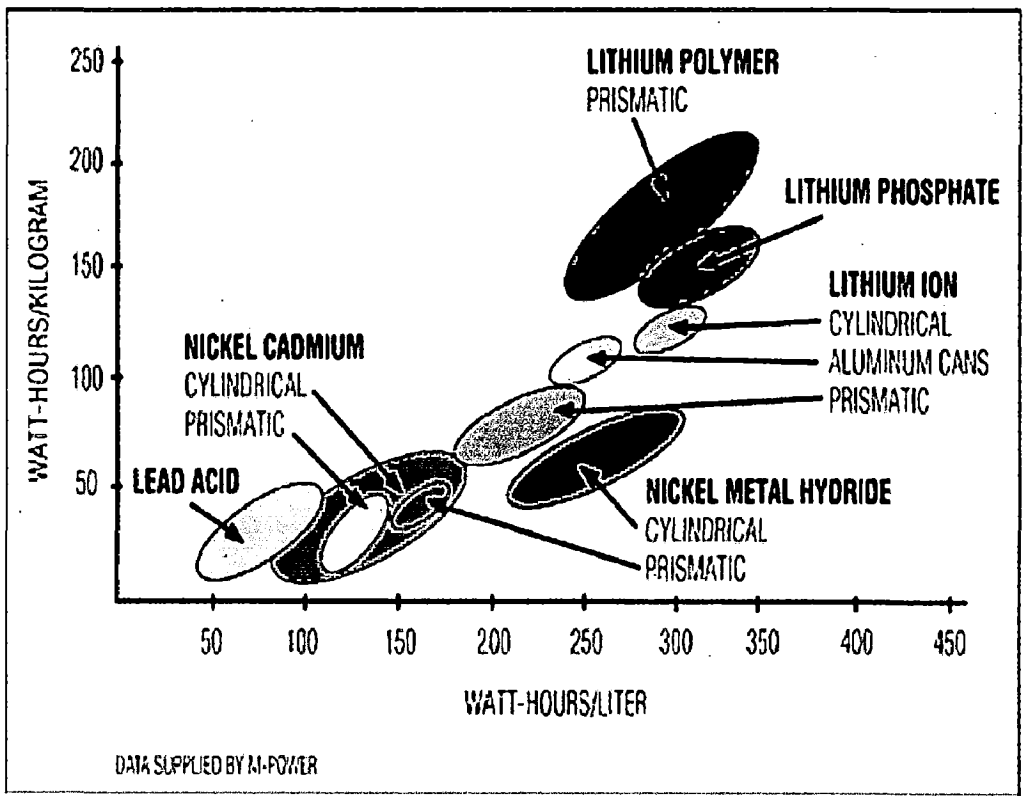

Figure 2.1: Energy density of different types of secondary batteries (Tarascon and Armand, 2001 and Brandt, 1994).

Fig. 2.1 shows that lithium-ion batteries deliver the highest energy density. Intensive research activities have been carried out all over world to enhance the energy density, cycle life and safety aspect of lithium ion batteries. Today, lithium-ion batteries dominate the rechargeable battery market due to their excellent performance.

2.2 HISTORICAL DEVELOPMENT OF LITHIUM ION BATTERY

The main motivation to use lithium metal as an anode in battery system is due to the fact that lithium is the most electronegative (i.e.-3.04V versus the standard hydrogen electrode), the lightest element (at. wt. 6.94 g/mol and density of 0.53 g/cm^3) and provides a higher energy density. The primary lithium batteries, which were developed in early 1970, used lithium metal as the anode. These batteries had higher capacity and energy density. The primary lithium batteries have lot of applications in electronic watches, calculators and implantable medical devices. Early development of rechargeable lithium batteries used TiS_2 as the positive electrode and lithium metal as the negative electrode with lithium perchlorate in dioxolane as the electrolyte [Whittingham, 1976]. TiS_2 is a stable compound with a layered structure for the repeated lithium intercalation and de-intercalation. However many problems associated with dendrites growing on surface of the lithium metal electrode were evident with this battery system. The dendrite formation is due to the reaction of lithium metal with liquid electrolyte. During large number of cycling, lithium starts depositing at the anode surface o, which grows in the form of dendrites, penetrate through the porous separator, and causes a short circuit resulting in a fire or an explosion. Such serious safety hazards prevented the further development of rechargeable lithium batteries. Afterwards scientists attempted to solve this problem by substituting metal with lithium-aluminum (Li-Al) alloys [Rao et al., 1997]. Dey demonstrated the possibility of formation of lithium alloy electrochemically in organic electrolytes [Dey, 1971]. Since then, many lithium alloys have been developed as alternative anode materials. The energy densities of lithium alloys are normally lower than the lithium metal by a factor of two or three [Baranski and Fawcett, 1982 and Sanchez et al., 1989]. Unfortunately, the volume changes related to the insertion/extraction of Li ions into/from alloy matrices are quite substantial (i.e. about 200-600%). These cause a fast distingration of alloy anodes by cracking and crumbling. Rechargeable lithium batteries using lithium alloys for the anode usually have a very short cycle life. Graphite carbon finds itself dimensionally stable during lithium insertion and extraction. Intercalation of lithium ions

corresponding to the composition LiC_6 results in only about 10 % increase in interlayer distance [Basu, 1981 and Yazami and Reynier, 2006]. Therefore, graphite became the choice for anode material, replacing lithium metal and lithium alloys. In the meantime, some progresses have been made in the research for intercalation materials such as oxides to replace the heavier chalcogenides [Murphy and Vanadium, 1979 and Mizushima et al., 1980]. Later, Goodenough et al. proposed the families of Li_xMO_2 (where M is Co, Ni or Mn) compounds as cathode materials with high Li/Li^+ potential versus the reference electrode [Mizushima et al., 1980 and Thackeray et al., 1983].

The combination of carbon based anode host, lithium transition metal oxide based cathode and an appropriate organic electrolyte has been engineered in lithium-ion battery technology since the end of the 1980s [Murphy and Vanadium (1979) and Lazzari et al., 1980]. Later, Sony [Nagaura and Tozawa (1990)], was the first to commercialize lithium ion battery in 1990s. This technology is called Li-ion or rocking chair batteries. To compensate the increased potential of negative electrode, higher potential insertion materials are required for cathodes. Commercial productions of lithium ion batteries are mostly taking all over world and these batteries are becoming the dominant over other sources especially for consumer electronics.

2.3 WORKING PRINCIPLE OF LITHIUM-ION BATTERY

Lithium metal free lithium batteries were originally termed as rocking chair batteries (RCB) by Armand (1980). The basic principle of operation for RCB system was partially derived from concentration cells, which consists of essentially identical electrodes containing different reactant concentrations [Hever, 1968]. The RCB concept was demonstrated using transition metal compound based cathode and anodes [Lazzari et al.,1980]. Later, new names for this technology have appeared as lithium ion, shuttlecock and swing electrode system, etc. However, the fundamental concept remained the same. A lithium ion battery consists of a cathode, an anode and an electrolyte (either in liquid or in solid state) containing dissociated salts. A micro-porous membrane acts as a separator between the cathode and the anode. The lithium insertion/extraction process occurring with a flow of ions through the electrolyte is accompanied by respectively a reduction/oxidation reaction of host matrix (electrodes) assisted by the flow of electrons through the outer circuit. When the cell is discharged the anode becomes negative (-) and cathode becomes positive (+) electrode and polarity of electrodes reverses when cell is being charged. The lithium ions shuttle between the

two electrodes through the electrolyte system. Figure 2 shows a schematic diagram showing the operating principle of lithium ion battery. During the charging process, lithium ions are

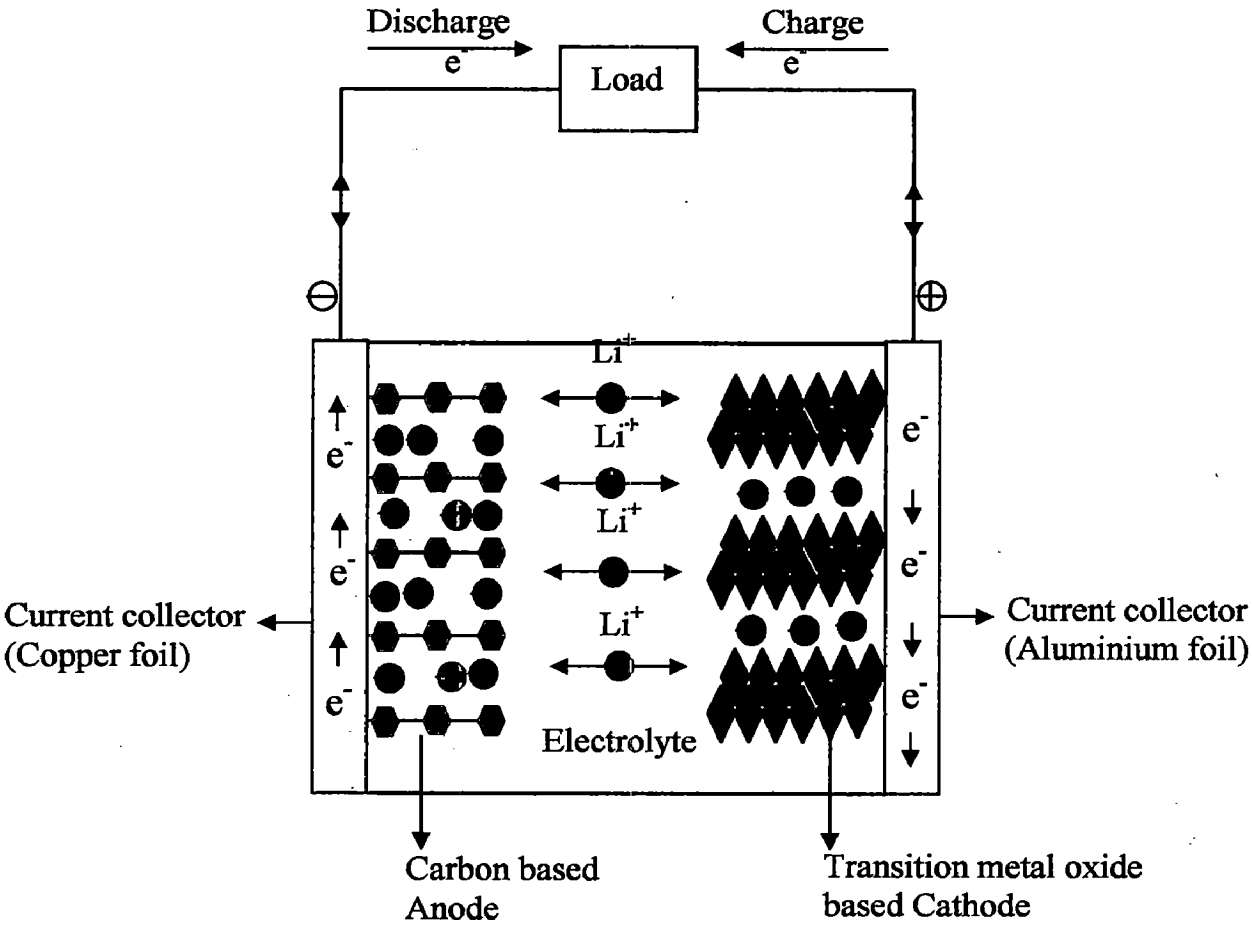

Figure 2.2: Schematic diagram of battery and its operation

extracted from the cathode host, pass through the electrolyte-separator combination and intercalate into anode host. Simultaneously, electrons are liberated from the cathode, go through the external circuit and are accepted by the anode material. The reverse process occurs during the discharging process. The reaction during charge and discharge are shown below

$$LiCoO_2 + yC = Li_{1-x}CoO_2 + Li_xC_y$$

$$yC + xLi + xe^- = Li_xC_y \qquad (2.1)$$

In order to achieve high cycling efficiency and long cycle life, the movement of lithium ion in anode and cathode hosts should not change or damage the host crystal structure.

The design of lithium ion battery requires careful selection of electrode pairs to obtain a high operating voltage (V). A high operating voltage can be realized with anode and cathode having smaller and higher work functions Φ_a and Φ_c respectively. The open circuit voltage V_{oc} of the cell be calculated from the following formula

$$V_{oc} = (\Phi_c - \Phi_a) / e \qquad (2.2)$$

where e is the electronic charge.

Carbon (hard carbon and graphitized carbon) with a potential range of 0.0-0.8V versus lithium metal is a major choice as the anode material host for lithium ion batteries. The cathode materials can be chosen from among spinel $LiMn_2O_4$, layered $LiCoO_2$ and $LiNiO_2$, which have discharge potential of around 4.0 V versus lithium metal. A battery with a combination of high potential cathode material and a low potential anode materials can be able to deliver a voltage of 3.6 ~ 3.8 V, which is three times more than that of Ni-Cd or Ni-MH batteries.

2.4 CATHODE MATERIALS FOR LITHIUM-ION BATTERY

In rechargeable lithium ion batteries, the cathode acts as the lithium ion source for the intercalation reaction. Therefore, the physical structure or electrochemical properties of the cathode materials are critical to the performance of whole battery. The principal properties required for cathode materials are, large negative Gibbs free energy during the discharge reaction, low molecular weight and high energy density, higher chemical diffusion coefficient of lithium (high power density), low possible or nil structural modification during intercalation and de intercalation (long cycle life), chemical stability, non toxic and inexpensive nature of the material.

The well researched cathode materials for lithium ion battery mainly include lithium cobalt oxides ($LiCoO_2$), lithium nickel oxides ($LiNiO_2$), spinel lithium manganese oxides ($LiMn_2O_4$), layered $LiMnO_2$ and olivine $LiFePO_4$.

2.4.1 Lithium Cobalt Oxides

$LiCoO_2$ based cathode has a high charge and discharge voltage of 3.6-3.8 V in a cell operation and this cathode has first been proposed by J.B Goodenough [Goodenough et al., 1980]. $LiCoO_2$ compound is a layered type (R_3M), with the oxygen in cubic close packed array. The Li^+ and Co^{3+} ions are located at octahedral 3a and 3b sites with ordered alternating (111) planes, including a hexagonal symmetry. [Ohzuku

and Udeda, 1994] explained the mechanism of reaction at $LiCoO_2$ electrode. Theoretical capacity of this material is about 274 mAh/g. However, only limited part of the lithium is reversibly extracted from and inserted into the electrode and resultant reversible capacity reaches to150 mAh/g after 1000 cycles [Delmas, 1989]. $LiCoO_2$, which is an active cathode material can be prepared by various synthesis methods. Solid-state reaction is commonly used by sintering a mixture of cobalt oxide and lithium carbonate at high temperature. However, sol-gel or organo-chemical synthesis for the $LiCoO_2$ has also been reported [Takeuchi and Thiebolt, 1988 and Crespi et al., 2000]. Due to limited source of cobalt, it is replaced by Ni and Al [Saadoune and Delmas, 1992 and Huang et al., 1999].

2.4.2 Lithium Nickel Oxides

$LiNiO_2$ is an attractive candidate for lithium ion batteries as the natural resource of Ni is relatively abundant compared to Co. Theoretical capacity of $LiNiO_2$ is closed to that of $LiCoO_2$. However, the practical capacity of $LiNiO_2$ cathode suffers from a large capacity-fading rate and poor thermal stability in highly oxidized state Ni^{4+}. Layered $LiNiO_2$ has been synthesized by using a variety of conditions including varied Li:Ni ratios, different sintering temperatures and atmospheres [Wang et al., 1998]. Many efforts have been made to improve the electrochemical performance of $LiNiO_2$ cathode by partial substitution of Ni with other metal element such as Mg, Al, Mn, Cr, Fe or Ti [Li et al., 1993 and Moshtev et al., 1995].

2.4.3 Layered $LiMnO_2$

$LiMnO_2$ system is most intensively investigated cathode material due to its low cost, non-toxicity and has ability to provide high energy density. Theoretically if all lithium ions can be reversibly extracted from and inserted into the $LiMnO_2$ structure, it can deliver specific capacity of about 270 mAh/g. Layered $LiMnO_2$ was successfully synthesized by an ion exchange technique from $NaMnO_2$ [Armstrong and Bruce (1996), and Capitaine et al.,1996]. When the lithium ions are removed from $LiMnO_2$, the Jahn-Teller Mn^{3+} ions are oxidized to Mn^{4+}, inducing the loss of monoclinic distortion. x-ray diffraction has identified that the layered $LiMnO_2$ is converted to a spinel structure during the charge and discharge cycling [Vitins and West, 1997]. The efforts have been made to stabilize this structure by replacing Mn with other metal element such as Al, Co, Ni, Cr, etc [Jang et al., 1998 and Spahr et al., 1998].

2.4.4 Spinel Lithium Manganese Oxides

The lithium insertion into and extraction from $LiMn_2O_4$ spinel provides an average of 4.0 V versus Li/Li^+, which is similar to $LiCoO_2$ and $LiNiO_2$. Spinel $LiMn_2O_4$ has the advantage over Co and Ni containing systems as the spinel is inexpensive, nontoxic and having larger thermal stability domain especially when overcharged. However, the theoretical capacity of $LiMn_2O_4$ is only 148 mAh/g. The fast capacity fading on cycling is another serious drawback for $LiMn_2O_4$ spinel electrodes. Spinel $LiMn_2O_4$ belongs to the cubic system with a space group of Fd3m, in which Li^+ , $Mn^{3+/4+}$ and O^{2-} ions occupy tetragonal 8a and octahedral 16d and 32 e position in cubic close packed (ccp) oxygen array. $LiMn_2O_4$ is an attractive cathode material; however, its capacity fades away slowly which prevents its wide commercial use. This fading is mainly due to Jahn-Teller distortion and instability of delithiated particle in electrolyte [Aurbach et al., 1999 and Guyomard and Tarascon, 1992]. To come out from this effect, doping the $LiMn_2O_4$ spinel structure with low valence ions is an effective approach by which Mn replaces ion partially by other low valence ions, the average valence of Mn will be increased above +3.5. Correspondingly, at the end of the 4.0 V discharge, the average valence of Mn is maintained slightly above +3.5. Because the Jahn-teller distortion starts at $Mn^{+3.5}$, low valence ion doping can suppress this effect in $LiMn_2O_4$ spinel. However, the theoretical capacity of $LiMn_2O_4$ decreases with increasing amount of dopant ions [Thackery, 1995]. In order to circumvent the Jahn–Teller effect, the doping of heteroatom e.g., Li, Al, Ti, V, Cr, Fe, Co and Ni into the spinel structure via sol–gel method is a preferable option [Dziembaj et al., 2003]

2.4.5 Olivine $LiFePO_4$

$LiFePO_4$ discovered by J.B. Goodenough is an electrochemically active lithium iron phosphate olivine compound [Padhi et al., 1997]. The lithium insertion/extraction mechanism is pure two-phase reaction with the end-members of $LiFePO_4$ and $FePO_4$, giving an extremely flat discharge curve at 3.5 V. The theoretical capacity of $LiFePO_4$ is 170 mAh/g. This is a new cathode material having potentially low cost, natural abundance of raw materials and environmentally friendliness. However, this material has some disadvanges of very low electronic conductivity in its pure form of the order of ($\sim 10^{-9}$ S cm^{-1}) and slow lithium diffusion in the solid phase. The electrical

conductivity is enhanced to 10^{-3} S cm^{-1} by doping with Mg, Al, Ti, Nb and W [Gouveia et al., 2005].

2.5 ANODE MATERIALS FOR LITHIUM-ION BATTERIES

Earlier lithium metal was used as an anode in lithium primary batteries. However, the problem of dendrite formation associated with this electrode makes it unsuitable for battery application. Therefore, various insertion electrode materials have been proposed to replace this negative electrode. Transition-metal oxides and chalcogenides, different carbons, lithium alloys, and polymers are few examples of this electrode material. Table 2.1 shows both the specific charges and the densities of lithium insertion materials, which are theoretically lower than that of metallic lithium [Whittingham, 1978 and Nesper, 1990]. Fig. 2.3 shows the comparisons of volumetric and gravimetric energy densities of different types of anode materials for lithium ion batteries.

Table 2.1. Characteristics of representative negative electrode materials for lithium batteries.

Anode Material	Molecular weight (g)	Theoretical specific charge (mAh/g)
Li	6.94	3862
LiC_6	79.00	372
LiAl	33.92	790
$Li_{21}Sn_5$	739.31	761
$LiWo_2$	222.79	120
$LiMO_2$	134.88	199
$LiTiS_2$	118.94	225

The basic requirements for anode materials of battery include: (i) lithium insertion/extraction potential should be as low as possible, (ii) maximum amount of lithium must be accommodated to achieve high specific capacity and (iii) the anode host should not get damaged structurally during insertion and deinsertion to obtain long cycle life.

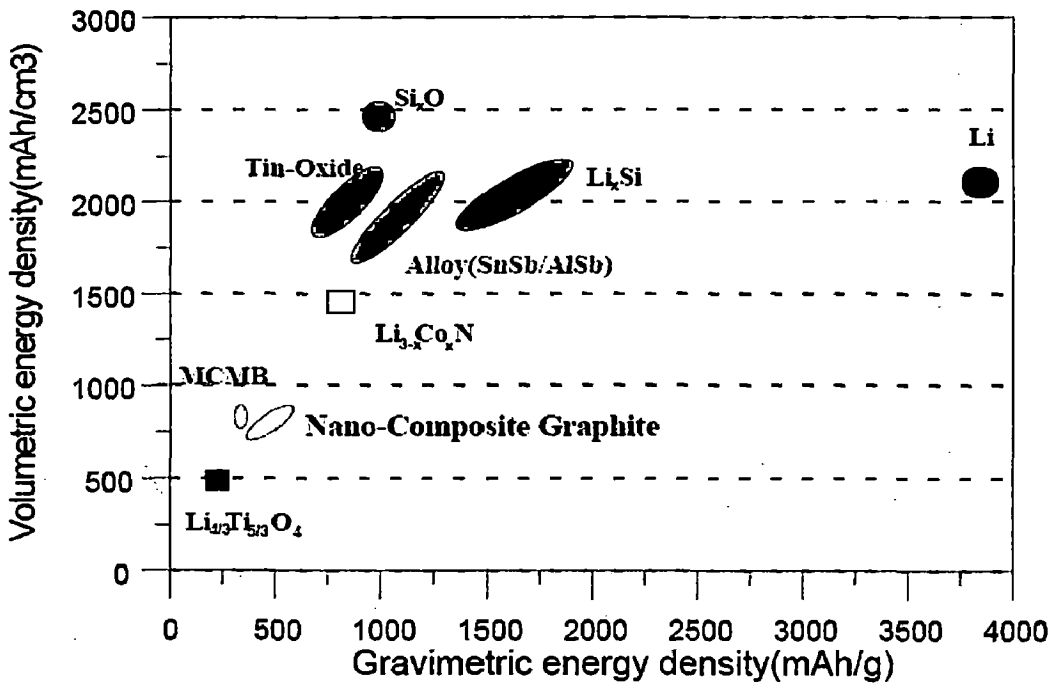

Figure 2.3: Anode Materials for Li-ion Battery (Tarascon and Armand, 2001).

2.5.1 Lithium Alloys as Negative Insertion Electrode Materials

The replacement of metallic lithium by lithium alloys has been under investigation since Dey [Dey, 1971] demonstrated the feasibility of formation of lithium alloys electrochemically in liquid organic electrolytes. The reaction usually proceeds reversibly according to the following equation (2.3)

$$Li_xM \underset{\text{charge}}{\overset{\text{discharge}}{\rightleftharpoons}} x\,Li^+ + x\,e^- + M \qquad (2.3)$$

The alloy anode materials have several advantages over carbon anode materials, such as higher energy density and operating voltage. Thus, the dendrite formation during reaction can be minimized resulting in improved safety and rapid charging capabilities. However, the alloy-based anode has some drawbacks such as solvent co-intercalation and volume changes during insertion and deinsertion reaction. This results in a fast disintegration of alloy anodes. The volume change of alloy anodes has a detrimental effect on the performance of batteries. Li alloys are formed at ambient temperature by polarizing the metal M sufficiently negatively in a Li^+ containing electrolyte. In most cases, even the binary systems Li-M are very complex. Sequences of stoichiometric intermetallic compounds and phases Li_xM with considerable phase range are usually formed during lithiation of the metal M (Fig. 2.3). The formation of

Li-M phases is reversible in many cases, so that subsequent steps and slopes are observed during discharge.

The matrix metals (M) for example, Al, Si, Sn, Pb, In, Bi, Sb and Ag, those form Li alloys electrochemically, some multinary alloys [Fauteux and Koksbang, 1993 and Nimon and Churikov, 1996] and aluminum alloys [Genies et al.,1988] have been studied as anode material. Generally, the matrix metals undergo major structural changes while alloying with lithium. In addition, in the case of pure aluminum, alloying with lithium occurs with several successive phase formations such as α -phase (up to 7 at % Li in LiAl), β-phase (a non-stoichiometric phase with ~ 47 to ~ 56 at % Li), and several other lithium-rich phases. Lithium alloys Li_xM have highly ionic character. For this reason, they are usually brittle. Thus, mechanical stresses, related to the volume changes, induce a rapid decay in mechanical properties and finally pulverization of the electrode. The charge densities of Li alloys are high, moreover the Li^+ mobility at room temperature in Li-rich phases is quite acceptable and hence higher charge densities can be achieved for charging and discharging [Huggins et al., 1989 and Baranski and Fawcett, 1982]. Therefore, many attempts have been carried out to improve the dimensional stability of alloy electrodes during cycling. The metallurgical structure and morphology of Li alloys (grain size, shape, texture, and orientation) strongly affect their dimensional stability [Besenhard et al., 1997, and Anani et al., 1988]. Thick electrodes consisting of large alloy particles are not flexible enough and degrade mechanically during cycling. A limitation of the cycling depth to very thin layers [Zlatilova et al., 1988 and Nohma et al., 1996] improves the cycleability.

One possibility for counteracting the mechanical degradation is the use of thin layers of alloys and small particle size (submicron / nanomaterials). In such layers relatively large dimensional changes of the crystallites do not cause particle cracking, as the absolute changes in the particle dimensions are small and hence electrode pulverization is suppressed. However, micron and submicron-structured multiphase matrix alloys show a large improvement in the cycling performance. In this case, the more reactive particles can also expand in the first charging (alloying) step into ductile surroundings of unreacted material [Besenhard et al., 1997 and Yang et al., 1996].

A similar concept of supporting small particles of electroactive Li alloys with less active or non-active matrices was introduced in 1981 [Boukamp et al., 1981]. The matrix material can be a conductive polymer [Maxfield et al., 1988], a porous

membrane [Besenhard et al., 1990], an inert metal-like copper [Besenhard et al., 1990] or another mixed conductor [Huggins, 1989]. If the mixed conductor matrix material is another Li alloy Li_xM, cycling has to be limited to a potential range in which Li^+ are not removed from Li_xM.

As the structural changes are common to alloying reactions, there have been attempts to limit these side effects on the electrode integrity. Among them, the active/inactive nanocomposite concept represents one attractive route. Several authors [Winter and Besenhard, 1999] have discussed this approach, which involves intimately mixing two materials, one reacting with lithium whereas the other acts as an inactive confining buffer. Within this composite, the use of nano-size metallic cluster as lithium host considerably suppresses the associated strains and therefore improves the reversibility of alloying reaction. By applying this concept through different systems such as SnO-based glasses, Sn-Fe-C and Sn-Mn-C [Idota et al., 1997, Mao and Dahn, 1999, Beaulieu and Dahn, 2000], the reversible capacity of such materials can be improved.

2.5.2 Silicon-Carbon Based Anode Materials for Lithium-ion Battery

The Si-C composites have attracted considerable interest because they show capacity as high as 1000 mAh/g for more than 100 cycles [Novak, 2004, Datta and Kumta, 2006]. In recent year, several authors have reported [Yang et al., 2003 and Wang et al., 2004] that the Si-C based composites, prepared by high energy mechanical milling and decomposition of organic precursors, show higher reversible capacity with respect to graphite and better capacity retention with respect to pure silicon. However Si-C based composite synthesized by thermal pyrolysis of polyvinyl chloride dispersed with nanosized silicon and fine graphite particles shows a reversible capacity of about 700 mAh/g with better cyclability than nanocrystalline silicon alone [Yang et al., 2003]. Composites based on Si and disordered carbon synthesized by pyrolyzing pitch and polysillane blends, shows a reversible capacity about 500 mAh/g with good cyclability [Larcher et al., 1999]. However, Si/C composite synthesized by decomposition of organic precursor shows a large irreversible loss in first cycle due to formation of disordered carbon, porosity and presence of hydrogen/oxygen in final product. The Si/C composite synthesized by moderate ball milling of different carbon (graphite, MCMB and disordered carbon) and nanocrystalline silicon [Wang et al., 1998 and 2004] shows high discharge and charge capacity (800-1400 mAh/g depending

on the composition studied) but exhibit poor capacity retention which is not suitable for practical commercial application. The Si-C composite synthesized by mechanical mixing of graphite and pre-milled Si powder for a period of about 15 min by using Spex shaker mill, shows a first discharge capacity of about 800 mAh/g with a fade in capacity about 1.25 % after 20 cycles for nominal 20 wt % of Si mixed graphite powder. The poor capacity retention may arise due to Si being not homogeneously distributed in carbon matrix and poor interface adhesion between carbon and Si during the short duration of milling. In this regard, extended milling may be useful to disperse the active silicon phase homogeneously in graphite matrix resulting in good capacity retention. However, the formation of SiC and amorphization of graphite during prolonged milling of graphite and Si [Kim et al., 2004] limit the feasibility of mechanical milling to synthesize Si-C composites for possible application as anode in Li-ion battery [Datta and Kumta, 2006]. It is reported that addition of soft metal (Sn) or certain polymers act as diffusion barrier to the reaction between Si and graphite to form SiC during extended milling [Kim et al., 2004]. Same authors also reported that polyacrylonitrile (PAN) has been used as diffusion barrier to prevent the formation of SiC for long time milling (about 15 h) using Spex shaker mill. The composite based on silicon and graphite where active silicon phase is homogeneously distributed in graphite matrix, and also coated with the thermally decomposed product of PAN has been proposed as suitable anode materials for probable use as anode for lithium ion batteries [Datta and Kumta, 2003]. The composite exhibits high reversible capacity and excellent capacity retention with 26% irreversible loss in first cycle [Datta and Kumta, 2006]. Some of these improvements may arise because the materials avoid cracking, thus maintaining better conduction pathways, or because they incorporate conductive additives such as carbon [Wilson and Dahn, 1995].

2.5.3 Carbon Based Insertion Electrode (Anode) Materials

In the rechargeable lithium ion batteries at present, carbon is used as an anode material. Carbon based anodes have an exceptional behavior for lithium ion battery. The main application of carbon is the use as a host anode accessible by lithium ions through electrochemical insertion, the lithium being provided by another insertion material used as host cathode. The electro-insertion reaction is a host/guest solid-state redox reaction involving electrochemical charge transfer coupled with insertion of mobile guest ions into the structure of a solid host, which is a mixed electronic and

ionic conductor. The major structural features of the host are kept after the completion of reaction. The intercalation is a special case of insertion. The term intercalation is used only in the condition if host is a layered structure and takes up guest within its interlayer gap, which may result in volume change and cause no structural changes.

There are different types of carbon material available commercially, including natural graphite, synthetic graphite, carbon black, active carbons, carbon fibres, cokes and various other carbonaceous materials prepared by the pyrolysis of different organic precursor in an inert atmosphere. These different types of carbonaceous materials have wide range of structure, texture and properties. On the basis of structure carbon based materials are divided in to the following three different categories (Fig. 2.4), (i) graphite (ii) non-graphitic glass like carbon also called hard carbon, which can not be graphitized even after heating it at high temperature and (iii) soft carbon, which can be graphitized easily by heat treatment [Wakihara, 2001]. Graphite is three-dimensional ordered structure however, the soft and hard carbons are two dimensional ordered sheet stacked randomly [Warren, 1934].

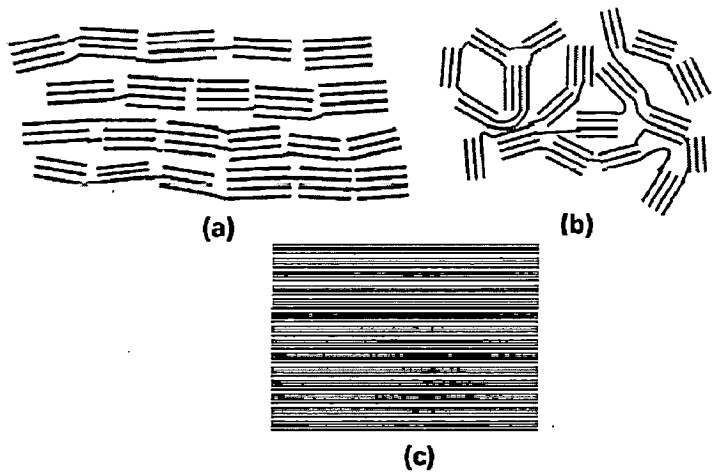

Figure 2.4: Different types of carbon (a) Soft carbon (b) hard carbon and (c) graphite (Franklin, 1951).

2.5.3.1 Structure of Graphitic carbon

The lamellar structure of graphite is two-dimensional material and presents a large anisotropy in atomic bonds. The sp^2 hybridization induces a covalent σ bond with three other carbon atoms in plane, which involves the formation of aromatic macromolecules in hexagonal net called graphene layer. The carbon-carbon in plane distance is 1.42Å, shorter than that in diamond (5.4Å). Another allotrope of carbon is

characterized by sp^3 hybridization. The σ bonds in graphite, present a higher electronic density, which explains their higher cohesion.

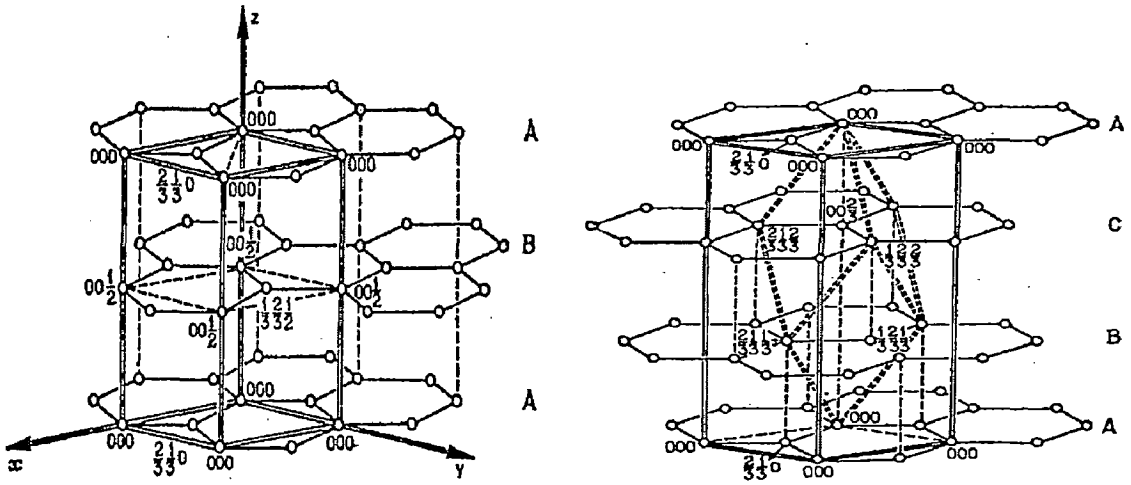

(a) (b)

Figure 2.5: (a) Structure of hexagonal graphite showing ABAB... stacking (from Wyckoff 1964) (b) Rhombohedral graphite showing ABCABC... stacking (Wyckoff 1964).

The graphene layers are superimposed parallel to each other and the cohesion of the material (between the graphene planes) is ensured by Van der Waals type bonds quite weak, which explains the easiness of cleavage of graphite and large distance between successive graphene planes (3.35 Å). There are two types of stacking ABAB.....hexagonal graphite (2H) and ABCABC....rhombohedral stacking (3R) shown in Fig.2.5.

The hexagonal graphite, also called α graphite, is the most common form. Its structure, firstly described by Bernal in 1924 [Bernal, 1924], was confirmed by Maugu in 1926 [Lipson and Stokes, 1942]. The unit cell belongs to the space group $P6_3/mmc$ with the following parameters: $a = 2.46$ and $c = 6.70$ Å.

Rhombohedral graphite, also called β-graphite, is characterized by a unit cell having $a = 3{:}635$Å, $\alpha = 39.5^{o}$ and a space group R3m̄, as shown by Lipson and Stokes in 1942. Often associated to the hexagonal form, this phase does not exist alone. Its presence is favored by milling, ultrasonic treatment up to 40%, but disappears by heating above 2000 °C or by intercalation/deintercalation of various species between the graphene planes [Boehm et al., 1955].

2.5.3.2. Electrochemical Li Storage in Graphite Carbon

The electro-insertion of Li^+ cations into carbon proceeds according to the following equation

$$Li_xC_n \underset{charge}{\overset{discharge}{\rightleftharpoons}} xLi^+ + xe^- + C_n \qquad (2.4)$$

During electrochemical reduction (charge) of carbon host, Li cations penetrate into the carbon and form a lithiated carbon Li_xC_n ($n \geq 6$ in LiC_n or $x \leq 1$ in Li_xC_6). Li ions release during oxidation, which is a discharge reaction. Lithium ions can intercalate between graphene layers to form LiC_6 intercalation compound. The theoretical capacity of graphite is 372 mAh/g, which is based on the reaction to form LiC_6 compound given by Eq. 2.4. The LiC_6 has a characteristic golden colour and belongs to the graphite intercalation compounds of stage 1. LiC_{12} has blue colour corresponding to stage 2 as shown in Fig. 2.6. This lithium intercalated highly oriented pyrolytic graphite (HOPG) sample has been synthesized during preliminary experiment in our laboratory.

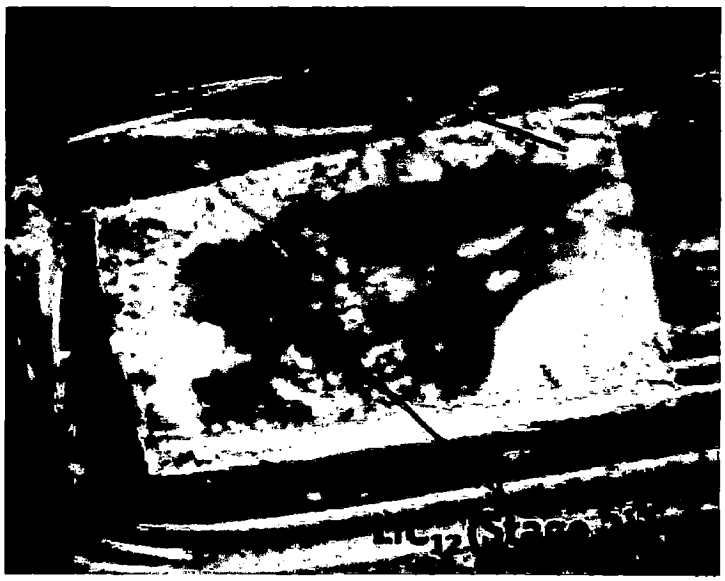

Figure 2.6: Lithium intercalated compounds (yellow and blue showing stage 1 and stage 2 respectively) synthesized in our laboratory.

Higher lithium storage capacities into carbon can be obtained with certain non-graphitic carbons and specifically treated graphite. The intercalation reaction proceeds mainly

through the basal planes, however it is also possible through defects site, unit cell and sub-division in basal plane and prismatic surface.

During intercalation, the stacking order of graphene layers becomes AA. Thus, two neighbouring layers of graphene in LiC_6 directly face each other (Fig. 2.7a). The energetically favored AA stacking sequence of LiC_6 has been proven by theoretical calculation [Song et al., 2001]. Due to hosted lithium the interlayer distance between the graphene layers increases moderately (by 10.3%) that has been calculated for LiC_6 [Moret, 1986]. The stacking order of the lithium interlayer is a Li-C_6-Li-C_6-Li chain exists along c-axis [Rossat et al., 1980]. In LiC_6, the lithium is distributed in such a way that the occupation of nearest neighbour sites is avoided (Fig. 2.7b). The perpendicular view of LiC_6 is shown in Fig 2.7c.

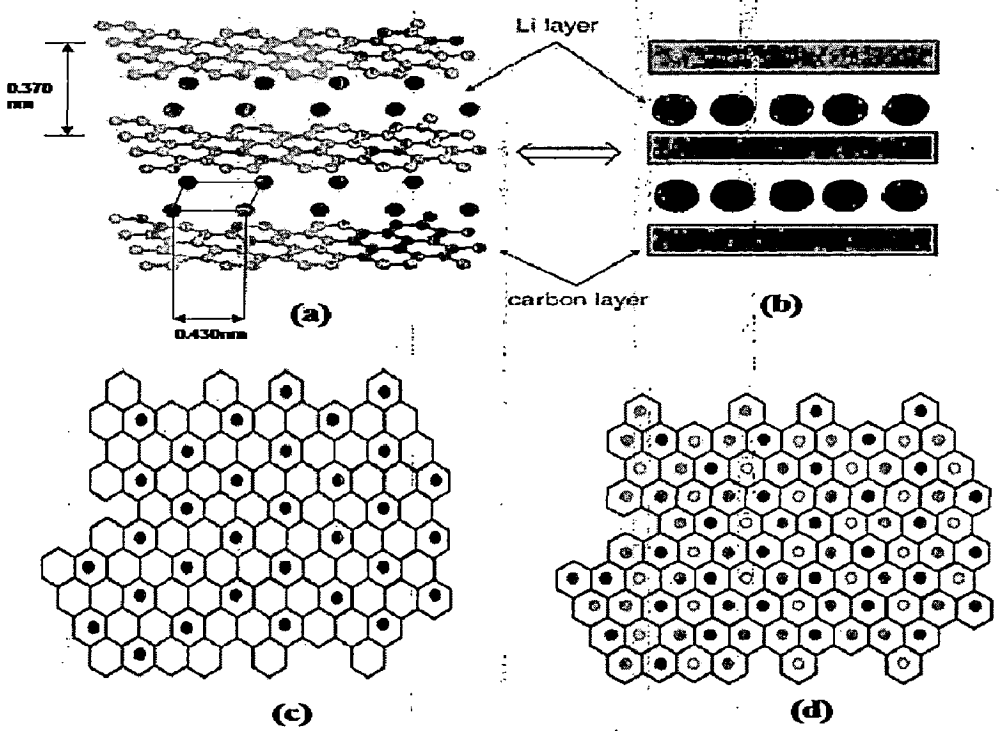

Figure 2.7: (a) Structure of LiC_6 showing the AA layer stacking (b) simplified representation (Song et al., 1996) (c) Perpendicular view of LiC_6 and (d) LiC_2 (Yazami and Reynier, 2006).

A higher lithium in-plane density by occupation of nearest neighboring sites is obtained in the phases LiC_2-LiC_4 which are prepared chemically from graphitic carbon under high pressure (~ 60kbar) and high temperature (300 °C) conditions [Nalimova et al., 1996]. The closest Li-Li distance in LiC_2 (Fig. 2.7d) results in higher chemical

activity of lithium than that of lithium metal (Li-Li bond length at 20 °C = 0.304 nm) [Weast et al., 1987]. However, under ambient condition LiC_2 decomposes slowly through various metastable intermediate Li/C phases to LiC_6 and metallic lithium.

2.5.3.3 Stage Formation by Lithium Intercalation

The stage formation in graphitic anode is the intercalation of lithium ions into periodic array of graphite. The stage formation is a process, which is described by stage index and is equal to the number of graphene layers between two nearest lithium layers. The stage formation is the thermodynamic phenomenon, which is related with energy required to open the van der Waals gap between the two graphite layers. The repulsive coulombic interaction between guest ions is less effective. As a result, few but highly occupied van der Waals gaps are energetically favored over a random distribution of guests. Staging phenomena and degree of intercalation can be easily observed during the electrochemical reduction of carbon-based materials in Li^+ containing electrolytes as shown in Fig 2.8.

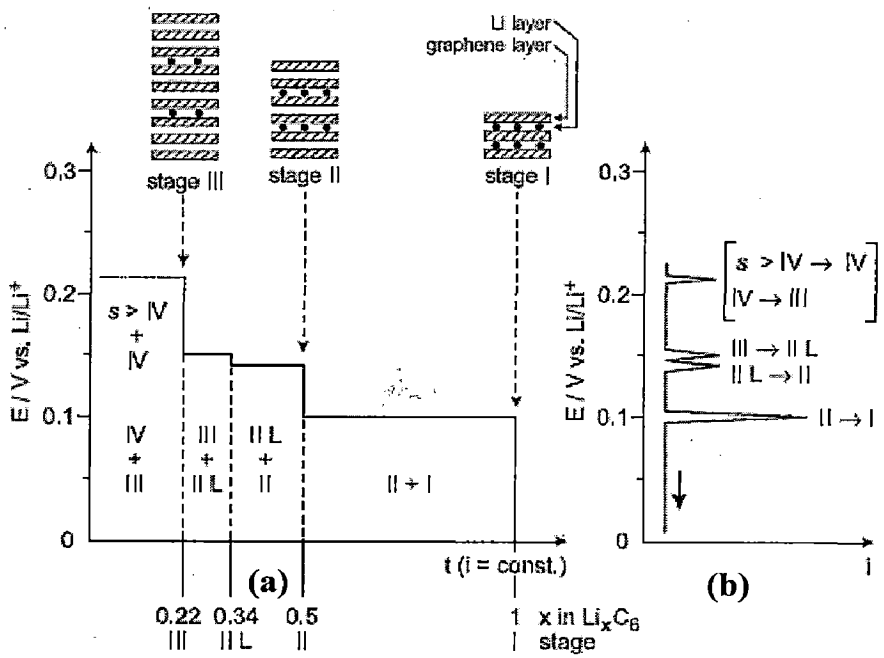

Figure 2.8: (a) Staging phenomena during intercalation of graphite constant current curve and (b) schematic voltametric curve [Besenhard and Fritz, 1983].

In the Fig. 2.8a plateau indicates two-phase regions (coexistence of two phases) [Fisher, 1987]. Under potentio dynamic control (linear potential sweep voltammetry, Fig. 2.8b, right) the current peaks indicate the two-phase regions. Apart from the stage s = I, four other binary phases, corresponding to the stages s = IV, III, II and I [Yata, 1995] were identified from electrochemical curves and confirmed by X-ray diffraction [Dahn, 1991] and Raman spectroscopy [Inaba et al., 1995]. The splitting of the second stage into two, s = II (x = 0.5 in Li_xC_6) and s = IIL (x = 0.33 in Li_xC_6), is due to different lithium packing densities.

2.5.3.4 Reversible and Irreversible Capacity

The charge discharge curve for Li^+ intercalation and de-intercalation of graphite at constant current clearly shows the staging phenomena as can be seen in Fig 2.9. There is no sharp change in curve between the two phase regions because (1) the

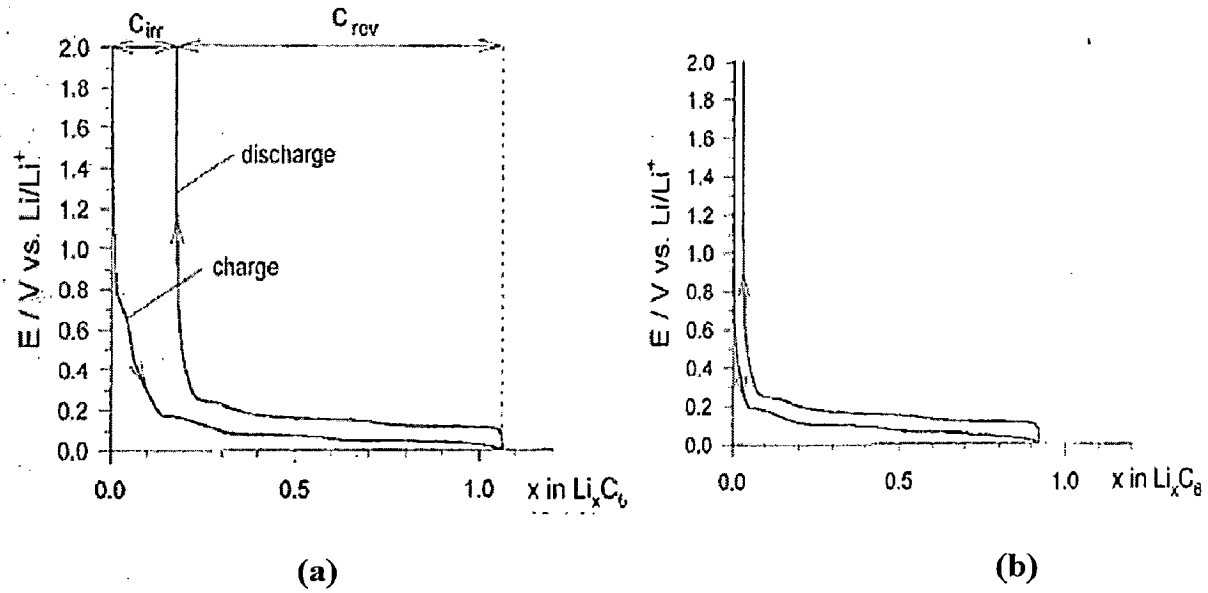

Figure 2.9: Typical schematic charge/discharge profile of graphite for first (a) and second (b) cycle [Winter et al., 1998].

packing density of LiC_6, (2) various type of over potentials cause the plateau sloping in galvenostatic measurements and (3) in practical cases, lithium intercalation does not exit homogeneously over the electrode. Theoretically, the Li^+ intercalation in carbon is fully reversible, however the charge consumed in the first cycle significantly exceeds the theoretical specific charge for the first stage LiC_6 of 372 mAh/g. The subsequent discharge recovers only 80-95% of this charge. In the second and subsequent cycles,

the charge capacity is lower and the recovery is close to 100%. The excess charge consumed in the first cycle is generally ascribed to irreversible reactions (i) of Li^+ with graphite and (ii) of the lithiated graphite with the electrolyte. However, the irreversible reaction of Li^+ with graphite is a minor part responsible for the excess charge. It is reported that reduction of impurities like H_2O or O_2 present on the carbon surface, also causes irreversible capacity [Bittihn et al., 1993]. The main part of irreversible charge capacity is due to reactions of carbonaceous anode with electrolyte, which consists of mixture of organic solvent and highly soluble lithium salt. The strong reducing power of graphite and other carbonaceous materials, at lithium intercalation potential leads to decomposition of electrolyte [Fong et al., 1990, Kanno et al., 1992]. In suitable nonaqueous electrolytes passivating films of Li^+ containing electrolyte decomposition products protect the carbon surfaces and electrolyte against further reaction with each other. These films are permeable to the electrochemically active charge carriers Li^+ cations, but impermeable for the electrolyte, i.e. that behaves as electronically insulating solid electrolyte interphase [Peled et al., 1997].

The charge losses due to reaction of lithium with carbon and surface impurities as well as the film formation on LiC_6 are associated with the irreversible consumption of lithium and the electrolyte. The corresponding charge loss is generally called irreversible charge capacity and the reversible lithium intercalation is called as reversible capacity.

2.5.4. Non-graphitic Carbon as Anode Materials of Lithium-Ion Battery

According to lithium intercalation, the nongraphitic carbons are classified with respect to their reversible charge capacity as high specific charge carbon and low specific charge carbon. The high specific charge carbon can store more lithium than graphite ($x>1$ in Li_xC_6), however, the low specific charge carbon can incorporate only considerably lower amount of lithium than graphite. The examples of low specific charge carbon are turbostratic carbons [Dahn et al., 1993], cokes [Satoh et al., 1995] and carbon blacks [Takei et al., 1995]. Their maximum stochiometric factor x in Li_xC_6 is typically about 0.5 to 0.8 (for graphite $x = 1$). In case of turbostratic carbons the low specific charge capacity is due the lower number of lithium site available in wrinkled and buckled structural segment [Zheng and Dahn, 1996]. However, cross-linking of carbon sheet in disordered carbons hampers the shift to AA stacking, which is necessary for accommodation of higher lithium amount into graphitic sites [Besenhard,

1994]. The use of composite carbonaceous materials comprising a core of graphite and a protective shell of disordered carbon combines the favorable lithium storage properties of graphite with the solvent co-intercalation retarding properties of non-graphitic carbons [Zheng and Dahn, 1995]. Fig. 2.9 shows the first Li^+ intercalation / deintercalation cycle of coke-containing electrode. The potential profile differs considerably from that of graphite, as the reversible intercalation of Li^+ begins at around 1.2 volt vs. Li/Li^+, and the curve slopes without any plateaus. This behavior is a consequence of the disordered structure providing electronically and geometrically non-equivalent sites, whereas for particular intercalation stage in crystalline graphite the sites are equivalent [Dahn et al., 1994]. Much effort has been concentrated on development of high specific charge carbonaceous materials. The carbons are synthesized at low temperature from 500 °C to 1000 °C and show reversible specific charge capacity from about 400 mAh/g to 2000 mAh/g depending on the synthesizing temperature, organic precursor and electrolyte used. These materials have been known since 1980s, when synthesized non-graphitic carbon with specific charge of about 300 mAh/g to 500 mAh/g [Imanishi et al., 1992]. Several models have been proposed for high specific charge [Zheng and Dahn, 1996]. Yazami [Yazami et al., 1995] proposed the formation of lithium multilayers on graphene sheet. Peled and co-worker [Peled et al., 1996] suggested that the extra charge reached by mild oxidation of graphite is attributable to accommodation of lithium at zig-zag and arm-chair faces as shown in Fig.2.10, between two adjacent crystallites and in the vicinity of defects and impurities. Sato et al. [Sato et al., 1994] suggested that lithium molecules occupy nearest neighboring sites in intercalated carbons (Fig.2.10a). Yata et al. [Yata et al., 1994] discussed the possibility of formation of LiC_2 in carbons with high interlayer spacing of about 400 pm (graphite: 335 pm). The extra lithium can be accommodated in nanoscopic cavities (Fig.2.10b). In literature, it is assumed that the small size carbon particles can store a considerable amount of lithium on graphite edges and surface in addition to the lithium located between the graphene layers (Fig. 2.10 c & d).

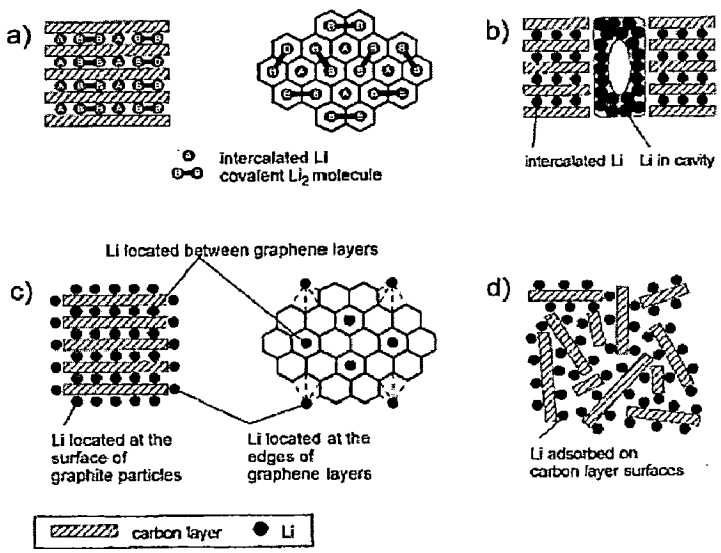

Figure 2.10: Schematic drawing of some mechanisms for reversible lithium storage in high specific charge carbonaceous materials as proposed in: a) [Yata, 1995], b) [Mabuchi et al., 1994], c) [Wang et al., 1995], and d) [Wang et al., 1995].

Several research groups studied the behavior of high specific charge carbons in detail. Both graphitizing (soft) and non-graphitizing (hard) carbons prepared below 800-900° C show very high specific charges, and exhibit a hysteresis as lithium uptake occurs close to 0 V vs. Li/Li^+ whereas lithium deinsertion occurs at much more positive potentials [Zheng and Dahn, 1995]. The extent of hysteresis is proportional to the hydrogen content in carbon. It has been suggested that lithium is somehow bound near the hydrogen [Wang et al., 1996]. Hydrogen can be removed by increasing temperature. The specific charge capacity achieved after removing hydrogen depends on the structure of carbonaceous materials, whether soft or hard [Zheng and Dahn, 1995]. If the heat treatment at higher temperature and the fraction of stacked layers with graphitic order increases, the specific charge also increases [Tatsumi et al., 1996]. By contrast, non-graphitizing (hard) carbons obtained at temperature about 1000 °C show less hysteresis. However, their high specific charge of several hundred mAh/g can be obtained only at a very low potential of few mV vs Li/Li^+. The reason for such high capacity is that lithium is adsorbed on both sides of single layer sheets that are arranged like a house of cards [Zheng et al., 1996].

Heat treatment at 1000 °C leads to a drastic reduction of specific charge of hard carbon [Mabuchi et al., 1995]. Even though the carbon based anode materials having high specific charge, they may have some serious drawbacks too. In many cases, very high irreversible specific charge is observed [Zheng et al., 1996] at higher cycles [Zheng and Dahn, 1995]. Carbons exhibiting hysteresis show poor cycling performance, and can be discharged only in a broad potential region of about 1-2 V [Zheng et al., 1996]. The cycling performance of non-graphitizing (hard) carbons heat-treated at 1000 °C is good and almost no hysteresis occurs [Winter et al., 1998]. In some cases [Zheng and Dahn, 1995] the electrode was indeed charged to potentials negative of 0V vs Li/Li^+ to achieve the high specific charge. Under such charging method lithium deposition occurs. In contrast, there is a difference of approximately 0.1V between the potential of graphitic LiC_6 and the potential of lithium deposition. Therefore, there is demand for carbons with high specific charge and graphite-like potential characteristics [Kasuh et al., 1997].

2.5.5 Modified Carbon as Anode Materials

Researchers have made different modifications in carbonaceous material in order to improve the performance of battery. The following sections discuss such modifications.

2.5.5.1 Oxidation of Graphite

It is reported that mild oxidation of artificial graphite could modify its electrochemical performance as anode material for lithium ion batteries [Peled et al., 1996]. The main effects of oxidation are the production of nanochannels and/or microspores and formation of dense layer of oxides. The former enhances the lithium intercalation [Wu et al., 2000], and latter inhibits the decomposition of the electrolyte. As a results the reversible capacity and coulombic efficiency in the first cycle increases. However, the oxidation should not be drastic, if graphite is over oxidized, an adverse effect may occur [Peled et al., 1996].

2.5.5.2 Coating by Polymers

The polymers (Polythiophene, polypyrole and polyaniline) coated carbon shows an improved electrochemical performance [Veeraghavan et al., 2000]. When polythiophene is coated on graphite, it acts as a conductor since it is electronically conductive. As a result, a pressing process can be omitted in assembly line of cell fabrication. Secondly, the polymer acts as binder. The polymer coating also decreases the contact of graphite with electrolyte and consequently the irreversible capacity decreases [Gabersces et al., 2001]. After coating with polymer (1) no classical binder is required to prepare mechanically and electrochemically stable anodes, and (2) irreversible capacity in the first cycle decreases probably due to the formation of more uniform passive film, whose growth is governed by the presence of polyelectrolyte molecule.

2.5.5.3 Carbon Host Containing Heteroatom as Anode Materials

With the progress of technology, new aspects such as modification and preparation of carbon anode materials by mild oxidation of graphite, carbon with heteroatom (e.g. N, B), coating with polymers and other kinds of carbons [Wu et al., 2003] are possible. The use of carbon insertion hosts containing one or more heteroatom, such as boron [Dahn et al., 1993] phosphorous [Cermignani et al., 1995] or others [Schönfelder et al., 1997] leads, in many cases, to carbonaceous materials with increased specific charge for lithium insertion. The influences of the heteroatoms have been discussed on basis of changes in electronic structure [Way and Dahn, 1994]. However, the interaction of heteroatom with the respective carbon neighbors has not yet been clarified fully [Wilson and Dahn, 1997]. Moreover, data reported by different groups seems contradictory [Weydanz et al., 1994].

In recent years, boron–doped carbon materials have received much attention for their use as host materials for lithium intercalation [Endo et al., 1999]. Experimental and theoretical investigations have pointed out that boron doping prompts an electron acceptor level, inducing positive holes in the energy band of graphite matrix, and hence the battery performance can be expected to be improved if boron-doped carbon is used in lithium ion batteries as an anode material [Lowell, 1967]. The number of valence band hole depends on boron concentration. In carbonaceous materials, boron atom is a graphitization catalyst, which can alter the host structure of carbon greatly [Endo et al., 2000]. Theoretical considerations suggest that the presence of boron substituted for

carbon in the lattice should be beneficial for lithium insertion/deinsertion behaviour of carbon material. Boron having one less electron than carbon and therefore acts as electron acceptor modifies strongly the electronic properties without any large distortion of the crystal lattice host material i.e of graphite. However, due to various side effects associated with boron doping this assumption has not found a clear experimental confirmation; despite several attempts have been made [Machnikowski et al., 2004, Mishra et al., 2005]. If the changes are concerned with structural factors such as the a-b axis crystalline size, stacking and defects in the basal planes, significant effects on electrochemical performance of the anode with respect to lithium insertion can be expected [Fujimoto et al., 1994].

Burgess et al [Burgess et al., 2008] show that boron doped carbon powders produced at 1000 °C have structural changes, as XRD data showed a decreasing d_{002}-spacing, indicating increased graphitization upon doping. The full width at half maximum of this peak decreases, probably due to an increase in grain size upon boron doping. Raman spectroscopy shows a decrease in the height of the G-band, due to the boron substitution. The intensity ratio of the G- to D-bands increases, indicating larger grain sizes in the powders.

Way and Dahn (1994) reported that boron-doped carbons having a composition of B_ZC_{1-Z} ($0 < z < 0.17$) and produced by chemical vapor deposition (CVD) method from benzene and boron trichloride (BCl_3) at a temperature as low as at 900 °C showed a very large Li storage capacity and a high-potential profile compared to a pristine carbon anode [Way and Dahn, 1994].

Kim et al. show the reduced charge capacity of boron-doped graphite and explained that this reduced capacity is related to boron occupying an active lithium insertion site, such as an edge-type site in graphite-like crystallite, and thus the presence of the boron would be expected to inhibit the lithium intercalation process. In addition, they observed the voltage profiles of boron-doped samples are higher than those of the un-doped samples. On discharging cycle for the boron-doped samples, shoulder plateaus are characteristically observed at about 1.3 V, which may be caused by filling of an electron acceptor level, so that lithium insertion yields a higher potential compared to that of the un-doped samples [Endo et al., 1999].

Frackowiaka et al. [Frackowiaka et al., 2008] have studied the lithium insertion/deinsertion behavior of a series of pure and boron doped graphite prepared from coal tar derived pitch. Materials treated with boron were pitch coke and graphitic

carbon produced by heat treatment at 1000 and 2900°C, respectively. The effect of electron acceptor properties of boron substituted for carbon in graphitic carbons is negligible. On the other hand, presence of boron accelerates the graphitization process.

2.5.6. Ball-Milled Graphite as Anode Materials for Li-ion Battery

Carbonaceous materials with higher capacities than graphite can be prepared either by chemical means (pyrolysis of an organic precursor) [Zheng and Dahn, 1996], or by a physical mean e.g. ball milling of graphite [Disma et al., 1996]. In order to improve the anodic performance, one way is to modify the graphite material (structure and morphology) by using ball mill. Disma et al. [Disma et al., 1996] show the effects of mechanical grinding on morphology and electrochemical performance of graphite and soft carbon powders with respect to lithium insertion. The morphology of the milled powder was found to depend strongly upon the nature of interactions (e.g., impact or shear) generated by the two kinds of mills used. By controlling milling conditions, graphite and soft carbon powders with well-defined morphology, d-spacing, surface area, and crystalline size can be made. They have shown a direct correlation between the irreversible and reversible capacity. The milled graphite and coke samples both have similar irreversible capacity (328 mAh/g) and reversible capacity (708 mAh/g) corresponding to chemical composition of Li_2C_6.

Wang et al. [Wang et al., 1998] show the effect of mechanical milling for 150 h on microstructure, morphology and electrochemical performance of graphite powders with respect to lithium insertion. The ball-milled graphite shows reversible capacity of about 700 mAh/g ($Li_{1.88}C_6$), however, a large hysteresis has been observed in charge and discharge profile. They have reported the reason for large reversible specific capacity, which is due mainly to Li doping at vacancies, micro cavities (or at the edges of the metastable carbon interstitial phase) and voids. The bonding change between the interstitial carbon and the carbon in aromatic plane that is induced by insertion of Li atoms leads to hysteresis. The reversible capacity becomes 37.8% of its initial capacity after twenty charge–discharge cycles. The potential hysteresis is attributed to the interstitial carbon atoms between the aromatic planes of the carbon atoms. The limited cycle life may be due mainly to some vacancies and microcavities being annihilated by both moveable and some bound interstitial carbon.

Ong and Yang (2000) have shown the effect of different atmospheres during the milling in planetary and vibratory mill. The effect of atmosphere on microstructure was found different when milled in oxygen and in an inert atmosphere. This phenomenon is most pronounced when it was milled in a planetary mill where the deformation forces are mainly shear in nature. Mechanically induced oxidation on the surface, probably along the edges of the graphene planes, is responsible for suppressing the fracture rate and preserving the crystallinity of natural graphite milled in oxygen. The discharge potential profile for the graphite sample milled in oxygen showed smaller potential plateau at 0.5 V and a more gradual rise above 0.5 V. The reversible capacity is slightly larger but the first cycle irreversible loss is more severe. This is attributed to its larger specific surface area, which is about four times greater than that of the as received graphite.

Highly divided graphite presents a great interest in electrochemistry since the path length for intercalated species is reduced, as the particle size is shorter. Also the thickness of graphite flakes plays an important role on the intercalation/deintercalation kinetics, due to the pressure applied by the graphitic matrix on the intercalant [Hooley, 1977]. The ground graphite powder presents different properties, according to different techniques used for milling. A planetary ball mill involved mainly friction on powder, which maintains the three-dimensional order of graphite since the interplanar distance is slightly increased (3.35 to 3.38 Å after 100 h milling). However, vibrant mill implies much violent shocks and the 3D graphite organization is destroyed even after short milling time, the graphite is almost amorphous and interplanar distance becomes as large as 3.60Å. The increase in interplanar distance is due to defects and dislocations inside the crystallites of graphite. The individual particles are particularly small but form agglomerates, which decrease the surface energy. Initially water was used as liquid medium and results concerning the shape and size of the particles (a diameter around 1 μm for a thickness of 20 nm) were relevant, but pollution was observed, due to the reaction of water with milling tools [Janot and Guerard, 2005 and Guerard, 2008]. The rhombohedral phase increases up to 20 % after 48 h of milling. Huang et al. [Huang et al., 1998] reported that with increasing rhombohedral phase lithium intercalation capacity increases. The defects on the basal plane along the boundaries between the 3R and 2H phases will reduce the incorporation impedance of lithium ions into the graphite lattice leading to an enhancement of capacity also. The boundary position within the crystallites can be occupied by lithium ions and hence increase the

capacity. The presence of liquid, together with graphite, decreases the violence of the shocks in the milling container and allows the preparation of highly anisotropic graphite (HAG). The irreversible capacity of the ball-milled graphite is much smaller than that of starting material i.e. 80 instead of 150 mAh/g in case of pristine graphite. This behavior is opposite to the general idea according to an irreversible capacity proportional to the specific surface area of graphite [Dahn et al., 1994]. However, the ball-milled graphite presents a large surface, roughly 100 times higher than that of initial graphite, but the grinding provokes a cleavage of the particle (not a breaking). This cleavage occurs probably at the most fragile parts of graphite grains (e.g. at the defects between graphene sheets) and involves a recovery of those defects, in which the SEI formation is important. The defects increase the active surface (presence of dangling bonds) and therefore, their elimination decrease strongly the SEI formation. This explains why the irreversible capacity can be lowered by ball-milling in dodacane and proves that the milling conditions are very mild [Janot and Guerard, 2005].

By milling powders within fluid (water, dodecane or hydrogen) together with stainless steel balls in a steel vial placed on planetary mill, it is possible to synthesize diverse materials well crystallized and highly anisotropic graphite, graphite lithium intercalated compounds, pure maghemite as well as its composites with graphite [Guerard et al., 2008].

2.5.7 Carbon Nanotubes as Anode Materials for Li-ion Battery

As discussed above, carbon anode materials are either graphitic or amorphous. Since the discovery of carbon nanotube (CNTs) in 1991 by Iijima [Iijima, 1991], CNTs have been investigated by many researchers all over the world. Their large length (up to several microns) and small diameter (a few nanometers) result in large aspect ratio. They can be seen as nearly one-dimensional form of fullerene. They show some unique properties including potentiality to be used as anode material of lithium ion batteries similar to other nanostructure materials (Sanyal et al., 2008 and Roy et al., 2007 and Chakravorty et al., 2000). Due to their unique structure and properties, they have wide applications e.g in energy storage (Ajayan and Zhou, 2001), electrochemical super capacitor (Baughman et al., 2002), field emitting devices (Smith and Silva, 2009), transistor (Baughman et al., 2002), nano probe sensor, and composite materials (Ajayan and Zhou, 2001).

There are several classifications of CNTs. Based on configuration; it can be divided into three kinds of CNTs, which are armchair, zig-zag and chiral ones. Based on the degree of graphitization they are divided into amorphous (Wu et al., 2003) and graphitic. Based on structure or number of walls they can be classified into single walled carbon nanotubes (SWCNTs) and multiwalled carbon nanotubes (MWCNTs) [Wu et al., 2002]. SWCNTs are considered as long wrapped graphene sheets and have length to diameter ratio of about 1000, so they can be considered as nearly one-dimensional structures. A SWCNT consists of two separate regions with different physical and chemical properties. The first is the sidewall of the tube and the second is the end cap of the tube. MWCNTs are considered as a collection of concentric SWCNTs with different diameters. The length and diameter of these structures differ a lot from those SWCNTs and hence properties differ from that of MWCNTs.

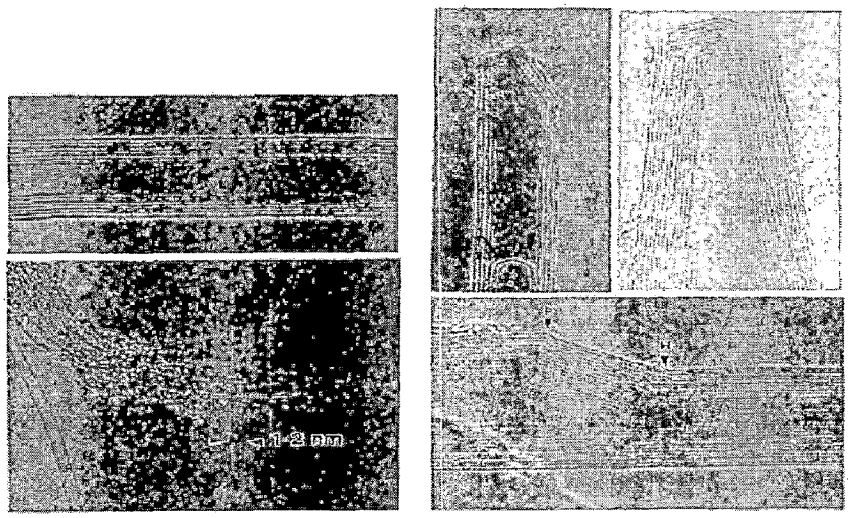

Figure 2.11: Different structures of MWCNTs. Top-left: cross-section of a MWCNT, Top-right: Symmetrical or non-symmetrical cone shaped end caps of MWNTs. Bottom-left: a SWCNT with a diameter of 1 or 2nm. Bottom-right: A MWCNT with defects [Ajayan and Ebbesen, 2003].

Top left and right of Fig. 2.11 show the HRTEM images of MWCNTs. Top left shows the cross section of MWCNT while top right image shows the MWCNTs have two different tube structures i.e. symmetrical and nonsymmetrical tube end. The HRTEM images of SWCNTs are shown in bottom left and right of Fig.2.11 with some defects are shown by arrow mark.

2.5.7.1 Synthesis Methods

Carbon nanostructures can be synthesized by various methods, but the important three processes are:

(1) Arc-discharge(AD)

(2) Laser ablation (LA) and

(3) Chemical vapor deposition (CVD)

However, in the present work, CVD technique has been used which is the only method that can give higher yields of CNTs/ carbon nano fibers (CNFs) economically with comparatively good quality (Mukhopadhyay et al., 1998) at moderate temperatures. The CVD technique has been discussed in detail in the following paragraphs, as this is also useful for synthesis of other carbonaceous nanostructuture materials (Haverkamp et al., 2003 and Silva et al., 1994).

2.5.7.2 Chemical Vapor Deposition (CVD) Method

The schematic diagram of CVD technique for synthesis of CNTs is shown in Fig. 2.12. In this process, the chemical constituents react in the vapor phase near or on a heated substrate to form a solid deposit. Its first practical use was developed in 1880s in the production of incandescent lamps to improve the strength of the filaments. There are many variants of this process and nowadays it is used in combination with PVD (physical vapor deposition) processes. Nowadays CVD makes extensive use of plasma (physical phenomenon) and reactive PVD (evaporation or sputtering) occurs in a chemical environment.

In the present method, porous anodic aluminum oxide (PAAO) samples, having catalyst deposited in their pores are placed in a ceramic boat, which is then placed inside a tube furnace. At first ammonia, gas is supplied at about 500 °C to reduce the catalysts. Later carbon precursor gas (acetylene) is supplied when the temperature reaches at about 650 °C. The gas supply is stopped after a flow of 10 minutes. Furnace is allowed to cool and the samples bearing CNTs are taken out from the furnace when it is cooled. The details of the experimental work are given in Chapter-3.

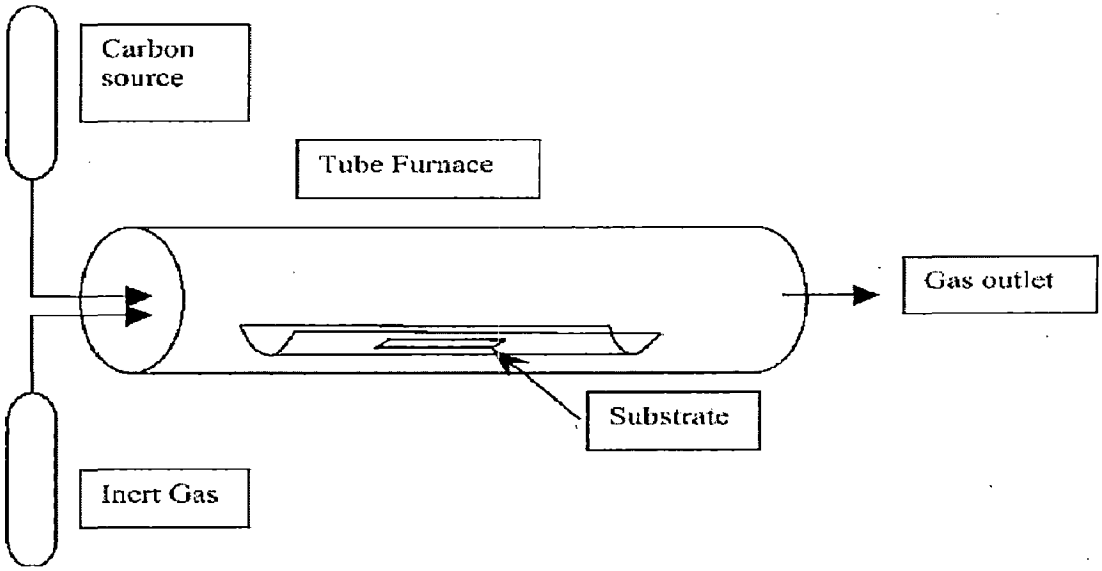

Figure 2.12: Schematic representations of the CNTs synthesizing apparatus. (Öncel and Yürüm, 2006).

CVD is widely used because the installation and recurring cost of the CVD process is lower compared to other methods. The overall energy utilized to the system to grow CNTs is lower than that required for laser ablation or arc discharge techniques. For this reason, the reaction needs to be catalyzed by metallic particles (usually Fe, Ni or Co), which decompose the carbon source at their surface (Boskovic et al., 2002) and therefore, sometimes this process is referred to as catalytic chemical vapor deposition (CCVD). The laser ablation and arc discharge methods do not necessarily need catalyst, unlike CVD. A relatively high product purity and large-scale production can be obtained by CVD method (Maruyama et al., 2002). The entire thermal or catalytic CVD process, generally, consists of two steps, namely, catalyst preparation and CNT deposition or growth. Catalyst may be prepared and placed in many ways. In the present thesis work, catalyst has been deposited at the bottom of the pores using A.C. electro deposition method, which has been explained in chapter-3. The growth process involves heating the catalyst loaded PAAO substrate to moderate temperatures in the range of 550 to 650 °C in the furnace. The upper limit of temperature is set considering the aluminum, which is the underlying material of the PAAO and has a melting point of 660 °C. However, using plasma enhanced CVD or using metallo-organic CVD, the results, which are obtained at such high temperatures in conventional CVDs, can also

be obtained at about 200 °C. Carbon is deposited on the catalyst surfaces, which on precipitation develops CNTs/ CNFs.

2.5.7.3 Growth Mechanism of Carbon Nanotubes

The exact mechanism of CNTs formation is not known. The growth mechanism is still a subject of controversy, and more than one mechanism might be operative for the formation of CNTs. In the present work the catalytic decompositions focus on the catalytic growth of CNTs by chemical vapor deposition (CVD). The growth model is generally based on the concept of the VLS (vapor–liquid–solid) theory developed by Wagner and Ellis (1965). In this model, molecular decomposition and carbon solution are assumed to occur at one side of the catalytic particle, which then becomes supersaturated [Tibbetts et al., 1984]. Carbon diffuses from the side where it decomposes to another side where precipitation takes place from the solution [Baker, 1989]. However, this model does not explain clearly the driving force responsible for carbon diffusion within the catalyst particle. Some authors reported that driving force originates from the temperature gradient created in the particle by exothermic decomposition of the carbon sources (hydrocarbon) at the exposed front faces and endothermic deposition of carbon at the rear faces, which are initially in contact with the support face. However, because of a much lower surface energy of the basal planes of the graphite compared with its prismatic planes, it is energetically favorable for the precipitate with the basal planes as the cylindrical planes [Tibbetts et al., 1984]. The metal–support interactions are found to play a determinant role for the growth mechanism [Cassel et al., 1999].

The growth of CNTs by catalytic decomposition of precursor vapors has been postulated as either base or tip growth (Baker, 1989). Generally, the reason for this difference has been stated as under. If the adhesion between the substrate and catalyst is stronger, base growth is observed (Song et al., 2004 and Bower et al., 2000). Tip growth is observed in two cases. First, if the adhesion is less or secondly if part of the catalyst gets broken and remains at the top, encapsulated by the tip of the growing tube, which is also growing vertically upwards. FE-SEM studies indicate residual Co-Fe catalyst in the base of the tubes, indicating a tip growth mechanism could be responsible for the tube growth. Fan et al., 2003 demonstrated that the nucleation pathway for SWCNTs on a metal surface by a series of total energy calculations using density functional theory. Incorporation of pentagons at an early stage of nucleation is

energetically favorable as they reduce the number of dangling bonds facilitating curvature of the structure and bonding to the metal. In the presence of the metal surface, nucleation of a closed cap or a capped single-wall carbon nanotube is overwhelmingly favored compared to any structure with dangling bonds or to a fullerene.

Weak interactions between catalyst particles and substrate yield tip-growth mode whereas strong interactions lead to base-growth. The tip growth mode is shown in Fig. 2.13. Baker and others (Baker, 1978; Charlier and Iijima, 2001; Dai, 2001) have proposed the tip growth model for the formation of CNTs. The catalyst particles of some transition metal elements or alloys (e.g., Ni, Co, and Fe) are frequently represented as an inverted truncated cone, out of which the nanotube grows. Carbon must be supplied at the top surface from some carbon-containing gas that is 'cracked' at the surface.

There are various reports (Zhu et al., 2006) indicating that CNTs have grown in base growth or root growth mode. The base growth mode of SWCNTs formation is shown in Fig. 2.14.

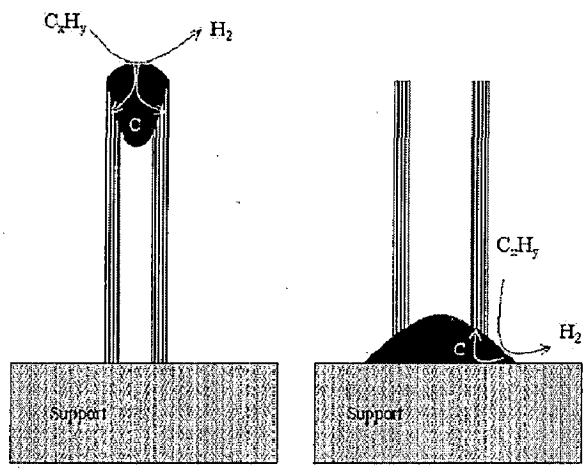

Figure 2.13: The two growth modes of filamentous carbon (Baker 1989 and Cassel et al., 1999).

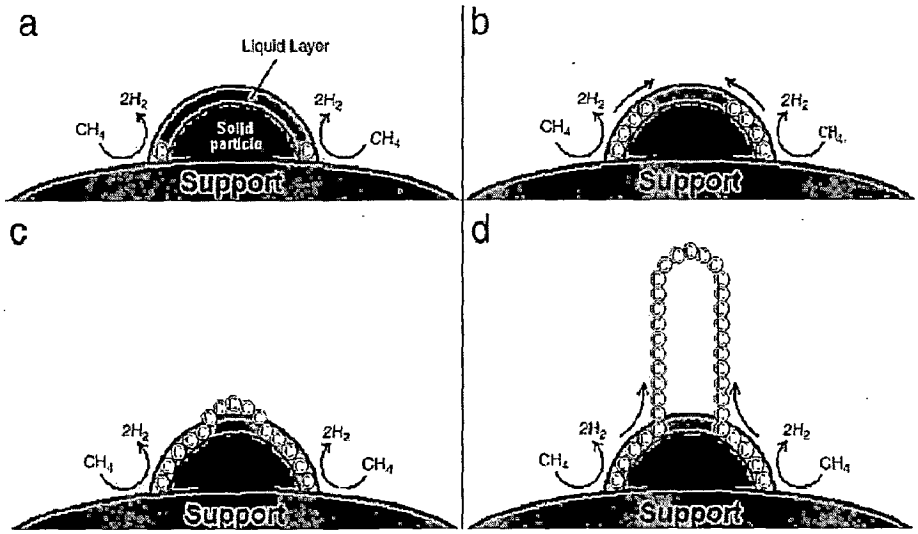

Figure 2.14: Schematic view of the nucleation of a cap and a SWCNT (a) Hydrocarbon decomposition, (b) Carbon diffusion in the surface layer. (c) Super-saturation of the surface and formation of the cap. (d) Growth of a SWCNT (Nagy et al., 2004).

2.5.7.4. Catalyst Used for Growth of CNTs

More often metal used for CNTs formation are iron, cobalt and nickel. Both SWCNTs and MWCNTs can be grown with these metals [Kim et al., 2001]. Cobalt based catalyst mostly gives MWCNTs [Ivanov et al., 1994], with a small amount of SWCNTs. Nickel based catalyst generally gives MWCNTs [Seidel et al., 2004] and seldom to SWCNTs [Cassel et al., 2003]. Mixtures of transition metals act as much better catalyst than a single metal for CNTs synthesis. Iron-nickel alloys yield MWCNTs, iron-cobalt produces SWCNTs [Dai et al., 1996] and with nickel-cobalt, SWCNTS are obtained [Li et al., 2001]. Other than iron, the metals cobalt nickel and palladium have been used as catalyst. These metals alone are generally non-active catalysts but they are used to improve the performance of classical catalyst. Molybdenum is the most important, when added to iron [Yoon et al., 2002] or to cobalt [Liao et al., 2003]. Except a few researchers [Chen et al., 1997] all have reported the formation of SWCNTs with iron-molybdenum or cobalt-molybdenum catalyst. Magnesium–nickel oxide has also been used as catalyst for MWCNTs growth [Lueking and Yang, 2002]. The specific ability of transition metals to catalyze CNT formation is mostly linked to their catalytic activity for the decomposition of carbon compounds, their ability to form carbides and the possibility for carbon to diffuse through and over

the metals with extreme rapidity [Sinnott et al., 1999]. Even all catalysts are 3d-metals, they do not yield exactly the same results. This is related to three important properties for catalyst activity i.e. electronic structure, carbon solubility and stabilization of the catalyst material [Dupuis, 2005]. The ability of a catalyst metal to dissociate hydrocarbon or CO molecules is linked to its electronic structure. Overlap of unfilled 3d-orbitals with carbon orbitals can favor the dissociation process. It should be further investigated that whether the interaction between metal 3d and carbon orbital have an effect on the further growth process [Fonseca et al., 1996]. The carbon solubility of the catalyst material might be an important factor since carbon is believed to diffuse through the catalyst nanoparticle during the growth process. From the experimental results, it seems that Fe_3C forms during CNTs growth on iron particles but its actual role in catalysis process remains unclear. The addition of other components or mixture of transition metal generally exhibits better result in term of catalytic activity and CNT quality [Cabero et al., 1996]. This can be explained by the changes that occur in the electronic structure of metal. Such changes in electronic structure can yield lower activation energy and consequently the requirement of lower growth temperature. Secondly, catalyst composed of several components can form either stable complexes or solid solutions, which remain in the form of small nanoparticles until the beginning of growth process or stable alloys, preventing the formation of species leading to a change of the catalytic behavior [Alvarez et al., 2001] occurs. The size of the catalyst nanoparticles seems to be the determining factor for the diameter of CNT grown on it. Only the small nanoparticles are able to catalyze formation of CNT. This can be explained as those small particles can exhibit peculiar electronic properties due to unusual high ratio surface atom/bulk atom. On the other hand, growth mechanism implying formation of carbon cap on nanoparticle surface reduces its unusual high surface energy. Finally, the crystallographic orientations of catalyst nanoparticles are also crucial for CNT growth [Ivanov et al., 1994].

2.5.7.5. Electrochemical Storage of Lithium into CNTs

For CNTs the capacity is highest if all interstitial sites (inner shell van der Waals spaces, inter tube channels and inner cores) are accessible for lithium intercalation. CNTs are interesting intercalation host for lithium because of their structure and chemical bonding. CNTs might have a higher saturation composition than graphite as guest species can intercalate in the interstitial sites and between the

nanotubes. Therefore, CNTs are expected to be suitable high energy density anode materials for rechargeable Li-ion batteries [Gao et al., 1999].

2.5.7.6. Electrochemical Storage of Lithium into MWCNTs

MWCNTs consist of graphitic sheet rolled into closed concentric cylinders. The concentric cylinders are separated by van der Waals spacing of about 34 pm, slight larger than the interlayer spacing in graphite, 33.5 pm. Their external diameter is in nanometer range and length is in micrometer scale. They contain impurities and defects, whose amount depends upon preparation conditions. Most impurities such as catalyst particles, graphite and disordered carbons can be removed by purification. The electrochemical performance of the CNTs depends on their preparation conditions.

MWCNTs produced with electric arc discharge show an exfoliation of graphene layers when lithium intercalates using a 1M $LiPF_6$ electrolyte dissolved in EC, PC and DMC (v/v/v = 1:1:3). Lithium intercalates between the graphene layers by formation of stage compound. However n-stage compounds with n higher than 2 is not observed [Maurin et al., 2000]. MWCNTs prepared by catalytic decomposition without purification show high irreversible capacity. After purification and annealing, irreversible capacity decreases and the decrease is more with increase in annealing temperature [Leroux et al., 1999].

Similar to the behavior of amorphous and graphitic carbon, the structure of MWCNTs also play a major role for both specific capacity and cycle life [Wu et al., 1999]. Slightly graphitized MWCNTs exhibit a high specific capacity of 640 mAh/g during the first cycle due to doping of lithium into regions unorganized graphite structure, micro pores, edge sites and surfaces of graphitic structure. In contrast, well-graphitized MWCNTs show a lower capacity of 282 mAh/g during the first charge. Both of them display an evident voltage hysteresis of about 1 V, which is higher than that H-containing carbon. Perhaps this is due to a longer diffusion distance for deintercalating lithium. After 20 charge/discharge cycles, the charge capacity of slightly graphitized MWCNTs fades to 65.3% of their original charge capacity, but the well-graphitized MWCNTs maintain 91.5 % of their original charge capacity due to their stable structure [Wu et al., 1999]. Like modification of other kinds of carbons by doping heteroatom [Wu et al., 2002], CNTs can also be doped by heteroatom [Mukhopadhyay et al., 2002]. Reversible capacity after doping increases from 156 to 180 mAh/g in the first cycle with almost equal coulombic efficiencies of 55-58%,

which is from enhanced 3D ordering by B-doping. The coulombic efficiency increases to more than 92 % after the second cycle [Yang et al., 2002].

CNTs can also be oxidized to improve their electrochemical properties. After oxidation by acid, the total discharge capacity during the first cycle becomes 660 mAh/g, and reversible part is only 200 mAh/g. During oxidation in the mixture of acid, the residual acids play an important role. The H_2SO_4 and HNO_3 can easily permeate through the graphene sheets to generate defects or pores in graphene sheets causing increase in reversible capacity [Shiraishi et al., 2002].

2.5.7.7 Electrochemical Storage of Lithium into SWCNTs

SWCNT can be considered to be formed by the rolling of a single layer of graphite (Graphene) into seamless cylinder having a diameter close to 1 nanometer. The way the graphene sheet is wrapped is represented by a pair of indices (n, m) called the chiral vectors. The integers *n* and *m* denote the number of unit vectors along two directions in honeycomb crystal lattice of graphene. They have nearly uniform diameters and are self organized into long crystalline ropes in which parallel nanotubes are also bound by van der Waals forces. The diameter of a rope is typically 10-50 nm corresponding to 30-600 tubes per rope. It can be prepared by thermal decomposition of CO under high pressure with catalysts, arc discharge or by laser ablation [Clay et al., 2000].

Lithium ions can be reversibly intercalated into SWCNTs, and the reversible capacities can range from 460 mAh/g corresponding a stoichiometry of $Li_{1.23}$ C_6, to 1000 mAh/g ($Li_{2.7}C_6$) after introduction of defects by ball milling [Gao et al., 2000]. The purified SWCNTs show a reversible saturation composition of $Li_{1.7}C_6$ (632 mAh/g). This value is higher than LiC_6, which is ideal value for graphite and correspond to a capacity of 372 mAh/g. The SWCNTs synthesized by laser ablation method after purification was treated differently by impact ball milling in air for up to 20 minutes. The untreated purified SWCNTs show the first discharge capacity corresponding to chemical formula $Li_{5.4}C_6$, however the reversible capacity, C_{rev} is corresponding to $Li_{1.6}C_6$. A large hysteresis between discharge and charge cycle was observed in all samples measured. This hysteresis is related to the kinetics of occurring electrochemical reaction. The experiments have shown that cutting nanotubes to smaller segment can reduce hysteresis [Gao et al., 2000]

The ball-milled samples as an anode showed a better performance. The reversible capacity increases with increasing time showing a maximum capacity after 10 minutes of ball milling and corresponding to $Li_{2.7}C_6$. Due to the milling CNTs, they fractured and shortened in the length. However, the exact mechanism for the enhanced Li intercalation capacity in ball-milled SWCNTs is not known. It is suggested that the enhanced capacity is related to degree of disorder within the bundles, and lithium diffusion into the inner cores of fractured nanotubes.

Shimoda et al. [Shimoda et al., 2002] also used SWCNT bundles synthesized by laser ablation. Their purified samples contain over 90 % SWCNTs bundles with a length of 10 μm and a bundle diameter of 30-50 nm, while the average diameter of an individual nanotube was estimated as 1.4 nm. The purified bundles were processed to shorter ones by sonication in solution of H_2SO_4 and HNO_3 for 10-24 hours. After chemical etching of CNT bundle of length 4μm capacity turned out to be 744 mAh/g is corresponding to the chemical formula Li_2C_6. However, bundle with length 0.5 μm the is corresponding to $Li_{2.1}C_6$. These results show that etching of CNTs gives better results.

2.6 ELECTROLYTE FOR LITHIUM ION BATTERIES

The basic requirements for an electrolyte in Li-ion battery are as follows:

1. High ionic conductivity to minimize the cell resistance and resistive heating.
2. High chemical stability in order to prevent decomposition of electrolyte on the surface of highly reducing anode and on highly oxidizing cathode.
3. Electrochemical stability to tolerate the high voltage difference between anode and cathode, which is > 4 V, without being reduced or oxidized.
4. It should be ideally electronic insulator to avoid the short-circuiting of the electrodes and ionic conductor.
5. Electrolyte potential should have limited variations as a function of Li^+ content.
6. Low melting point to provide sufficient conductivity at sub-ambient temperatures, prevents solidification, and phase separation.
7. High boiling point to provide safety and prevention of explosions that may result from high-pressure buildup in the cell.
8. It should be non toxic and should have lower coast

Electrolyte of lithium ion batteries plays an important role in determining the electrochemical performance. Since the mean charge/discharge voltage remains above 3.0 V, an aqueous electrolyte is not useful as it decomposes during cell reactions. Presently electrolytes in lithium ion battery consist of a lithium salt of non-coordinating anions dispersed in an organic solvent. Solid electrolytes are also under development for use in lithium ion battery. Recently polymer based electrolytes have attracted wide attention.

The liquid based electrolytes require to have high solubility in dipolar aprotic solvents and sufficiently high conductivity (> 5 mS/cm) along with the compatibility with all cell materials. The commonly used lithium salts are $LiClO_4$, $LiAsF_6$, $LiPF_6$, $LiSO_3CF_3$ and $LiN(SO_2CF)_3$ dissolved in organic liquids with a large stability are considered as possible electrolytes. $LiPF_6$ to some extent is more suitable than other salts [Matsuda et al., 1986]. Other commonly available salts have many disadvantages, $LiAsF_6$ is poisonous, $LiClO_4$ is explosive, $LiBF_4$ is problematic on the negative side (reaction of BF_4^- anion on the anode surface) and $LiSO_3CF_3$ forms solution of too low conductivity [Kanamura et al., 1996]. The solvent used for electrolytes are usually aprotic organic solvents. Mainly used solvents are PC (Propylene carbonate), DEC (diethyl carbonate), THF (Tetrahydrofurane) etc. and combination of them [Arakawa and Yamaki, 1987]. The alkyl carbonates were chosen due to their acceptable anodic stability. The other properties, such as good conductivity of their solution, a reasonable temperature range between freezing and boiling points, sufficiently low toxicity and acceptable safety features are attractive.

Many types of polymers have been developed as solid electrolytes for lithium ion battery [Aurbach et al., 1995 and Apetecchi et al., 1997]. Two types of polymer electrolytes used are pure solid polymer electrolyte (SPE) and gelled polymer electrolyte system. The SPE based electrolyte usually has poor conductivity but strong mechanical stability [Armand, 1994], however gelled polymer electrolytes system have good conductivity but not mechanically so strong. The other polymers such as polyvinylidene fluoride (PVDF), polymethyl methacrylate (PMMA) and poly acrylonitrile (PAN) etc. are also used as electrolyte [Abraham and Alamgir, 1990 and1993].

Based on extensive literature survey in this chapter it is concluded that carbonaceous materials are the best-suited anode materials for lithium ion batteries. The increase in energy density of present generation cells is due to use of different types of

carbon materials. Still the future trends are focused on the development of carbonaceous materials having higher energy density and higher specific charge. Carbon and graphite with low crystalline size can expect higher capacities. The expectation for carbon and graphite as anode materials should be strengthened more and more. In this context, the thesis work is focused on synthesis of different types of carbon based anode materials (low crystalline size, carbon nanotubes and modified carbon by adding heteroatom) and their performance in cell as anode. In this regard, novel catalysts (lithium transition metal oxide based) have been used for synthesis of CNTs of different morphologies. The lithium based catalysts have been chosen because of possibility of lithium insertion into CNTs during growth process and hence improvement in electrochemical behavior of such materials. The attempts for improvement of carbon-based materials by modifying the synthesis process are discussed thoroughly in following chapters.

EXPERIMENTAL TECHNIQUES

3.1 INTRODUCTION

The main objectives of the present investigations are to synthesize carbon based anode materials and study their structural and electrochemical characterizations. This chapter describes (a) synthesis of (i) bulk and nanocrystalline samples (ii) catalyst particles and preparation of substrate by anodiziation of alumininum sheet, (b) the structural and microstructural characterizations of the materials synthesized and (c) electrochemical characterization i.e. electrode preparation, cell construction, charge/discharge cycle tests of all synthesized samples. The polycrystalline samples have been prepared by using solid-state reaction sintering and ball milling route. The catalysts used were synthesized by sol-gel process. The carbon nanostructure samples were prepared using catalytic chemical vapor decomposition (CVD) method. The thermal analyses (TG) of host carbon based (ball-milled) material have been carried out to study the effect of particle size on weight loss of materials. The x-ray diffraction (XRD) analysis is used to determine the crystal structure of the materials. The carbon based host anode materials (graphite based as well as nanostructure carbon materials) have been characterized by Raman spectroscopy, as the carbon nanostructures have the presence of non negligible sp^2 carbons organized into fragments (islands) which can be correlated (by structure and Raman response of the materials) to an ideally perfect 2-dimensional crystal of graphite (graphene). Scanning electron microscopy (SEM) coupled with energy dispersive x-ray analyser (EDAX) has been employed to examine the morphology and chemical composition of the powdered samples. The structural characterization of the carbon nanostructure samples have been carried out using transmission electron microscope (TEM). The experimental procedure followed is shown in Fig.3.1, in the form of flow diagram.

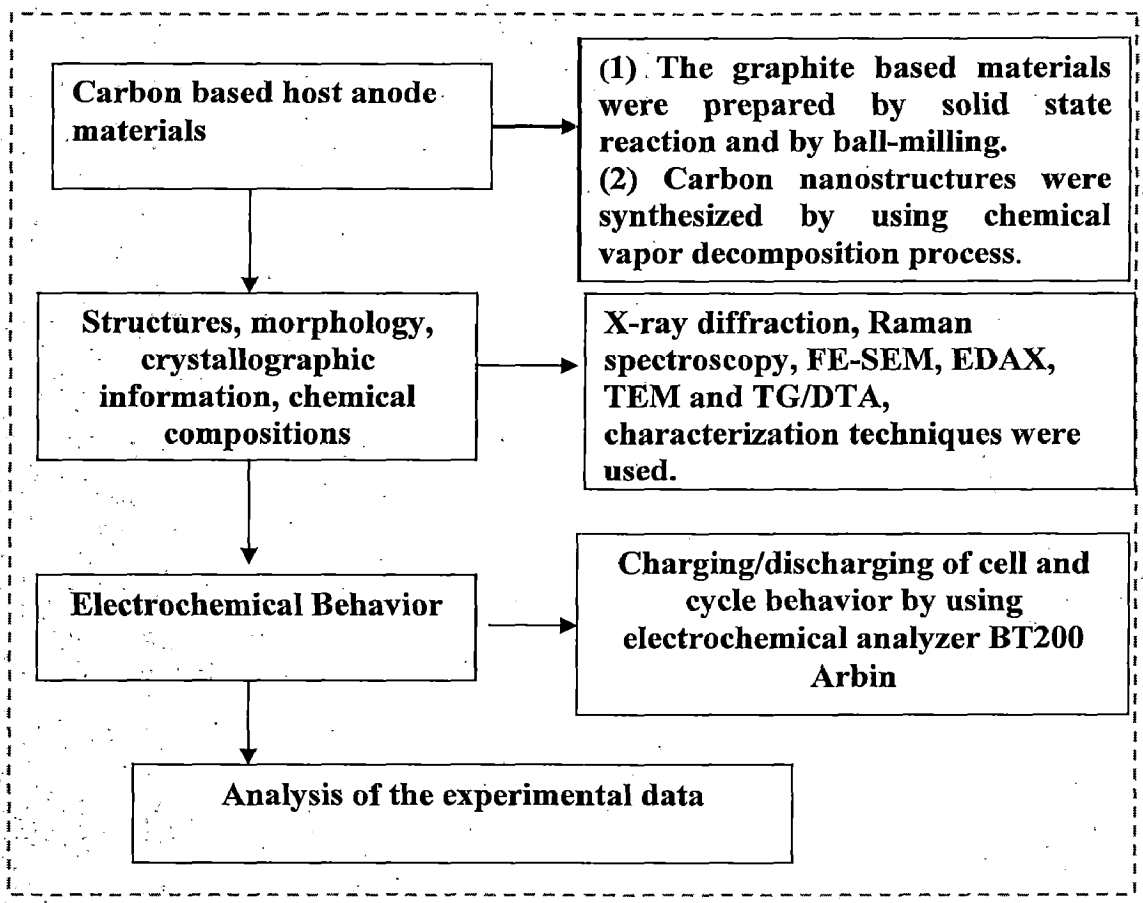

Figure 3.1: Schematic flow diagram of experimental work out.

3.2 SAMPLE PREPARATION

The bulk polycrystalline samples of graphite-silicon and graphite-boron systems were prepared by solid-state reactions. For carbon nanostructure preparation, the required catalyst compounds were synthesized by sol gel process. The details of these processes are described in the next subsections.

3.2.1 Solid State Reaction Method

Solid-state reaction is the most common method for the synthesis of materials. In this method, the solid reactants are heat treated to a suitable temperature for a compound formation. In the synthesis of graphite based anode materials, the following steps are performed (i) weighing of the powders, (ii) powder mixing, (iii) grinding and calcinations of the powder mixtures, (iv) pelletizing and sintering of the samples. These steps are shown in the Fig. 3.2.

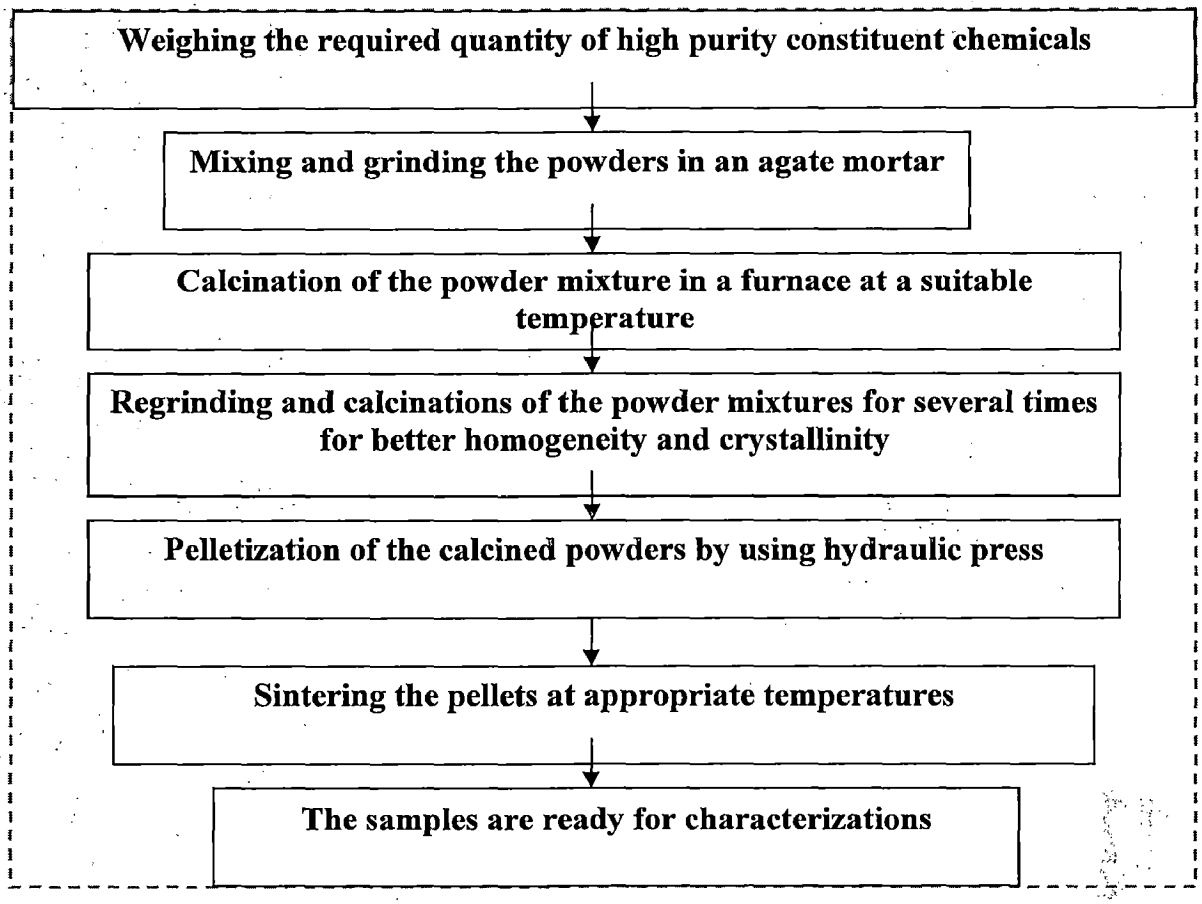

Figure 3.2: The detailed steps for the formation of the compounds by solid-state reaction method.

In the first step after weighing and mixing of the required materials calcinations have been carried out. The reactions involving decomposition of solids or chemical reaction between solids are referred as calcinations. Calcination process normally takes place at temperatures below the melting point of the product materials. Unwanted volatile matter e.g. the residue of the liquid medium used for ball-milling etc., is removed in the initial stage of the calcinations. The calcination conditions are important factor for controlling shrinkage during the sintering. The calcined powder was pressed (at a pressure level of 10 to 20 tons) in the form of cylindrical pellets using hydraulic press. The heating of a solid to a high temperature, below its melting point, to make complete reaction between precursor materials is known as sintering. Sintering converts the material into a denser structure of crystallites joined one another at grain boundaries.

Powder preparation by solid-state reactions generally has an advantage in terms of production cost. However, the powder quality is also an important consideration for electrode materials. The powder is generally agglomerated and a

grinding step is required to produce powders with better characteristics [Greskovich, 1976]. Incomplete reactions, especially in poorly mixed powders, may produce undesirable phases. The need to calcine the starting material at a higher temperature raises the cost. Despite the several disadvantages, this conventional process has still been widely used in industries. There are several reports [Tanaka et al., 2001, Zhou et al., 2003 and Wang et al., 2007] on the synthesis of anode materials for lithium ion battery by solid-state methods.

3.2.2 Sol-gel Method

In sol–gel method, the materials are obtained from solution via gelation. The high homogeneity of the constituent elements and the mild processing conditions of the sol–gel synthesis, such as moderate preparation temperature, makes it possible to obtain unique materials, not accessible with other techniques. Sol-gel processing is a well established method used in laboratories and industries all over the world, and a large number of review articles and books have been published on this topic [Livage, 1986, Zelinski and Uhlmann, 1984 and Pierre, 1991]. In general, the sol-gel involves the transition of a system from a liquid sol (mostly colloidal) into a solid gel phase. Using the sol-gel process it is possible to fabricate ceramic materials in a wide variety of forms e.g. ultra fine powders, thin film coatings, microporous inorganic membranes and extremely porous aerogel materials. The starting material used in the preparation of the sol is usually inorganic metal salts or metal organic compounds. In the typical sol-gel process, the precursors are subjected to a series of hydrolysis and polymerization reactions to form a colloidal suspension or a sol. Further, the processing of the sol enables one to make ceramic materials in different forms. With further drying and heat treatment, the gel is converted into dense particles. The sol-gel process also has other potential advantages over other traditional processing techniques such as better homogeneities, low processing temperature and improved material properties. The detailed steps for the synthesis of the materials by sol-gel method are shown in the Fig. 3.3. The required amounts of high purity nitrates of precursors were dissolved in the double distilled water to form an aqueous solution. An equal amount of citric acid by weight was added to this solution for polymerization with continuous stirring. This solution further heated on a hot plate at temperature of ~80°C until a dry thick sol was formed.

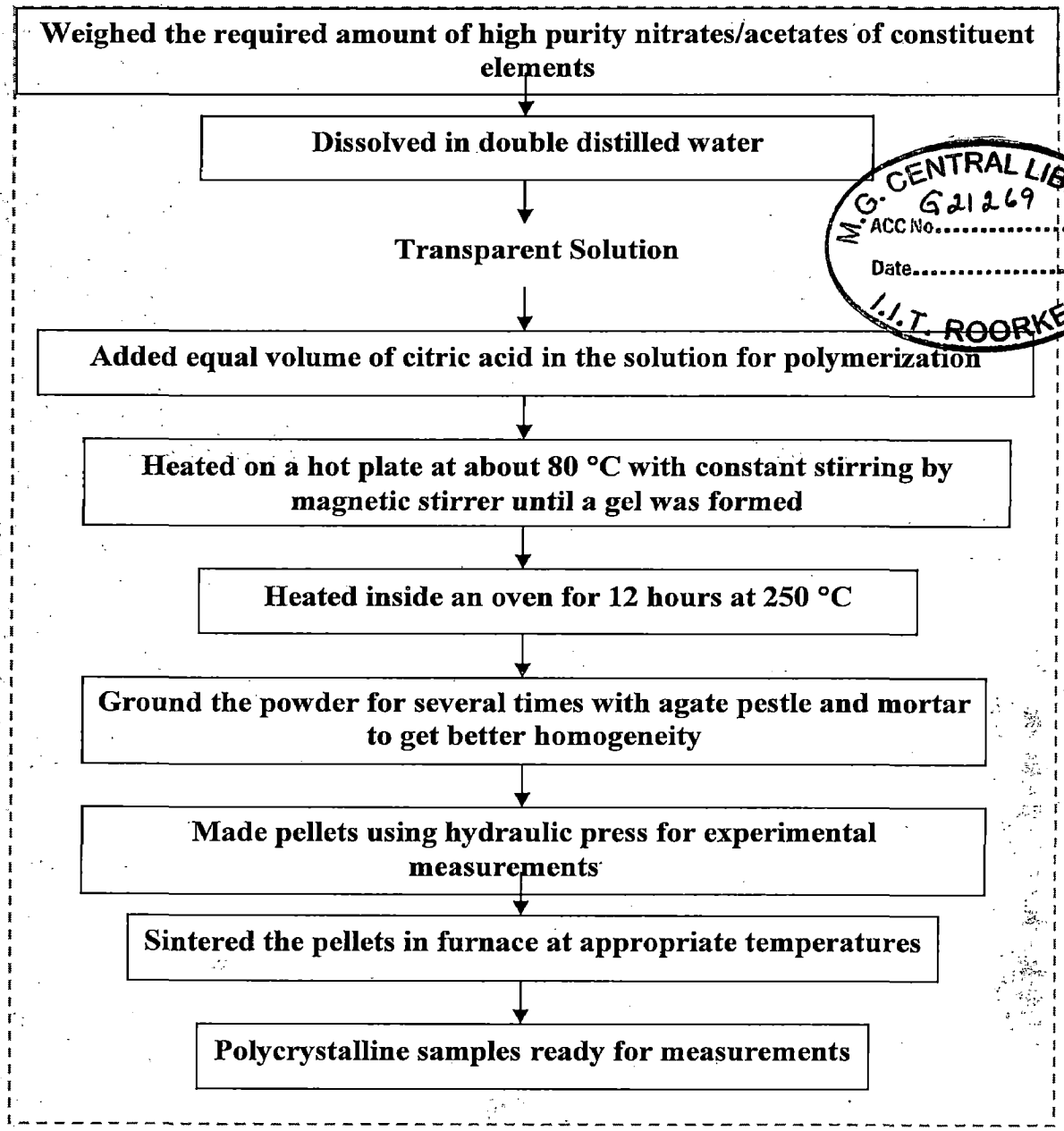

M.G. CENTRAL LIBRARY
ACC No. G21269
Date
I.I.T. ROORKEE

Figure 3.3: The detailed steps for the synthesis of the studied materials by sol-gel method.

This was further decomposed in an oven at a temperature of 250 °C to get the dry fluffy material. The polymeric precursor thus obtained was calcined at 350 °C for 12 h. The resulting powder was pressed in the form of pellets and then sintered at desired temperature. There are several reports [Wu et al., 2002 and Wu et al., 2003] on the synthesis of electrode materials synthesized by sol-gel based methods.

3.2.3 Synthesis of Anodic Alumina Templates

One-dimensional nanomaterials such as nanotubes and nanowires have been synthesized by several methods, which include laser ablation, chemical vapor deposition (CVD) and template-assisted growth. Template-assisted growth is a nanomaterials fabrication method that uses a template, which has nanoporous structure with uniform diameter and length [Masuda and Fukuda, 1995]. Because the size and shape of the nanomaterials depend on the nanoholes of the template, therefore, fabrication of a template with uniform pore diameters is very important. Figure 3.4 shows an example of alumina template with uniform pore diameter and length.

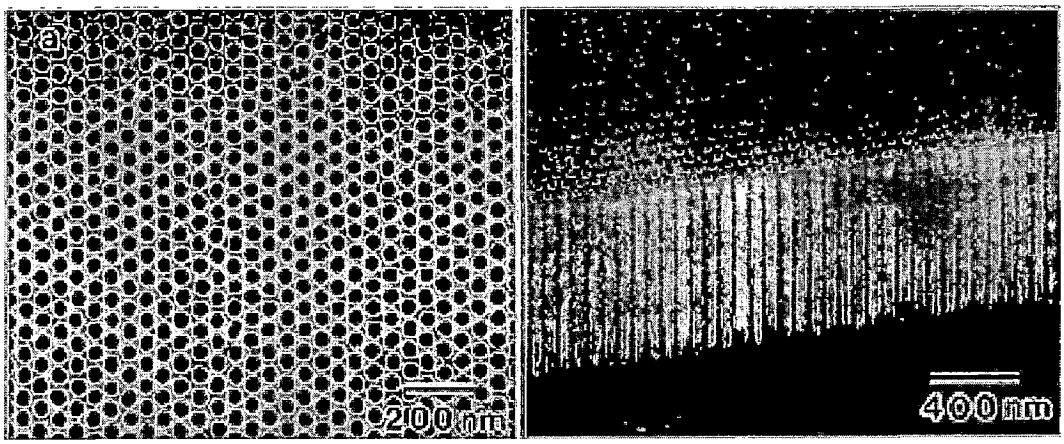

Figure 3.4: SEM image of well-ordered nanoporous arrays (a) top view (b) side view.

Fabrication of an ordered nanoporous array was first introduced by Masuda and Fukuda (1995). They have used two-step anodization process. The step of anodization process is applying a fixed voltage to a substrate in the presence of acid electrolyte to obtain an oxide layer with self-organized nanopores [Pan et al., 2004]. Masuda and Fukuda were able to obtain highly ordered nanohole array by two-step anodization method using 0.3M oxalic acid solutions as an electrolyte and constant voltage of 40 V. The schematic of the two-step anodization process is shown in Fig 3.5. The oxalic acid, phosphoric acid and sulfuric acid are used as electrolytes for anodization process. For the formation of anodized alumina template (AAT), the first step anodization time and the voltage are the main factors in determining the regularity and size of the nanopores.

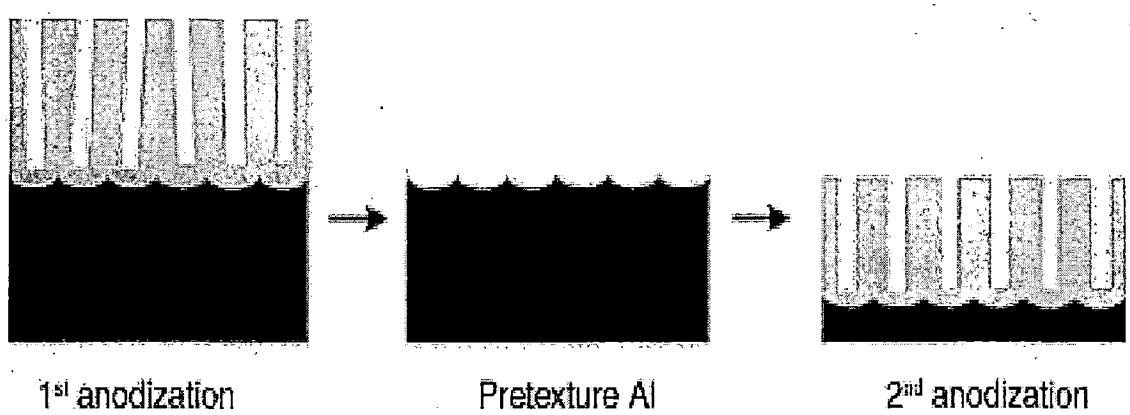

Figure 3.5: Schematic of two-step anodization process.

As shown in Fig. 3.5, well-ordered nanoporous arrays can be obtained by etching the oxide layer with irregular pores. As the anodization time increases a smoother pretexture is formed which can increase the regularity of the pores. Therefore, the anodization time is one of the main factors for fabrication of ordered nanoporous arrays.Li et al. (1998) and Oh et al. [Oh et al., 2005] determined that the order of the nanoporous arrays increases with increase in anodization time. The optimum time for the first step anodization is different for different aluminum film thickness.

The voltage is another factor in determining the regularity and size of the nanopore arrays. Virk (2005) studied the effect of voltage by using three different anodization voltages of 30, 40, and 50 V. Virk determined that as the anodization voltage increases, the diameter of the pores also increases. The anodization is carried out at different voltages in different electrolytes. The voltages that give ordered nanoporous arrays for these electrolytes are shown in Table 3.1.

Table 3.1: Diameter obtained by anodization of aluminum in different electrolytes [Shingubara et al., 2004].

Acid/voltage	Hole diameter (nm)	Cell diameter (nm)
H_2SO_4/25–27 V	>13	50–60
$(COOH)_2$/40 V	>25	90
H_3PO_4/195 V	>200	500

3.2.4 Ball-Milling

The ball milling is generally used as a mechanical grinding of powders initially different in nature up to the preparation of new powder, homogeneous in composition. The milling has been carried out in cylindrical containers called vials using grinding balls. The grinding can be done in presence of inert atmosphere to avoid side reactions. The powder particles are fractured and therefore new highly reactive surfaces can react with surrounding gases [Janot and Guerard, 2005].

Two opposite phenomena are induced by milling process. In one case, the particles split as the result of internal strain developed by the high pressure applied to grains and on the other hand, the highly divided particles tend to agglomerate due to the high reactivity of their surfaces in order to minimize the surface energy [Benjamin and Schelleng, 1981].

The ball milling in liquid media is realized for a long time in order to avoid agglomeration of powder, but very few studies are reported on this subject [Gilman and Nix, 1981 and Watson et al., 1998]. One can classify these syntheses into two categories, according to the liquid role as lubricant and / or as dispersal medium. The liquid medium also helps to avoid the sticking of materials on the milling tools and the formation of aggregates of the powder. Therefore, the preparation of finely divided powders is possible using this technique. The choice of the liquid is a major concern. The liquid used must have a low viscosity and a low vapor pressure at room temperature.

Different milling parameters influence the kinetics of the milling as well as the microstructure of the powders prepared. Milling parameters depend on the type of mill.

The required milling time for the preparation of a material depends on the nature of the material, but also on the other milling conditions. In general, for a given material, longer the milling duration is, smaller the particle size will be. However, longer milling duration leads to higher energy consumption and increases the risk of contamination probability due to the abrasion of milling tools.

The frequency of shocks is proportional to the charge ratio. If the charge ratio is high then the particles split more. The increase in charge ratio allows diminishing the milling duration since some equivalence between these parameters exist. In some cases, a large intensity of milling can induce an amorphization of material and one has to decrease the milling time [Schaffer and McCormick, 1992].

Size and nature of ball have an immense effect on plastic deformations and the applied constrains on the powders. If all the other milling conditions are same, the particles become smaller with larger balls size [Schaffer and Forrester., 1997].

Effect of the rotation speed of the vials is very effective as the shocks create heat due to the plastic deformation of the powder particles. The heat is dissipated into the vial and the local temperature increases which is proportional to the collisions violence and hence to the rotation speed. However, the local and instantaneous temperature increase is difficult to measure, but Eckert et al. [Eckert et al., 1988] have shown that due to this local warming the temperature can rise as high as 400 °C with highly energetic milling.

The most common mills are of planetary, vibrant, attritors and cannon-ball types. The planetary or vibrant mills are largely used in laboratories. Their capacity is of several grams, whereas the industry deals with attritors or cannon-ball mills, whose capacity can be as high as several tons of powders.

The choice of the mill is drastic and depends on the powder quantity to prepare (especially at the industrial scale). It depends also on the type of desired shocks. Vibrant type mills (SPEX) involve mainly frontal shocks, whereas the planetary mills induce both head on and friction shocks. The present work deals with graphite powder, whose tendency to cleave is favored by friction and, thus the planetary mill has been used [Christian and Vecchio, 2005].

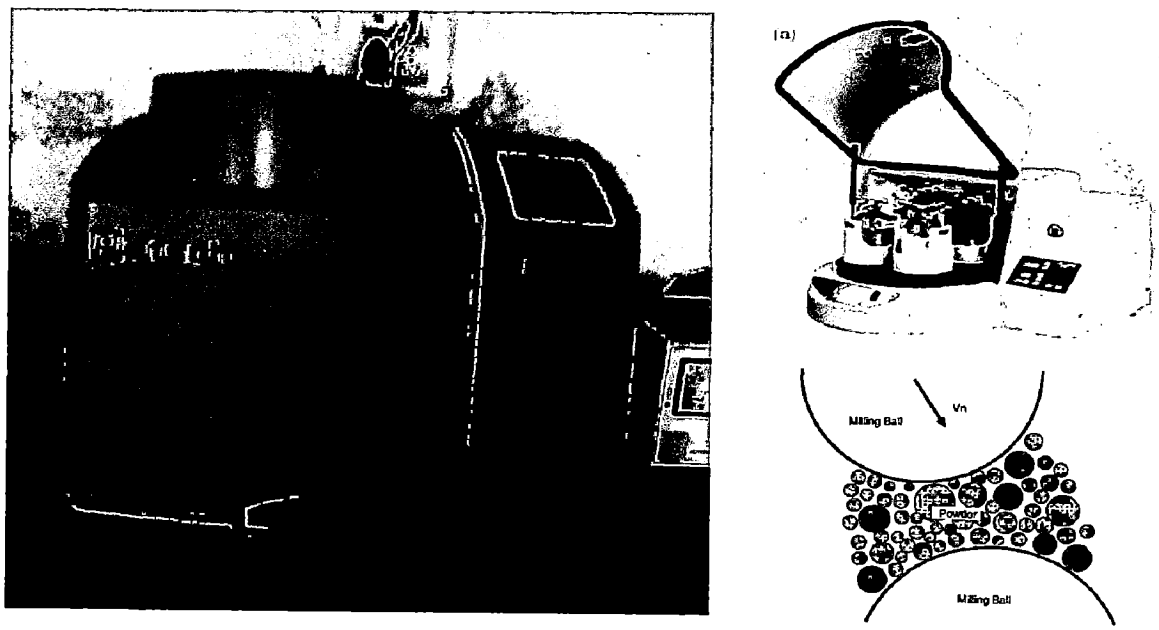

Figure 3.6: Ball-mill (planetary ball-mill) used for milling of graphite powder.

In planetary ball mill, a few hundred grams of the powder can be milled at a time (Fig. 3.6). These are arranged on a rotating support disk and a special drive mechanism causes them to rotate around their own axes. The centrifugal force produced by the vials rotating around their own axes and that produced by the rotating support disk both act on the vial contents, consisting of material to be ground and the grinding balls. Since the vials and the supporting disk rotate in opposite directions, the centrifugal forces alternately act in like and opposite directions. This causes the grinding balls to run down the inside wall of the vial due to the friction effect, followed by the material being ground. The grinding balls lifting of and traveling freely through the inner chamber of the vial and colliding against the opposing inside wall.

3.2.5 Chemical Vapor Deposition (CVD)

Chemical vapor deposition (CVD) is a versatile process suitable for the preparation of coatings, powders, fibers and monolithic components [Pierson, 1999]. With CVD, it is possible to produce most metals, many nonmetallic elements such as carbon and silicon as well as a large number of compounds including carbides, nitrides, oxides, intermetallics, and many others. This technology has become essential for manufacturing of semiconductors and other electronic components, for coating of tools, bearings, and other wear resistant parts and in many optical, optoelectronic and corrosion applications.

Chemical vapor deposition may be defined as the deposition of a solid on a heated surface from a chemical reaction in the vapor or gas phase. It belongs to the class of vapor-transfer processes, which is atomistic in nature that is the deposition species are atoms or molecules or a combination of these. Beside CVD, they include various physical-vapor deposition processes (PVD) such as evaporation, sputtering, molecular beam epitaxy and ion plating. CVD has several important advantages, which make it the preferred over other processes in many cases. These can be summarized as follows:

(1) It is not restricted to a line-of-sight deposition, which is a general characteristic of sputtering, evaporation and other PVD processes. Deep recesses, holes and other difficult three-dimensional configurations can usually be coated with relative ease.

(2) The deposition rate is high and thick coatings can be readily obtained (in some cases thick up to centimeters) and the process is generally competitive and, in some cases, it is more economical than the PVD processes.

(3) CVD equipment does not normally require ultrahigh vacuum and generally can be adapted to many process variations. Its flexibility is such that it allows many changes in composition during deposition and the co-deposition of elements or compounds is readily achieved.

The synthesis of CNTs by CVD is achieved by putting a carbon source in the gas phase and using an energy source, such as a plasma or a resistively heated coil, to transfer energy to a gaseous carbon molecule. Commonly used gaseous carbon sources include methane, carbon monoxide and acetylene. The energy source is used to crack the molecule into reactive atomic carbon. Then carbon diffuses towards the substrate, which is heated and coated with a catalyst, (different transition metal oxides of . Ni, Fe or Co). CNTs will be formed if the proper parameters are maintained. CNTs synthesis by CVD method is essentially a two-step process consisting of a catalyst preparation step followed by actual synthesis of nanotube. The synthesis temperature of CNTs by CVD is generally within the 650-900 °C [Ren et al., 1999].

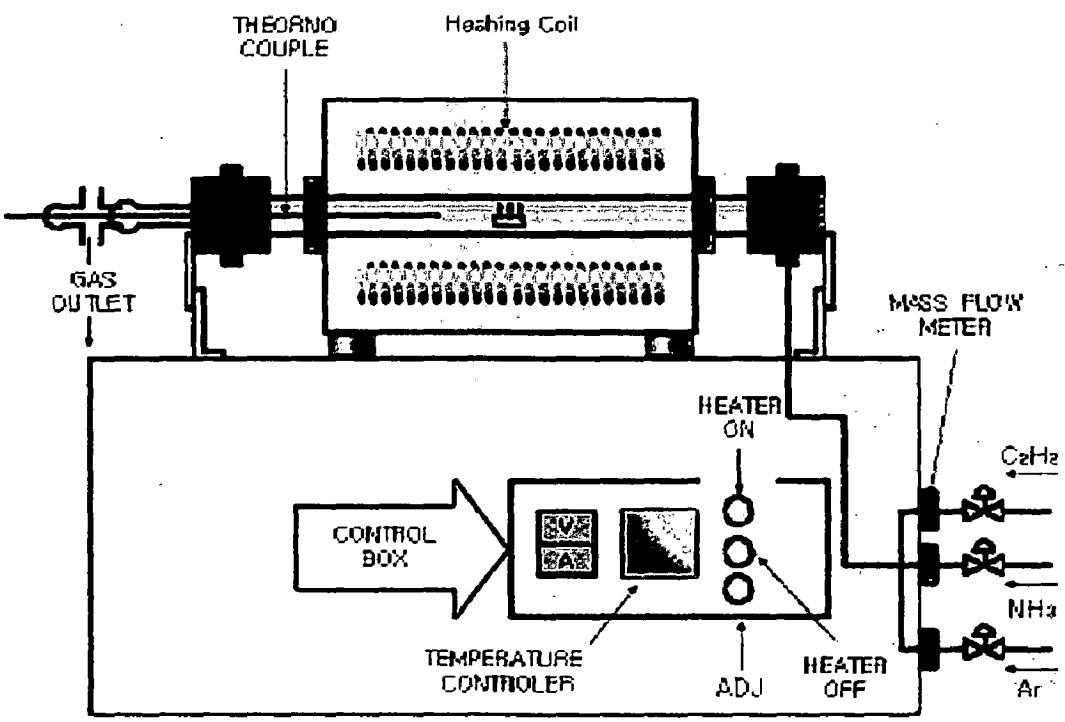

Figure 3.7: Chemical vapor déposition setup.

3.3 THERMAL ANALYSIS

Thermal properties provide information on structural change as well as energy of transformation involved in the materials with increasing temperature. Several methods are commonly used and these are distinguished from one another by the property, which is measured. The methods are thermogravimetry analysis (TGA) for weight loss, differential thermal analysis (DTA) for temperature difference and differential scanning calorimetery (DSC) for heat difference etc. However, in the present study TGA has been used.

3.3.1 Thermal Gravimetric Analysis (TGA)

TGA is a simple analytical technique that measures the weight loss (or weight gain) of material as a function of temperature. As materials are heated, they can lose weight from a simple process such as drying, or from chemical reactions that liberate gasses. Some materials can gain weight by reacting with atmosphere in testing environment. Since weight loss and weight gain are disruptive processes to the sample material, knowledge of the magnitude and temperature range of those reactions are necessary in order to design adequate thermal ramps and holds during those critical reaction periods.

A sample of the test material is placed into a alumina boat that is supported on or suspended from an analytical balance located outside the furnace chamber. The balance is zeroed and the sample cup is heated according to a predetermined thermal cycle. The balance sends the weight signal to the computer for storage, along with the sample temperature and the elapsed time. The TGA curve is the plot of the TGA signal converted to weight changes on the Y-axis against the reference material temperature on X-axis.

3.3.2 Differential Thermal Analysis

DTA involves the heating or cooling of a test sample and an inert reference under identical conditions, while recording any temperature difference between the sample and reference material. This differential temperature is then plotted against time, or against temperature. Changes in sample, which leads to the absorption or evolution of heat which, can be detected relative to the inert reference.

3.3.2.1 Instrumentation

The key feature of a differential thermal analysis kit is sample holder comprising thermocouples, sample container, furnace, temperature programmer and a recording system. The schematic illustration of DTA set-up is shown in Fig. 3.8.

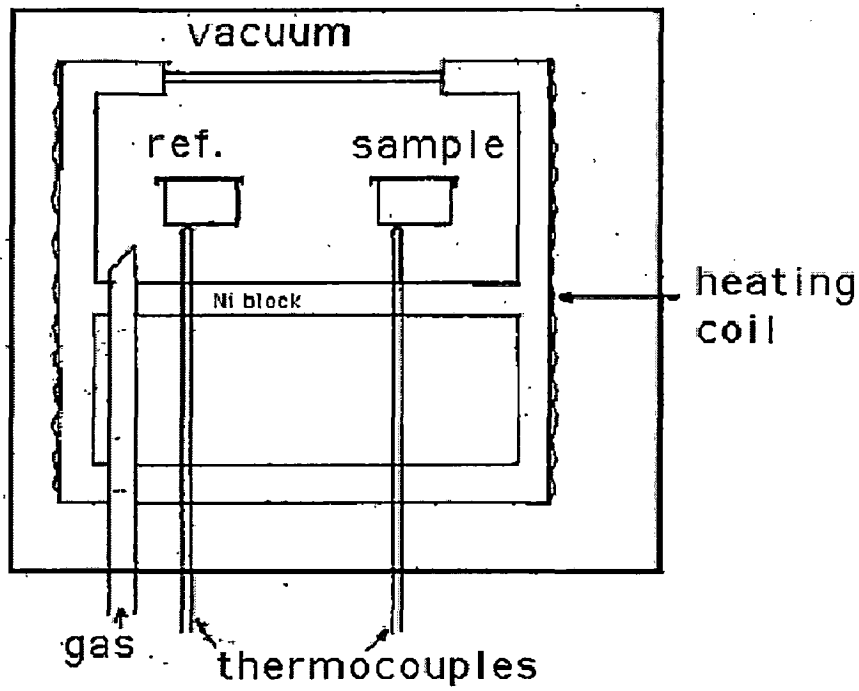

Figure 3.8: Schematic diagram of DTA setup (Bhadeshia, 2002).

3.4 X-RAY DIFFRACTION (XRD)

X-ray powder diffraction is a non-destructive technique widely applied for the characterization of crystalline materials. This method has been traditionally used for phase identification, quantitative analysis and the determination of structural imperfections [Cullity and Stock, 2001]. In the present investigations, this powder diffraction technique is employed for the phase identification and structural characterization of bulk and nanostructure carbonaceous materials. The Bruker AXS D8 Advance powder diffractometer, with CuK_{α} radiation (λ=1.5406 Å), operating at 40 kV and 30 mA, has been used in the present work.

Some solids can be prepared only as microcrystalline powders and hence their structure cannot be determined using single crystal diffraction technique. Moreover, the structures of some materials, which are in the form of hydrocarbons and resins, cannot be determined by single crystal diffraction methods. In such cases, we can determine the structure of the material using powder diffraction data. The ability to determine the

crystal structures using powder diffraction promises to open up many avenues in structural sciences. Powder diffractometer projects the three-dimensional lattice into a one-dimensional lattice. One can determine the orientation, unit cell dimensions, stress/strain, crystal structure, etc, from the information obtained in the powder diffraction data pattern.

The modern x-ray diffraction technique, which is used in powder diffractometer, gives a series of peaks instead of diffraction rings. In these techniques, a detector is used instead of the film. A convergent incident ray is used to give a good peak resolution. The powder is filled in the hole of a sample holder. The set up requires that if reflection is obtained when the beam is incident at an angle θ with the lattice plane, the reflected beam is recorded at an

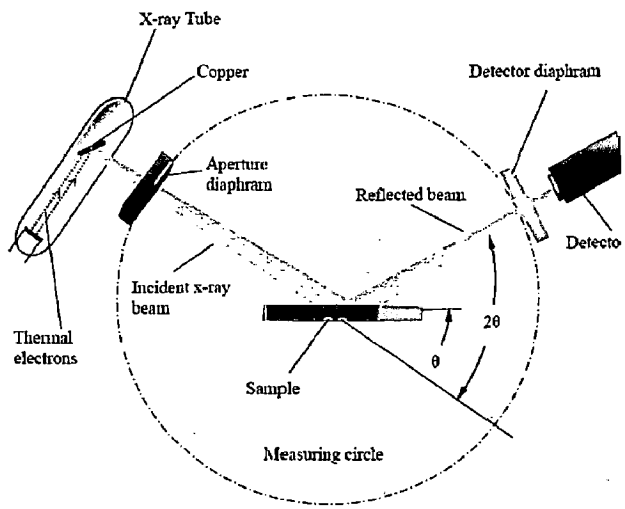

Figure 3.9 Schematic diagram of X-ray diffractometer, in which θ is a glancing angle and 2θ is a diffraction angle.

angle of 2θ, which is referred to as θ-2θ scan, which is shown in Fig. 3.9. The powder diffractometer uses an X-ray detector like a proportional or scintillation counter to measure the positions of the diffracted beams. Diffractometer is a widely used method because it measures the intensities directly.

3.4.1 Indexing of X-ray Diffraction Patterns

When a powder sample of crystalline material is placed in a diffractometer and irradiated by x-ray beam, a characteristic pattern is recorded known as the diffraction pattern. The diffraction pattern is unique for each crystalline material. The positions of

the peaks give information that can be used to determine the cell parameters, and from the intensities of the peaks, the crystallinity of the materials can be determined. Each peak present in the pattern has its own set of indices. More than one diffraction peak can be located exactly at the same position. The process of determining the indices (hkl) associated with an individual peak is known as indexing the pattern. The position of diffraction peaks and the interplanar spacing (d-value) that they represent, provide information about the location of the planes in the crystal structure. Each peak measures a d-spacing that represents a family of lattice planes. Each peak also has an intensity, which differs from others in the pattern and reflects the relative strength of the diffraction. The accurate determinations of the interplanar spacing, lattice parameter etc. provide an important basis for understanding various properties like crystal structure, crystal size, strain and defects in crystal of the material. The materials used is mostly graphite based which has a hexagonal crystal structure, the relationship between the d-spacing and lattice parameters for the hexagonal system is given by equation [Wilson, 1962].

$$\frac{1}{d^2} = \frac{4}{3}\left[\frac{h^2 + hk + k^2}{a^2}\right] + \frac{l^2}{c^2} \qquad (3.1)$$

and the volume of the unit cell (V) = $\frac{\sqrt{3}}{2} a^2 c$ Å^3. (3.2)

Each reflection assigned by *(hkl)* values, equates the interplanar spacing with unit cell parameters. The typical assignments of *(hkl)* values to the reflections are called indexing. In most of trial methods, the system is assumed cubic initially and thus by reducing above equation to simpler forms. The trials for indexing of all the observed reflections are made with lowering the lattice symmetry to tetragonal, orthorhombic and so on. The observed unit cell parameters are refined using their calculated indices and observed d-values by using X-pert high score plus software. The unit cell parameters are fed to adjust in the best way to fit the observed experimental data. It needs to be mentioned here; the solutions obtained are trivial and cannot be free from mistakes. It is always user's decision for judging the accuracy of unit cell parameters.

3.4.2 Crystallite Size Determination

When the size of the individual crystals is less than about 0.1 μm (1000 Å), the term "particle size" is usually used, but the term "crystallite size" is more precise. The x-ray diffraction technique can be successfully used to determine the crystallite size of the materials. This is based on line broadening phenomenon during x-ray diffraction. For large crystallites, the diffraction peaks occur only at precise Bragg angle locations. This is because of the cancelling of the diffractions by incoherent scattering at other angles by lattice planes within the large crystal structure. If the particle size is smaller such that there are insufficient lattice planes to effectively cancel all incoherent scattering at angle close to the Bragg's angle and net result will be a broadening of the diffraction peak around the Bragg's angle. This phenomenon of widening of diffraction peak is related to incomplete cancellation of small deviations from the Bragg's angle in small crystallites and is known as particle size broadening. Particle size broadening is differentiated from the normal width of diffraction peaks related to instrumental effects. In most cases, the particle size broadening will not be observed with crystallite size larger than 1μm. Although a considerable amount of theoretical and experimental work have been done on powder profiles to determine the crystallite size and lattice strain. The theories proposed separately by Wilson [Wilson, 1962], Warren-Averbach [Warren et al., 1950] and Scherrer's are considered as the most promising among all for the purpose. When the width, $\beta_{1/2}$ (full width at half maximum) of the diffraction peak is ascribed to small crystallite size, the broadening caused by small crystallite size can be related to the grain size by Scherrer's formula. The formula is given below, which used to estimate the crystallite size (P) of very small crystals from the measured width of their diffraction curves.

$$P = \frac{K\lambda}{\beta_{1/2}\cos\theta_B} \tag{3.3}$$

where P is the crystallite size, λ is the wavelength of the X-ray used, K is the shape factor which has a typical value of around 0.9 (1.84 La) and $\beta_{1/2}$ is the full width at half maximum (FWHM), which was determined after correction by a factor for instrumental broadening, using Eq. (3.4).

$$b = \sqrt{b^2_{\exp} - b^2_{inst}} \tag{3.4}$$

In this equation β_{exp} is the FWHM of graphite Bragg peak, β_{inst} is the instrumental broadening determined by silicon standard.

3.5 RAMAN SPECTROSCOPY

Raman spectroscopy is a technique used in condensed matter physics and chemistry to study vibrational, rotational, and other low-frequency modes in a system [Placzek, 1934] and is primarily a structural characterization tool. The spectrum is more sensitive to the change in lengths, strengths, and arrangement of bonds in a material than it is to the change in chemical composition. The Raman spectrum of crystals likewise responds more to details of the defects and disorder than to trace impurities and related chemical imperfections in carbon based anode materials.

3.5.1 Basic Principle

When monochromatic light illuminates upon a molecule and interacts with the electron cloud, small fraction of it is scattered in all directions. The spectrum of the scattered light is found to consist of same frequencies. These additional lines of same frequencies have a small fraction about 0.1% is elastically scattered light of the same frequency as that of the incident light (Rayleigh scattering). An even smaller fraction of incident light about 1 photon in 10^6 or 10^7, will be scattered inelastically (Raman scattering), either towards lower frequencies (Stokes scattering) or higher frequencies (anti-Stokes scattering), than the incident light. The differences in energies between the incident photons and inelastically scattered photon correspond to vibrational frequencies of scattering molecule and intensity is proportional to the fourth power of scattered radiation. For the spontaneous Raman effect, the molecule will be excited from ground state to a virtual energy state and relax into a vibrational excited state, which generates Stokes Raman scattering. If the molecule was already in an elevated vibrational energy state, the Raman scattering is then called anti-Stokes Raman scattering.

The Raman spectra of carbon based anode materials containing a variable amount of sp^2 structures have been extensively studied. The application of Raman spectra have been applied on carbon based materials like graphite, diamond, amorphous

carbon and most notably on CNTs. All these materials are characterized by the presence of sp^2 hybridization of the carbons organized into fragments (islands) which can be correlated (in terms of structure and in terms of their Raman response) to an ideally perfect 2-dimensional crystal of graphite (graphene). The crystallite size, La (crystalline size in a-direction) calculated using a relation of $L_a = 44/R$ derived experimentally by Tuinstra and Koenig (1970). Usually the particle size has relatively little effect on Raman line shapes unless the particles are extremely small i.e. less than 100 nm. For this reason, high-quality Raman spectra can be obtained from powders and from polycrystalline bulk specimens like ceramics and rocks by simply reflecting the laser beam from the specimen surface. The measurements for solid samples can be measured in the 90° scattering geometry by mounting a slab of the solid sample or a pressed pellet of a powdered sample so that the beam reflects from the surface but not into the entrance slit.

3.5.2 Instrumentation

A typical conventional Raman system consists of the following basic components: i) an excitation source, usually a visible-light laser; ii) optics for sample illumination and collection of sample-scattered light; iii) a monochromator; and iv) a signal processing system consisting of a detector and a data processing unit. A diagram showing the various components of a Raman spectrometer is shown in Figure 3.10.

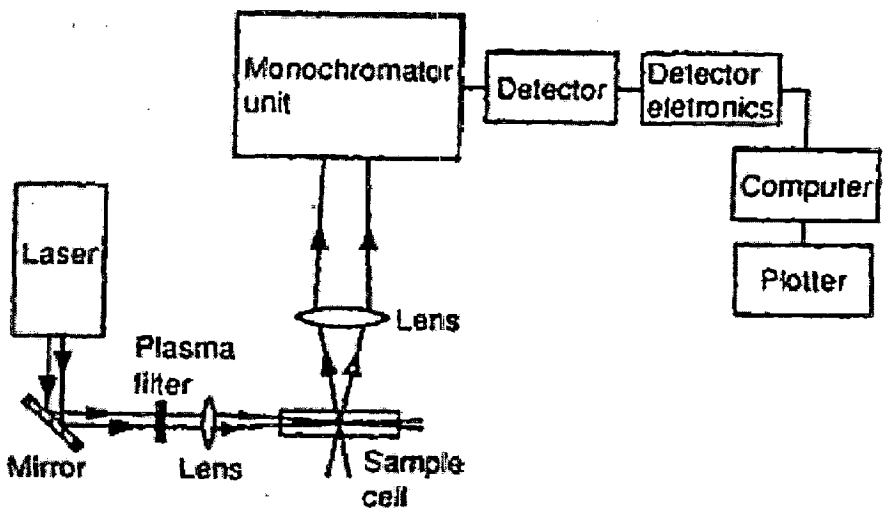

Figure 3.10: Various components used in Raman Spectrometer [Agarwal and Atalla, 1995].

A sample is mounted in a chamber and laser light is focused onto it with the help of a lens. Generally, liquids and solids are sampled in a pyrex capillary tube. Solids either are sampled as pellets or are examined directly without any sample preparation. The scattered light is collected using another lens and is focused at the entrance slit of the monochromator. Monochromator slit widths are set for the desired spectral resolution. The monochromator effectively rejects Raleigh scattering and stray light and serves as a dispersing element for the incoming radiation, sometimes more than one monochromator is used to obtain high resolution and / or better suppression of the Rayleigh line. The light leaving the exit slit of the monochromator is collected and focused on the surface of a detector. This optical signal is converted to an electrical signal within the detector and further manipulated using detector. In a conventional Raman system using a photomultiplier tube (PMT) detector, the light intensity at various frequencies is measured by scanning the monochromator. In contrast, when a multichannel detector is used, a spectral range is simultaneously recorded.

Generally, there are two types of geometries in which a sample is studied in Raman spectroscopy (Fig. 3.11). In the 90° geometry, the laser beam direction and the axis of the collection lens are at 90° to each other. On the other hand, in the 180-degree scattering geometry (also called back scattering mode) these two axes are coincident. The 90° scattering geometry is frequently used in the conventional approach, whereas both 90° and 180° modes are used in the FT (Fourier transform) Raman spectroscopy [Richard et al., 1992].

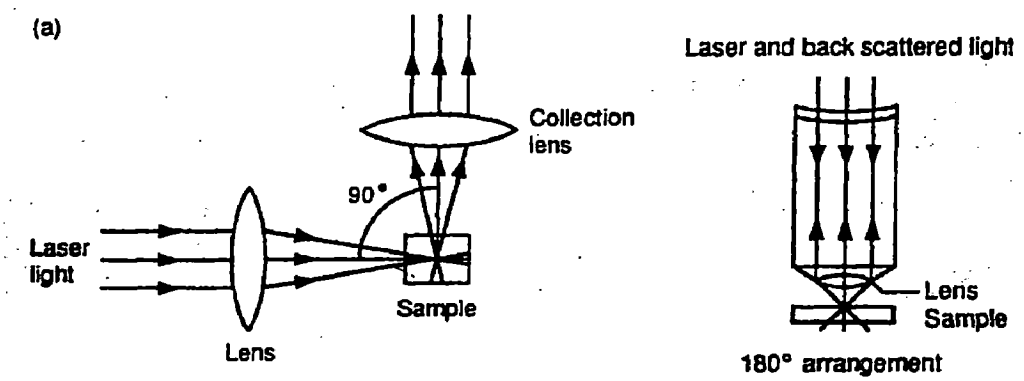

Figure 3.11: Different geometries of sample study in Raman spectrometer (Agarwal and Atalla, 1995).

3.6 FIELD EMISSION SCANNING ELECTRON MICROSCOPE (FE-SEM)

The field emission scanning electron microscope (FE-SEM) is a powerful tool which is capable of producing high-resolution images of a sample surface and is used to measure many characteristics of the sample such as composition, surface topography etc. [Goldstein and Yakowitz, 1975 and Heal et al., 1972]. In the present study, FEI QUANTA field emission scanning electron microscope has been used. The FE-SEM uses electrons instead of light to form an image. A beam of electrons is produced at the top of the microscope by heating of a metallic filament. The electron beam follows a vertical path through the column of the microscope. It makes its way through electromagnetic lenses, which focus and direct the beam down towards the sample. The types of signals produced, when the focused electron beam impinges on the specimen surface, includes secondary electrons, back scattered electrons, characteristics x-rays, Auger electrons and photons of various energies. FE-SEM is an advanced version of SEM in which, a field-emission cathode is used in the electron gun which provides narrower probing beams at low as well as high electron energy, resulting in both improved spatial resolution and minimized sample charging and damage.

In FE-SEM, the primary signal of interest is the variation in secondary electron emission that takes place as the electron beam is swept in raster across the surface of a specimen due to differences in surface topography. The secondary electrons are confined near the beam impact area, which permits images to be obtained at relatively high resolution (~10 nm). FE-SEM images have a characteristic three-dimensional appearance due to large depth of focus of the scanning electron beam and are useful for judging the surface structure of the sample.

3.6.1 Principle of Field Emission Scanning Electron Microscopy

There are several different modes of operation of the SEM, each corresponding to the collection of different types of signals arising from the incident primary electron beam. A schematic diagram of electron interaction with specimen is shown in Fig.3.12.

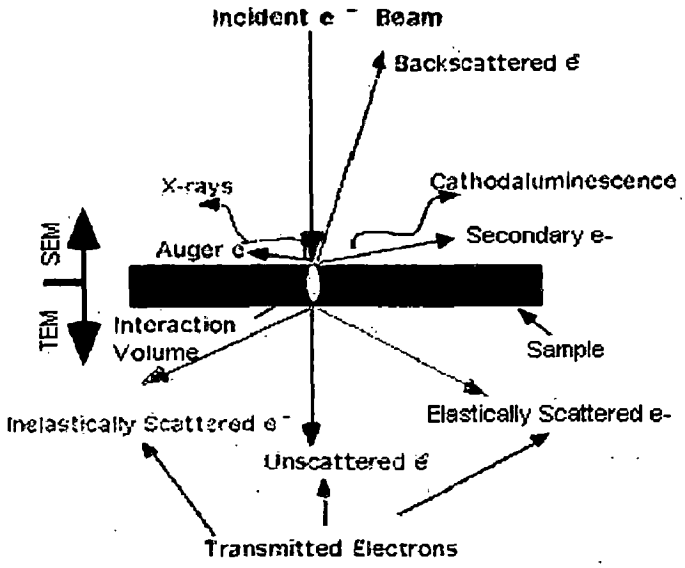

Figure 3.12: A schematic diagram of electron interaction with a thin specimen.

The five main modes are as follows:

(1) ***Emission mode***: The secondary electrons emitted from the specimen are collected by detector. These electrons may have energies less than 50 eV and comes from the material within approximately 5 nm of the specimen surface. This is the most common mode of operating the SEM. It is suitable for obtaining information concerning the surface of the specimen.

(2) ***Reflective mode:*** The primary electrons back scattered from the specimen are collected by detector. These electrons have an energy range close to the energy of incident primary electron beam and they come from the material within a few microns of the specimen surface. This mode provides information, which is more characteristics of the bulk materials.

(3) ***Absorptive mode:*** In this mode, an electrical lead is attached to the specimen and the current, which flows through the lead to earth, is used as signal. Any local increases in the number of secondary emitted electrons or primary reflected electrons causes a corresponding local decrease in the absorbed current. Consequently, absorptive mode images are complementary in contrast to emissive and reflective mode images.

(4) ***Transmission mode***: For this mode, those electrons that completely penetrate thin specimens are collected. These electrons have a wide energy

range, depending on the nature and thickness of specimen. This mode often enables thicker specimen to be examined and high contrasts are to be obtained.

(5) ***X-ray mode:*** For the x-ray mode, the emitted X-rays are collected and used as the signal. Either the x-rays are used as they arise (non-dispersive), or particular wavelengths are selected (dispersive) with the aid of a crystal spectrometer or pulse-height analyzer. This mode is the basis of X-ray probe micro-analyzer.

3.6.2 Working of FE-SEM

In the present investigations, we have used the SEM in its most common mode e.g. emission mode by collecting the secondary electrons. The block diagram of SEM is shown in Fig. 3.13. The electrons from a heated filament are accelerated by a voltage in the range of 10 to 30 kV, and directed toward the centre of an electron optical column consisting of different magnetic lenses.

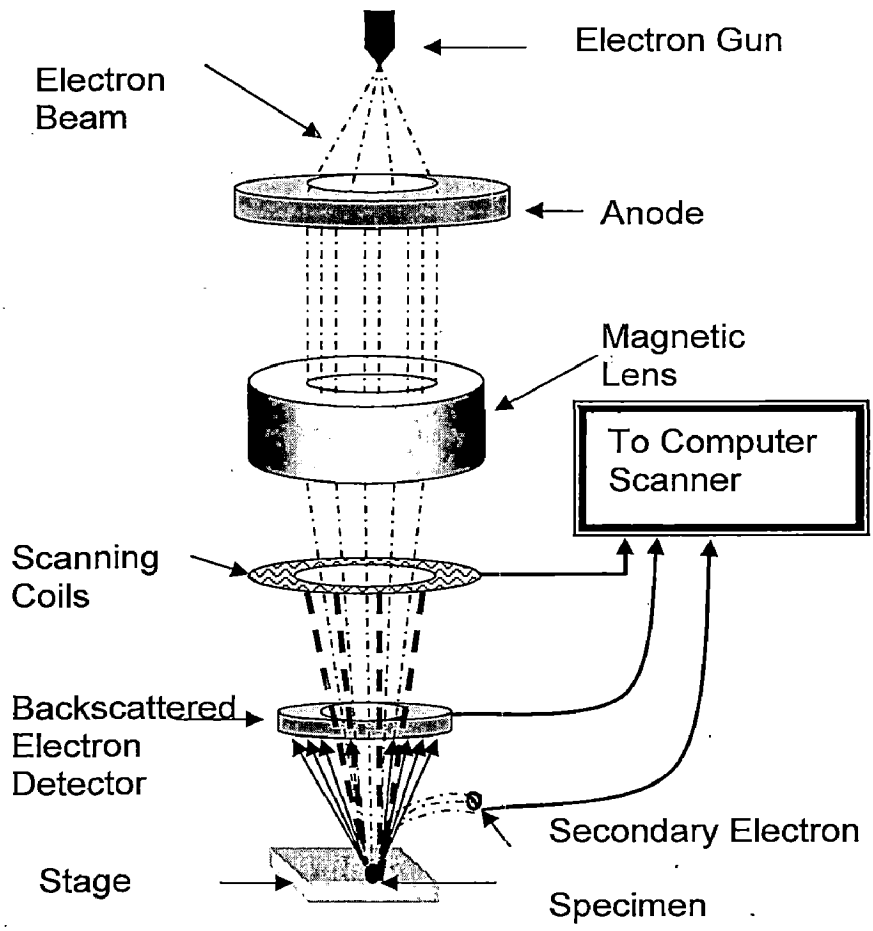

Figure 3.13: Schematic diagram of Scanning electron microscope.

These lenses cause the electrons to be formed into a fine electron beam that fall onto the surface of a solid specimen and made to scan on a raster on the surface by a deflection system. The electron beam incident on the specimen surface results in the emission of secondary electrons in this emissive mode. Detectors collect the secondary or backscattered electrons, and convert them to a signal that is sent to a viewing screen similar to the one in an ordinary television, producing an image. The time duration associated with the emission and collection of secondary electrons is negligibly small compared to the time associated with the scanning of incident electron beam across specimen surface. Hence, there is one-to-one correspondence between the numbers of secondary electrons collected from any particular point on the specimen surface.

The following requirements are needed for preparing samples in SEM:

(1) Removal of the water, solvents or other materials that could vaporize while in the vacuum.

(2) Firmly mounting of the samples.

(3) Coating of gold on non-metallic samples, such as ceramics, bugs, plants etc., to make them electrically conductive. Metallic samples are placed directly into the SEM.

3.7 TRANSMISSION ELECTRON MICROSCOPE

TEM is a microscopy technique whereby a beam of electrons is transmitted through an ultra thin specimen, interacting with the specimen as they pass through. An image is formed from the interaction of the electrons transmitted through the specimen, which is magnified and focused by an objective lens onto an imaging device such as a fluorescent screen or a layer of photographic film, or to be detected by a sensor such as a CCD (charge coupled device) camera. A typical block diagram of TEM is shown in Fig. 3.14. It is an important tool for materials characterization. It is generally used to study the (i) Morphology (ii) Crystallographic Information and (iii) Compositional Information (if so equipped) of materials [Grundy and Jones, 1976, Goodhew, 2001 and Fultz and Howe, 2007].

3.7.1 Principle of Transmission Electron Microscopy

A transmission electron microscope (TEM) works much like a slide projector. A projector shines a beam of light through (transmits) the slide, as the light passes

through, it is affected by the structures and objects on the slide. These effects result in only certain parts of the light beam being transmitted. The transmitted beam is then projected onto the viewing screen, forming an enlarged image of the slide. TEM works the same way except that they shine a beam of electrons (like the light) through the specimen (like the slide).The transmitted part of the beam is projected onto a phosphor screen, which can be viewed.

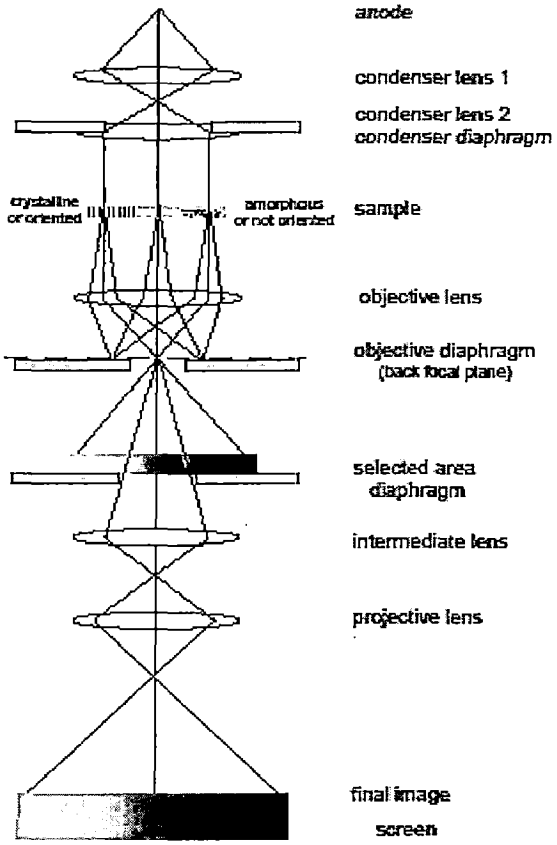

Figure 3.14: Schematic diagram of transmission electron microscope in image mode.

3.7.2 Imaging Mode Methods

3.7.2.1 Bright field

The most common mode of operation for a TEM is the bright field-imaging mode. In this mode the contrast formation, when considered classically, is formed directly by occlusion and absorption of electrons in the sample. Thicker regions of the sample, and / or regions with a higher atomic number will appear dark, whilst regions

with no material in the path of the beam will appear bright and hence the term "bright field" is used.

3.7.2.2 Diffraction contrast

Samples can exhibit diffraction contrast, whereby the electron beam undergoes Bragg scattering, which in the case of a crystalline sample disperses electrons into discrete locations in the back focal plane. By the placement of apertures in the back focal plane, i.e. the objective aperture, the desired Bragg reflections can be selected (or excluded), thus only parts of the sample that are causing the electrons to scatter to the selected reflections will end up projected onto the imaging apparatus. If the reflections that are selected do not include the unscattered beam (which will appear up at the focal point of the lens), then the image will appear dark wherever no sample scattering to the selected peak is present, as such a region without a specimen will appear dark and is known as a dark-field image.

Applications for this method include the identification of lattice defects in crystals. By carefully selecting the orientation of the sample, it is possible not just to determine the position of defects but also to determine the type of defect present. If the sample is orientated so that one particular plane is only slightly tilted away from the strongest diffracting angle (known as the Bragg angle), any distortion of the crystal plane that locally tilts the plane to the Bragg angle will produce particularly strong contrast variations. However, defects that produce only displacement of atoms that do not tilt the crystal to the Bragg angle (i.e. displacements parallel to the crystal plane) will not produce strong contrast.

3.7.2.3 Diffraction

As previously stated, by adjusting the magnetic lenses such that the back focal plane of the lens is placed on the imaging apparatus a diffraction pattern can be generated. For thin crystalline samples, this produces an image that consists of a series of dots in the case of a single crystal, or a series of rings in the case of a polycrystalline material. For the single crystal case, the diffraction pattern is dependent upon the orientation of the specimen. This image provides the investigator with information about the space group symmetries in the crystal and the crystal orientation to the beam path. This is typically done without utilizing any information but the position at which the diffraction spots appear and the observed image symmetries.

Analysis of diffraction patterns beyond point-position can be complex, as the image is sensitive to a number of factors such as specimen thickness and orientation, objective lens defocus, spherical and chromatic aberrations. Although quantitative interpretation of the contrast shown in lattice images is possible, it is inherently complicated and can require extensive computer simulation and analysis. More complex diffraction behavior is also possible, with phenomena such as Kikuchi lines or convergent beam electron diffraction (CBED) providing additional information, beyond structural data, such as sample thickness.

3.7.3 Sample Preparation

The TEM is used heavily in material science, metallurgy and the biological sciences. In each case, the specimens must be very thin and able to withstand the high vacuum present inside the instrument. Sample preparation in TEM can be a complex procedure. TEM specimens are typically hundreds of nanometres thick, as the electron beam interacts readily with the sample, an effect that increases roughly with atomic number. High quality samples will have a thickness that is comparable to the mean free path of the electrons that travel through the samples, which may be only a few tens of nanometers. Preparation of TEM specimens is specific to the material under analysis and the desired information to obtain from the specimen. As such, many generic techniques have been used for the preparation of the required thin sections. In materials science and metallurgy, the specimens tend to be naturally resistant to vacuum, but must be prepared as a thin foil, or etched so some portion of the specimen is thin enough for the beam to penetrate. Constraints on the thickness of the material are limited by the scattering cross-section of the atoms from which the material is comprised. Materials that have thickness as well as dimension small enough to be electron transparent, such as powders or nanotubes can be quickly produced by the deposition of a dilute sample containing the specimen onto support grids or films. For powder samples, first a small amount of sample is dispersed in acetone or methanol. The container is the ultrasonicated for 1 hr so that the powder particles are dispersed in the liquid. Then 2-3 drops of the solution so obtained is poured on to the TEM grid and dried for 5-10 minutes.

3.7.4. Indexing of Polycrystalline Diffraction Rings

In order to understand the geometry of electron diffraction, consider a simple ray diagram of in Fig. 3.15. A beam of electrons impinges on a crystalline specimen. Some of the electron pass through the specimen without interaction, and hit the screen, which is at a distance L from the specimen, at O. Other electrons are diffracted through an angle 2θ by the crystal planes of spacing d, and these electrons hit the film at A, which is a distance r from O. From simple geometry, we see that for small angles of diffraction

$r/L = \tan 2\theta = 2\theta = \sin 2\theta = 2 \sin \theta = \lambda/d$

$$rd = \lambda L \qquad (3.5)$$

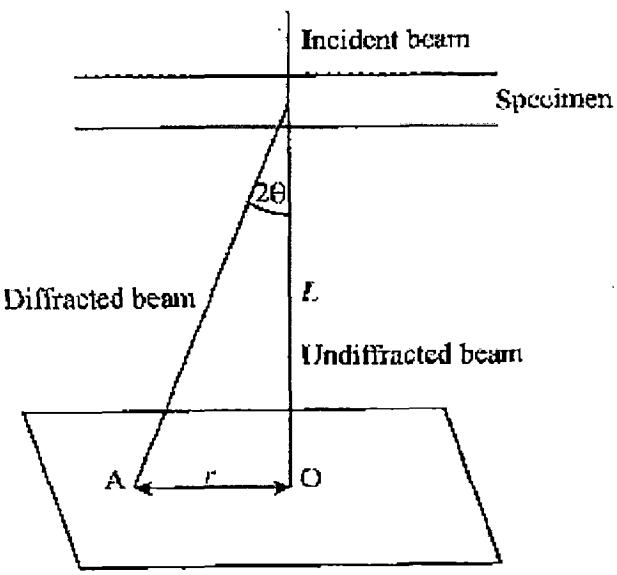

Figure 3.15: Schematic diagram showing the geometry of diffraction pattern formation [Goodhew et al., 2001].

where L is camera length and λ is wavelength of the electron beam, both are constant for an instrument. $L\lambda$ is called camera constant. It can be seen that the distance of a diffraction spot from the undiffracted spot, r, is therefore inversely proportional to the d-spacing of the diffracting planes. If the camera constant is known for the instrument, than one can determine d simply by measuring r on the pattern. In Fig. 3.15, typical ring diffraction pattern obtained for a polycrystalline sample is shown. The red lines are the diameters (D) of particular rings from which r ($r = D/2$) can be easily calculated.

Since each *r* corresponds to a particular d value, one can index the rings. Indexing of the rings can also be verified by using XRD analysis.

3.8. ELECTROCHEMICAL MEASUREMENTS

The electrochemical measurement of cell has been carried out in different step as discussed below.

3.8.1. Electrode Preparation

Preparation of the electrodes involves mixing the sample with small amounts of carbon black, a binder material and an organic solvent for the binder. The mixture is then subsequently spread over a copper foil, which acts as a current collector to form the electrode. The carbon black additive is used to increase the conductivity of the electrode. The binder used is polyvinylidene fluoride (PVDF) diluted in N-methyl-2-pyrrolidinone (NMP). NMP is also added to thin out the slurry so that it can be spread evenly onto the electrode.

The electrode materials were hand mixed with active material, carbon black and PVDF binder in NMP solvent by mortar and pestle to form viscous slurry. Electrodes were prepared by coating of slurries on copper foil, which acts as a current collector. The electrodes were dried in vacuum oven for 12 hrs and then pressed between steel rollers. The particular area of electrode has been cut in square shape, which has been used as anode of cell.

3.8.2 Cell Fabrication

Cylindrical cells made of Teflon were assembled for all electrochemical testings. A micro porous plastic film (cellguard) was used as separator. The cell consists of the prepared electrode as the positive electrode, lithium metal as the negative electrode, a celgard separator and electrolyte. The main steps used in fabrication of cell are shown in Fig. 3.16. However, the detailed schematic diagram of the cell is shown in Fig.3.17, which shows the positions of electrodes and celguard inside a cell. The electrolyte used was 1M $LiPF_6$ in a 1:1 volume ratio of ethylene carbonate (EC) and diethyl carbonate (DEC). The spacer is used to provide cell stack-pressure that essentially keeps all parts of the cell in electrical contact. These cells are connected in an argon-filled glove box having oxygen and moisture contents both less than 0.1 ppm.

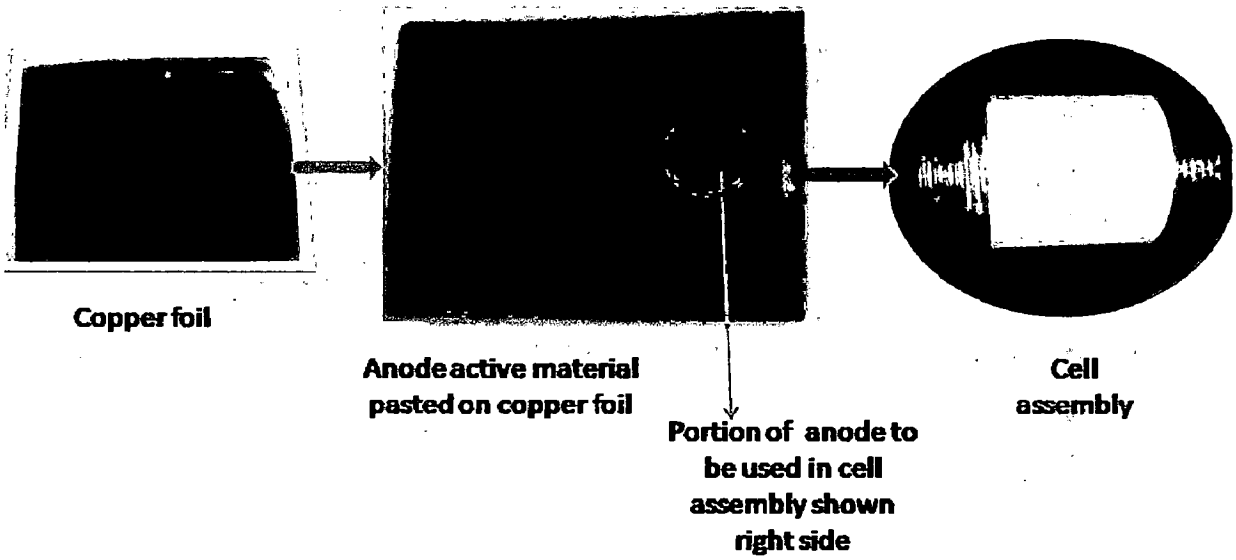

Figure 3.16: Different steps used for cell-fabrication.

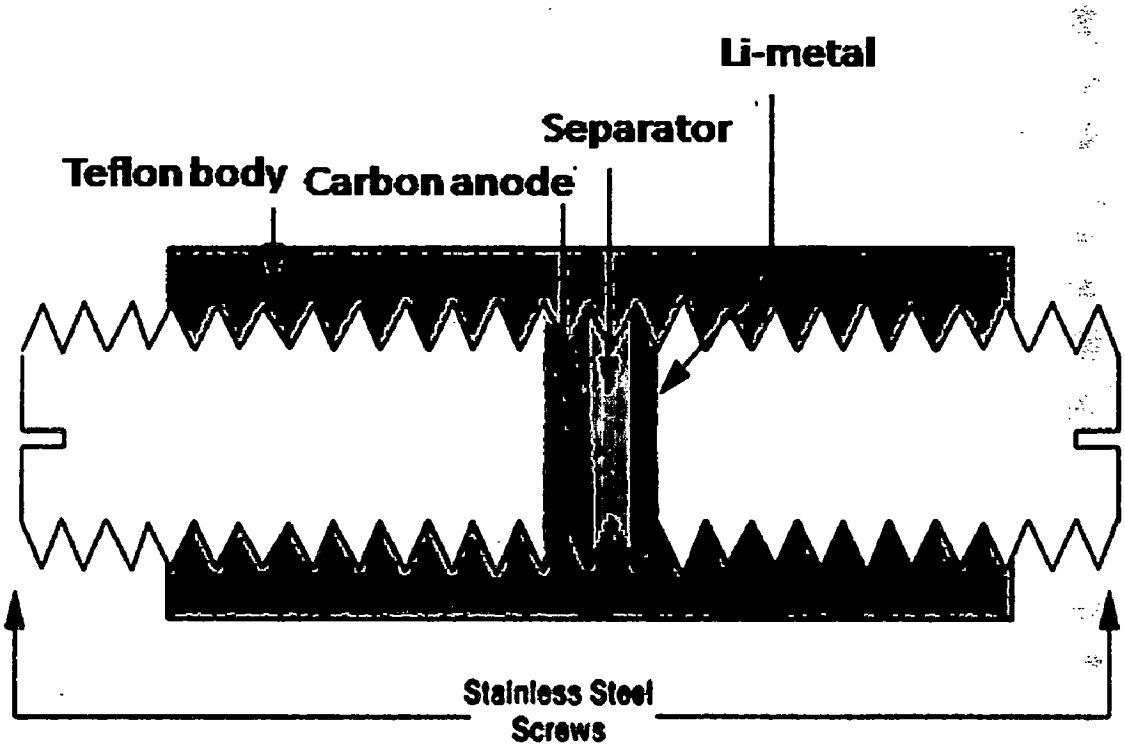

Figure 3.17: Schematic diagram of cell used for electrochemical testing.

3.8.3 Electrochemical Testing

Electrochemical testing of active electrode materials is done using lithium metal as the anode in order to isolate the chemical potential of the material under study. This is possible since Li-metal has a constant chemical potential. The voltage of a real cell as given by following equation,

$$V=\frac{-(V_{cathode}-V_{anode})}{e} \qquad (3.6)$$

depends on the chemical potential of both the electrodes and thus if two intercalation compounds were used, one could not determine which features in the voltage profile correspond to which electrode. In a real lithium ion cell, carbon based material would be used as the anode, however, in the test cells used the carbon based material is the cathode as the tests have been conducted with respect to lithium metal as counter electrode. The discharge cycle for this half-cell corresponds to the insertion of lithium into the carbon-based material. This is opposite to the real cell situation where the discharge process corresponds to the transfer of lithium from the carbonaceous material to the transition metal oxide cathode.

The test cells were cycled under constant current conditions using a electrochemical analyzer (Arbin BT-200). In constant current cycling, a constant current is applied to the battery and the resulting change in the cell potential as a function of time is monitored. From one complete charge-discharge cycle, the gravimetric capacity is derived from the total charge passed per unit mass of the active electrode material, following the equation

$$\text{Charge capacity}=\frac{I(mA)\times t(hours)}{w(gm)} \qquad (3.7)$$

where I is the current in mA at which cell has been cycled, t is the time in hours and w is weight of active materials in gram.

STRUCTURAL AND ELECTROCHEMICAL BEHAVIOR OF CARBON NANOSTRUCTURES

4.1 INTRODUCTION

Since the discovery of carbon nanotubes (CNTs) by Iijima (Ijima, 1991), enormous interest and effort have been devoted to their synthesis, characterization and application for their unique properties. CNTs have high electrical conductivity, mechanical properties, chemical stability [Yang et al., 2003]. The ability of reversible redox reaction of CNTs makes them suitable for use as anode material of lithium ion batteries. Carbon structures are widely used as anode materials in order to overcome safety problems. Therefore, several types of carbon materials exhibiting different morphologies and texture have been investigated for use as anode of Li-ion batteries. The requirements of energy for future of consumer product mostly used in electrical vehicle with improved high performance (large capacity, good rate capability, cycle life and environmental friendly) anode materials are under investigation. In this context CNTs (single walled and multiwalled carbon nanotubes i.e. SWCNTs and MWCNTs) have been evaluated as an efficient electrode material as they are able to store large amount of Li^+ reversibly [Chen et al., 2002, Leroux et al., 1999, Shimoda et al., 2002, Lu and Chung, 2001]. The electrochemical behavior of raw CNTs, open CNTs, doped CNTs and their byproducts have been reported in literature [Yang and Wu, 2001 and Yang et al., 2005]. Some of the commercial lithium ion batteries presently use CNTs as an efficient filler to extend the battery cycle life [Endo et al., 2001]. The electrochemical behavior of carbon-based materials depends on their morphology and microstructures. In this context, an attempt is made to improve the electrochemical behavior of cell by using anode prepared from CNTs having different morphologies.

In this chapter, the synthesis and structural characteristics of catalysts powder, substrate (anodized alumina) and CNTs have been described and the results are discussed. The catalyst particles used for the synthesis of carbon nanostructures were prepared by sol-gel route. The acetate and nitrate of metal salts and citric acid were used as starting

materials to synthesize the catalyst particles. The metal acetate/nitrate salts were dissolved in double distilled water at room temperature to prepare separate solutions, which were added together and homogeneously mixed by using magnetic stirrer at 80 °C until the formation of gel takes place. The thick gel obtained was placed into furnace, heated at 350 °C for 2 h in order to remove organic contents, and was calcined at higher temperature (750 to 800 °C) to prepare the powder. The catalyst particles were dispersed in isopropanol and then the mixture spread over the substrate of anodized aluminum oxide (AAO). The AAO substrate was prepared by anodization of pure aluminum. A thin strip of aluminum was first electropolished in ethyl alcohol and perchloric acid (in ratio of 4:1 by volume) bath by applying 20 V for 1 min at room temperature. The electro-polished aluminum strip was anodized at constant voltage of 40 V for 1 h in 3-wt % oxalic acid electrolyte. The CNTs were synthesized at two different temperatures of 580 and 650 °C on the catalyst $LiNi_{0.5}Co_{0.5}O_2$. Different types of carbon nanostructures having straight, coil, ribbon, waved and bead morphologies have been observed in the synthesis using novel catalysts of $LiNi_{0.5}Co_{0.5}O_2$, $LiMn_{1.8}Fe_{0.2}O_4$, $LiFePO_4$, $LiCu_{0.5}Zn_{0.5}O$ and $LiMn_2O_4$ respectively. The CNTs were synthesized by chemical vapor deposition (CVD) at 650 °C on the catalyst surface. The substrate (anodic aluminum oxide) with catalyst deposited on it was placed on an alumina boat, which in turn was placed in a tubular furnace. When the temperature of the furnace was reached at 530 °C, the ammonia gas was made flowing at the rate of 60 sccm (standard cubic centimeter per minute) and as the temperature was raised to 650 °C acetylene gas was also introduced at 20 sccm for 20 min. The carbonaceous nanostructures deposited at substrate were removed and purified in a solution of 6M HNO_3 in order to remove catalyst particles as well as amorphous carbon. Further, the purified materials were washed thoroughly using distilled water and dried in a vacuum oven at 170 °C. The final products after purification were used as active anode material for lithium ion battery. The electrochemical performance of two different types of carbon nanostructures i.e. tubes and ribbons synthesized have been studied using cell fabrication.

4.2 CATALYST PARTICLES USED

The morphology and microstructure of CNTs influence the electrochemical behavior of lithium ion cell. In this regard, successful attempts have been made by

producing different types of carbon nanostructures. In order to have carbon nanostructure of different shapes and sizes, catalyst plays a crucial role. The catalyst is one essential key in the catalytic chemical vapor deposition process (CCVD) for synthesis of CNTs.

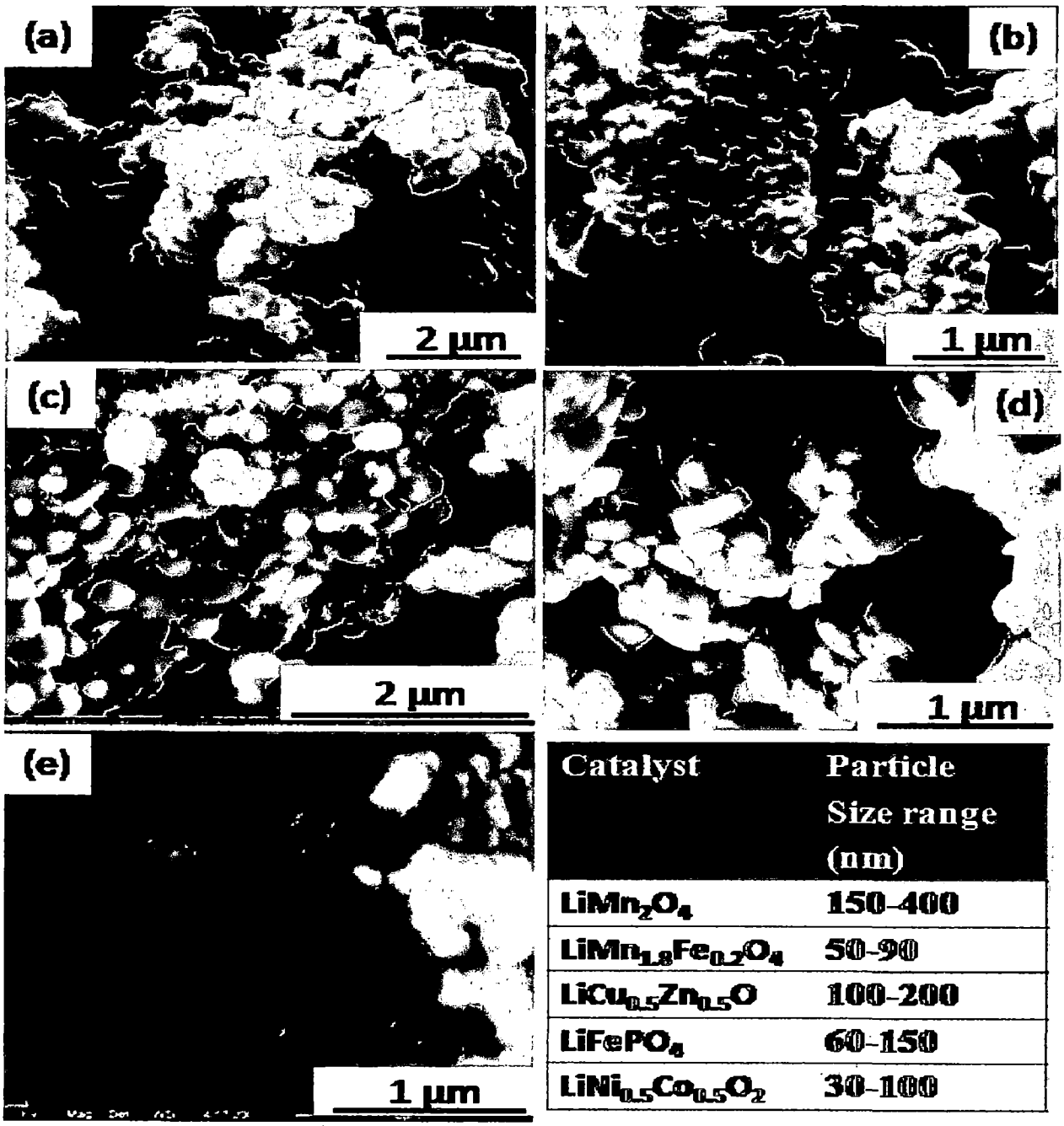

Catalyst	Particle Size range (nm)
$LiMn_2O_4$	150-400
$LiMn_{1.8}Fe_{0.2}O_4$	50-90
$LiCu_{0.5}Zn_{0.5}O$	100-200
$LiFePO_4$	60-150
$LiNi_{0.5}Co_{0.5}O_2$	30-100

Figure 4.1: FE-SEM micrograph of catalysts particles of (a) $LiMn_2O_4$ (b) $LiMn_{1.8}Fe_{0.2}O_4$ (c) $LiCu_{0.5}Zn_{0.5}O_2$ (d)$LiFePO_4$ (e) $LiCo_{0.5}Ni_{0.5}O_2$.

Changing the nature of catalysts (in terms of chemical composition, electronic structure, carbon solubility and morphology), the quality and types of carbon nanostructures change [Dupuis, 2005]. The FE-SEM micrographs for all the catalysts synthesized are shown in Fig.4.1. Both the $LiMn_2O_4$ and $LiMn_{1.8}Fe_{0.2}O_4$ particles (Fig.4.1a & b) have quite similar morphologies having truncated octahedron with clear facetted surfaces. The particle size for pristine $LiMn_2O_4$ lies in the range of 150-400 nm. The particle size of Fe doped $LiMn_2O_4$ is smaller and falls in the range of 50-90 nm. The reduced particle size is perhaps due to the nucleation rate, which is higher than the growth rate in the case of Fe doped sample. The most of the conventional catalysts used for synthesis of CNTs are transition metals (Fe, Co and Ni etc) and combination of these metals. In this study, the catalysts chosen are compounds, which consist of lithium and at least one transition metal. The catalyst containing two or more metals yields synthesized materials of better quality or at lower reaction temperature [Lee et al., 2000]. The morphology of $LiCu_{0.5}Zn_{0.5}O_2$ particles is shown in Fig 4.1c. The potato and rounded shapes morphology is observed for these particles. The particle size lies in the range of 100-200 nm. The $LiFePO_4$ particles, which are used as cathode materials in lithium ion battery, are also used as catalyst for synthesis of CNTs. The FE-SEM micrograph for $LiFePO_4$ powder is shown in Fig. 4.1d. The particles have elongated shape and sizes lying in the range of 50-150 nm. The micrograph of $LiCo_{0.5}Ni_{0.5}O_2$ powder is shown in Fig. 4.1e, which shows that particles are of irregular shape and existent as an aggregate morphology. The particle size of the powder lies in the range of 40-125 nm. The particle sizes of all the different types of catalysts prepared are in the nanometric range and hence are suitable for the catalyst for CNTs growth. The size and composition of the catalyst nanoparticles seem to be the determining factor for the diameter of the CNTs grown on it [Dai et al., 1996]. This can be explained by the fact that such nanoparticles exhibit peculiar electronic properties [Lopez et al., 1999] due to the unusual high ratio of surface atom/bulk atom and for particles of such size range; the atoms on the surface have modified electron density. The chemical composition of catalyst also affects the growth of CNTs. As the Fe, Co, Ni and combination of these catalysts do not

yield exactly the same results, which clearly indicate the effect of chemical composition on types of CNTs produced [Colomer et al., 1999 and Klinke et al., 2001].

4.3 ANODIZATION

This section presents the results of anodization carried out in phosphoric, oxalic, and sulphuric acid baths on pure aluminum (PA). The anodized aluminium templates have been synthesized for the growth of CNTs. Anodic aluminum oxide (AAO) template is one of the promising approaches owing to the possibility of tailoring the size and density of their pores [Jeong et al., 2002] and hence the size of CNTs grown on it. AAO based substrate is necessary for the growth of catalyst free CNTs, which are required for many functional devices to eliminate their disadvantages when the metal particles are undesirable. Template synthesis of carbon nanotube from AAO membrane has also been regarded as a convenient method. The AAO template acts as self-catalyst and is useful for low temperature growth of CNTs.

The oxidation of aluminum during anodization process has been monitored by the oxidation current versus time graph. Figure 4.2 shows a typical current-time curve for the two-step anodization under constant-voltage mode at voltage of 40 V in 3wt% oxalic acid bath maintained at 18 °C. The current is very high at the beginning of the reaction. This high current is due to higher conductivity of pure aluminum metal. The current decreases sharply from A to B as shown in Fig. 4.2, which is attributed to the alumina barrier layer formation and the initiation of nanopores formation. The current begins to increase from B to C due to the increase in resistance as the barrier thickness reduces in front of the forming pores. This fluctuation becomes steady when equilibrium between formation and dissolution of oxide is established. Fig. 4.2 shows that this type of curve can be used to control the oxidation period and consequently to stop the anodization process precisely when the required pores are formed.

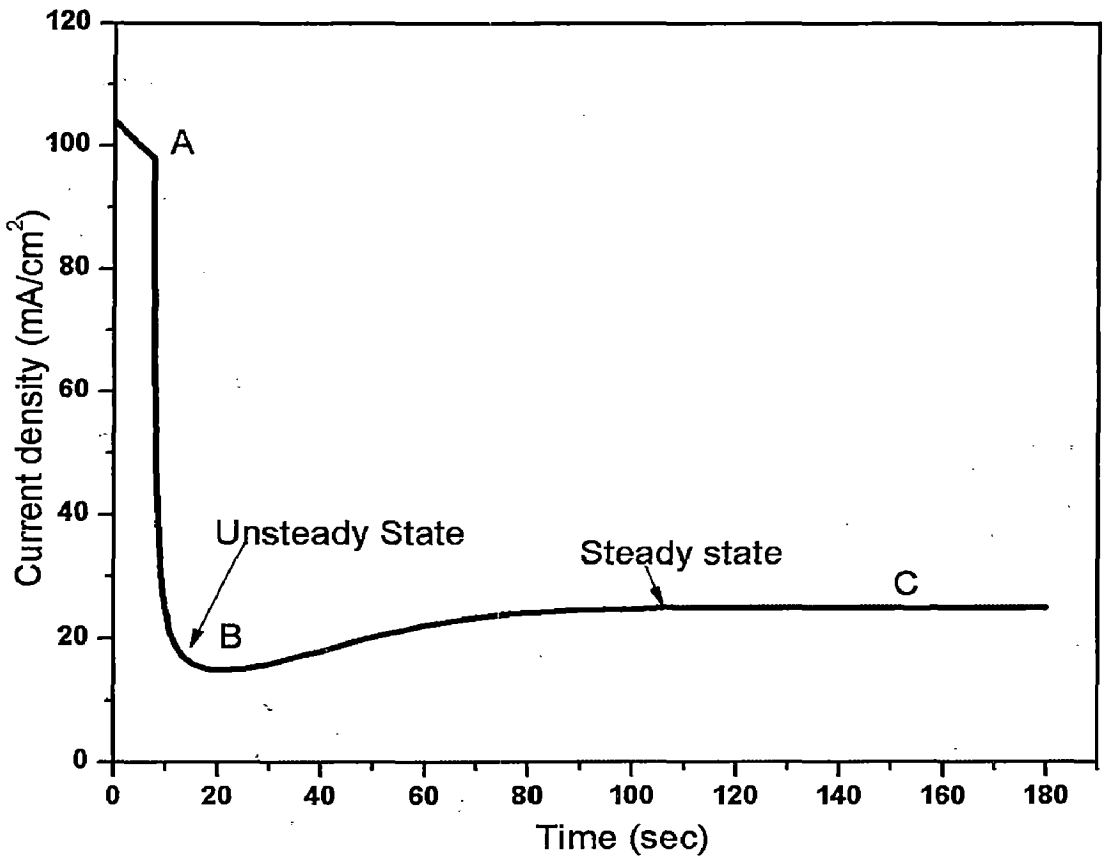

Figure 4.2: Typical current density-time curve for anodization process under constant-voltage mode at a voltage of 40 V and in a 3-wt% oxalic acid bath, maintained at 25 °C.

4.4. EFFECT OF ACID BATH USED FOR ANODIZATION

Three different acidic (phosphoric, oxalic and sulphuric acid) baths have been used in order to obtain the pores of different sizes. Prior to anodization, pretreatment of the aluminum strip is an important step for obtaining ordered porous structure in the anodized alumina and the process consists of mechanical polishing, annealing, degreasing and finally electro polishing. The pure aluminum samples (99.95%, Merck, Germany) have been used in the present study. The aluminum strip shown in Fig.4.3a has good surface finish and hence no mechanical polishing has been carried out for this. The FE-SEM micrograph of aluminum sample with visible rolling marks is shown in Fig.4.3b. The annealing of the samples was carried out at 500 °C in Ar gas atmosphere. The electro polishing was carried out in the solution of ethyl alcohol and perchloric acid (in ratio of 4:1

by volume). The electro-polished portion of aluminum strip is shown in Fig. 4.3c. The electro polished and the unpolished areas in the sample surface are seen bright and dull respectively and can be distinguished easily by naked eye. The anodization has been carried on the electropolished area.

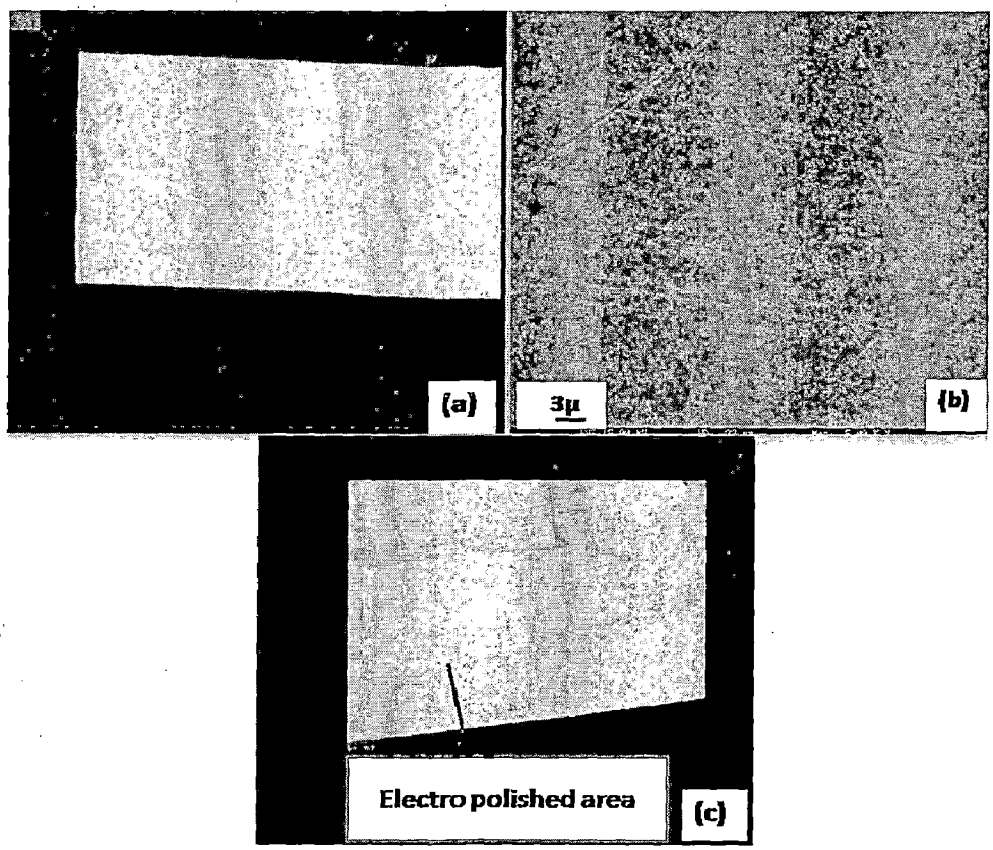

Figure 4.3: (a) Pure aluminum sample as-received, (b) FE-SEM micrograph of the unpolished surface and (c) surface showing electro polished area.

The electro-polished samples of aluminum were used for anodization in three acid electrolyte baths. Figure 4.4 shows the top portion of anodized aluminum strip anodized at 100 V in 5 wt % phosphoric acid bath at 20 °C. The rolling marks are seen in the anodized sample, which were also present in pure aluminum sample as shown in Fig. 4.3b. The FE-SEM micrographs of anodized aluminum are shown at different magnifications in Fig. 4.4 a, b & c. The ordered pore structure is clearly observed (Fig. 4.4 a). As the received sample consists of rolling marks, the pores are aligned in the rolling direction as can be seen from

Fig.4.4 (a, b & c). The pore diameter and Fast Fourier Transform (FFT) from FE-SEM image were determined using Image J software. The FFTs are shown in the respective figures as insets (Fig.4.4b). The frequency histogram of pore diameter of anodized sample is shown in Fig. 4.4d. The histogram is symmetrical and a very intense peak appears at the center i.e. at about 90 nm (pore diameter), which indicates that the pore structure consists of uniform sized pores. The anodization process has been carried out for longer time (1 hour) in order to get regular porous structure. Initially there is very irregular pore structure as the pores are created randomly on the surface sample. However, due to the repulsive forces between neighboring pores during the long anodization time, self-organized pores occur. As a result, hexagonally arrays are obtained at the interface between the porous alumina layers. Li et al. proposed a mechanical stress model to explain the formation of hexagonally ordered pore structure. They considered that the oxidation takes place at the entire metal/oxide interface by migration of oxygen containing ions from electrolyte. The dissolution and thinning of oxide layer is mainly due to the hydration reaction of formed oxide layer. Porous alumina is formed when Al^{3+} ions drift through the oxide layer. After the formation of pores, they grow perpendicular to the surface when the field-enhanced dissolution at the electrolyte/oxide interface is equilibrated with oxide growth at oxide/metal interface. The average pore diameter is about 100 nm. However, the range of pore diameter is quite large and is 50 to 170 nm. This variation in pore diameter may be attributed to the presence of scratches at the surface of as received samples, which are more reactive portion relative to rest of the sample and have larger pore diameter. The FE-SEM image at higher magnification (Fig. 4.4c) shows the separate boundaries between pores. The excellent nanopore structures with almost regular inter-pore distance and pore diameter also can be seen in same Fig. 4.4c. The FFT image shows six distinct spots on the edge of the hexagon (Fig. 4.4b). The FFT image indicates that the larger size domain with less disordered region between the domains and regularity in pore structure. The FFT image and the histogram for pore diameter confirm the regular pore arrangement in substrate.

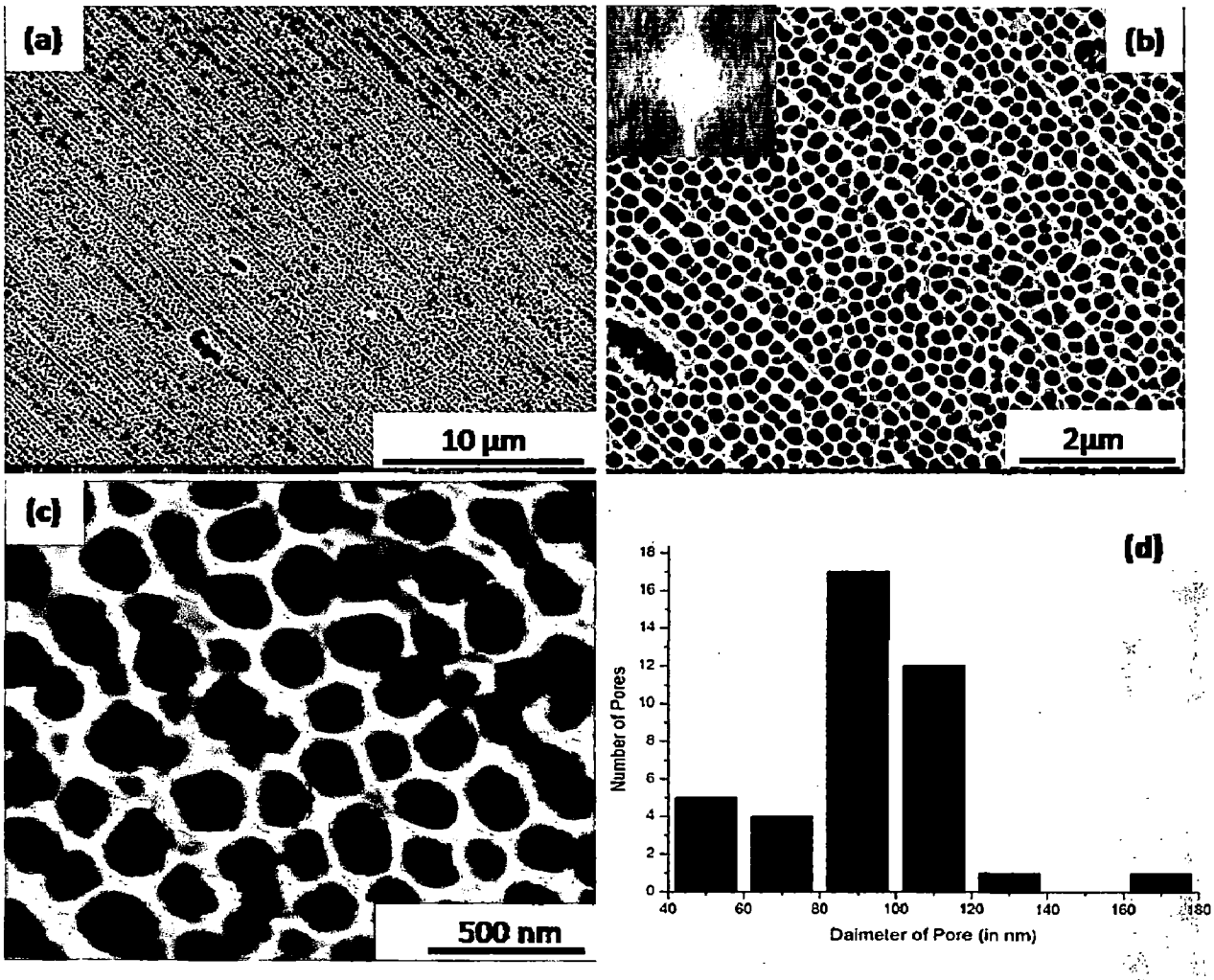

Figure 4.4: FE-SEM micrograph of AAO image obtained with H_3PO_4 solution carried out for 60 minutes at 100 V (a) pore structure all over the sample (b) FFT image as inset (c) boundaries between pores and (d) frequency histogram of distribution of pore diameter.

Figure 4.5 shows the typical FE-SEM micrographs, histogram for pore diameter and FFT as an inset of the top surface of anodized alumina template prepared in oxalic acid bath. The electro-polished aluminum strip was anodized at constant voltage of 40 V for 1 h in 3-wt% oxalic acid bath. The durations of the first and second step anodization were 20 and 60 mins respectively. The top view of pore structure after second step anodization at different magnification shows well ordered pore structure (Fig. 4.5 b &c). Pore diameter varies from 20 to 60 nm as measured by using Image J software. The frequency histogram for pore diameter after second step anodization shows a single strong peak at about 43 nm

and the intensity of the peak is significantly higher than that of the other peaks within histogram (Fig. 4.5 d). The FFT image of top view of second step anodization, which consists of six visible spots at the edge of hexagon indicate that the pore structure is regular for large area of sample (Fig.4.5a).

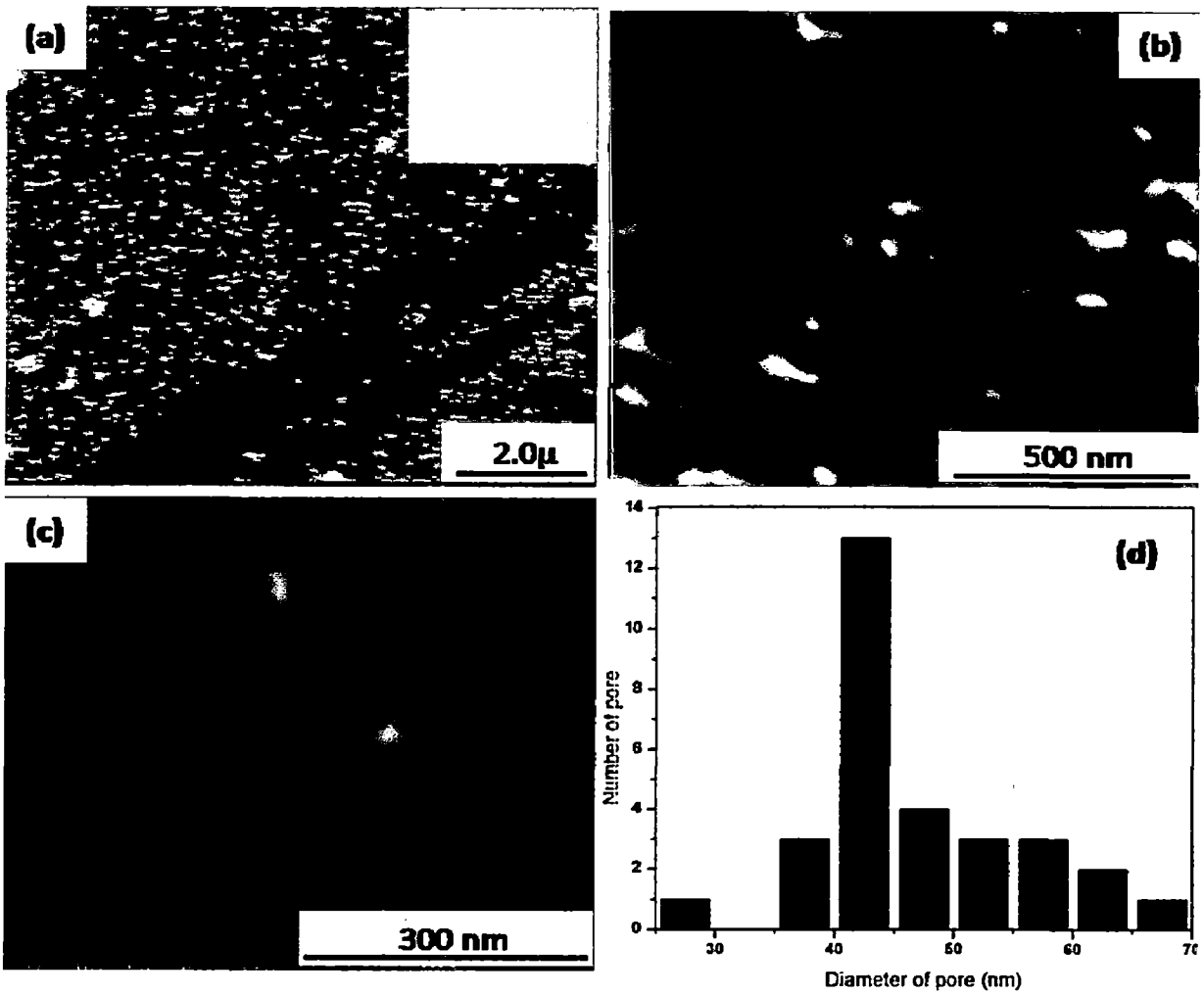

Figure 4.5: FESEM micrograph of AAO image obtained with oxalic acid electrolyte carried out at 40 V for 60 minutes (a) regular pore structure, (b) regular pore structure with separate boundaries (c) at higher magnification and (d) frequency histogram of distribution of pore diameter.

The average pore diameter obtained due to anodization in oxalic acid bath is about 42 nm which is smaller compared to that obtained using phosphoric acid bath, which has required higher voltage for pore formation.

Figure 4.6 shows the FE-SEM micrograph of the surface structure, FFT as inset (Fig.4.6 b) and histogram (Fig. 4.6d) of pore diameter of anodized aluminium using sulphuric acid bath. The two-step anodization has been carried out by anodization for 30 min at 22 V. The pores on the surface are distributed in regular hexagon in some localized

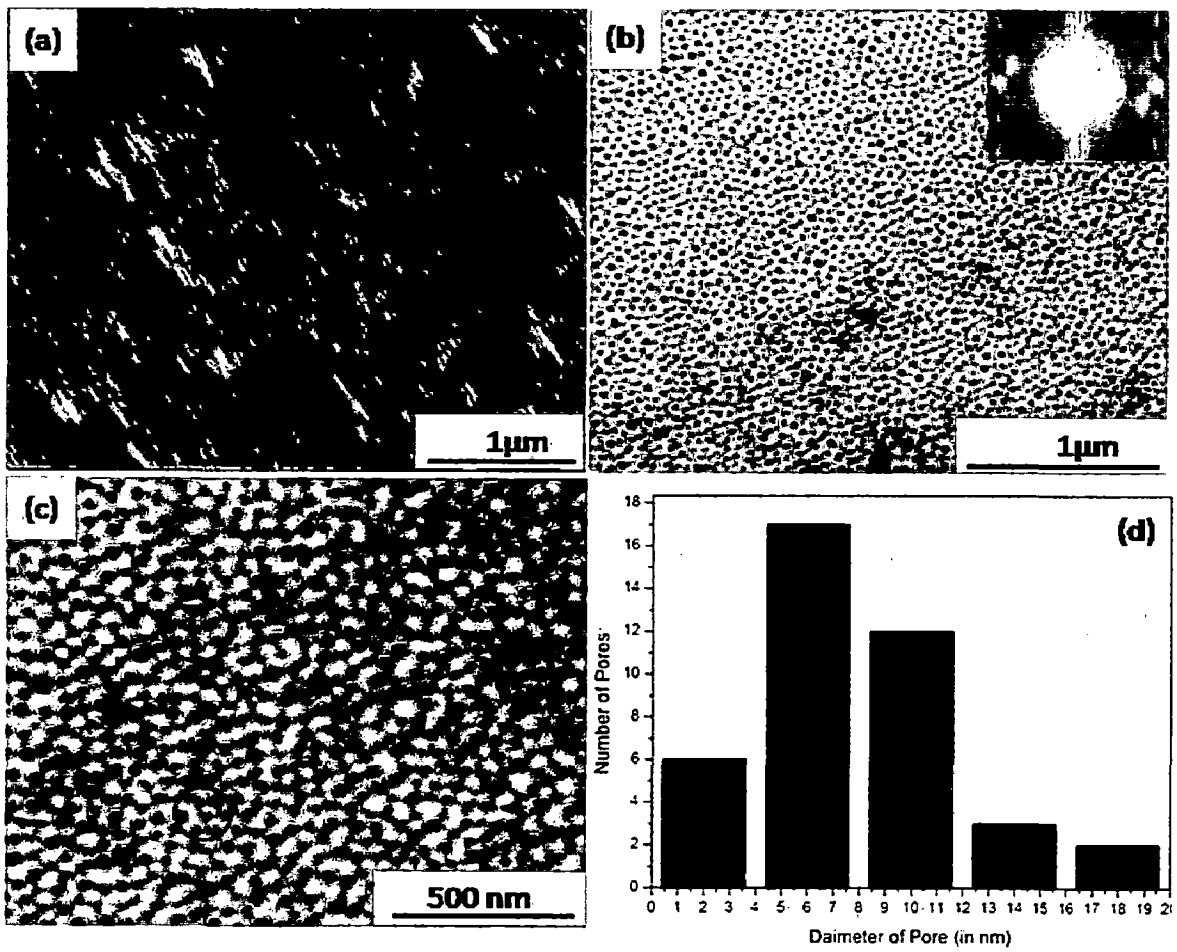

Figure 4.6: FESEM micrograph of AAO image obtained with H_2SO_4 solution carried out at 24 V for 60 minutes (a) pores distributed all over sample (b)at magnification 1,20,000X (c) at magnification 2,40,000X and(d) frequency histogram of distribution of pore diameter .

regions (shown by red circles) as seen in highly magnified image (Fig. 4.6c). The histogram in Fig.4.6 d is asymmetrical with a very strong peak at about 6 nm (pore diameter), however, the other higher peak at about centered at 10 nm also present. The

diameter of pores obtained with sulphuric acid is smallest among three acid bath used in this study. The FFT image of anodized sample in sulfuric acid is shown as in inset of Fig.4.6b. This FFT image is quite different from that observed with phosphoric and oxalic acids for which clear six spots are arranged at edge of hexagon. However, in case of sulphuric acid the FFT image obtained is completely filled disk-shaped area and wide flattened profile indicate the interpore distance, being the centre-to-centre distance between two neighboring pores varying across the area of the sample. Thus, the anodized alumina of different pore diameters was obtained with different acid electrolytes bath used. The overall results are summarized in table 4.1. All of them have been used as substrate for growth of CNTs.

Table 4.1: The pore diameter obtained by using different electrolyte bath

Electrolyte	Voltage (V)	Average Pore diameter (nm)
H_3PO_4	100	90
$H_2C_2O_4$	40	45
H_2SO_4	22	10

4.5 DEPOSITION OF CATALYST PARTICLES ON SUBSTRATE

The catalyst particles were deposited on the surface of anodized alumina substrate prior the CVD process for CNTs synthesis. The catalyst particles were dispersed in ethanol using ultrasonication technique (for 10 min) and a few drops of the liquid was spread over the surface of substrate (anodized aluminum) which was rotated in a spin coater for uniform distribution of catalyst particles all over the surface of the substrate. The top view of substrate deposited with catalyst particle is shown in Fig. 4.7a. The clusters of catalyst are seen on the surface of the substrate. Fig. 4.7b shows the EDX spectrum of catalyst particles deposited on the surface of substrate, which confirms the chemical composition of catalyst particles. The atomic as well as weight percent of elements are tabulated as inset of Fig.4.7b. The substrate (anodized alumina) also acts as catalyst for CNTs growth. CNTs

growth as observed on the surface shown (Fig. 4.7 d) by red circles indicates the catalytic action of anodized alumina for CNTs growth.

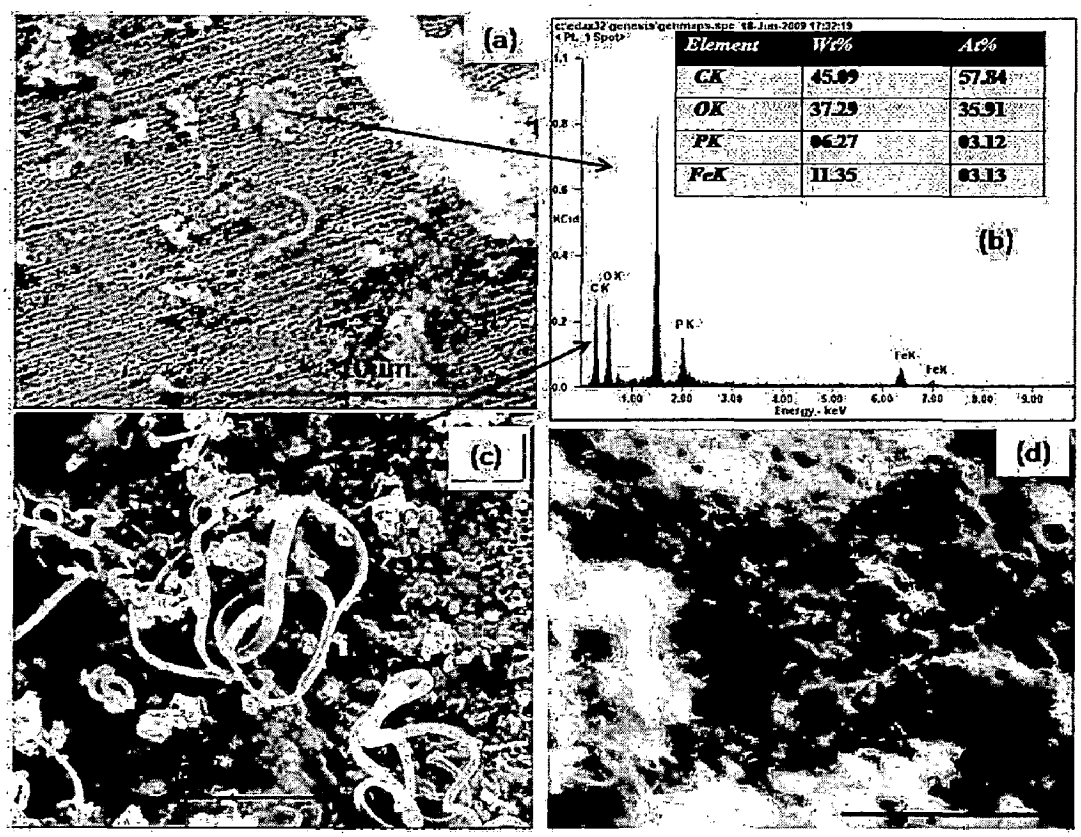

Figure 4.7: (a) Top view of substrate deposited with catalyst particle (b) EDX spectrum of deposited catalyst particle (c) growth of carbon nanostructure from catalyst (d) and anodized alumina as self-catalyst.

4.6 CATALYTIC GROWTH of CNTs BY CVD

The catalyst deposited substrates were used as support for growth of CNTs in CVD process. Mostly the accepted model for growth of carbon filament is based on the concept of the vapor-liquid-solid (VLS) theory [Wagner and Ellis, 1964 and Baker, 1989]. In this model molecular decomposition of carbon source, occurs at one side of the catalyst particle, which becomes supersaturated due to limited solid solubility of carbon in catalyst particle. Carbon diffuses from the side where it has been decomposed to another side where it is precipitated from solution. The driving force for carbon diffusion within the catalytic particle is considered to be originated from the temperature gradient created in the

particle by exothermic decomposition of hydrocarbon at the exposed faced and endothermic deposition of carbon at rear faces [Kanzow and Ding, 1999]. Due to the much lower surface energy of basal planes of the graphite compared to prismatic planes, it is energetically favorable for the filament to precipitate with the basal planes as the cylindrical planes [Tibbetts, 1984]. The catalyst-support interactions are found to play a determinant role for the growth mechanism. Weak interaction yield tip growth mode whereas strong interactions lead to base growth. The details of the mechanism are described in chapter 2. In the present study, both types i.e. tip as well as base growth modes have been observed for CNTs.

4.6.1 Effect of Temperature on Structure of CNTs

The effect of growth temperature has been observed on the morphology and structure of CNTs, as temperature is most important parameter in the synthesis of CNTs. In the present study, CVD has been carried out at two different temperatures. The upper limit of temperature was fixed at 650 °C, which is lower than the melting point (660 °C) of the aluminium, which is underlying material of the porous anodized alumina film. Hence, CVD has been carried out at temperatures lower than melting point of aluminum, viz 580 and 650 °C using the same type of anodized aluminum substrate and catalyst ($LiNi_{0.5}Co_{0.5}O_2$). The structural properties of CNTs grown at two different temperatures were analyzed and are discussed in following paragraph.

The FE-SEM micrographs of CNTs are shown in Fig.4.8. The CNTs grown at 580 °C show the mixture of carbonaceous material (mostly amorphous) with little amount of CNTs. The yield of CNTs is very less in this case. This implies that the decomposition temperature of 580 °C is not adequate for the growth of the CNTs. However, the yield of CNTs grown at the temperature of 650 °C is more as compared to that grown at 580 °C as can be observed in Fig. 4.8 (c & d). The diameter and length of CNTs are also larger in the case of the higher temperature synthesis. The axial as well as curving growths (Fig. 4.8c) have been observed. The curving morphology is due to inhomogeneity and anisotropy of the growth on the surface of supporting catalyst particles which may have generated stress

in nanotubes causing them undergoing periodic bending and twisting to result in formation of a regular helix [Iijima, 1991].

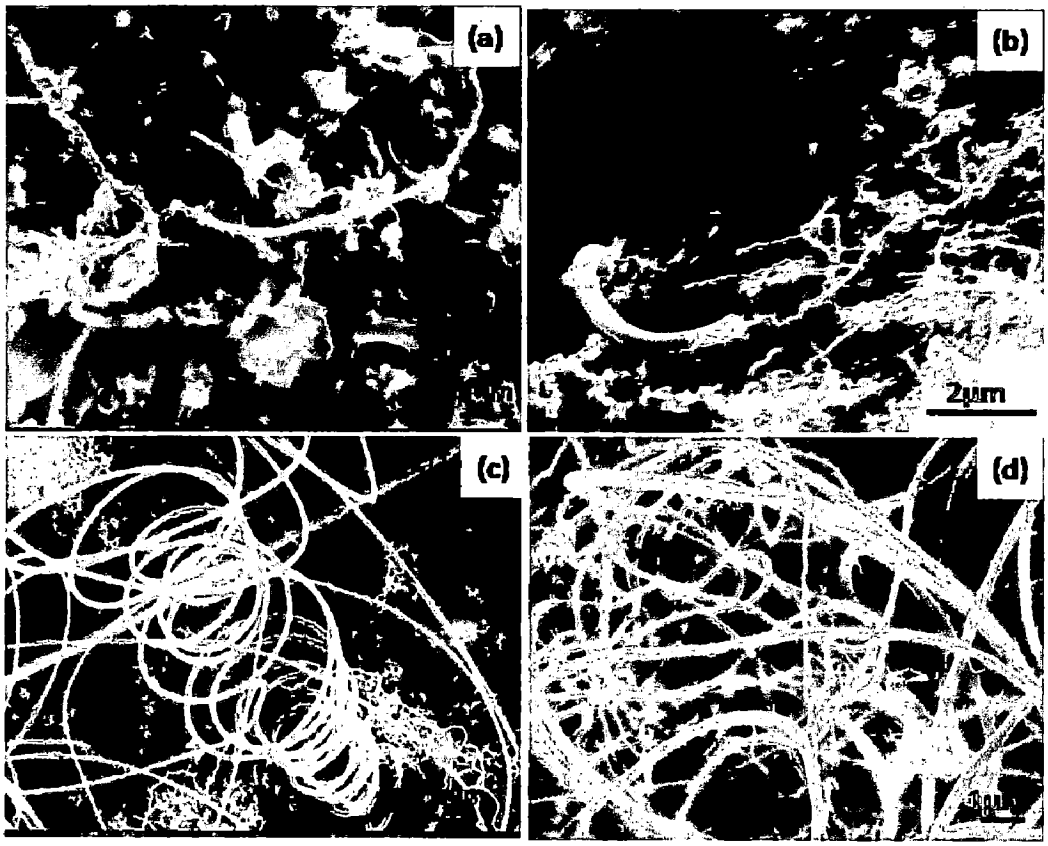

Figure 4.8: FE-SEM image of CNTs grown by catalytic decomposition of acetylene gas over $LiNi_{0.5}Co_{0.5}O_2$ at 580 °C (a & b) and at 650°C (c & d).

The TEM observations have further revealed morphologies of CNTs. The TEM micrographs of CNTs grown at 650 °C are given in Fig.4.9 (a & b). The tubes are mostly multi-walled having hollow core with inner diameter of about 18 nm and outer diameter of about 40 nm with wall thickness of about 10 nm. It has been observed from the TEM micrograph that the outer diameter of the CNTs varies from 12 to 50 nm. The selected area diffraction pattern shown as an inset in Fig.4.9b indicates (002) plane of graphite. From FE-SEM and TEM observations, one can conclude that the tubes are of mostly multi-walled type.

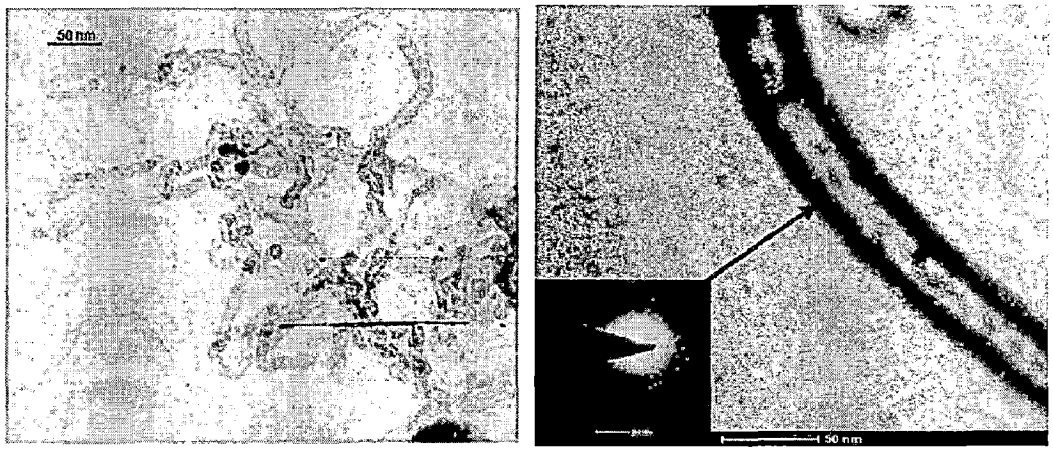

(a) (b)

Figure 4.9: TEM micrograph of CNTs synthesized at 650 °C by catalytic decomposition of acetylene gas over $LiNi_{0.5}Co_{0.5}O_2$, (a) Morphology of tubes and (b) large inner diameter of tube with SAD pattern as inset.

XRD patterns of CNTs at 580 and 650 °C are shown in Fig. 4.10 (a & b). The interlayer spacing, d_{002} are 3.44 and 3.42 Å for CNTs synthesized at 580 and 650 °C respectively. These *d*-values are slightly higher than d_{002} = 3.4 Å, found for MWCNTs grown over other catalysts and is about 2.1% higher than d_{002} =3.35 Å for pure graphite. The increase in *d*-values is related to the possibility of lithium insertion into CNTs during their growth through the catalyst containing lithium $LiNi_{0.5}Co_{0.5}O_2$ used in the present study. This possibility of lithium insertion during growth is also confirmed by observing the shift in G-band of Raman spectra of same CNTs. The effect of temperature on structure of CNTs is obvious as shown in Fig. 4.10. The CNTs grown at 650 °C (Fig.4.10b) are more crystalline than that synthesized at 580 °C (Fig.4.10a). The (002) peak of CNTs synthesized at 650 °C, is sharper and has higher intensity. The sharpness of the (002) interlayer-stacking peak of graphite is a measure of the extent of graphitization, indicating that the CNTs synthesized at 650 °C are much more graphitic than that synthesized at 580 °C. The L_c (crystalline size in c-direction), calculated for CNTs grown at 580 and 650 °C

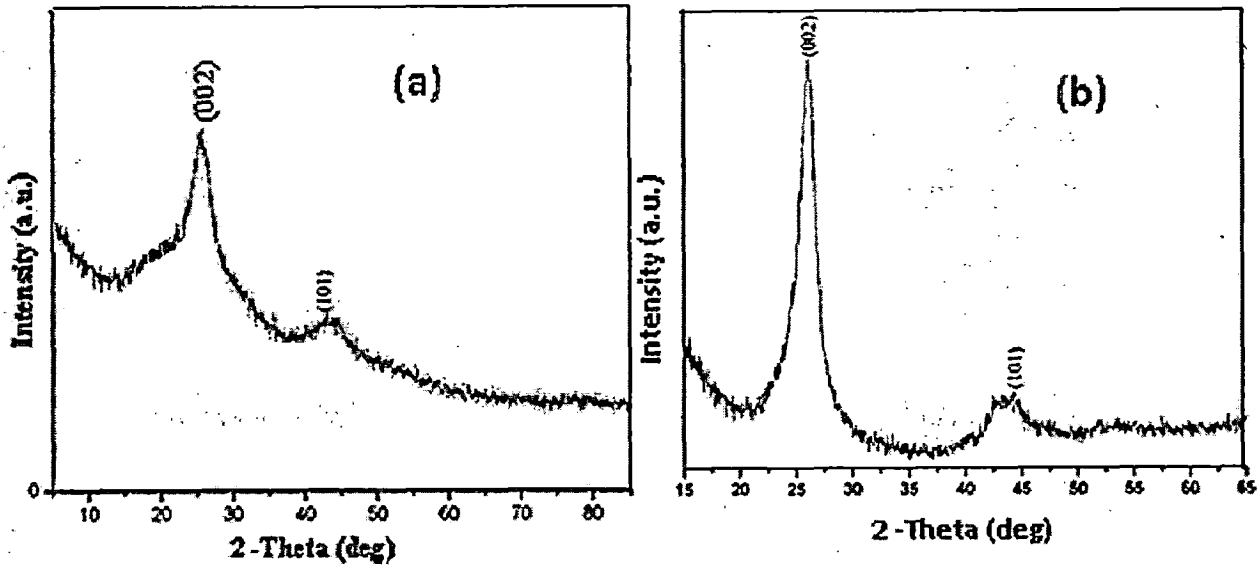

Figure 4.10: XRD patterns of CNTs, synthesized by catalytic decomposition of acetylene gas over $LiNi_{0.5}Co_{0.5}O_2$ at (a) 580 °C and (b) 650 °C.

from the peak (002) of the patterns have been determined as 2.9 and 4 nm respectively, which are higher than the reported 1.4 and 2.4 nm for CNTs synthesized over catalyst of iron oxide from acetylene and ethylene gases respectively [Wu et al., 1999]. The higher L_c observed in the CNTs synthesized in the present study indicates a higher degree of graphitization.

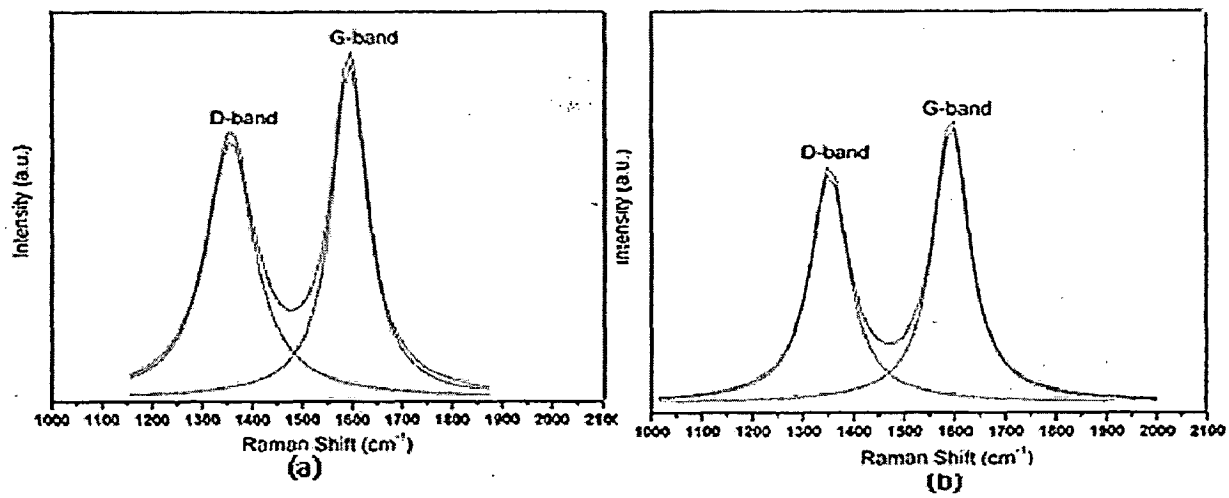

Figure 4.11: Raman spectra of CNTs synthesized by catalytic decomposition of acetylene gas over $LiNi_{0.5}Co_{0.5}O_2$, at (a) 580 °C and (b) 650 °C.

Raman spectra of synthesized CNTs were recorded in selected wave number range between 1000 and 2100 cm^{-1} and are shown in Fig.4.11. The main Raman lines of CNTs synthesized at 580 (See Fig.4.11a) and 650 °C (See Fig.4.11b) are observed at around 1596 and 1352cm^{-1}. The band centered around 1596 cm^{-1} corresponds to the G mode (E_{2g} modes) representing the movement of two neighboring carbon atoms in graphene sheet in opposite directions [Hiura et al., 1993]. The 1352 cm^{-1} band, assigned to the D mode, which is generally not an active Raman mode in graphene, but it is attributed to the presence of defects in curved graphene sheet, tube ends, and staging disorder [Bacsa et al., 1994]. The ratios $R_1 = A_{D1}/A_{G1}$ and $R_2 = A_{D2}/A_{G2}$, where A_D and A_G correspond to the areas of D and G-bands respectively. This value of R is used to estimate the structural defects present in samples. In the present study, these ratios are 1.06 and 0.85 for CNTs synthesized at the temperatures of 580 and 650°C respectively. The up-shift of G-band of CNTs, compared to that of graphite and MWCNTs as mentioned above, is perhaps due to the oxide catalyst containing lithium contributing to structural modification of the CNTs or charge transfer to carbon atoms due lithium doping into CNTs as reported by Bendiab et al. in the case of SWCNTs [Bendiab et al., 2001].

4.6.2 Effect of Catalytic Particles on Structure and Morphology of CNTs

The influence/effect of different catalysts on the morphology and crystal structure of carbon nanostructure grown on similar type of anodized aluminum substrates and subjected to same type of CVD parameters have been studied with the following catalysts

(i) $LiNi_{0.5}Co_{0.5}O_2$

(ii) $LiFePO_4$

(iii) $LiCu_{0.5}Zn_{0.5}O$

(iv) $LiMn_2O_4$

(v) $LiMn_{1.8}Fe_{0.2}O_4$

4.6.3 Morphology of CNTs

4.6.3.1 CNTs grown with $LiNi_{0.5}Co_{0.5}O_2$ Catalyst

The results of elemental analysis of CNTs purified in HNO_3 are tabulated in Fig.4.12 as an inset. The carbon and oxygen contents are 91.39 and 8.61 at % respectively. The oxygen content is higher than 1.63 wt % reported for CNT sample, prepared by arc-discharge and treated with mixture of $LiNO_3$ and HNO_3 [Yang et al., 2005]. The presence of oxygen in sample is attributed to have derived from the following sources – the oxide catalyst, oxygen adsorption from atmosphere and HNO_3. A very intense peak of carbon along with a minor peak of oxygen can be seen from the EDX pattern shown in Fig.4.12. The presence of Au as a trace element is due to gold coating made on the sample for FE-SEM observations.

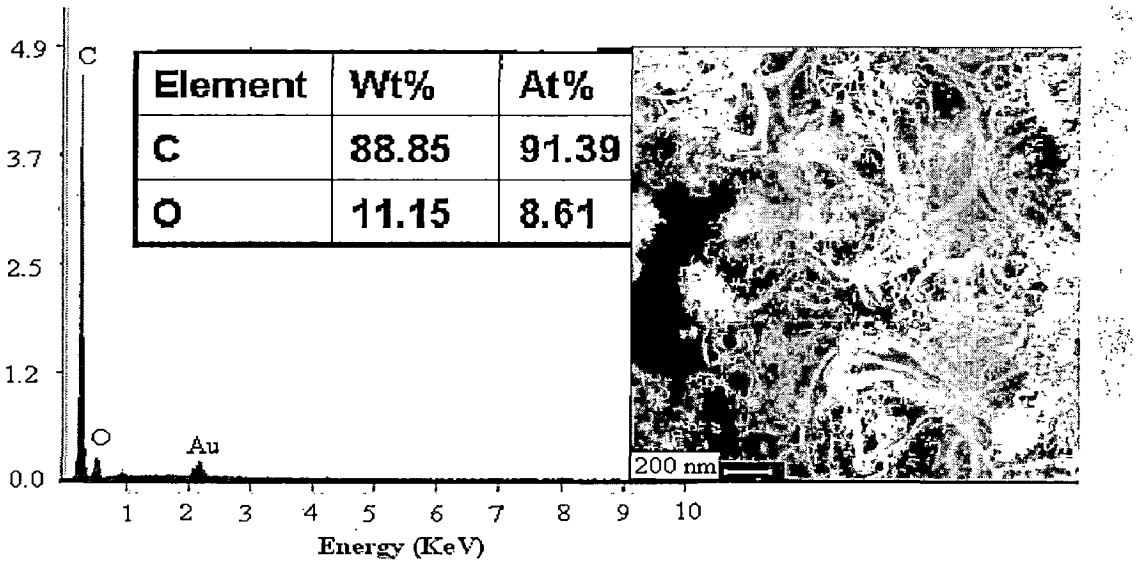

Element	Wt%	At%
C	88.85	91.39
O	11.15	8.61

Figure 4.12: Elemental analysis by EDX of CNTs synthesized by catalytic decomposition of acetylene gas over $LiNi_{0.5}Co_{0.5}O_2$.

Figure 4.13 (a, b, c & d) show the FE-SEM micrographs of CNTs having different morphologies i.e. curving (Fig.4.13a), straight (Fig.4.13 b) and helical (Fig.4.13 c & d). The most attractive approach for formation of straight CNTs is direct growth by CVD with an external force. The external forces can be originated from the gas flow [Zhong et al., 2007] or interactions with substrate surface. The helical growth is not very commonly observed as mentioned earlier. Theoretical calculation also predicted that various forms of

helical CNTs structures are possible and are energetically and thermodynamically stable [Ihara et al., 1993]. Several other mechanisms of formation of coiled CNTs were also reported in literature. The mostly accepted model is the localized stresses and anisotropic rates of carbon deposition on catalytic particles [Zhong et al., 2003]. Coiled CNTs are attracting

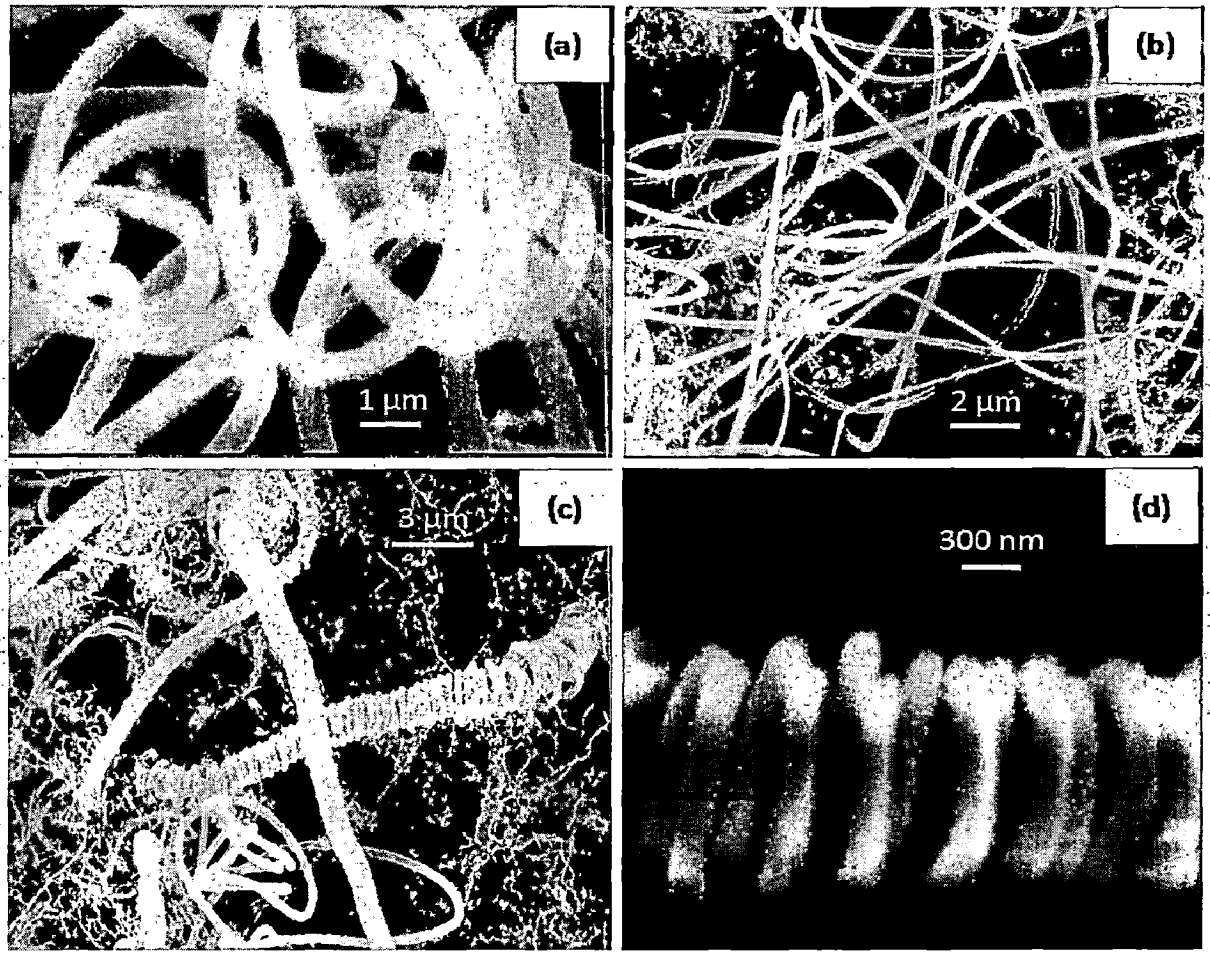

Figure 4.13: FE-SEM image of CNTs grown at 650 °C by catalytic decomposition of acetylene gas over $LiNi_{0.5}Co_{0.5}O_2$, (a) curving morphology, (b) straight morphology, (c) coiled morphology and (d) coiled CNTs at higher magnification.

because their specified morphology enables them to be used as high performance electromagnetic wave absorber, sensors, nanoscale mechanical springs and generation of magnetic beam.

The TEM observations have further revealed different morphologies of CNTs. A few representative TEM micrographs are given in Fig.4.14 (a, b, c & d). The tubes are

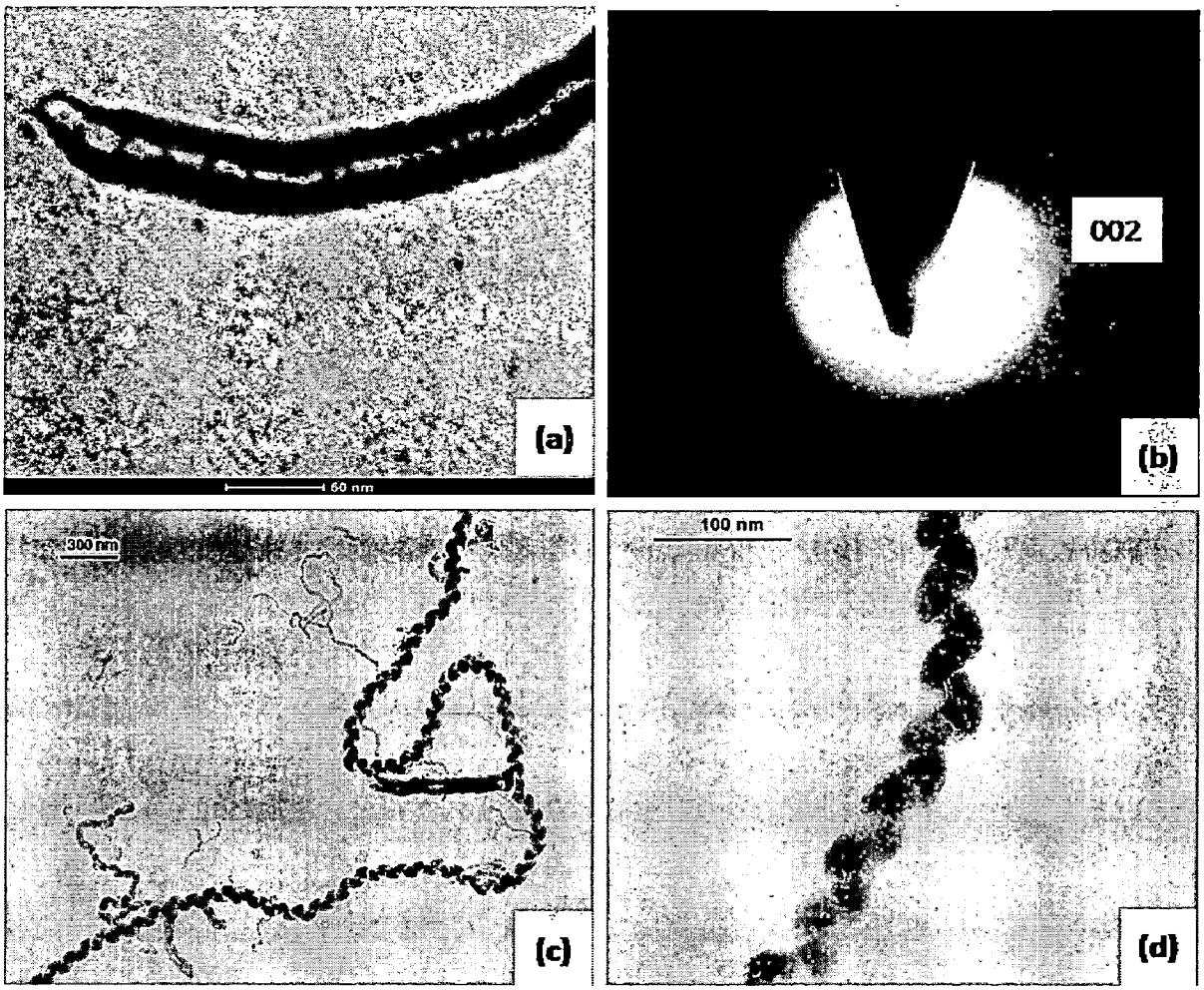

Figure 4.14: TEM micrographs of CNTs showing inner channel in (a) SAD pattern in (b) and helix morphologies both in (c) and (d) synthesized by catalytic decomposition of acetylene gas over $LiNi_{0.5}Co_{0.5}O_2$.

mostly multi-walled having hollow core with inner diameter of about 8 nm and outer diameter of about 40 nm. It has been observed that the outer diameter of the CNTs lies in between 5 and 40 nm. The selected area diffraction (SAD) pattern, shown in Fig. 4.14(b),

reveals a pair of bright diffraction spots from (002) plane of graphite along with a diffuse ring. The graphite is therefore a mixture of crystalline and microcrystalline. The interplanar spacing calculated from diffraction spots is about 3.41 Å. The TEM images of helical CNTs are shown in Fig.4.14(c & d). The outer diameter and the length of the tube are about 40 nm and over 5 μm respectively. From FE-SEM and TEM observations, it is concluded that the tubes are of mostly multi-walled with wall thickness of 32 nm. However, Dai et al. (1996) have obtained SWCNTs with mixed catalysts of cobalt and nickel and mixed oxides of these metals have also helped in growing SWCNT on silicon substrate [Kong et al., 1998]. The metal clusters are assumed to form by reduction of catalytic oxides in the reducing atmosphere of hydrocarbon gases during growth of CNTs. These clusters, though small, are in liquid state and dissolves carbon, which are decomposed from hydrocarbon gas. CNTs grow from these clusters. It is interesting to observe that in presence of Li, the growth of CNTs changes from single walled to multi-walled.

4.6.3.2 CNTs grown with $LiFePO_4$ Catalyst

Carbon nanostructure was synthesized using a novel catalyst ($LiFePO_4$) for different morphologies. Iron and iron oxide based catalysts have been widely used for growth of CNTs/CNFs. Such catalysts are preferred because higher yield can be obtained with these catalysts than using other catalyst based on nickel and cobalt [Hernadi et al., 1996 and Pan et al., 1999]. Lithium influences the carbon nanostructure when used along with Ni and Co in the catalyst [Lemos et al., 2005]. The new catalyst used in present study combines the effects of both Li and iron.

The FE-SEM image of the carbon nano-ribbons (CNRs) on the substrate is shown in Fig. 4.15 (a, b & c). The very high yield of CNRs as can be seen in Fig. 4.15a has been observed with this catalyst. Such a high yield is due to presence of iron. There is also a small amount of carbonaceous nanomaterials having spherical morphologies. Longer and flat nanoribbons are shown at higher magnification in Fig. 4.15c. The energy dispersive x-ray spectroscopy (EDX) spectrum of the synthesized CNRs is shown in Fig. 4.15d, which indicates that the initiation of the growth of CNRs has taken place from the catalyst

$LiFePO_4$ particle as evident from Fe and P detected in EDX at a point from where one of the CNR has emerged. Although ammonia gas was fed together with acetylene during growth of nanostructure, there is no indication of nitrogen in EDX spectrum. In the present study long, thin (almost transparent) CNRs were formed from catalyst particles. The catalyst particles allow the formation of graphene layer of limited dimension growing from its faces without curling it up as a tube or fiber (Fig. 4.15 c).

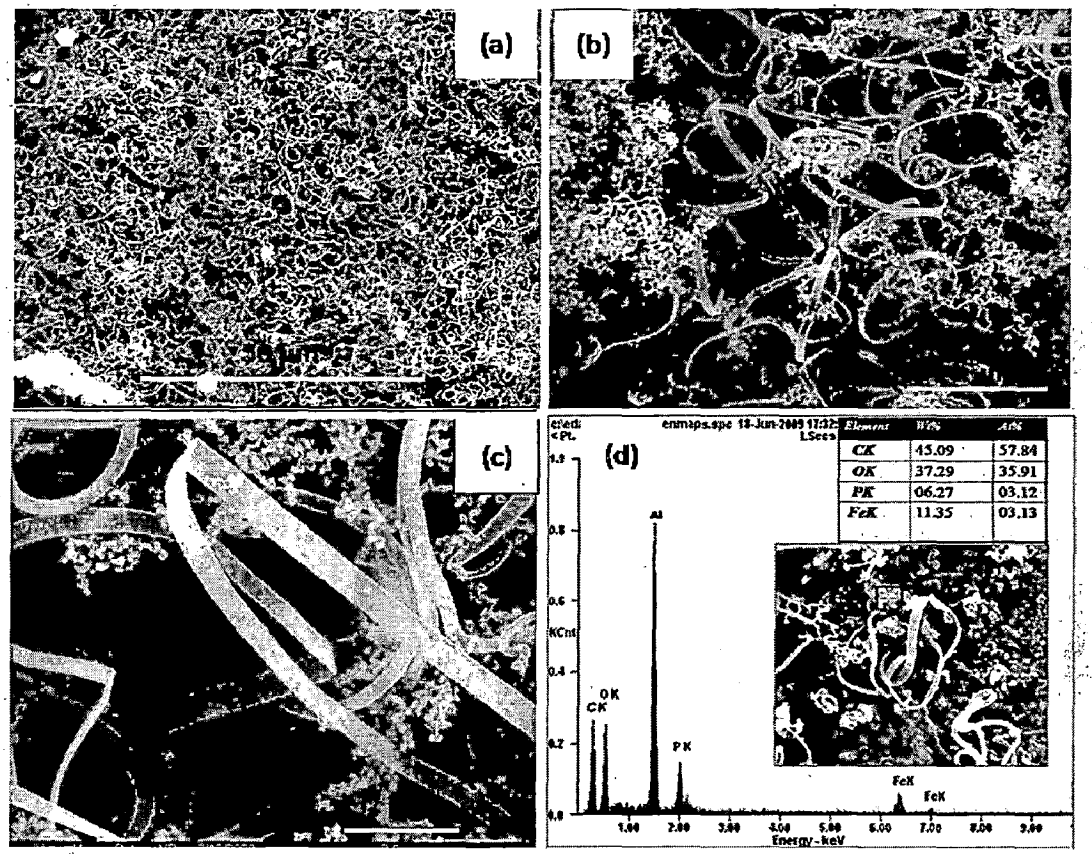

Figure 4.15: FE-SEM micrographs (a) shows high yield (b) CNRs at magnification X 4 K, (c) at X 16 K, (d) and growth of CNRs starts from catalyst shown by red mark.

The synthesis of CNRs by using iron-based catalysts have been reported earlier [Chen et al., 2005 and Mahanandia et al., 2008]. The growth of CNRs was usually explained by vapor-liquid-solid (VLS) mechanism and catalytic anisotropy mechanism. It is possible that under prevailing reducing environment the iron based catalyst compound reduces and

formed nanoclusters of iron and acts as a catalyst for CNRs formation [Hernadi et al., 1996]. In the present study, the catalyst particles were observed at the bottom of the nanoribbon (Fig.4.15 d) from where it starts to grow and confirms the growth mechanism. However, for ribbon type structure (Fig. 4.15 and 4.16) it is believed that the morphology of catalyst particle (anisotropy) is responsible. Their elongated flat surfaces (Fig. 4.1d) are supporting in formation of ribbon type morphology. However, the exact mechanism for growth of ribbon by using this novel catalyst has still been unexplored and need to be examined carefully.

Figure 4.16 (a, b & c) show the TEM images of carbon nanostructures obtained with catalyst $LiFePO_4$ at different magnifications. The TEM images confirm that the

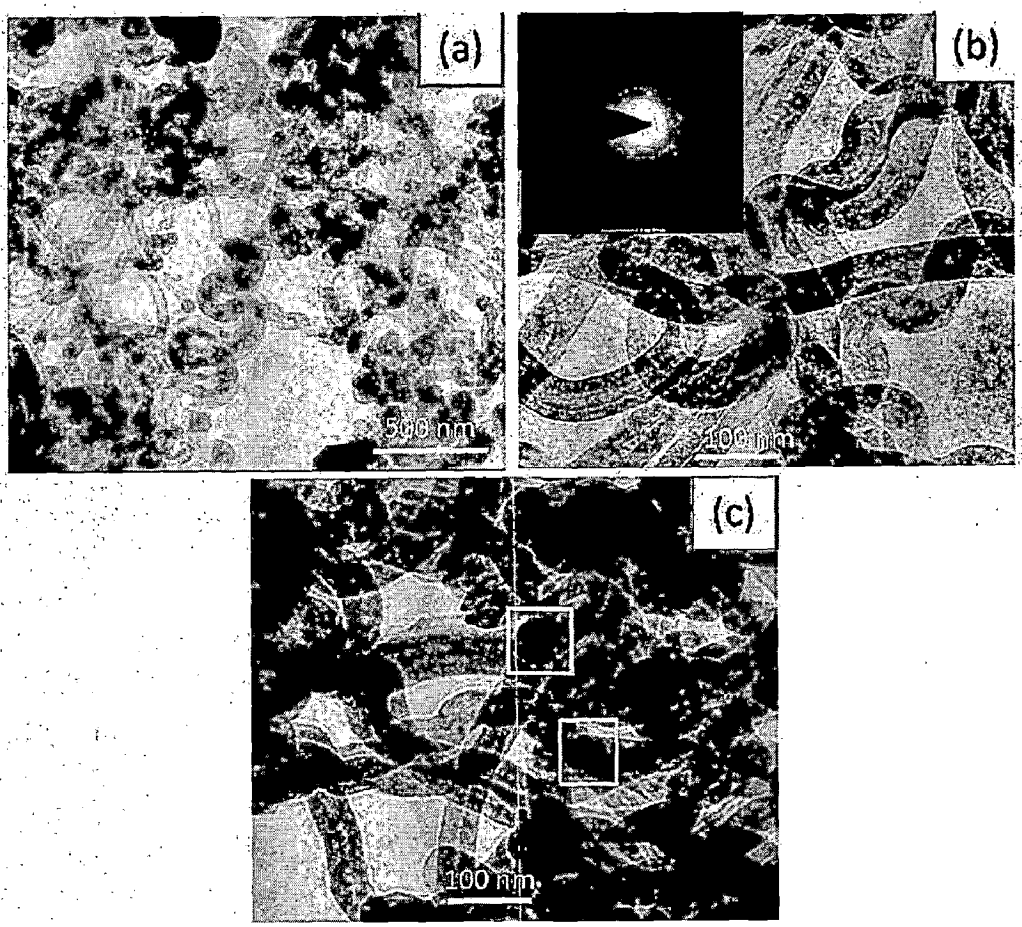

Figure 4.16: (a) TEM micrographs show ribbon type structure (b) at higher magnification and inset showing the SAD pattern of CNRs (c) growth of CNRs from catalyst as shown inside a by square boundaries.

Synthesized material consists of CNRs in major proportion. The ribbons are relatively uniform and their width varies between 50 and 80 nm. The selected area diffraction pattern of CNR, as given in the inset of Fig. 4.16b, shows clear pair of spots from (002) plane having interlayer spacing of 3.40 Å. The growth of CNRs from catalyst particles are observed in TEM micrograph as shown by squared boundary in the Fig.4.16c. This confirms the catalytic action of $LiFePO_4$ and results are consistent with the FE-SEM micrograph and EDX.

4.6.3.3 CNTs grown with Mixture of Lithium Zinc and Copper Oxide Compound ($LiCu_{0.5}Zn_{0.5}O$)

The synthesis of carbon nanostructure was carried out with a novel catalyst, which consists of Li, Cu and Zn oxides in order to have nanostructure with different morphology. As in above case, changing the chemical composition of catalyst particle, the morphologies of synthesized carbon nanostructure change. This compound as catalyst for CNTs growth has not been reported earlier in the literature. Ivanov et al. (1994) have tried to use copper as catalyst for synthesis of CNTs but have found only amorphous carbon. Copper, a non-transition metal with its 3d shell completely filled, was observed to yield only amorphous carbon [Ivanov et al., 1994]. One may therefore speculate that overlap of metal having 3d empty orbital with carbon valence orbital plays not only a role in the hydrocarbon dissociation process, but also an essential part in the initial stage of the CNTs growth process, since it allows chemisorptions of the carbon cap edges to the catalyst nanoparticles. However, when copper mixed with nickel was used as catalyst, carbon filament structure has been observed [Kim et al., 1992]. They have proposed that metals that readily wet graphite will produce highly ordered carbon filament structures. However, it should be further investigated if and how the unfilled 3d-metal orbitals have an effect on the growth process and thus on the graphitization of whole CNTs. In view of above literature, synthesis of the mixture of lithium zinc and copper oxide has been synthesized and used as a catalyst for synthesis of CNTs.

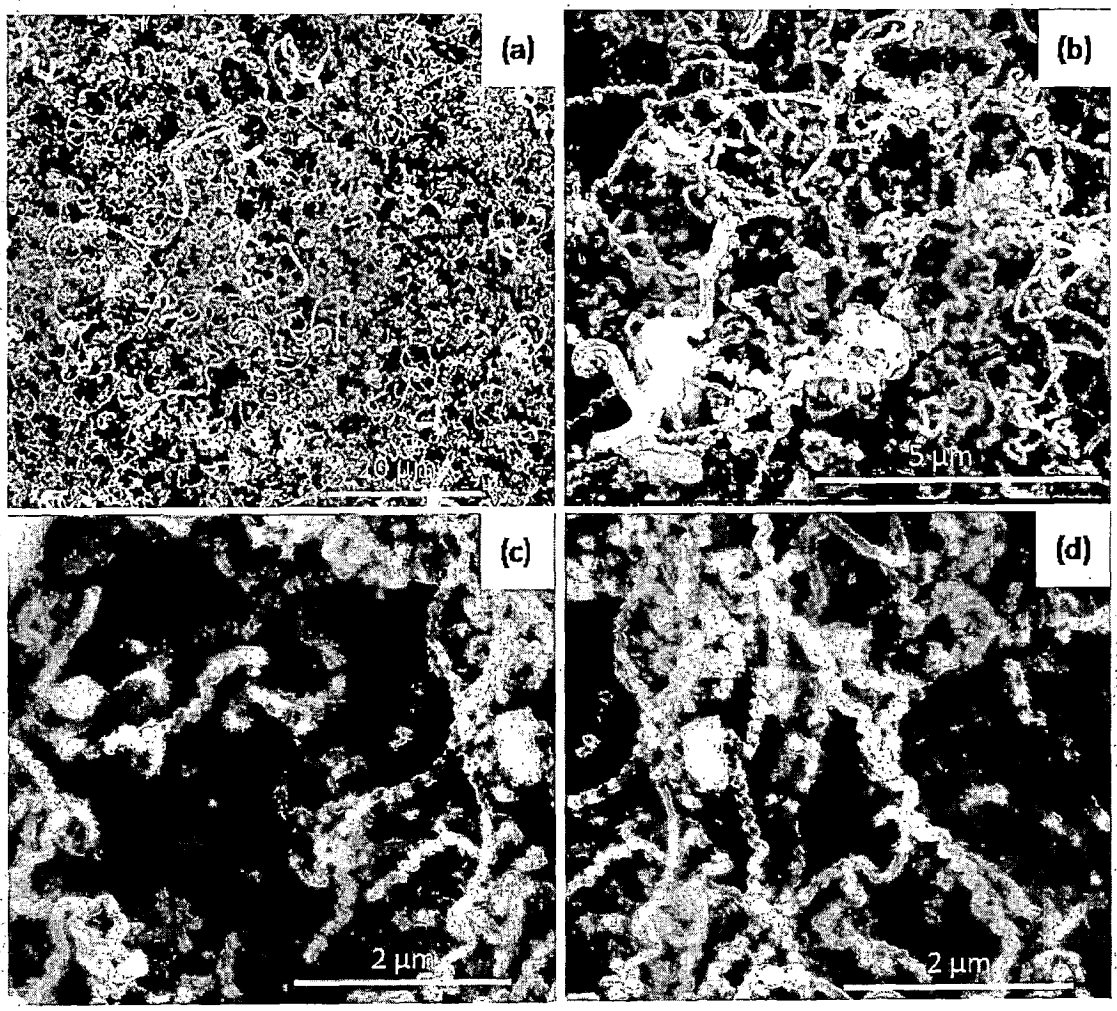

Figure 4.17: FE-SEM micrograph of CNTs grown with a mixture of lithium Zn and Cu oxide catalyst shows wavy structure (a) higher yield (b, c & d) at different magnifications.

The FE-SEM micrographs of CNTs synthesized by using this catalyst are shown in Figs.4.17 (a, b, c & d). Figure 4.17a shows the high yield of CNTs with this catalyst which also shown at higher magnifications (Fig. 4.17 c & d). FE-SEM micrograph shows a unique CNT array in which more than 90 % of the CNTs are not straight and they are wavy in nature as have been generated by bending periodically within fixed intervals throughout their entire length. The regularly bent CNTs are proposed for applications such

as mechanical nanospring devices, high-resolution AFM tips and nanocircuit interconnection in nanodevices. The formation of the wavy structure is attributed to the two groups of catalyst used for synthesis of CNTs.

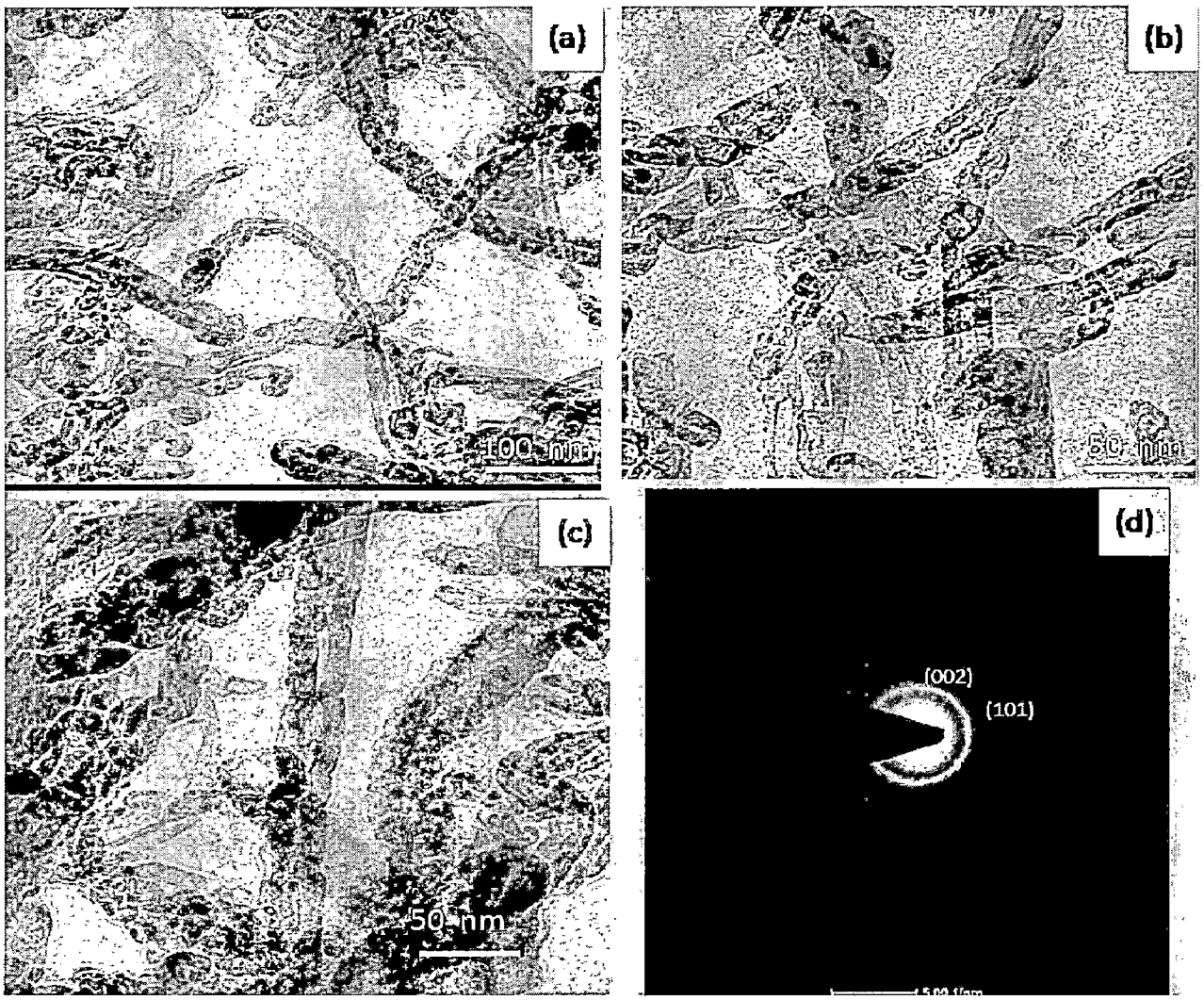

Figure 4.18: TEM micrographs of CNRs synthesized with a mixture of lithium Zn and Cu oxide catalyst (a) wavy structure (b) wavy structure at higher magnification(c) bamboo type morphology (d) SAD pattern showing the polycrystalline nature of CNTs.

One of the catalysts is more active and results in higher growth rate of CNTs than other catalyst. The van der Waals force sticks nanotubes together whenever they grow together.

The CNTs with higher growth rate are forced to bend periodically and formed a wavy structure. As mentioned above that copper does not support CNTs growth, however, when mixed with the Li and Zn its electronic structure changes and hence acts as a high rate catalyst. Further detailed study is necessary to understand the role of catalyst particle for the formation of such CNTs.

Figure 4.18 (a, b & c) shows the TEM micrographs of CNTs grown with catalyst mixture of lithium Zn and Cu oxide. The TEM results further confirm the wavy structure of CNTs as observed in FE-SEM. Some bamboo like structure was also observed in TEM image of CNTs grown with this catalyst. The outer diameter of CNTs measured from TEM images lie in the range of 15-40 nm, however, inner diameter is about 8 nm. The selected area diffraction pattern of CNTs using this catalyst is shown in Fig.4.18d. Two continuous rings are observed in SAD pattern, which confirms the polycrystalline nature of CNTs. The brightest diffraction ring corresponding to a layer distance of 3.45 Å and is considered to be of (002) plane of graphite. The next continuous ring seen in diffraction pattern corresponds to (101) plane of graphite for which the interlayer spacing is 2.05 Å.

4.6.3.4 CNTs grown with $LiMn_2O_4$ Catalyst

The $LiMn_2O_4$ has also been used as the catalyst for the synthesis of carbon nanostructure. However, the parameters for CVD are same as used with other catalysts. Changing the chemical compositions of the catalyst particles the morphology of synthesized carbon nanostructure changes as discussed above for different transition metal based lithium containing compounds. The FE-SEM micrographs of carbon nanostructure obtained using this catalyst are shown in Fig. 4.19 (a & b). The carbon nano beads (CNBs) were obtained with this catalyst. The carbon spheres are attached in the form of string (Fig.4.19 a & b). The CNBs are rarely reported in literature [Chang et al., 2009 and Walt A. de Heer, 2005]. The CNBs are either amorphous or polycrystalline having spherical, cubic, polyhedron and bloomed shape. They can be used as filler in composite material to

enhance the electrical conductivity, mechanical properties of matrix materials and as anode materials for lithium ion batteries.

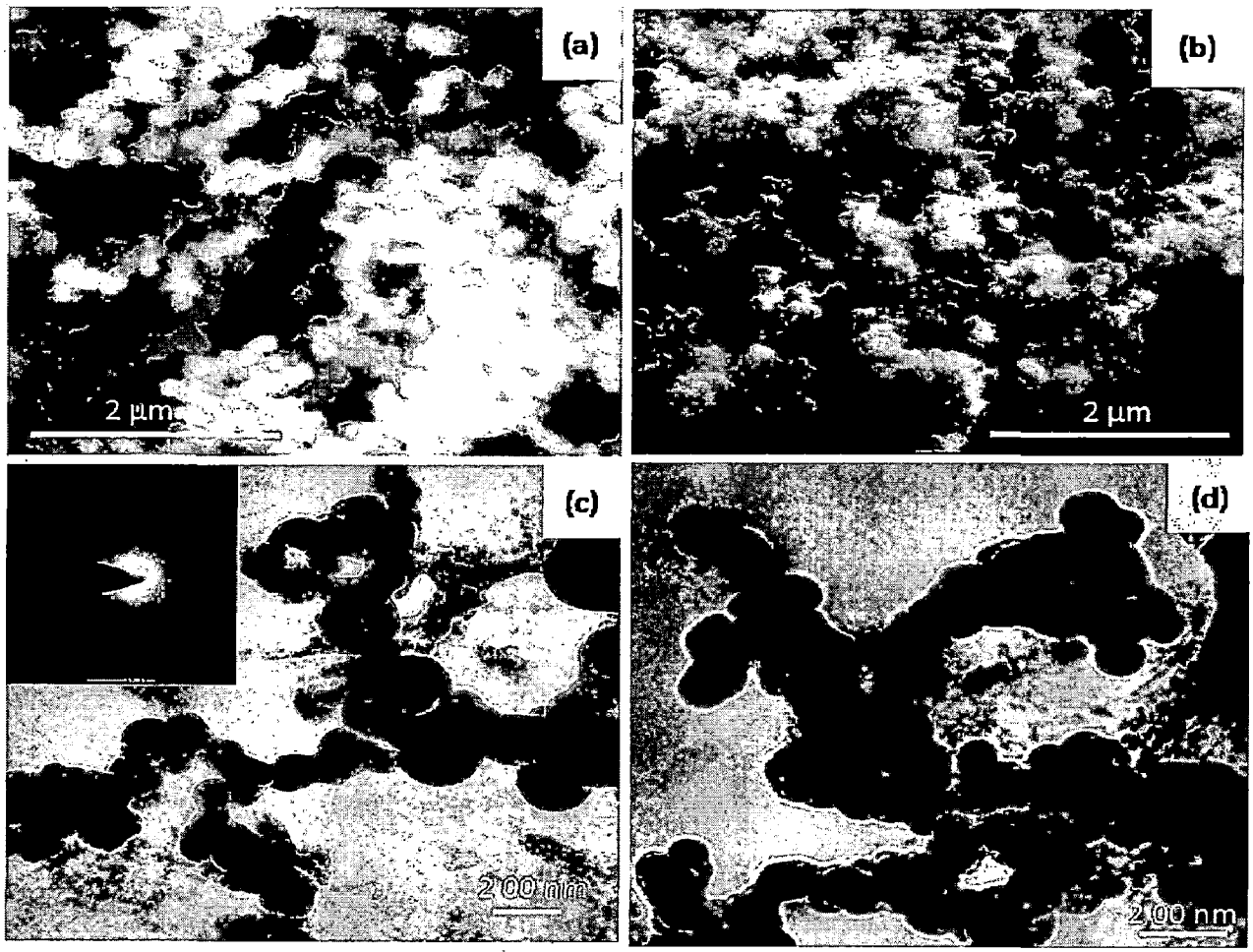

Figure 4.19: FE-SEM micrographs of CNBs showing (a) carbon nanoparticles joined together, (b) the high yield. TEM micrographs showing (c) SAD pattern of the amorphous nature of CNBs, (d) the cluster formation of CNBs.

The TEM images of CNBs are shown in Fig.4.19 (c & d). From the TEM micrographs it is confirmed that the shapes of bead are spherical/truncated octahedral joined and form cluster or string (Fig.4.19 b). The diameter of CNBs lies in the range of 50-100 nm. The SAD pattern of CNBs is shown as an inset of Fig. 4.19c. Hallow diffuse pattern indicates the amorphous nature of these structure. The formation of amorphous

carbon structure not CNTs by using this particular catalyst is attributed to the bigger size (> 100 nm) of catalyst particle. This indicates that the size of catalyst particle plays a crucial role for CNTs formation. Thus, the TEM and FE-SEM results confirm that the CNBs are formed when using $LiMn_2O_4$ as a catalyst.

4.6.3.5 CNTs grown with $LiMn_{1.8}Fe_{0.2}O_4$ Catalyst

The amorphous carbon structure has been observed when $LiMn_2O_4$ is used as catalyst. However, when the $LiMn_2O_4$ is doped with 2 mol% of Fe, the catalytic activity changes drastically.

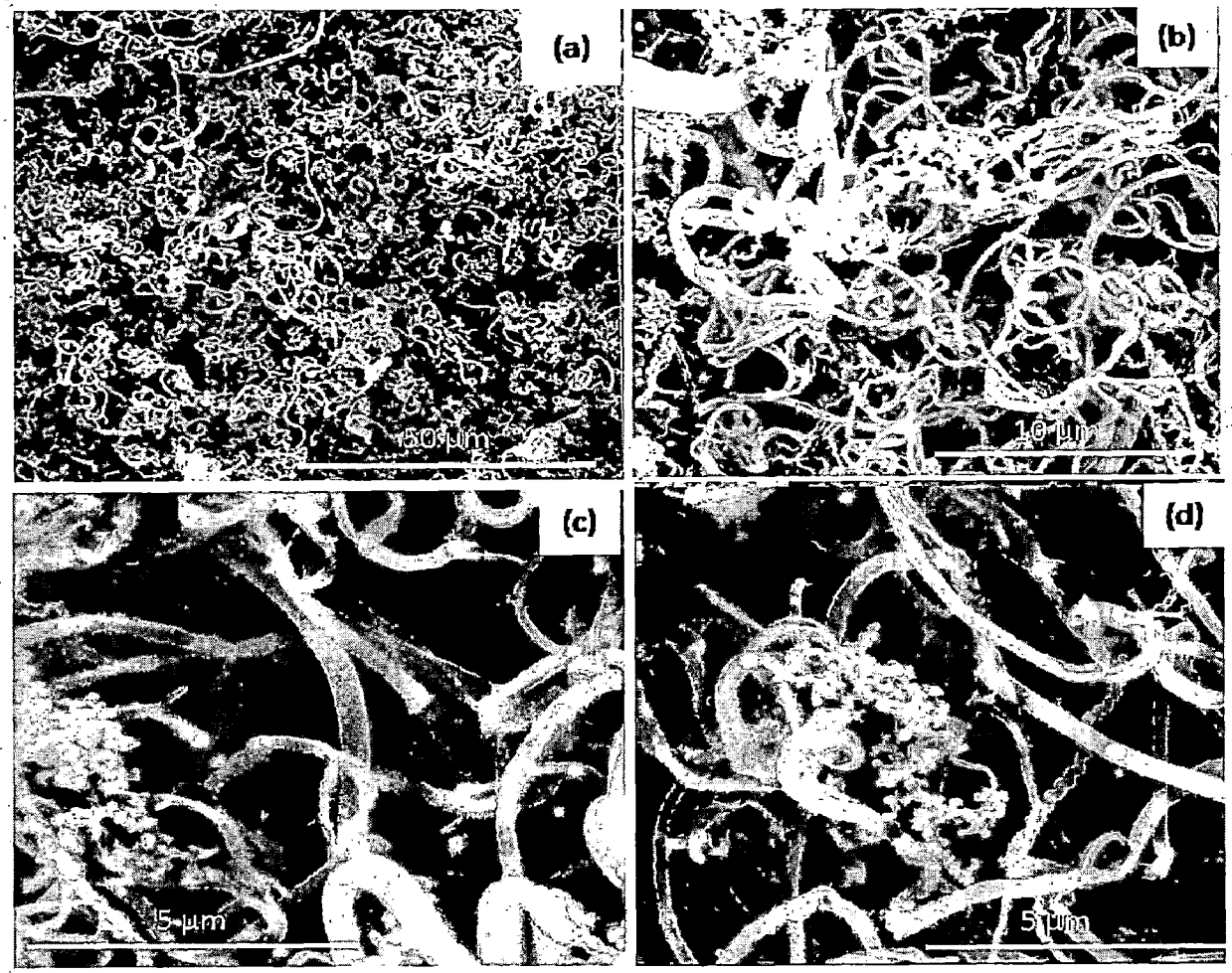

Figure 4.20. FE-SEM micrographs of CNTs grown with $LiMn_{1.8}Fe_{0.2}O_4$ catalyst (a & b) showing high yield (c) catalyst particles is shown at tip of CNTs (tip growth mode) (d) CNTs at different magnification and different area

The doped $LiMn_2O_4$ has been used as catalyst for CNTs growth and the FE-SEM results are shown in Fig.4. 20 (a, b, c & d) which confirm the growth of CNTs and catalytic activity of doped $LiMn_2O_4$. Figures 4.20a shows the high yield of CNTs synthesized with Fe-doped catalyst. FE-SEM images of CNTs shown at different magnifications show that the most of the tubes are either straight or curving morphologies. The tip growth mode has been observed for CNTs grown with this catalyst, as the catalyst particles can be seen at the tip of the tube.

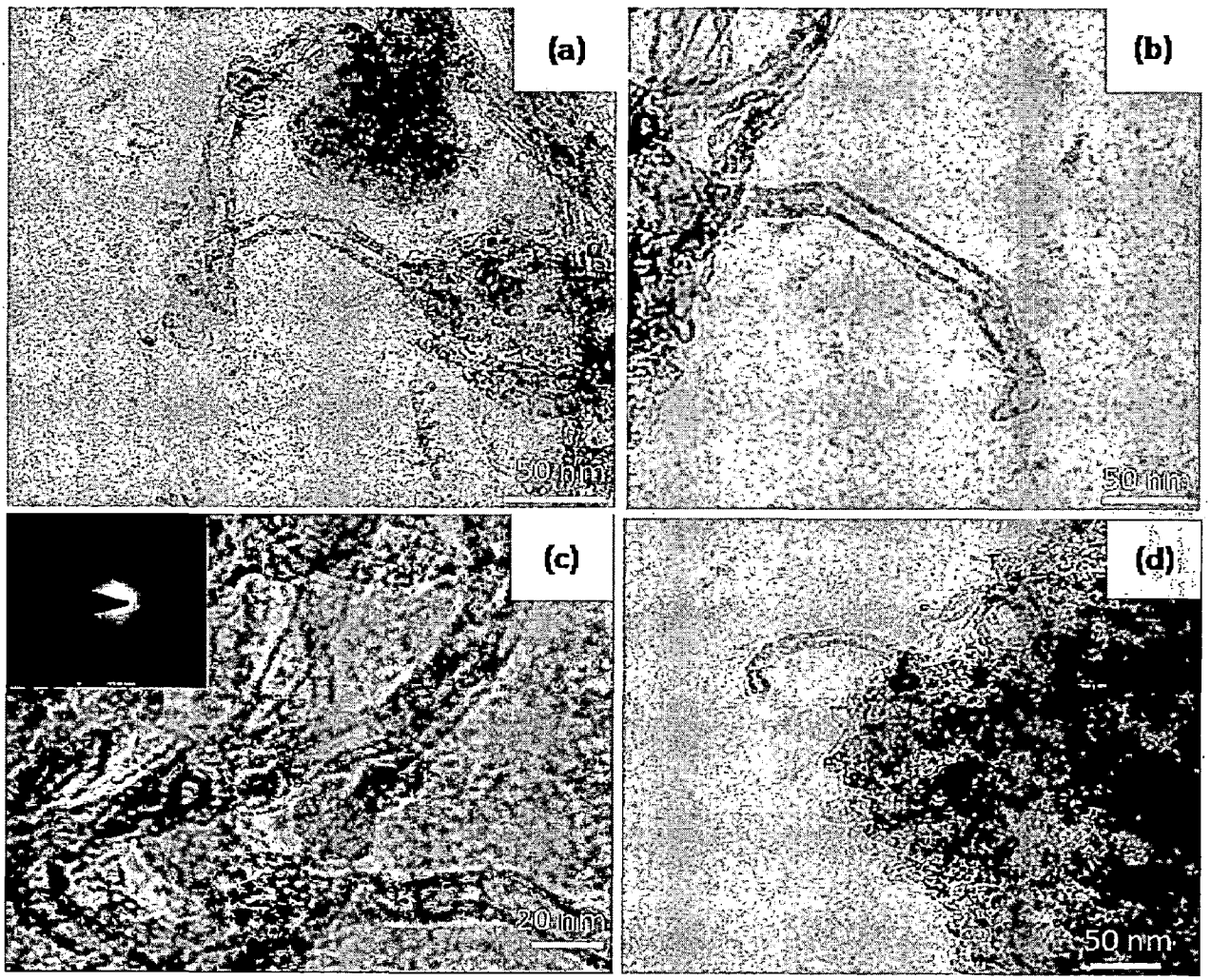

Figure 4.21: TEM micrographs of CNTs growth using catalyst $LiMn_{1.8}Fe_{0.2}O_4$ (a) Bamboo like structure (b) large inner diameter as compared to wall thickness (c) SAD pattern as inset (d) agglomerated tubes.

The TEM images of the CNTs grown using catalyst of Fe-doped $LiMn_2O_4$ are shown in Fig. 4.21 (a, b, c & d). The diameter of CNTs synthesized with this catalyst is smaller compared to that obtained with other catalysts used in this study. The average diameter of the tubes is in the range of 10-20 nm. The other special feature of the CNTs obtained with this catalyst is smaller wall thickness and hence larger inner diameter compared to the CNTs grown with other catalysts. The SAD pattern presented in the inset of Fig.4.21c shows a continuous ring corresponding to (002) peak of graphite. The SAD pattern indicates the polycrystalline nature of CNTs, which has been further confirmed by XRD result discussed in the following section.

Thus, carbon nanostructures grown with different catalysts particle have different morphologies and are appeared in different shapes as discussed above. Each shape may be useful for specific application. These shapes shall have significant impact only when they can be produced with uniform properties. Precise control on morphologies of CNTs and role of these novel catalysts is still a challenge, which requires attention for future work.

4.6.4 XRD Results

. XRD pattern of CNTs synthesized using the catalysts $LiNi_{0.5}Co_{0.5}O_2$, $LiFePO_4$, $LiCu_{0.5}Zn_{0.5}O$, $LiMn_2O_4$ and $LiMn_{1.8}Fe_{0.2}O_4$ are shown in Fig. 4.22 (a, b, c, d & e) respectively. The (002) peaks in all the XRD patterns of CNT samples grown with $LiNi_{0.5}Co_{0.5}O_2$, $LiFePO_4$ and $LiCu_{0.5}Zn_{0.5}O$ catalysts have almost similar shape and intensity.

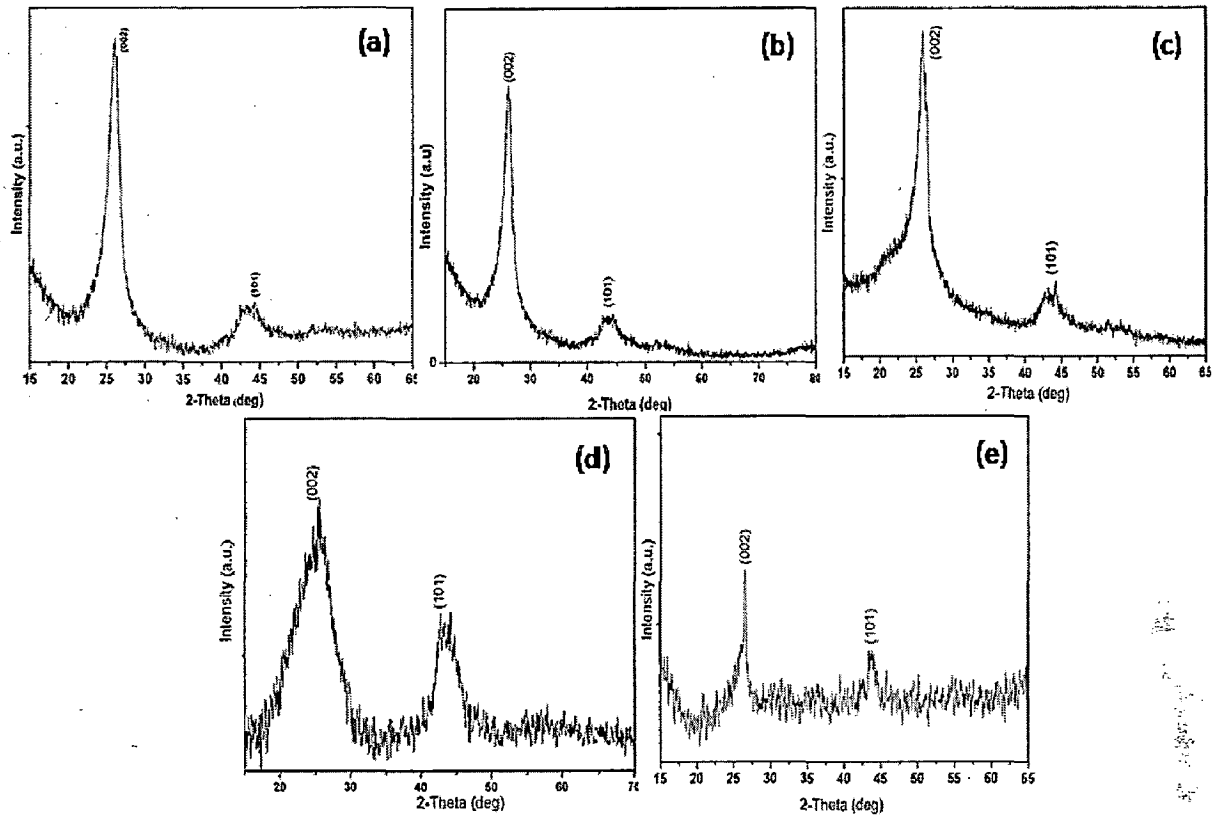

Figure 4.22: XRD patterns of CNTs, synthesized by catalytic decomposition of acetylene gas over (a)$LiNi_{0.5}Co_{0.5}O_2$ (b)$LiFePO_4$ (c)$LiCu_{0.5}Zn_{0.5}O$ (d)$LiMn_2O_4$ and (e) $LiMn_{1.8}Fe_{0.2}O_4$

However, the CNTs grown with $LiMn_2O_4$ catalyst indicate a small crystallite size carbon material, which was also, confirmed by FE-SEM and TEM Results. The (002) peak is very sharp for the CNTs grown with $LiMn_{1.8}Fe_{0.2}O_4$ catalyst. The interlayer spacing, d_{002} of CNTs obtained with different catalysts $LiNi_{0.5}Co_{0.5}O_2$, $LiFePO_4$ $LiCu_{0.5}Zn_{0.5}O$, $LiMn_2O_4$ and $LiMn_{1.8}Fe_{0.2}O_4$ used are 3.42, 3.42, 3.44, 3.45 and 3.41 Å respectively. These *d*-spacings are almost comparable with value calculated from SAD patterns of CNTs described in the section above. These values are marginally larger than d_{002} = 3.40 Å, found in MWCNTs grown over catalyst of iron particles on silica substrate [Dai et al., 1996] and is about 2.2 % higher than d_{002} = 3.35 Å for pure graphite. This increase in *d*-value could be due to the influence of novel catalysts used on the multi-walled structure developed in the present study. Subsequent processing of synthesized CNTs does not have

any effect on the structure, as there has been no obvious difference between the XRD patterns obtained for raw MWCNTs and those treated with the mixture of HNO_3 and $LiNO_3$ [Yang et al., 2005]. The broad peak (101) at about 44.45° in the XRD patterns of CNTs synthesized with different catalysts is due to stacking of graphene sheets generated by turbostatic nature. The turbostatic nature in CNTs develops because neighboring graphene sheets are parallel to each other, but translational and rotational correlations within a sheet plane are random [Kong et al., 1998]. The L_c (crystalline size in c-direction) calculated from the peak (002) of the patterns are 4.0, 4.2, 3.8, 2.1 and 4.2 nm respectively for CNTs grown with $LiNi_{0.5}Co_{0.5}O_2$, $LiFePO_4$, $LiCu_{0.5}Zn_{0.5}O$, $LiMn_2O_4$ and $LiMn_{1.8}Fe_{0.2}O_4$ catalyst respectively. The L_c calculated from XRD patterns are significantly higher for CNTs grown with catalysts $LiNi_{0.5}Co_{0.5}O_2$, $LiFePO_4$, $LiCu_{0.5}Zn_{0.5}O$ and $LiMn_{1.8}Fe_{0.2}O_4$ than the reported 1.4 and 2.4 nm for CNTs synthesized over catalyst of iron oxide from acetylene and ethylene gases respectively [Koizol et al., 2005]. The higher L_c observed in the carbon nanotubes synthesized in the present study indicates that CNTs are more graphitized than those grown over iron oxide based catalyst. The XRD and SAD patterns in the TEM results are quite similar.

4.6.5 Raman Spectra

First order Raman spectra of synthesized CNTs are recorded in selected wave number region ranging between 1100 and 2000 cm^{-1}, and are presented in Fig. 4.23. The peak appearing at different wave numbers of 1596, 1588, 1589, 1587 and 1589 cm^{-1} for CNTs synthesized with different catalysts corresponds to the G band. The other band that appears for CNTs at about 1334, 1344, 1359, 1352 and 1348 cm^{-1} are attributed to D-bands. However, the corresponding peaks for CNTs material grown over cobalt oxide catalysts occur at 1582 and 1350 cm^{-1} respectively, which are similar to those in graphite [Eklund et al., 1995 and Maurin et al., 2000]. The strong G-band corresponds to one of the E_{2g} modes (mode G) and represents the vibrational mode corresponding to the movement of two neighboring carbon atoms opposite to each other in a graphene plane. The D band is assigned to the D mode, which is generally not an active Raman mode in graphene sheet but its occurrence is attributed to defects in the curved graphene sheet, tube ends and staging disorder [Hiura et al, 1993]. The FWHM of G-band is estimated and are given in

table 4.2, which are three to four times higher than the width of about 20-22 cm^{-1} observed in MWCNTs grown by arc discharge as reported by Kastner et al. [Kastner et al., 1994]. The higher FWHM in case of CNTs grown with $LiMn_2O_4$ catalyst is due to amorphous form of CNBs. However, in case of CNTs grown with $LiCu_{0.5}Zn_{0.5}O$ having wavy shapes, consist of larger defects at the bent of tube, which is reason for larger FWHM, and higher intensity of D-band. Highly oriented pyrolytic graphite (HOPG) has a slightly lower FWHM value of about 15-18 cm^{-1}. The up-shift of G-band and larger FWHM for all types of carbon nanostructures, compared to that of graphite and MWCNTs are observed. This is perhaps due to the oxide catalyst containing lithium through its contribution to structural modification of the CNTs or charge transfer to carbon atoms due to an extent of lithium doping [Bendiab et al., 2001 and Claye et al., 2000]. The G-band up-shift has also been observed by earlier workers in their studies on lithium intercalated CNTs [Bendiab et al., 2001 and Claye et al., 2000].

Table 4.2. Raman spectral parameters of carbon nanotubes synthesized with different catalysts.

Catalyst	Peak position (cm^{-1})		FWHM (cm^{-1})	$R=I_D/I_G$
$LiMn_2O_4$	(G-band) (D-band)	1588 1334	76	6.0
$LiMn_{1.8}Fe_{0.2}O_4$	(G-band) (D-band)	1589 1334	82	4.7
$LiCu_{0.5}Zn_{0.5}O$	(G-band) (D-band)	1587 1359	95	5.2
$LiCo_{0.5}Ni_{0.5}O_2$	(G-band) (D-band)	1596 1352	66	0.9
$LiFePO_4$	(G-band) (D-band)	1589 1348	44	0.51

For polycrystalline graphite, the intensity ratio R (= I_D/I_G) is inversely proportional to L_a (crystalline size in a-direction), where I_D and I_G are the intensities of the D-band and the G-band respectively. Using an empirical formula, $L_a = 4.4 / R$ in the range of $0.001 \leq R \leq 1$ it is possible to estimate L_a in nm for laser excitation between 488 and 514 nm [Hiura et

al., 1993]. In the present study, the carbon nanostructures grown with $LiNi_{0.5}Co_{0.5}O_2$ and $LiFePO_4$ have *R*-values of 0.90 and 0.51 respectively those lie in the range mentioned as above. However, the *R*-values obtained for other CNTs are greater than 1 and hence the above formula for L_a is not applicable for calculation of crystalline size (L_a). The empirical formula is, therefore, valid and has been used to estimate L_a as 4.88 and 3.90 for CNTs grown with catalyst $LiNi_{0.5}Co_{0.5}O_2$ and $LiFePO_4$ respectively. Interestingly, the *R* values of 0.9 and 0.51 obtained with oxide catalyst $LiNi_{0.5}Co_{0.5}O_2$ and $LiFePO_4$ respectively in the present study are lower than 1.2 observed in MWCNTs grown over catalyst of iron oxide [Wu et al., 1999], indicating a little higher ordering along the graphene sheet of MWCNTs obtained in the present study. This has also been confirmed by x-ray diffraction analysis.

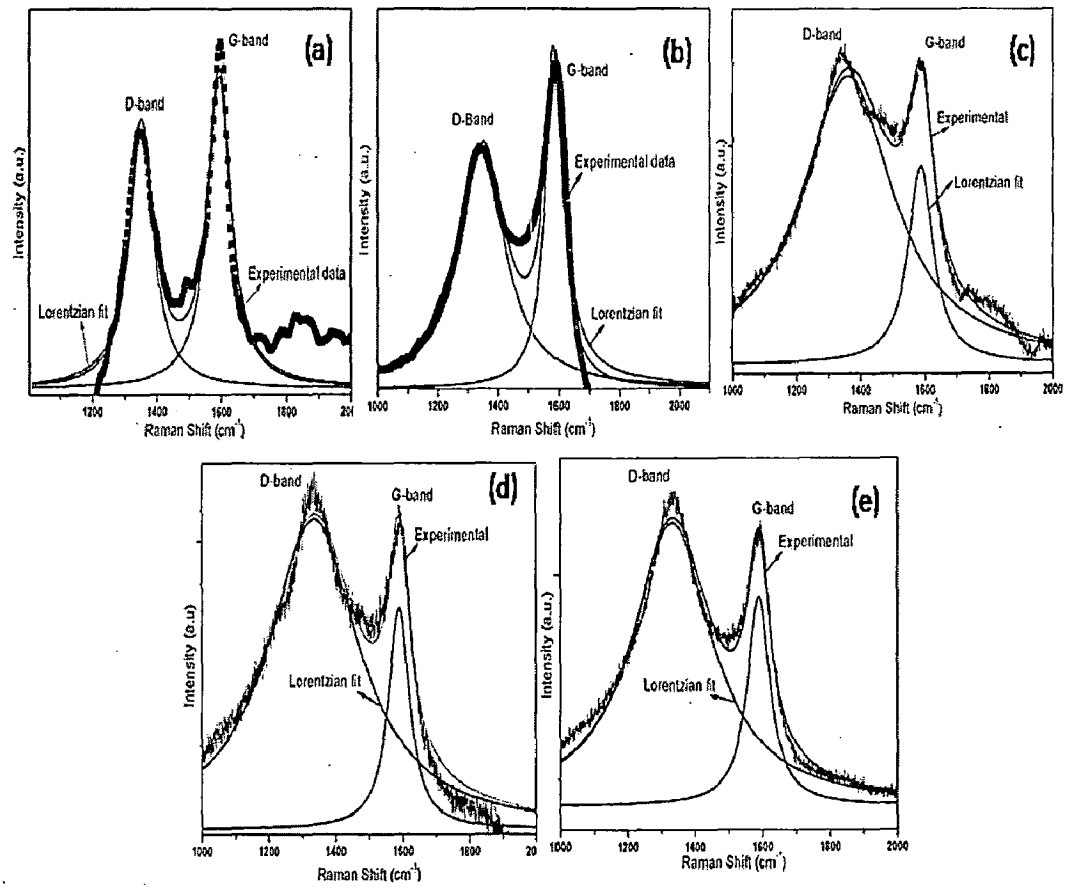

Figure 4.23: Raman spectra of CNTs, synthesized by catalytic decomposition of acetylene gas over (a) $LiNi_{0.5}Co_{0.5}O_2$ (b) $LiFePO_4$ (c) $LiCu_{0.5}Zn_{0.5}O$ (d) $LiMn_2O_4$ and (e) $LiMn_{1.8}Fe_{0.2}O_4$.

4.6.6 Electrochemical Measurements

Five different types (morphologies) of carbon nano structures have been grown by using five different novel catalysts in the present study. However, due to limited accessibility of Electrochemical analyzer, the electrochemical analyses have been carried out for only two types of nanostructures using them as anode in Li-ion cell. The nanostructures grown using $LiNi_{0.5}Co_{0.5}O_2$ and $LiFePO_4$ are well graphitized compared to CNTs grown with other catalysts. The XRD patterns and Raman spectra of these two nano structures show that the defects in materials are less compared to other samples.

The cell consists of a positive electrode, which was prepared using a copper foil as a current collector and on one side of which, slurry of 90% active material, 7% binder PVDF and 3% acetylene black was pasted with the help of doctor blade and dried at 140 °C for 24 hours in a vacuum oven. Li metal foil has been used as negative electrode and the electrolyte containing 1M $LiPF_6$ dissolved in 1:1 mixture by volume of ethylene carbonate (EC) and diethyl carbonate (DEC) was used in the cell. The cell was tested at 20°C by using computer-controlled cycler (Arbin BT 200) at constant current of 100 μA in a voltage range of 0.05 - 2.5V.

4.6.6.1 Electrochemical Behavior of CNTs Grown With $LiNi_{0.5}Co_{0.5}O_2$

Figure 4.24 shows typical voltage profiles obtained by galvanostatic measurement of first charge and discharge of CNTs in the voltage range between 0.05 and 2.5 V at a constant current of 100 μA. The open circuit voltage (OCV) of the cell immediately after assembling is 3.4 V showing that electrode (anode) is in delithiated state. Upon discharge of the cell, the voltage drops rapidly at the beginning and reaches a value of 1.3 V. The initial high OCV > 3.0 V have been attributed to the presence of oxygenated group on the electrode surface [Yang et al., 2005]. The presence of oxygen in sample is confirmed by the elemental analysis (Fig.4.12). It can be seen from the Fig. 4.24 that the plateau in the discharge curve starts at about 0.9 V, which may be due to the lithium intercalation into CNTs as reported by Yang and Wu (2001). There is also another voltage plateau at about 0.8 V, which is perhaps associated to electrolyte decomposition and formation of SEI on the surface of CNTs. The large Li-insertion capacity of 765 mAh/g was observed in first

discharge (lithiation) cycle and such capacity corresponds to the chemical formula $Li_{2.25}C_6$ of the lithium-intercalated compound.. The first discharge capacity obtained is higher than typical values of 602, 362 and 466 mAh/g observed in MWCNTs grown over catalysts of ferrocene and thiophene by CVD using various carbon compound precursors such as benzene, cyclohexane and n-hexane [Claye et al., 2000].

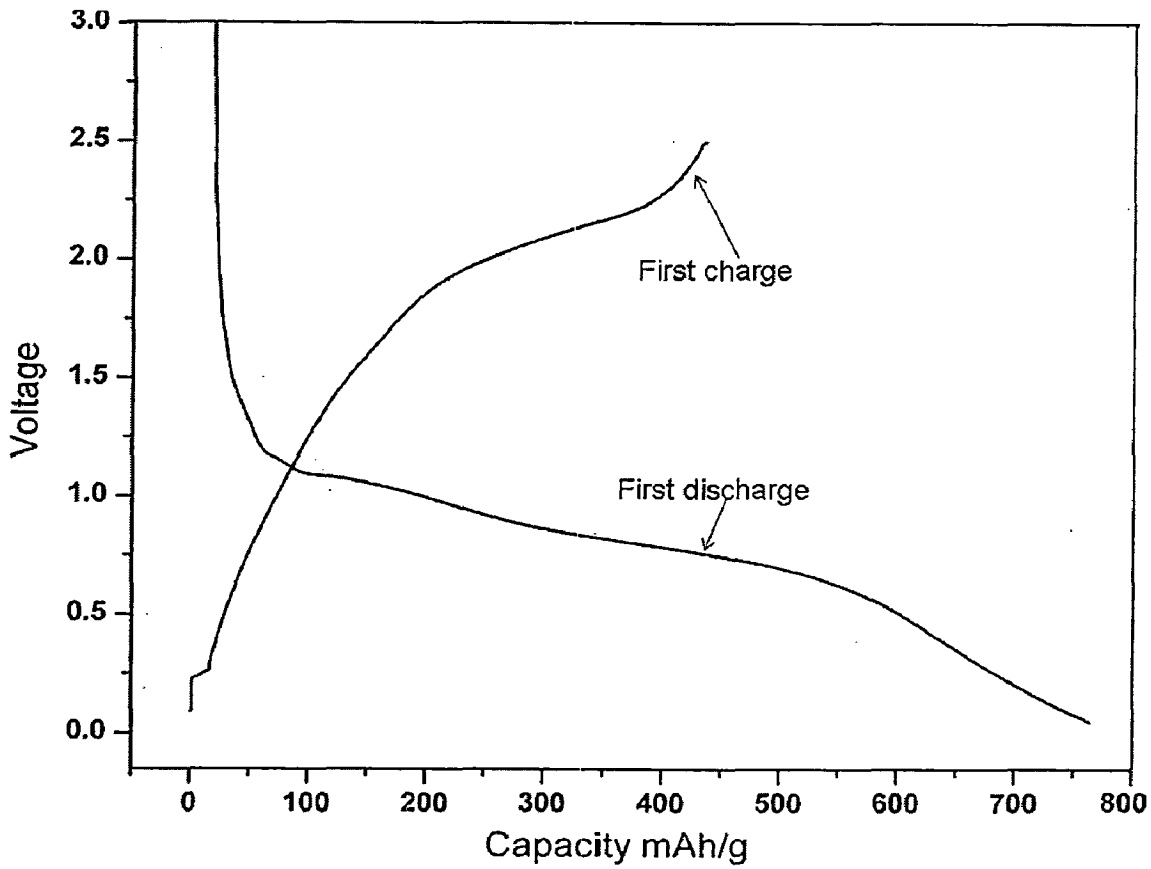

Figure 4.24: Typical first charge-discharge profile of a cell Li / $LiPF_6$ (in EC:DEC) / electrode of CNTs synthesized by catalytic decomposition of acetylene gas over $LiNi_{0.5}Co_{0.5}O_2$, in terms of the voltage of the electrode containing CNTs measured against the lithium metal foil.

The high capacity in MWCNTs grown in the present study could be due to insertion of lithium into regions like micro-pores, edge sites and surface of the tubes, where there is no organized graphene structure [Wu et al., 2003 and Wu et al., 1999]. In the next cycle, the

capacity decreases to 485 mAh/g, which is still higher than the theoretical charge capacity of graphite (~372mAh/g) corresponding to chemical formula LiC_6. The decrease in charge capacity of MWCNTs in the second cycle as observed in the present study is still significantly higher than the capacity of 100-400 mAh/g, obtained in CNTs grown over catalysts of cobalt or iron oxide particles and of open-ended CNTs [Frackowiak et al.,1999, Koizol et al., 2005 and Hsoeh et al., 2003]. The reversible capacity of 485 mAh/g obtained in MWCNTs in the present study is higher than 200 mAh/g observed by Yang et al. [Yang et al., 2005] in MWCNTs grown by arc discharge and purified by treating with mixture of $LiNO_3$ and HNO_3. The measured capacity could become still higher if lower cut-off voltage was taken as 0 or 0.01V, lower than the 0.05 V used in the present study. The decreasing capacity with charge-discharge cycling is one of the important factors preventing application of CNTs in commercial Li-ion batteries. Since the CNTs have been synthesized in this study using oxide catalyst $LiNi_{0.5}Co_{0.5}O_2$, the structure of CNTs is somewhat modified as indicated by XRD pattern and Raman spectra. Thus, there is relatively larger charge capacity compared to those observed in CNTs grown over cobalt catalyst and CNTs treated with a mixture of HNO_3 and $LiNO_3$ [Yang et al., 2005].

Figure 4.25 reveals the discharge profiles for 2nd to 11th cycles showing a plateau at around 1.3 V. This plateau voltage is higher than that observed in the first discharge cycle as shown in Fig. 4.24. A gradual fading of capacity with the number of discharge cycles is evident from Fig. 4.25. However, the capacity fading decreases with the number of cycles.

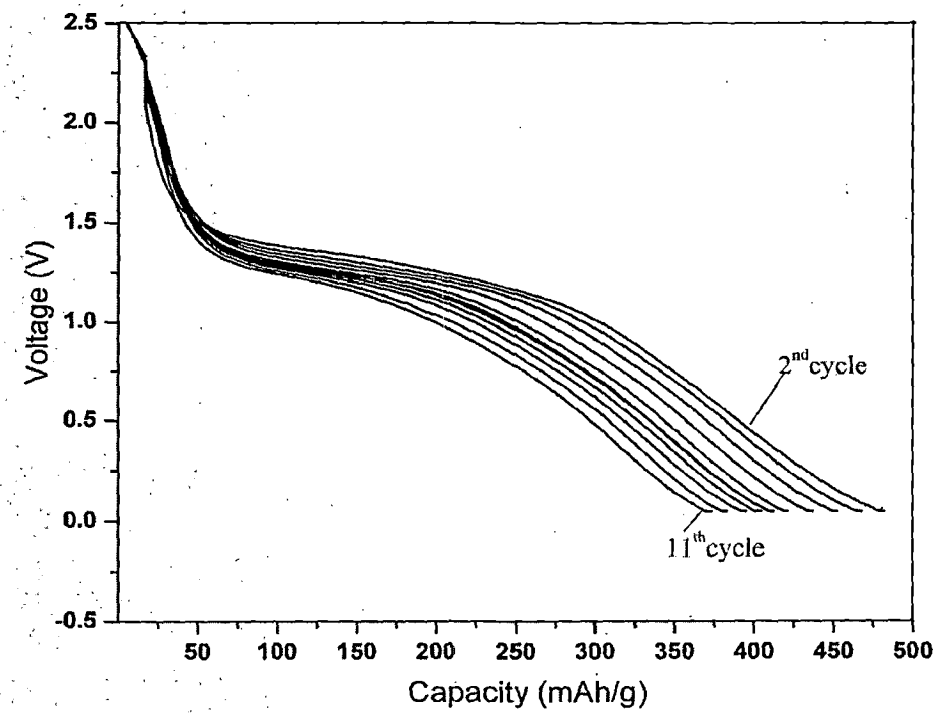

Figure 4.25: Discharge profile measured against lithium foil for 2nd to 11th cycle, indicating capacity-fading behavior with number of cycles for electrode of CNTs synthesized by catalytic decomposition of acetylene gas over $LiNi_{0.5}Co_{0.5}O_2$.

Figure 4.26 shows that the coulombic efficiency, defined as the ratio of charge capacity to discharge capacity, has low initial value of 64% but increases in the second cycle and saturates at 96.6 % in the succeeding cycles. The reason for low coulombic efficiency in first cycle is due to the large irreversible capacity. The large irreversible capacity in first cycle of carbon based anode materials is common and is attributed to the decomposition of electrolyte and formation of the solid electrolyte interface (SEI) at about 0.8 V [Naji et al., 1996]. Irreversible trapping of lithium by surface functional group of carbon is also considered as possible cause of large irreversible capacity and hence, lower coulombic efficiency [Aurbach et al., 1995]. The extent of decomposition is directly related to the specific area of carbon-based materials. The efficiency remains almost constant until the measurements were made at the end of 11th cycle.

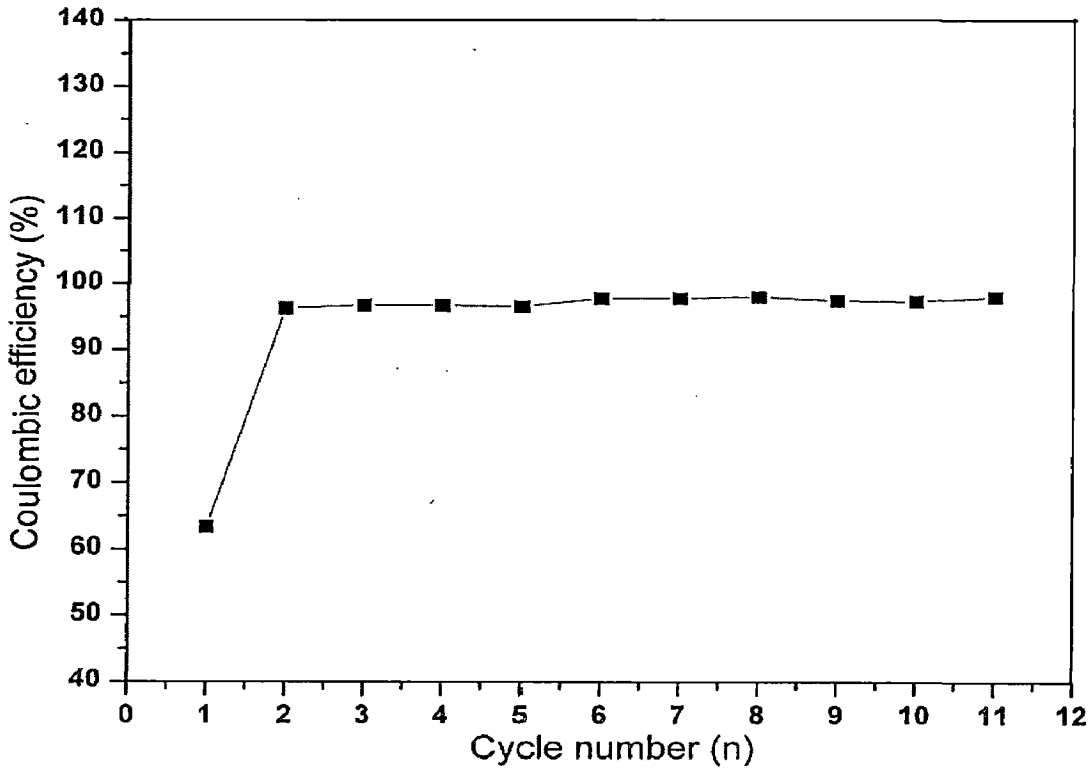

Figure 4.26: Variation of coulombic efficiency with number of cycles in cells with electrode made of CNTs synthesized by catalytic decomposition of acetylene gas over $LiNi_{0.5}Co_{0.5}O_2$.

The coulombic efficiencies reported from studies up to 5 cycles for SWCNTs is 84% [Britton, 2007] and 83-95 % up to 5 cycles in MWCNTs synthesized by CVD from different sources over iron particle catalyst [Claye et al., 2000]. Thus, the efficiency in the present study is found to be relatively higher, though not very significantly, for the cycles between 2 and 11.

4.6.6.2 Electrochemical Behavior of carbon nanostructures Grown With $LiFePO_4$

A Teflon cell was assembled in an Ar-filled glove box having oxygen and moisture level below 0.1 ppm, for electrochemical measurements. The cell was fabricated in a similar way as discussed in above section. The cell was tested at 20 °C by using computer-

controlled cycler (Arbin BT 200) at constant current of 100 μA in a voltage range 0.05 and 2.5V.

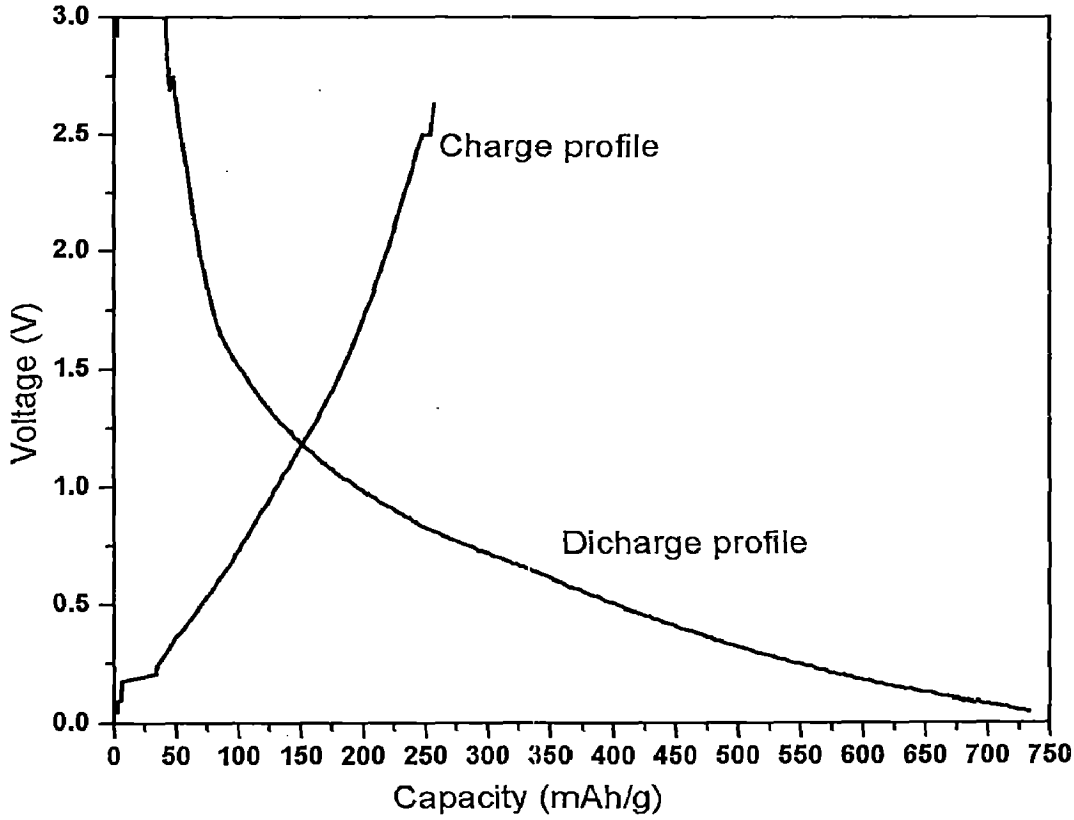

Figure 4.27: Typical first charge-discharge profile of a cell Li / $LiPF_6$ (in EC:DEC) / electrode of CNRs.

After purification of CNRs for removing the catalyst particle and amorphous carbon, electrochemical measurement has been carried out. Figure 4.27 shows the first charge and discharge voltage profiles of CNRs as anode in lithium ion cell. The average discharge plateau is below 0.6V, which is proper for application as anode material. The first discharge (lithium insertion) capacity as calculated from Fig. 4.27 is 725 mAh/g. The open edges of ribbons are suitable for Li-insertion and this is perhaps the reason for high discharge capacity observed. This capacity is nearly similar to that of MWCNTs grown with conventional catalysts (e.g. Co and Fe). The discharge profiles for 2nd to 14th cycle are shown in Fig. 4.28. The reversible capacity at room temperature has been estimated to be

about 340 mAh/g and reduces to 335 mAh/g at 14th cycle, up to which the measurements were made.

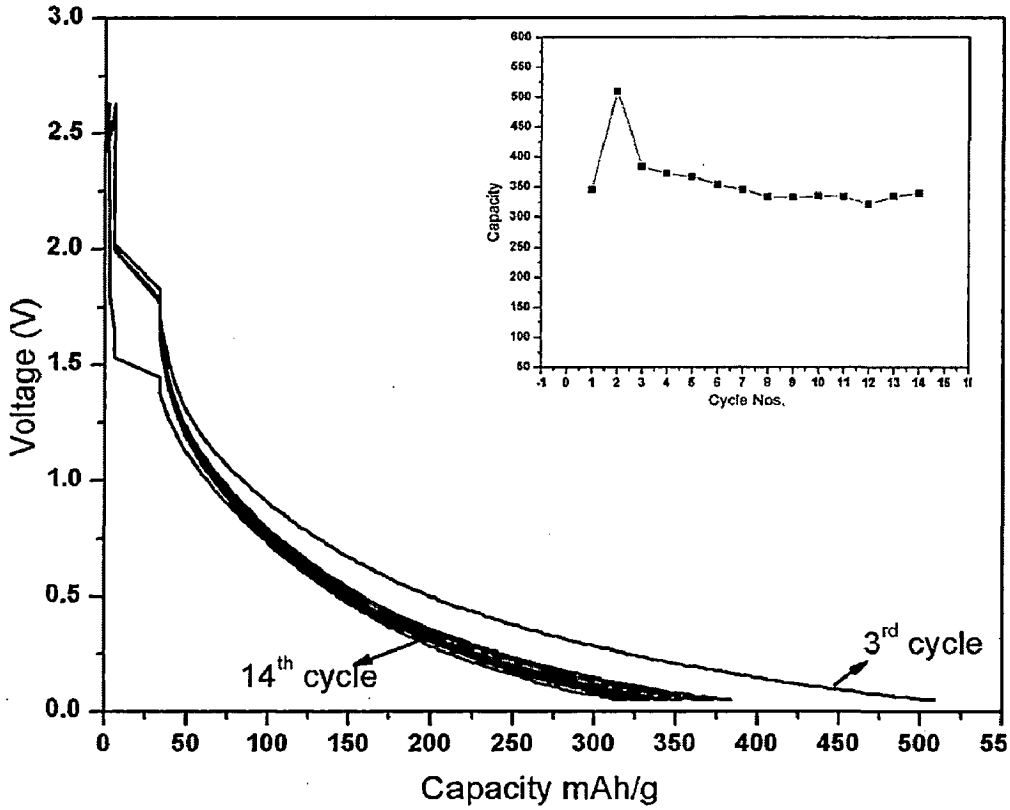

Figure 4.28: Discharge profiles measured against lithium foil for 2nd to 14th cycles, and inset showing variation of coulombic efficiency with number of cycles in cells with electrode made of CNRs.

The plot of capacity versus cycle number as an inset is shown in Fig. 4.28, which indicates the fluctuation in capacity during initial cycles. The capacity becomes 500 mAh/g in 3rd cycle and again drops to 380 mAh/g in the 4th cycle. The columbic efficiency calculated as the ratio of charge to discharge capacities has been stabilized at about 98 % from the fifth cycle onward. The coulombic efficiencies reported from studies up to 5th cycles for SWCNTs is 84% [Britton, 2007] and for MWCNTs grown with iron particle catalyst is 83-95 % [Hsoeh et al., 2003]. These results show that the CNRs synthesized with a novel catalyst has little higher reversible capacity as well as capacity retention as anode, demonstrating its potential for application in Li-ion battery. The first discharge capacity of both types of carbon nanostructures i.e. CNTs and CNRs is quite similar as mentioned

above. However, the nature of discharge/charge profile is quite different. In case of CNTs, a clear voltage plateau can be seen; however, discharge profile is slopping in case of CNRs.

4.7 SUMMARY

CNTs have various tubular morphologies and can be made in different shapes. Each shape has its special properties and is suitable for specific application. The control of morphology of CNTs is still a challenge. A successful attempt has been made in the present study to control the morphology of CNTs by using various novel catalysts and the results are discussed in this chapter. Different types of carbon nanostructures viz. straight, coils, ribbon, nanobeads and waved morphologies have been synthesized by using five different catalysts such as $LiNi_{0.5}Co_{0.5}O_2$, $LiFePO_4$, $LiCu_{0.5}Zn_{0.5}O$, $LiMn_2O_4$ and $LiMn_{1.8}Fe_{0.2}O_4$. These catalysts have for the first time been used to grow carbon nanostructures. The lithium-based compounds have been chosen as catalyst due to a possibility of lithium insertion into CNTs during synthesis. The shift in G-band of CNTs confirms the lithium insertion during growth process. The benefit of lithium present in CNTs is to change electrical and mechanical properties and hence is a technologically important in many areas like hydrogen storage, super capacitor and in space application as thermal resistance. In the present study, the presence of lithium in CNTs improves rate capability of cell as its presence reduces diffusion length of lithium ion and increase conductivity of electrode; however, detail study is required in this direction. It has also been established through this study that CNTs could be grown on compound oxide catalysts, which are different from conventional catalysts, based on transition metals and their alloys. The effect of temperature on synthesis of CNTs shows that the tubes synthesized at temperatures of 580° and 650 °C have better graphitization compared to those synthesized at lower temperature.

The results of carbon nanostructures synthesized using different catalysts have been analyzed and compared. The electrochemical behavior of the MWCNTs and CNRs grown using the catalysts $LiNi_{0.5}Co_{0.5}O_2$ and $LiFePO_4$ respectively has been studied as anode in a lithium ion cell. The reversible capacity of the MWCNTs is about 485 mAh/g, which is higher than that of the reversible capacity 100-400 mAh/g, reported for MWCNTs grown

over conventional catalysts. This confirms that by changing morphology one can change electrochemical properties of CNTs. The coulombic efficiency of MWCNTs is 96.6%, which is better than the coulombic efficiency of 84–95% up to 5 cycles, as reported for SWCNTs and MWCNTs grown over conventional catalysts.

In this chapter, the synthesis of CNRs using $LiFePO_4$ as a catalyst by thermal CVD of acetylene at 650 °C has been demonstrated for the purpose of materials synthesis strategy. The TEM and FESEM images show that the materials have ribbon type morphology having width of 50–80 nm. The SAD pattern and XRD results of the synthesized materials are consistent. The first order Raman spectrum of CNRs grown using the catalyst $LiFePO_4$ shows that up-shift of G-band indicating the insertion of lithium during growth process and higher crystallinity compared to MWCNTs grown with conventional catalysts. Electrochemical properties of CNRs show higher reversible capacity (340 mAh/g), capacity retention of 335 mAh/g up to 14th cycle and higher coulombic efficiency (98 %). As evident from the literature, the synthesis of CNRs using catalyst $LiFePO_4$ and the application of CNRs as anode material for Li-ion battery is reported in this thesis for the first time. Such improvement in electrochemical behavior of these carbon nanostructures is related to their structural properties. The capacity observed for both types of carbon nanostructure is quite similar, however they have different voltage profiles. The flat voltage profile has been observed for CNTs grown using $LiNi_{0.5}Co_{0.5}O_2$ catalyst however, the discharge profile of CNRs is sloping in nature. The different nature of discharge plateaus shows the effect of morphology on electrochemical behavior of carbon nanostructures when used in lithium ion cell.

STRUCTURAL AND ELECTROCHEMICAL BEHAVIOR OF CARBON HOST CONTAINING HETEROATOMS (B, Si) AS ANODE MATERIALS

5.1 INTRODUCTION

This chapter has been divided into two sections. In the first part, the results of boron-doped graphite have been analyzed and discussed. The second part consists of results and discussion of structural and electrochemical behavior of ball milled Si-graphite material as anode. To improve the anode performance carbon in the form of graphite is doped to change the chemical composition of the bulk and the surface, and the electron distribution of host materials. The use of carbon host containing one or more types of heteroatom such as boron [Dahn et al., 1993], silicon [Wilson and Dahn, 1995], phosphorous [Schönfelder et al., 1997] or other [Matsuda et al., 1993] improve carbonaceous materials in term of increased specific charge for lithium insertion. Boron is assumed to act as an electron acceptor in carbon host and thus to cause a shift in the intercalation potential to more positive value and an increase of the reversible capacity due to more electronic sites. The silicon as heteroatom in carbon host would seem to be possible alternative to pure graphite or carbon anode due to its higher intercalation capacity. However, the large capacity fade observed during initial cycling makes such electrode unsuitable for commercial purposes. In the present work, an attempt has been made to improve the anode performance of such materials in lithium ion battery. In the first section, the results of boron-doped graphite have been analyzed and discussed.

5.2 STRUCTURAL AND ELECTROCHEMICAL PROPERTIES OF BORON DOPED GRAPHITE AS ANODE IN Li-Ion CELL

In this section, the effect of boron doping on structural and electrochemical properties have been analyzed and discussed. Anode properties of graphite doped with 1, 3 and 5 wt% boron have been compared with that of undoped graphite. Graphite (99.5%, sd fine), and boron (99 %, Himedia) powders both in crystalline form were mixed in liquid (methyl alcohol) medium for 2 hours using agate mortar and pestle. The powder mixture after drying was annealed at 1400 °C for 5 h in an Ar gas atmosphere to remove the organic contents and other impurities. The powder after annealing has been further heat treated at high temperature (2300 °C) in an inert (Ar) gas atmosphere. Different experimental techniques have been used to study the boron doped graphite samples. The results of the doped and the undoped graphite have been compared and discussed.

5.2.1 Microstructural Studies

FE-SEM micrographs of graphite powder and boron doped graphite powders are shown in Fig. 5.1. The powders have plate like morphology and layers of graphite are stacked together. The microstructure of graphite powder changes significantly by doping with boron. Fig. 5.1a shows the separate graphite particles. However, smooth layers and larger crystallites have been observed in boron-doped samples as seen in Fig.5.1 (b, c & d). The estimated grain sizes of graphite powder lie in the range of 0.4 to 8 μm, and increases up to 12 μm on boron doping. The increase in grain size of boron-doped graphite is due to the applied heat treatment at high temperature and boron acting as a catalyst for grain growth [Sogabe et al., 1996]. The change in microstructure and disappearance of crystal boundaries are perhaps due to rearrangement of crystal domain after boron substitution in graphite structure [Sogabe et al., 1996]. However the exact mechanism of such a redistribution of crystal boundaries due to boron doping is not known yet, but it is perhaps due to the fact that at high temperature viscosity of molten boron became low enough to flow so smoothly and joined the boundaries.

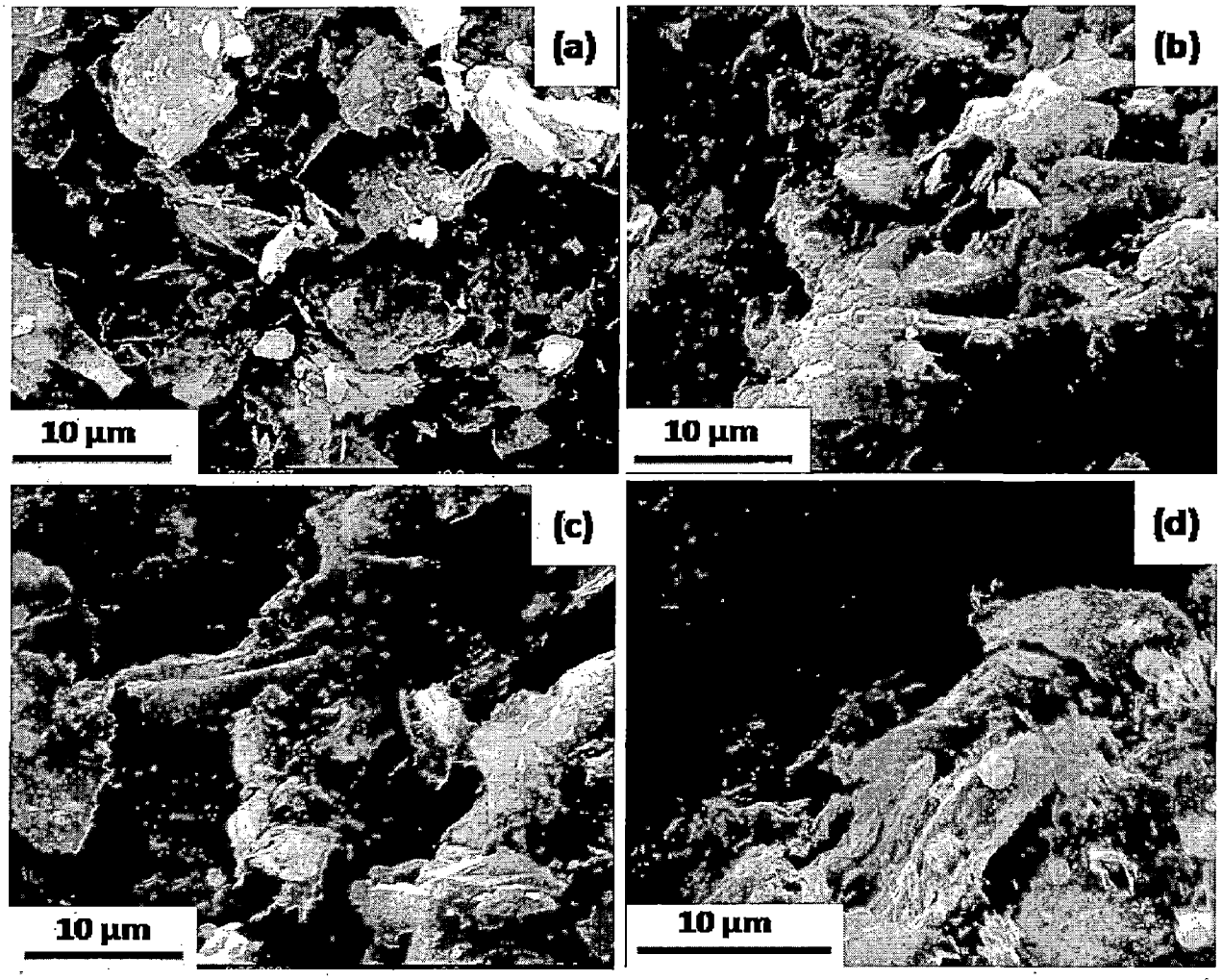

Figure 5.1. FE-SEM micrographs of (a) undoped graphite and doped graphite with (b) 1 wt %, (c) 3 wt%, (d) 5 wt % of boron.

5.2.2 X-ray Diffraction

Figure 5.2 shows the X-ray diffraction patterns of the graphite and boron doped graphite samples. The peaks of boron and boron carbide are present along with graphite in the XRD pattern. The maximum solubility of boron in graphite is reported as 2.35 at % [Lowell, 1967], so the carbide phase formation is due to the larger boron content than the required quantity for solid solubility. Decrease in interlayer spacing (d_{002}) and marginal shift of (002) graphite peak have been found for boron-doped graphite samples as shown in Fig. 5.2b and given in table 5.1. The decrease in d_{002} is attributed to the decrease of π-electrons in between the graphene layers.

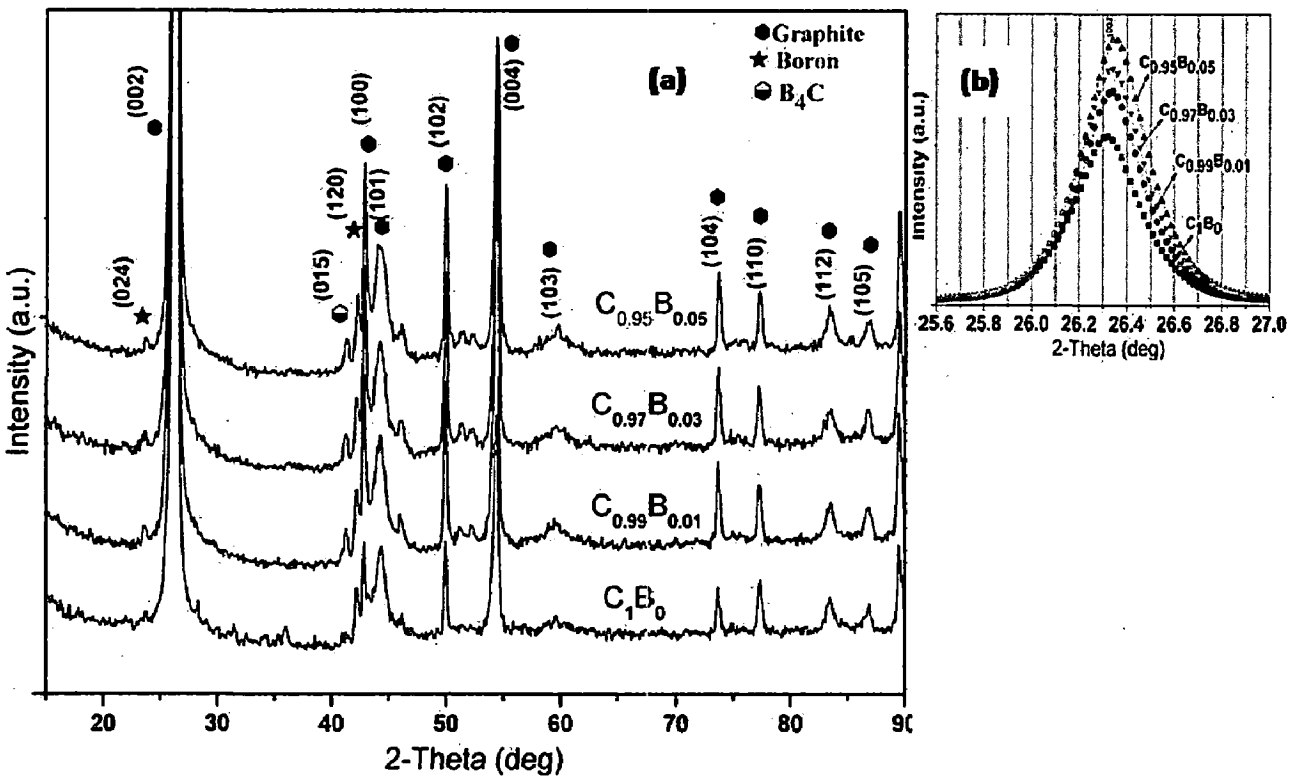

Figure 5.2: x-ray diffraction patterns of graphite and graphite doped with boron of 1 wt%, 3 wt% and 5 wt %.

Boron is in the state of lower valence than carbon is and therefore the boron acts as an electron acceptor [Endo et al., 1999]. The reduction in d_{002} values with increase

Table 5.1: Crystallite size of graphite and boron doped graphite calculated from XRD patterns.

Sample composition (wt%)	d_{002} (Å)	$L_{c\ (002)}$ (Å)	$L_{a(110)}$ (Å)
$B_0C_{1.0}$	3.365	266	590
$B_{0.01}C_{0.99}$	3.344	292	615
$B_{0.03}C_{0.97}$	3.341	294	620
$B_{0.05}C_{0.95}$	3.340	298	618

in B content is perhaps due to B has smaller atomic size than C in graphite lattice, resulting in adjacent graphite planes closer and simultaneously yielding a contraction in the structure along the *c*-axis [Murty et al., 1977 and Hagioet al., 1989]. The (002) and (004) peaks become sharper for boron-doped samples. The sharpness in the peaks is due to the heat treatment at high temperature, which reduces unorganized region and develops more ordered region in the structure [Dresselhaus et al., 1988]. The (112) peak is sharper and more intense in the case of boron-doped graphite samples than that for un-doped graphite (Fig 5.2a), which is an indicative of enhanced stacking of the graphitic layers in boron doped graphite than that of un-doped graphite [Murty et al., 1977. The boron-doped samples show larger crystallite sizes in c- as well in *a*-direction (L_c and L_a values) compared to that for pure graphite (table 5.1), indicating that the larger degree of stacking has been resulted by B doping. The gradual shift in the position of peak (002) shows that boron has been-doped substitutionally in hexagonal graphite planes.

5.2.3 Raman Spectroscopy

Raman spectra of graphite and boron-doped graphite powders are shown in Fig.5.3. The first order Raman spectra have been collected to determine crystalline ordering in graphite and boron and silicon mixed graphite powder in terms of various spectral parameters such as intensity, peak position and FWHM. The spectral parameters, which were obtained after Lorentzian fitting of the spectra, are tabulated in table 5.2. The shoulder peak (D′-band) at around 1620 cm^{-1} has been found to appear for the boron-doped sample. The position of the peak centre of D′-band remains unchanged on further doping of boron, however with increasing boron content the FWHM of this peak increases compared to that for the graphite as shown in table 5.2.

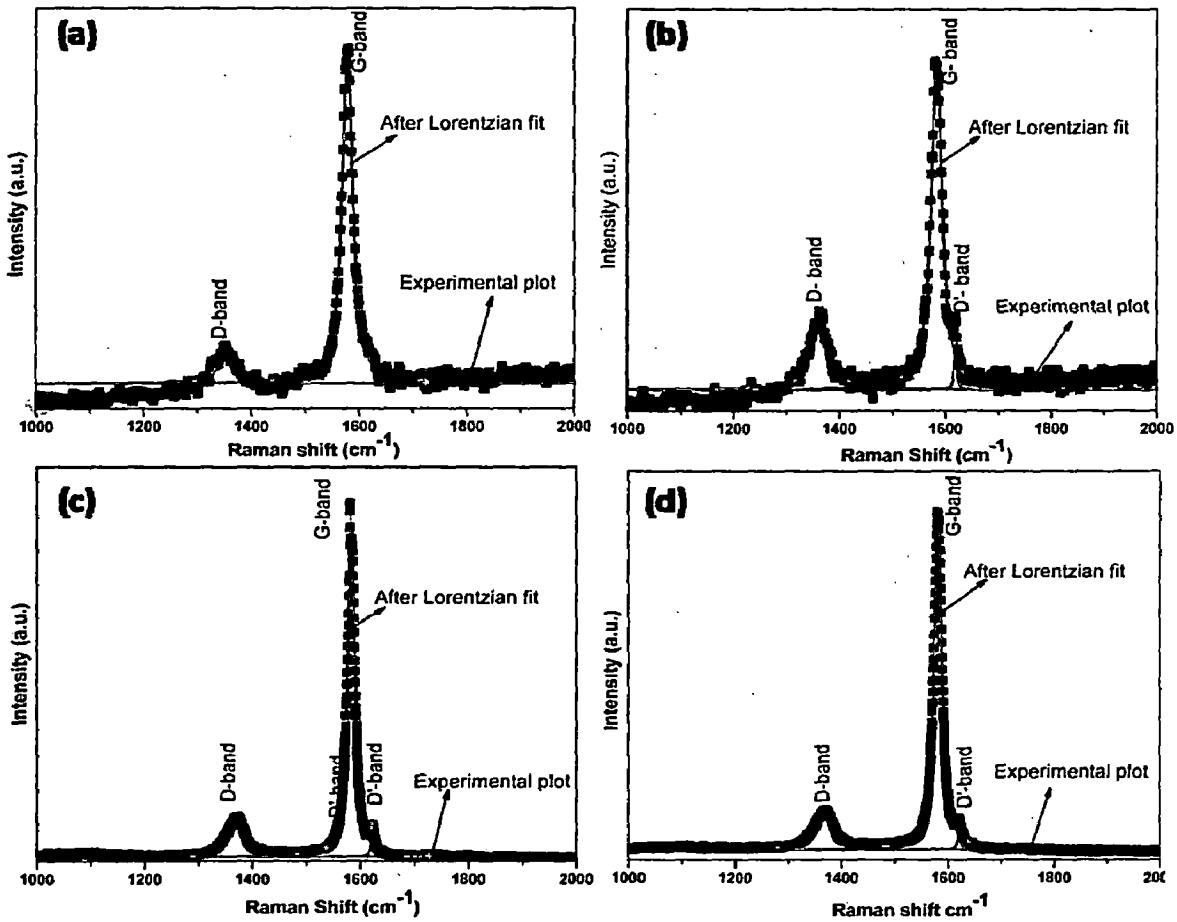

Figure 5.3: First order Raman spectra of pure graphite and boron-doped graphite: (a) $C_{1.0}B_{0.0}$ (b) $C_{0.99}B_{0.01}$ (c) $C_{0.97}B_{0.03}$ and (d) $C_{0.95}B_{0.05}$.

This peak is associated with the boron-carbon vibrations, which is influenced, by the smaller number of electrons in boron, causing a redistribution of π-bonding and a difference in the bond length of boron-doped neighboring carbons compared with un-doped or ordinary C-C vibrations in graphite [Chieu et al., 1982]. The substitution of boron atom into graphite layer leads to the formation of three carbon-boron (C-B) bonds and that the bond length of C-B (1.48 Å) is slightly longer than that of C-C (1.41 Å) (Hishiyama et al., 2001) bond. G-band of graphite at 1578 cm^{-1} shifts towards the higher wave number side with an associated intensity lowering compared to pure graphite (table 5.2), which may be due to boron doping. Boron doping creates local disorder in graphite lattice. Such shift in G-band of graphite has been also observed for graphite intercalation compounds [Katagiri et al., 1996]. The spectral positions in Raman spectra depends strongly upon size and type of near neighbor bonds, and hence are related to the local symmetry present in the structure of the materials [Kim et al., 2000]. The relative intensity ratio (R) between D-band to G-band depends on both

degree of graphitization and the ordering in graphite plane [Fong et al., 1990]. The R-value is sensitive to the concentration of graphite edge planes and crystal boundaries relative to standard graphite planes and hence gives information about disorder in graphitic structure [Way and Dahn, 1994]. The R-values for boron-doped samples as can be seen from the table 5.2, is significantly larger than for the pure graphite samples. This indicates the presence of the local structural distortions and vacancy formation in the graphite planes due to boron doping [Endo et al., 1999].

Table 5.2: Raman spectral parameters obtained after curve fitting experimental spectra using Lorentzian bands (G, D, D′).

Sample		Peak centre (cm^{-1})	FWHM (cm^{-1})	$R=I_D/I_G$
$C_{1.0}B_0$	(G-band)	1578	23	0.13
	(D-band)	1351	28	
$C_{0.99}B_{0.01}$	(G-band)	1583	16	0.30
	(D-band)	1362	36.54	
	(D′-band)	1620	3.35	
$C_{0.97}B_{0.03}$	(G-band)	1585	17	0.32
	(D-band)	1367	40	
	(D′-band)	1622	6.0	
$C_{0.95}B_{0.05}$	(G-band)	1585	24	0.35
	(D-band)	1369	42	
	(D′-band)	1622	7.0	

5.2.4 Electrochemical Behavior of Boron-doped Graphite

Figure 5.4 shows the first charge/discharge profile of cell constructed with graphite and boron doped graphite as anode and lithium metal as counter electrode. As the graphite based materials act as positive electrodes and the lithium metal behaves as negative electrode, the intercalation of lithium ions in this system is considered as the discharge process. The long discharge profile below 0.22 V corresponds to lithium intercalation in both graphite and boron doped graphite samples. During the first discharge of graphite and boron doped graphite samples a shoulder plateau has been observed at about 0.82 V, which is caused by electrolyte decomposition on surface of graphitic materials. The capacity corresponding to these shoulder plateaus causes

irreversible capacity of the cell [Way and Dahn, 1994]. However, the plateau at about 0.82 V do not appear in the second and subsequent cycles as shown in Fig.5.5, indicating no further decomposition of electrolyte takes place.

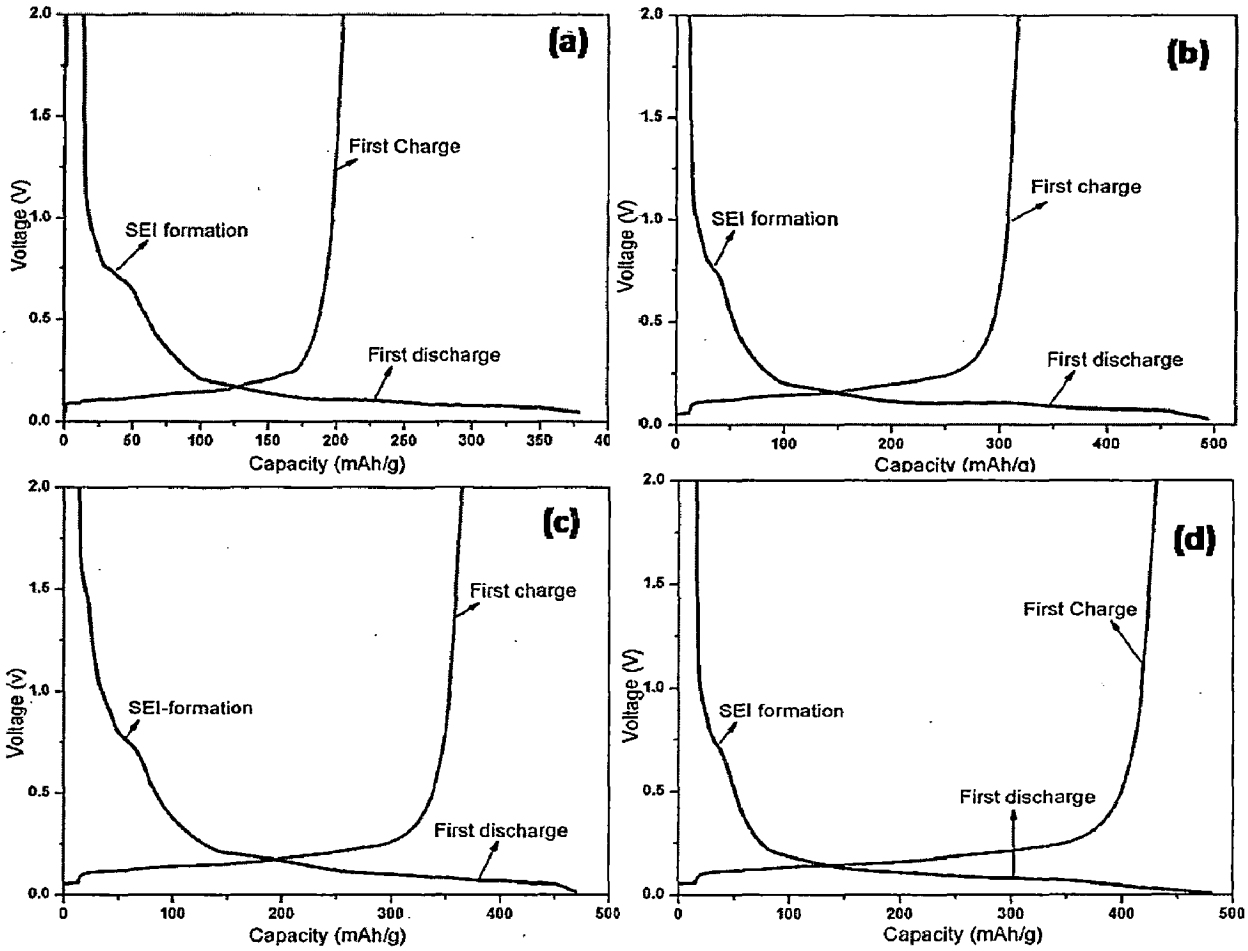

Figure 5.4: Charge capacity and potentials during first discharging/charging cycles of (a) undoped graphite, (b) $B_{0.01}C_{0.99}$, (c) $B_{0.03}C_{0.97}$ and (d) $B_{0.05}C_{0.95}$ samples.

The first discharge and charge capacities of undoped graphite are 370 mAh/g and 175 mAh/g respectively causing an irreversible capacity of 195 mAh/g. However, the irreversible capacity decreases with increasing boron content. The irreversible capacities become 140, 90 and 50 mAh/g respectively for 1, 3 and 5 wt % boron doped samples. Way and Dahn (1994) have also reported similar trends. They have shown that boron doped carbon with composition B_xC_{1-x} ($0<x<0.17$) prepared by chemical vapor deposition (CVD) from benzene and boron trichloride at 900 °C has a significantly increased reversible capacity than pure carbon materials. They explained

that electron acceptor nature of boron is responsible for increased capacity in boron-doped graphite. The average voltage plateau for boron-doped samples occurs at a voltage 0.25 V that is slightly higher than that occurs for graphite at about 0.15 V. The increase in voltage of the plateau for boron-doped samples is due to change in electronic structure of the host material. Due to the presence of boron in graphite, chemical bond between lithium and boron-doped graphite becomes strong which leads to increase bond strength. As a result, the potential of lithium in boron doped graphite host increases relative to that in the pure graphite material and hence voltage plateau shifts upward [Way and Dahn, 1994]. The increased voltage makes faster recharge of lithium-ion cell.

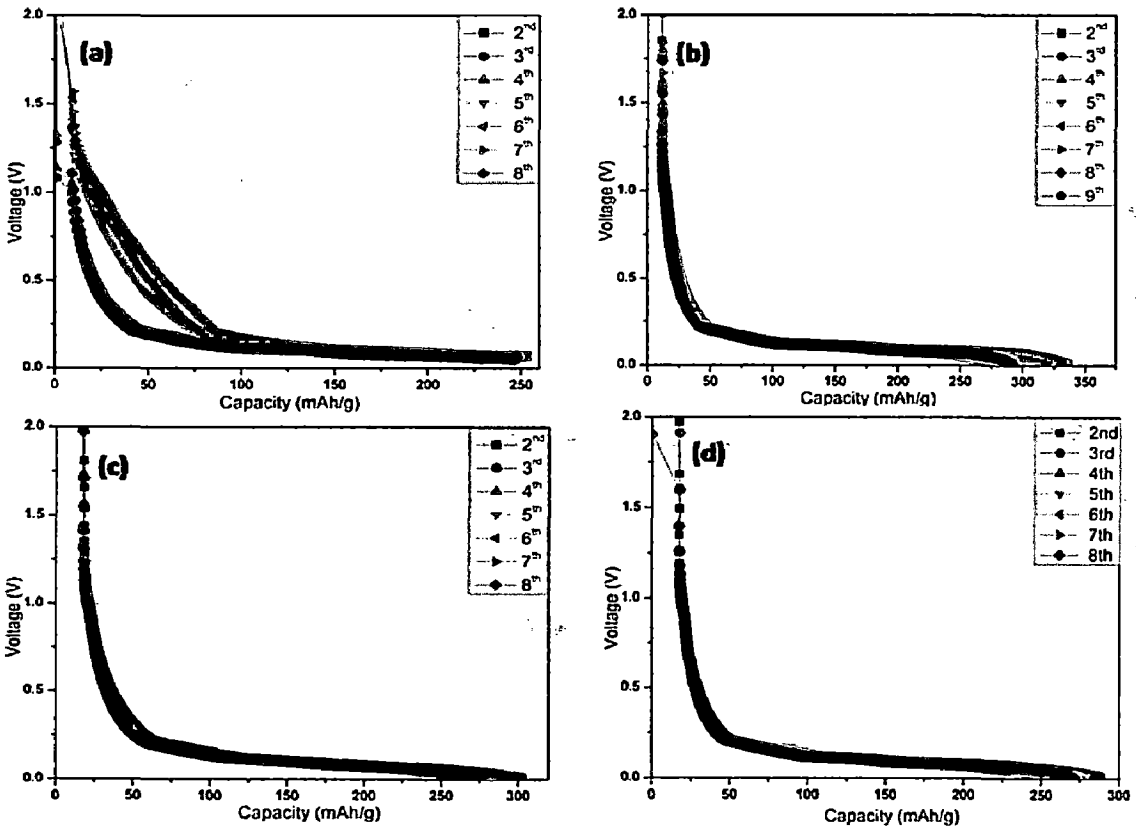

Figure 5.5: Discharge profiles against lithium metal foil for all cycles studied from second cycle for the samples of (a) undoped graphite, (b) $B_{0.01}C_{0.99}$, (c) $B_{0.03}C_{0.97}$ and (d) $B_{0.05}C_{0.95}$.

Figure 5.5 shows the discharge profiles of graphite and boron-doped graphite samples studied upto 9 cycles for $B_{0.01}C_{0.99}$ and upto 8 cycles for other samples. The discharge profiles of the materials for all the compositions are flat and therefore

suitable for battery application. Way and Dahn (1994) reported that the boron substituted B_xC_{1-x} ($0<x<0.17$) produced by chemical vapor deposition (CVD) from benzene and boron trichloride precursors at 900 °C have reversible capacity higher than that of graphite. However, in their experiment they have observed sloping voltage profile and most of cell capacity is obtained at a higher voltage compared to present study. The flat voltage profiles have been observed for all boron doped graphite based anode materials and majority of cell capacity appears at voltage lower than 0.2 V in present study. The flat voltage profile and capacity at lower voltage are the requirements for better performance of battery. The boron-doped graphite materials synthesized directly at high temperature appear to be useful as anode material in lithium-ion battery. These materials have specific capacity better than pure graphite and flat discharge profile compared to those of disorder carbon and boron doped graphite material synthesized by Way and Dahn (1994) by using CVD method.

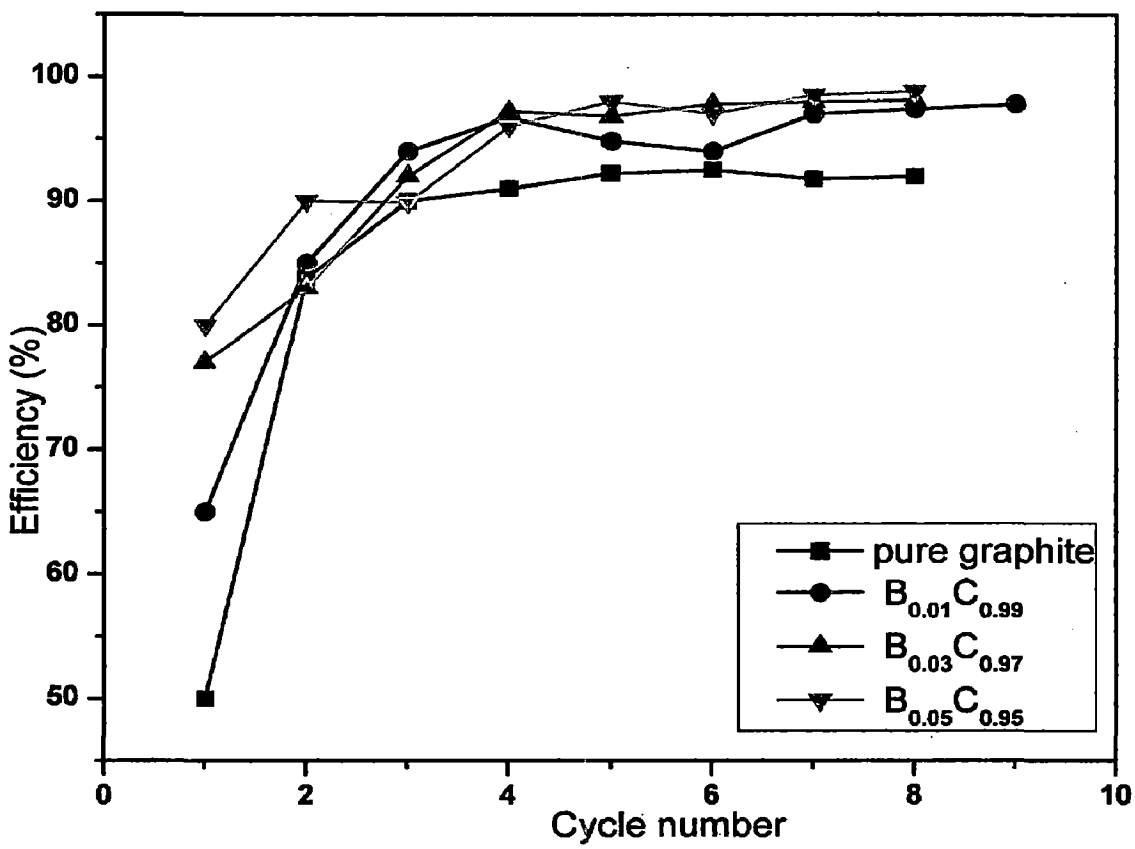

Figure 5.6: Plot of cycle efficiency and cycle number in the pure graphite and boron-doped samples.

Figure 5.6 shows the variation of coulombic efficiency with number of cycles for undoped graphite and boron-doped graphite samples. The doped samples have better coulombic efficiency compared to undoped graphite sample. The coulombic efficiency of undoped graphite in first cycle is 50% and the efficiency becomes constant at about 92 % from fourth cycle onwards. The coulombic efficiency of all boron doped samples is higher compared to that of the undoped graphite. The first cycle efficiencies of boron doped samples are 65, 77 and 80 % for 1, 3 and 5 wt% respectively. Higher coulombic efficiencies between 95-98 % have been observed from fourth to eighth charge-discharge cycles for all the boron doped samples. The increase in coulombic efficiency is related to the change in electronic structure of graphite by boron doping. The boron (trivalent) has electron acceptor nature in graphite matrix, and forms trigonal sp^2 hybrid bond with C atoms in graphite structues [Endo et al., 1999]. The procedure used for synthesis of such boron doped graphite anode material is also economically relevent.

5.3 BALL MILLED GRAPHITE-SILICON BASED ANODE MATERIALS FOR LITHIUM-ION BATTERY

Silicon seems to be a possible alternative for graphite or carbon based anode material because its lithium insertion capacity is highest among all known anode materials. However, large capacity fade has been observed in silicon-based anode when used in lithium ion cell. This problem has prevented the silicon anode for commercial application. To overcome the problem of capacity fading, better capacity retention and to have better cycle life for Si anodes, various approaches have been used.

In the present study, different compositions of C-Si (1, 5, 10 and 15 wt % Si) system have been milled in liquid medium (methanol) using planetary ball mill. The milled powder was annealed at 1200 °C for 5 hours in Ar gas atmosphere to increase the homogeneity of Si into graphite matrix. The structural characterization of the powder mixture after annealing has been carried out by using FE-SEM, XRD and Raman spectroscopy. The annealed powder was used as active anode material in the test cell. The cell was tested at 20 °C by using computer-controlled cycler at a constant current of 150 μA between 0.05 and 2.5V. The structural and electrochemical properties of this system have been investigated and are discussed in following sections.

5.3.1 Thermal Studies

Figure 5.7 represents a typical thermo gravimetric analysis (TGA) showing thermogram of weight loss as a function of temperature for unmilled graphite and Si-mixed graphite under nitrogen atmosphere. The TGA data of the graphite powder without milling, shows a negligible weight loss of about 2.25 % up to 895 °C, after which the weight loss is increased to 5 % up to 1200 °C. The weight loss is due to removal of H_2O, CO and CO_2 [Nagano et al., 1999]. The weight loss for all Si-mixed and milled graphite powder begins at 200 °C, which corresponds to the removal of liquid content used during milling. The weight losses for pure graphite and Si % mixed graphite have similar trends.

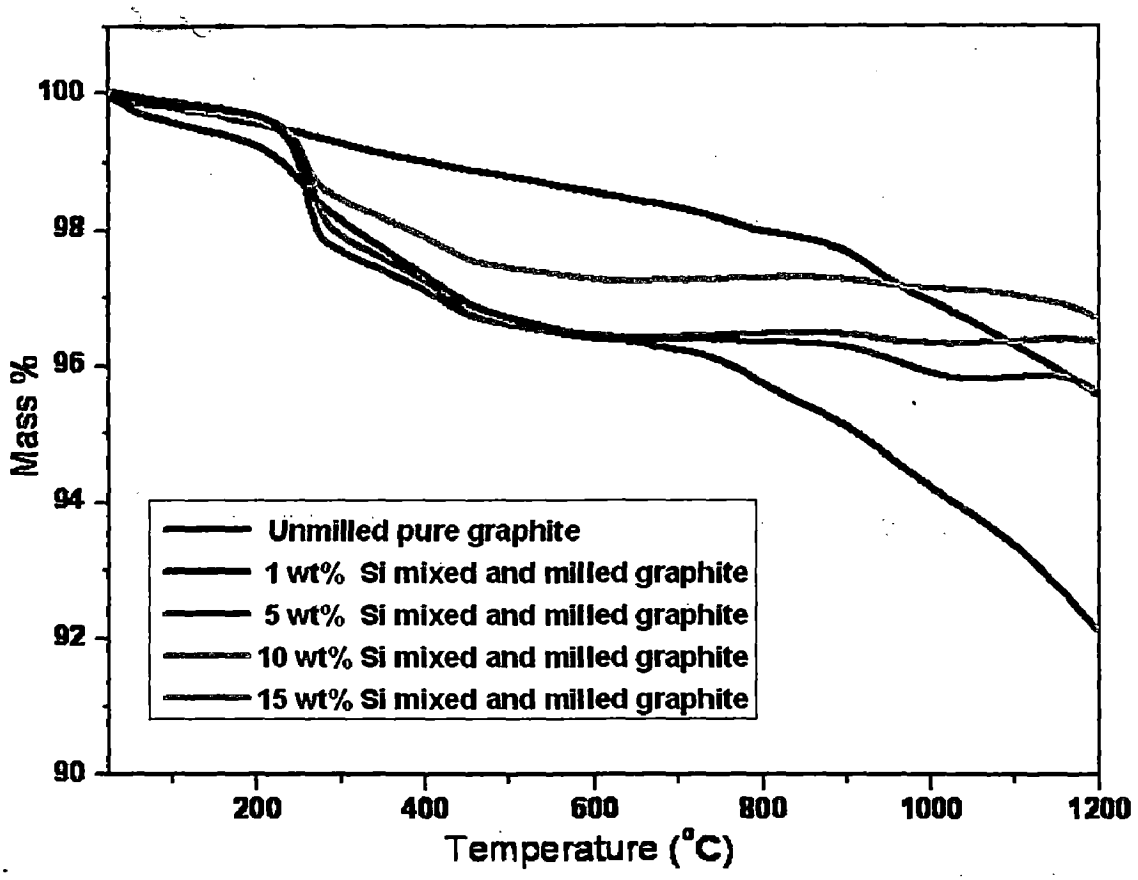

Figure 5.7: Thermo gravimeteric analysis of unmilled graphite powder and milled Si-graphite powder.

5.3.2 Microstructure/Morphology Analysis

Elemental analysis of the powders with different compositions obtained by ball milling and heat-treatment of the Si-graphite samples are shown in Fig 5.8. The EDX spectra confirm the presence of different elements in the mixture. The carbon and silicon peaks can be seen in EDX spectra of all samples. The spectra show that intensity of silicon peak increases with increases in silicon content. The unmarked peak in the spectra is due to gold coating used for sample preparation for microstructural analysis. Elemental composition of the mixture in wt% and at% are presented in tables given as inset of Fig 5.8. The Si particles are uniformly distributed in the matrix, which is confirmed by EDX analysis carried out in different regions.

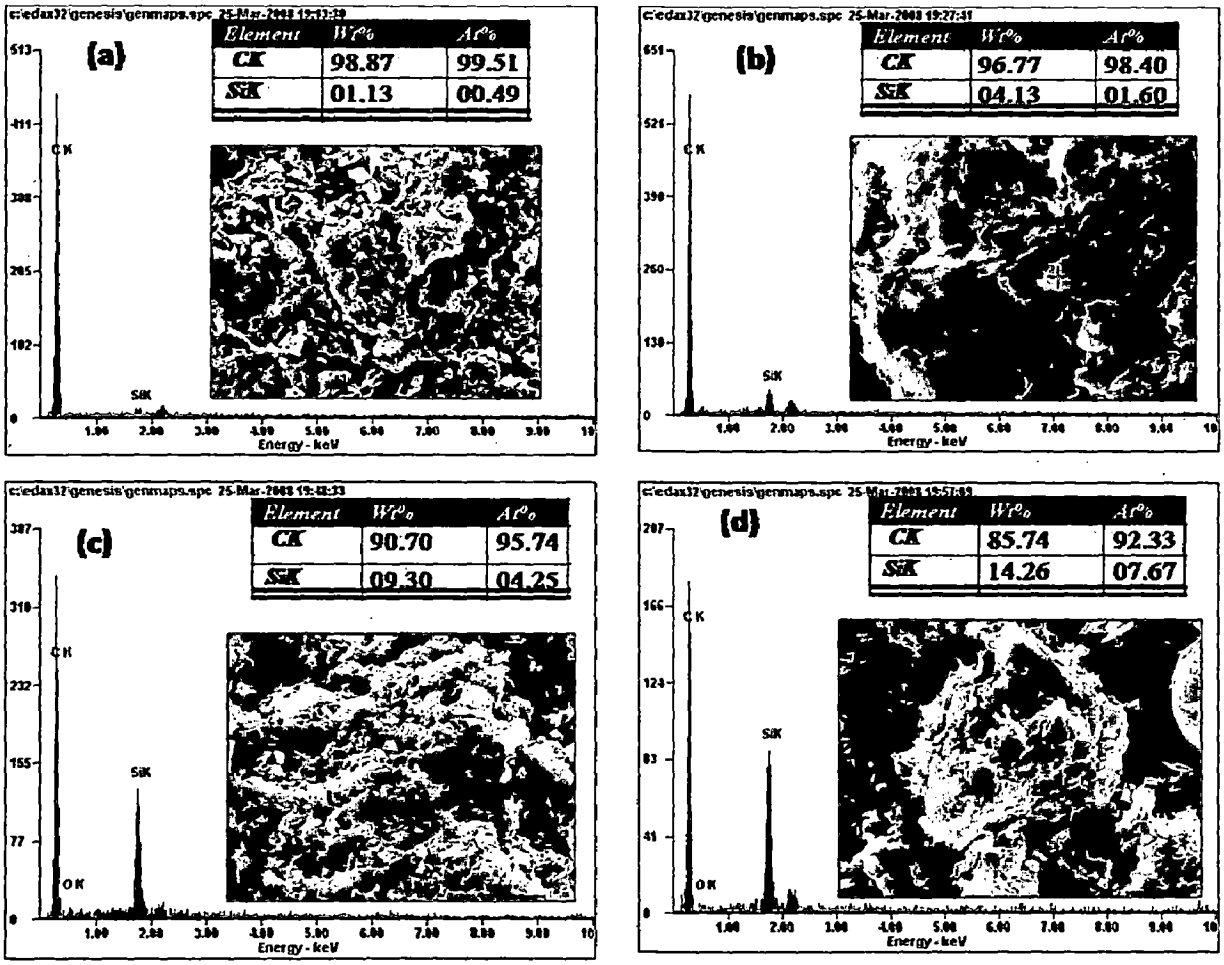

Figure 5.8: EDX spectra of (a) Si 1wt% (b) Si 5 wt % (c) Si 10 wt % and (d) Si 15 wt % mixed graphite powder.

FE-SEM images of pure graphite and graphite-Si mixtures of the four different compositions and ball milled for 5 hours and heat treated at 1200 °C are shown in Fig. 5.9. The pure graphite powder has stacked layers and separated plates like morphology as shown in the Fig.5.9. The morphology of the graphite powder changes after milling of the silicon mixed powder and heat-treating the same. The disappearances of the crystal boundaries are due to rearrangement of crystal domain after heat treatment. The average grain size of pure graphite is about 5.0 μm, which increases in silicon mixed samples and becomes about 10 μm due to heating at high temperature. The particle size of Si powder used is in the range of 0.2 to 0.5 μm and these Si particles are present on the surfaces of graphite flakes. Due to the milling, the defects are induced on the surface and edges of graphite flakes and such behaviour is favorable for lithium

insertion. The Li-ions are adsorbed on the basal plane and then migrates over the surface to defect sites where they facilitate the lithium intercalation.

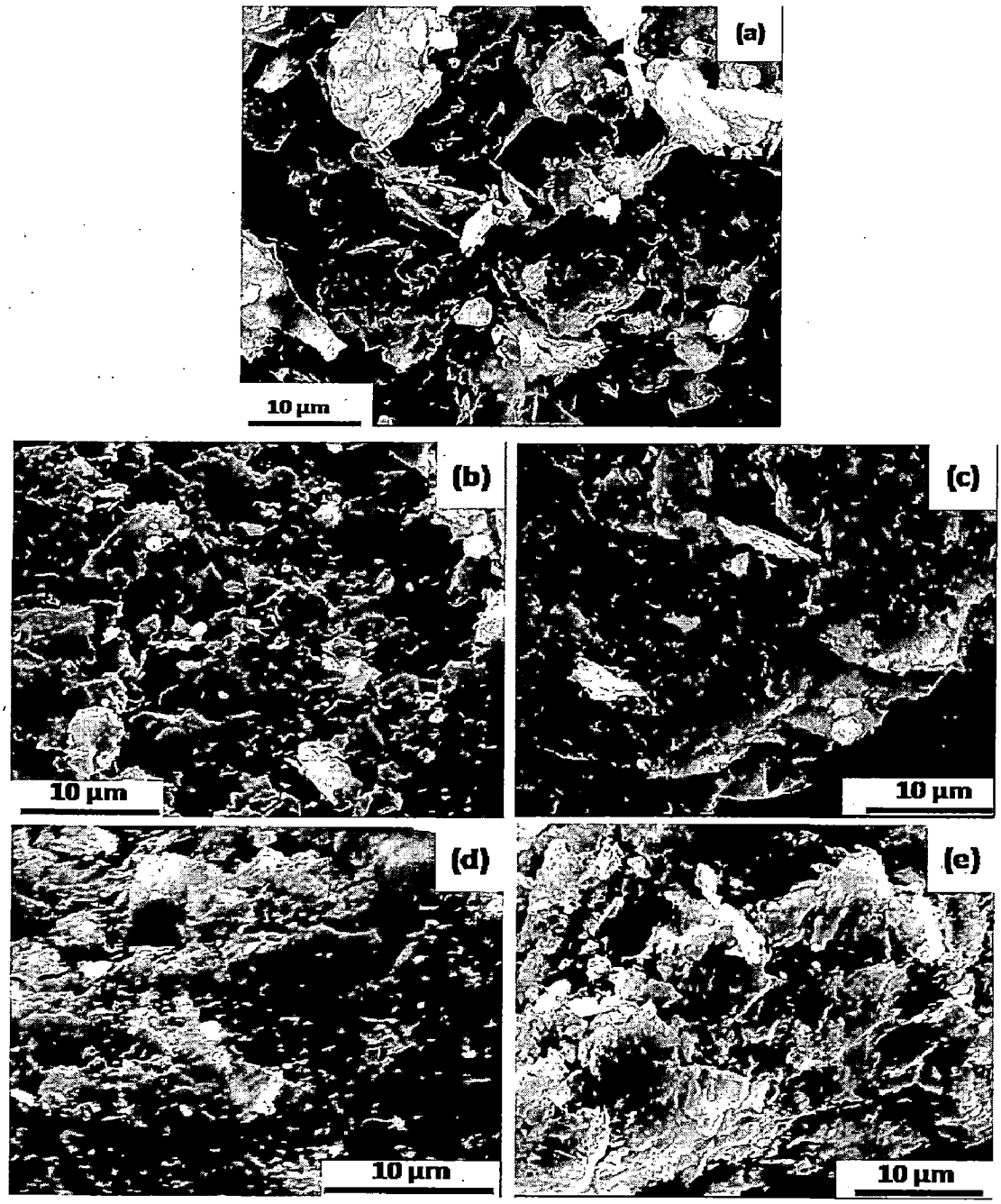

Figure 5.9: FE-SEM images of (a) pure graphite, (b) Si 1wt%, (c) Si 5 wt%, (d) Si 10 wt% and (e) Si 15 wt% mixed graphite powder.

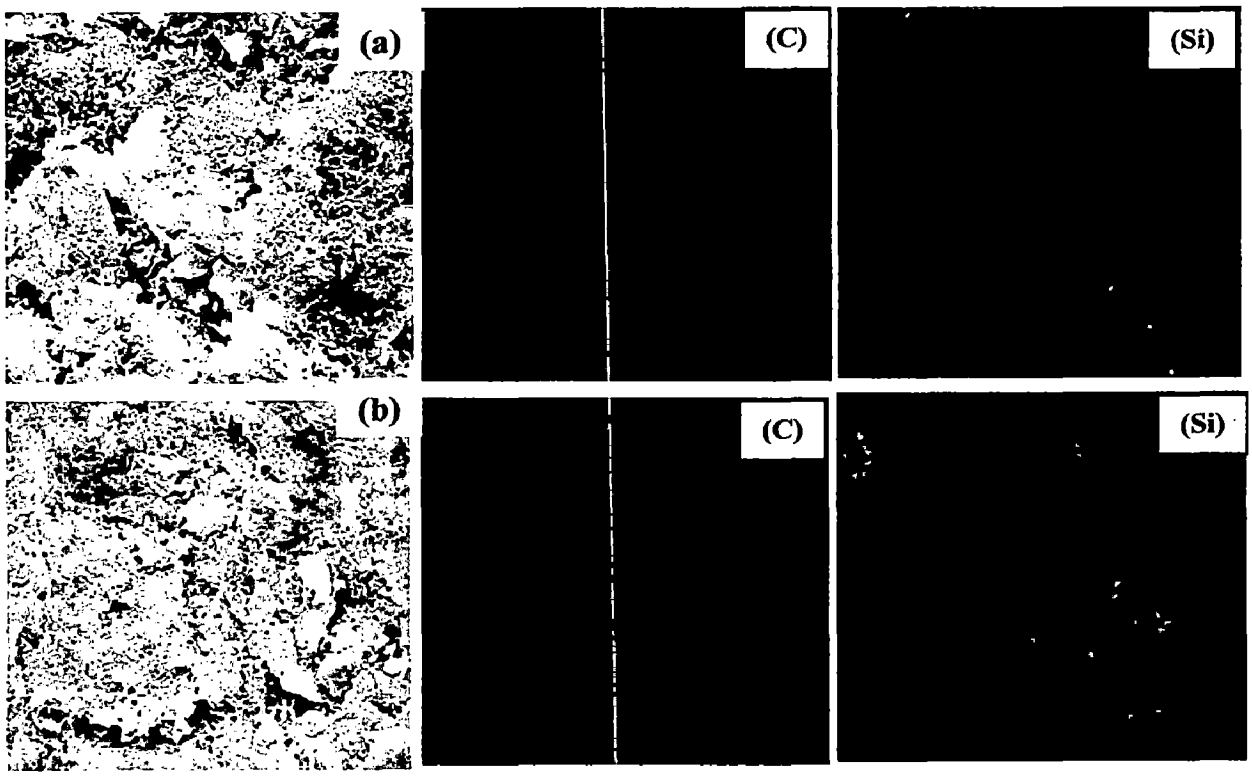

Figure 5.10: EDX mapping of Si-graphite mixture prepared by ball-milling of (a) Si 1wt% (b) Si 15 wt % mixed graphite.

The EDX mapping of the different elements was conducted to analyze the distribution of the species within the mixture of Si 1 and 15-wt % mixed graphite (Fig 5.10). The bright spots correspond to the elements of carbon and silicon present in the mixtures. The bright spots in red and in green correspond to the carbon and silicon respectively in the mixtures. Based on the EDX elemental map it can be seen that Si is distributed in graphite uniformly for 1-wt% Si in Fig. 5.10(a). However, clustering /agglomeration are present in 15-wt% Si-mixed graphite (Fig. 5.10(b)). These clusters perhaps have Si rich phases, which is either Si, or SiC phases. These indicate that a uniform distribution of Si on all particles is not easily achieved with higher Si contents by ball milling. The SiC phase increases Li-insertion resistance in anode host material and hence this phase is undesirable for anode material. The effect of this phase can be seen in electrochemical section.

5.3.3 X-ray Diffraction Analysis

XRD patterns of the pure graphite and silicon mixed graphite powders of different compositions, ball milled and heat-treated are shown in Fig 5.11. The XRD peak of SiC can be clearly observed from the XRD patterns of 5 wt% Si mixed graphite, and the intensity of X-ray peak corresponding to Si increases with increase in Si content and attains maximum for 15 wt % Si mixed graphite sample. The Si phase does not appear for 5-wt % Si, which is perhaps due to the SiC phase formation consumes entire Si content.

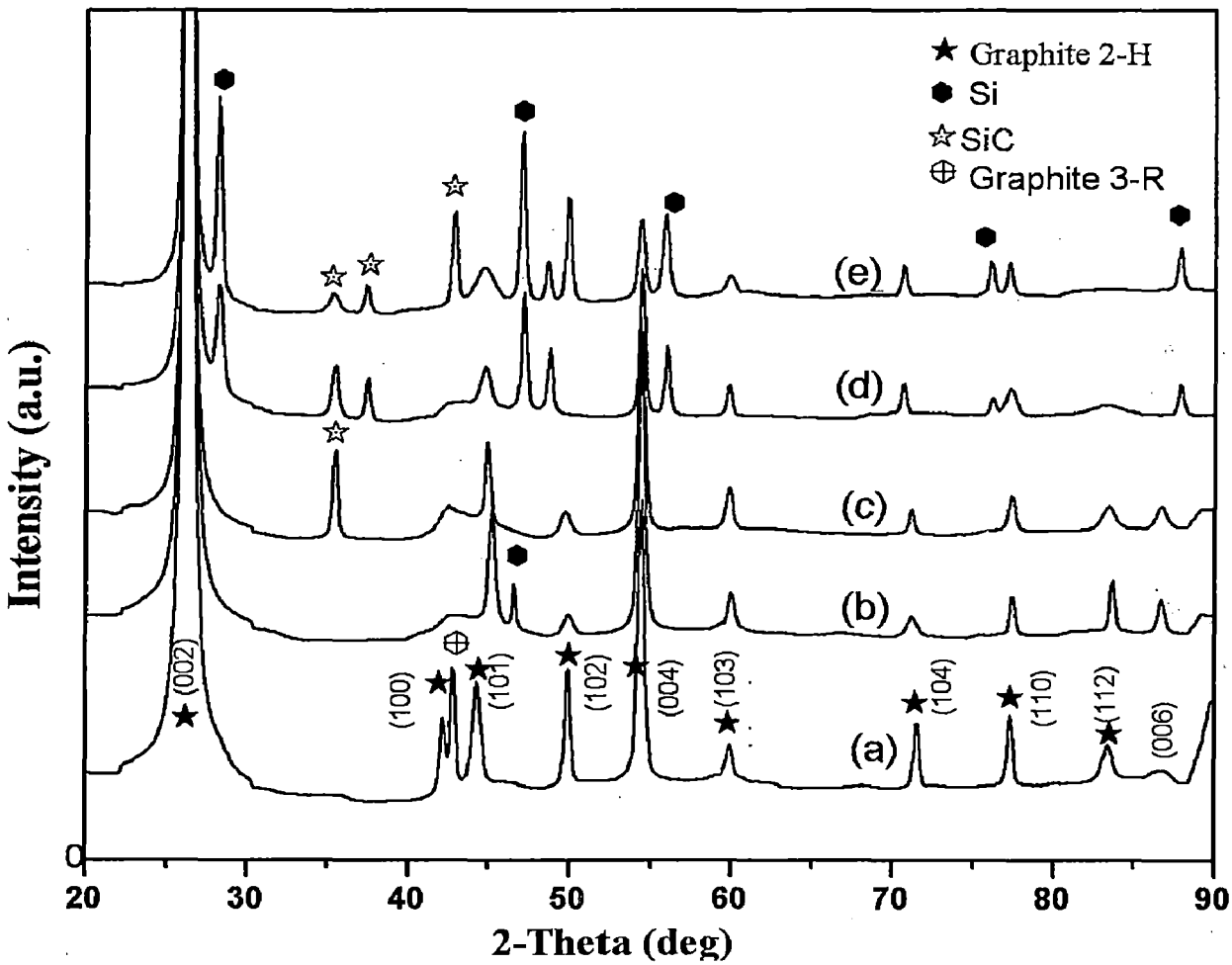

Figure 5.11: XRD pattern of (a) pure graphite, (b) 1 wt% Si, (c) 5 wt % Si, (d) 10 wt % Si and (e) 15 wt % Si mixed graphite powders ball milled for 5 hours and heat treated at 1200 °C.

The intensity and sharpness of (002) peak of graphite decreases with increase in Si content is shown separately in Fig. 5.12(a). This is due to disorderness in the graphite

structure, which increases with increase in Si content. The full width at half maximum (FWHM) has been calculated after the eliminations of background and instrumental broadening. The FWHM of (002) graphite peak increases from 0.24 for pure graphite to 0.31 for Si 1 wt% mixed graphite and increases marginally with further increase in Si content. However, FWHM of (101) peak increases form 0.41 for graphite to 0.52 for 15 wt % sample as shown in Fig.5.12 (b).

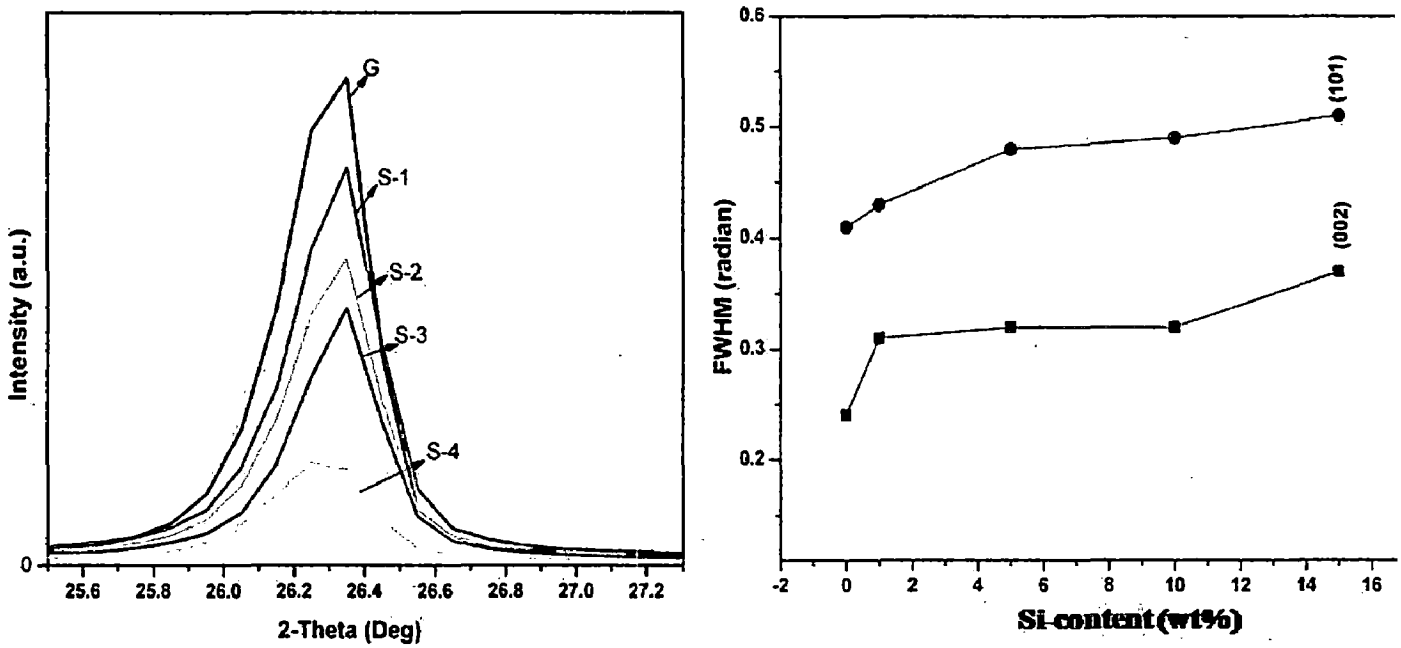

Figure 5.12: The effect of Si content on graphite powder on (a) (002) peak intensity and (b) FWHM of (002) and (101).

The SiC phase starts appearing at the composition of 5-wt% Si (i.e. 2.2 at % Si) and the number of peaks corresponding to this phase increases with increase in Si content. However, Wilson and Dahn reported that SiC is formed in carbon containing nanodispersed Si atoms if the content of Si exceeds 11 at % [Wilson and Dahn, 1995]. The formation of SiC phase with low at% Si may be due to processing conditions i.e. prolonged milling as well as heat treatment done (at 1200° C) in the present case. The SiC phase is electrochemically inactive and undesirable for anode in lithium ion battery. The effect can be observed in the electrochemical behavior of SiC rich composition of 15-wt % Si.

5.3.4 Raman Spectroscopy

Raman spectra of graphite ball-milled and heat-treated Si 1wt% and Si 15 wt % mixed graphite have been recorded in selected wave numbers ranging between 1000 and 2000 cm^{-1} and are presented in Fig. 5.13. Figure 5.13a, shows Raman spectrum consisting of an intense band at 1578 cm^{-1} and a weak band at 1351 cm^{-1}, for the pure graphite.

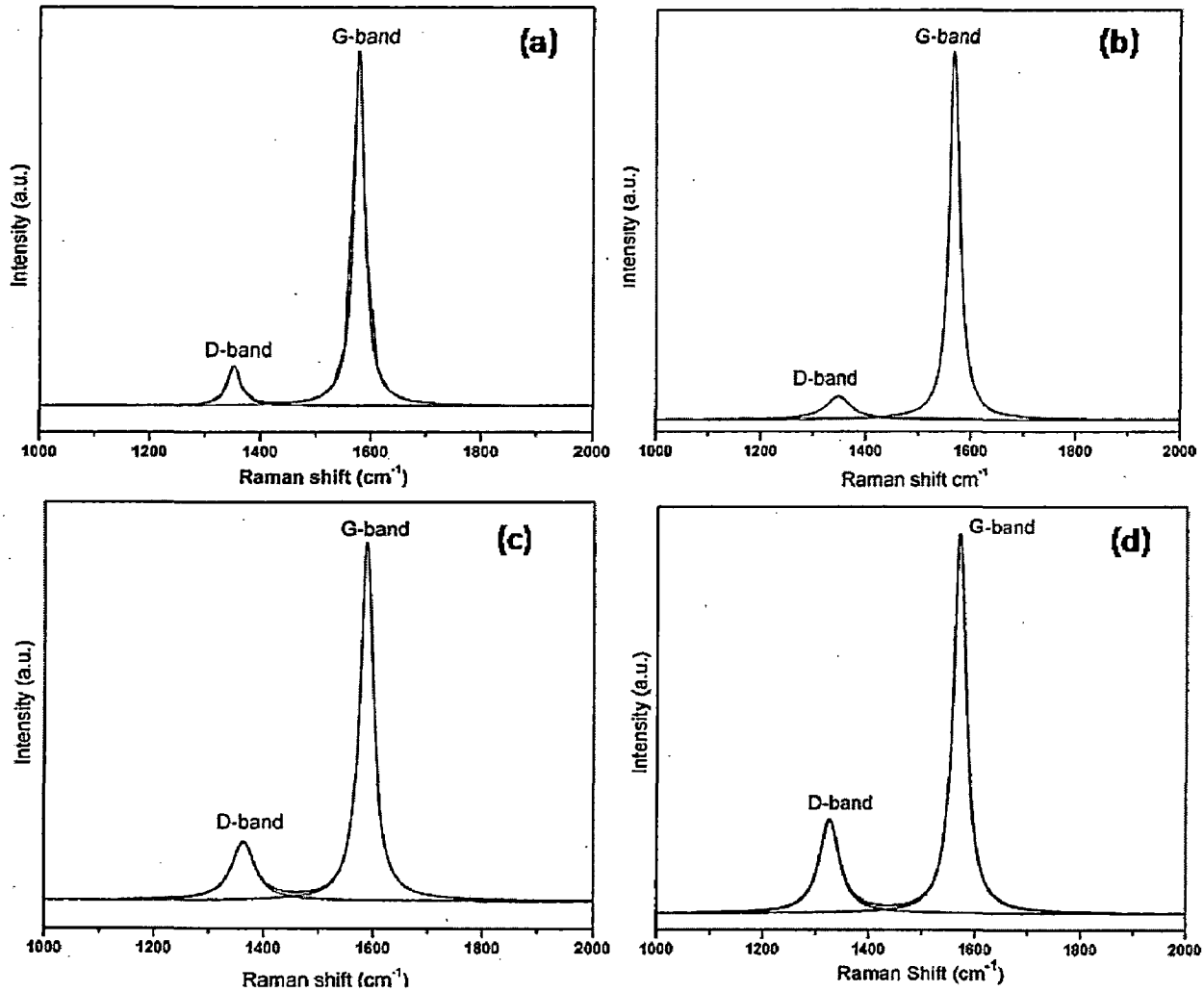

Figure 5.13: Raman Spectra of (a) Pure graphite (b) Si 1wt% (c) Si 10 wt% and (d) Si 15 wt% mixed graphite.

However, the G-band for Si 1 wt % and 15 wt% mixed graphite sample are found shifted towards higher wave number i.e. at 1582 and 1587 cm^{-1} respectively. The upward shift may be due to disorganized carbon by the presence of Si in graphite matrix [Wada et al., 1980]. The relative intensity ratio ($R=I_D/I_G$) of D and G bands, peak position and FWHM are tabulated for pure graphite and Si 1 wt% and 15 wt%

mixed graphite in table 5.3. The *R* depends on structural characteristic of carbon [Kastner et al., 1994], and the value of *R* provides information about the perfection of graphite layered structure, reflecting the edge plane or boundary of graphite crystal faces. The increase in *R* implies the increased defect structure and consequently decreases in degree of graphitization [Wang et al., 2004]. The *R* as can be seen in table 5.3 increases with increasing Si content. The FWHM also increases with increasing Si content as depicted in table 5.3. Thus, the results of Raman spectra support the XRD results.

Table 5.3: Raman spectroscopic parameters obtained after curve fitting experimental spectra using Lorentzian bands (G, D).

Sample	Area under peak	Peak centre (cm^{-1})	FWHM (cm^{-1})	$R = I_D/I_G$
Graphite (G-band)	25805	1578	22	0.13
(D-band)	3382	1351	28	
1 wt% Si (G-band)	17946	1583	24	0.15
(D-band)	2689	1348	54	
5 wt% Si (G-band)	581551	1587	29	0.28
(D-band)	164583	1363	57	
15 wt% Si (G-band)	17519	1588	40	0.55
(D-band)	9763	1351	48	

5.3.5 Electrochemical Behavior

The typical charge and discharge profiles of pure graphite, Si 1 wt % and 15 wt% graphite ball milled and heat treated at 1200 °C are shown in Fig. 5.14 (a, b & c). The discharge and charge profiles were measured in the voltage ranging from 0.05 to 2.0 V at a constant current of 150 μA. Upon discharge of the cell, the voltage drops rapidly at the beginning and reaches a value at around 0.8 V for all the compositions studied i.e for pure graphite and silicon mixed graphite. The plateau observed in the discharge profile (Li insertion) at the voltage of 0.8 V is attributed to the formation of solid electrolyte interface (SEI). It can be seen that the plateau at 0.8 V in Fig. 5.14(a)

is larger than that in Fig. 5.14(b & c). This result shows that the large amount of Si is helpful in preventing the SEI formation, which causes irreversible capacity of the electrode.

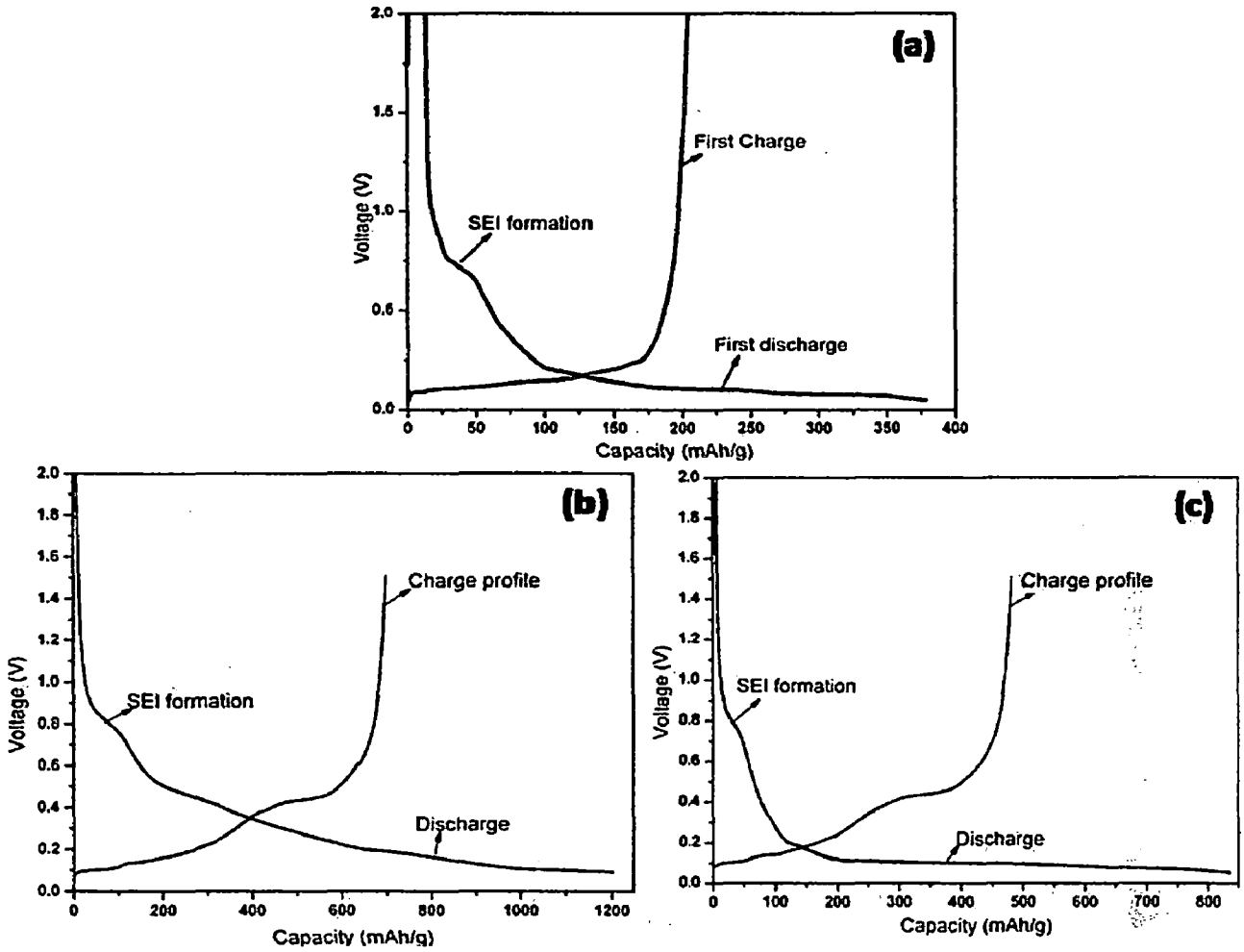

Figure 5.14: Charge capacity and potentials during first discharging/charging cycles of (a) pure graphite, and the graphite samples containing (b) Si 1 wt% (c) Si-15 wt%

A large voltage plateau starts at around 0.2 V and becomes almost flat below 0.1 V for both the compositions as can be seen from Fig.5.14 (b& c). The plateau at around 0.2 V is due to Li intercalation into graphite corresponding to the formation of stage-4 compound [Billaud et al., 2002]. However, the insertion voltage of Si in first cycle occurs at around 0.1V, so the plateau at this voltage is due to formation of Si-Li alloys [Wu e al, 2008]. This shows that Li-ion can be inserted both in graphite as well as in Si. However, in charging profiles, the voltage increases slowly and two plateaus are formed at 0.2 and 0.4 V. From initial charge–discharge profile, it is evident that

graphite-Si anodes operate in narrow potential range between 0.0 and 0.4 V as shown in Fig. 5.14 (b & c) which would be suitable for Li-ion battery. However, the plateau at about 0.4 V does not appear in charge profile of pure graphite sample. The first discharge and charge capacities of pure graphite are 370 mAh/g and 175 mAh/g respectively causing an irreversible capacity of 195 mAh/g. The first discharge (Li insertion) and charge capacities (Li deinsertion) of Si 1 wt% sample have been estimated as 1200 and 700 mAh/g respectively amounting to the irreversible capacity of about 500 mAh/g. However, the first discharge and charge capacities estimated for Si 15 wt% are 835 and 482 mAh/g resulting to irreversible capacity of about 353 mAh/g (Fig.5.14.b &c). The charge profiles of Si-mixed graphite are quite different from pure graphite. The additional voltage plateau can be seen for both Si-1wt% and 15-wt% mixed graphite which, is not present in charge profile of pure graphite indicating the new reaction (insertion of Li into silicon) takes place. It has been reported that in pure Si based anode materials, during the alloying reaction the initial reaction resistance decreases, since Li-Si alloys have higher electronic conductivity than that of pure Si. During de-alloying, process the resistance increases since volume contraction takes place giving less effective electronic contact between particles with increase in contact resistance and charge transfer resistance. As a result, complete de-alloying reaction cannot take place [Kasavajjula et al., 2007, Liu et al., 2005]. This may be one of the reasons for large irreversible capacity in first cycle; however the irreversible capacity is lesser in the present case in comparison to others, as reported earlier for different C/Si composite anode materials [Kasavajjula et al., 2007]. The larger irreversible capacity in first cycle is also due to SEI formation, irreversible Li^+ trapping and loss of active material. The first discharge capacity for graphite- Si 15 wt % is lower than that of Si 1 wt % anode and this decreased discharge capacity is attributed to the SiC phase present in the 15 wt% compositions. This phase (SiC) is electrochemically inactive and may act as buffering of Si for further alloying with Li in the matrix. Figure 5.15a shows the discharge profile from 2nd to 5th cycle of Si 1 wt% composition. The 2nd discharge cycle has a lower voltage plateau in comparison to that of the first discharge cycle. However, the discharge profiles of 2nd to 5th cycles are more flat than that of first discharge cycle. It can be seen that the SEI formation is not observed from 2nd cycle and higher. Similar results have also been found for the Si 15 wt % composition.

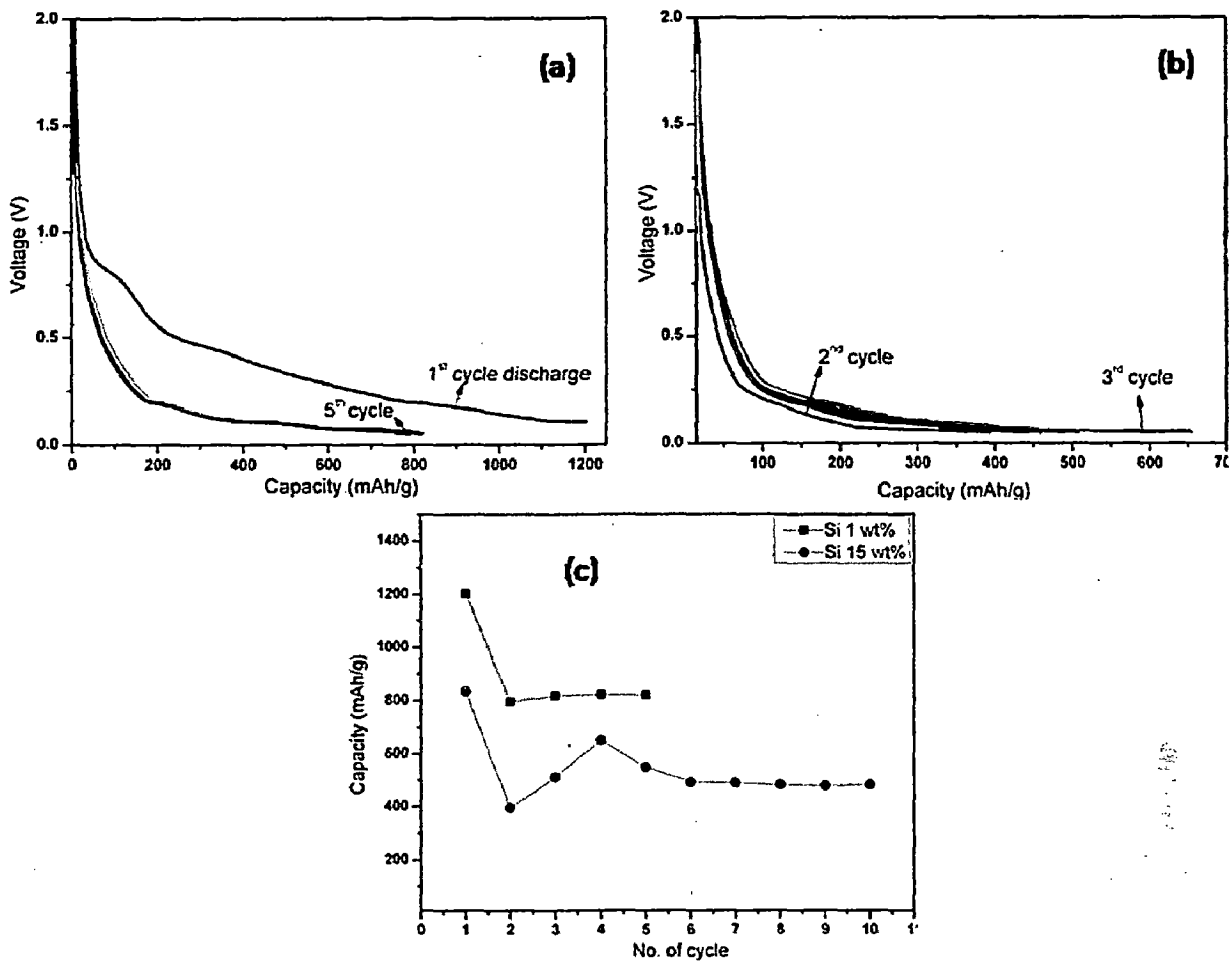

Figure 5.15: Discharge profile of (a) for Si-1 wt% (b) Si 15 % and (c) cycling behavior of both compositions.

Figure 5.15 c. shows that the cycle behavior of ball milled and heat-treated samples (1 and 15 wt% Si compositions). For Si 1 wt% sample the discharge capacity becomes almost constant from 2nd cycle onwards. The discharge profiles are overlapping and hence not visible clearly. The anodes prepared by powder of Si 1 and 15-wt % show first cycle columbic efficiency of 58 and 57 % respectively. The columbic efficiency of Si 1 wt% sample increases from 58 to 97% for 2nd cycle and become almost constant in subsequent cycles. The anode prepared with Si 15 wt% shows a fluctuation in discharge capacity upto 4th cycle initially and then it becomes constant (to about 83%) after 4th cycle and which remains nearly same for subsequent cycles as shown in Fig.5.15b. These results show that the Si is distributed homogeneously in graphite for Si 1 wt % as the large amount of graphite is helping in making larger electronic contact and hence reducing charge transfer resistance resulting

better capacity and capacity retention [Kasavajjula et al., 2007]. However, the larger irreversible capacity for this composition is due to larger amount of SEI formation. The amount of graphite is higher in this case. The anode made with Si 15-wt% shows the presence of unwanted phase (SiC) which acts as buffer (electrochemically inactive phase) and increases charge transfer resistance and hence all the Si is not taking part in Li-insertion and di-nsertion. This may be the reason of lower first discharge capacity and capacity retention of anode prepared with this composition. The EDX mapping of Si-15 wt% shows the clustering of Si-rich phase (SiC) may be the reason of lower capacity of this materials. The Li-ion cell that have used in present study is Teflon based cell however the real lithium ion cells are essentially constant volume devices which have non-compressible components. Such environments may show quite different behavior and the cycling behavior may improve when using silicon-based anode.

5.4 SUMMARY

In this chapter, two different carbon based host materials containing heteroatoms B and Si have been discussed as anode in lithium ion cell. Graphite and boron doped graphites having different compositions have been synthesized and analyzed. In this study elemental form of boron has been used as the source of boron doping, however other researchers used boron compounds for the source of boron. The benefit of using elemental boron is to synthesize boron doped graphite powder free from any impurities namely oxygen and hydrogen which affect the electrochemical behavior of the cell. The XRDs and Raman spectra confirm the doping of boron in graphite plane. The reversible capacity of boron doped samples increases with increasing boron content. Higher reversible capacity and coulombic efficiency (98%) have been observed for the samples as compared to other materials reported in literature. The cell capacity has been found to occur below 0.2 V with a flat discharge profile in all boron doped samples. However most of the cell capacity has been observed by Way and Dahn (1994) at higher voltage with slopping voltage profiles. The increased reversible capacity, flat discharge profile and higher coulombic efficiency of these materials make them promising candidates as anode in lithium ion rechargeable battery compared to coventional graphite. The boron doped graphite based anode materials have been synthesized by CVD method.

The four different compositions of graphite-Si system have been prepared by milling in planetary ball mill (in liquid medium) and heat-treated at 1200° C. In order to overcome the problem of capacity fading in Si/C based anode materials a new approach has been adopted in the present study. The Si and graphite powders have been milled in liquid medium and the dry mixture was heat treated at 1200 °C, for uniform distribution of Si in graphite matrix. However, various methods such as pyrolysis reactions, ball-milling (without heat treatment), coating of Si and chemical reaction of gels have been reported by various researchers. The EDX mapping technique that confirms the uniform distribution of Si in graphite matrix, is rarely reported elsewhere in the literature. The XRD and Raman spectra show that the increasing Si content favors disorder in graphite structure as indicated by increasing FWHM and decreasing intensity of (002) x-ray peak (and increasing D-band in Raman spectra. The Raman spectra of two compositions 1 and 15-wt% of Si show that I_D/I_G ratio and FWHM of G-band increase with increasing Si content. These results also confirm that presence of Si increases disorder in the graphite structure. Therefore, the results of Raman spectra and of XRD analysis are consistent. The performance of these two compositions as anode for Li ion cell shows that Si 1 wt % gives rise to the higher first discharge capacity, higher coulombic efficiency and capacity retention compared to the Si 15 wt %. The reversible capacity and coulombic efficiency obtained with the composition Si 1-wt% in the present study is higher compared to Si/C based anode material synthesis by different process. This improvement is related to the uniform distribution of Si in graphite, which is confirmed by EDX mapping indicating that the synthesis process used in present study is very useful for synthesis Si/C based anode materials. Only two extreme compositions have been tested as anodes in lithium ion cell because of the restricted availability of electrochemical analyzer.

BALL-MILLED GRAPHITE AS ANODE MATERIALS FOR LITHIUM ION BATTERY

6.1. INTRODUCTION

To improve the stochiometric limit of Li-ion intercalation into graphite (LiC_6) of 372 mAh/g of C_6 motivates the development of higher capacity anode materials [Idota et al., 1997 and Dahn et al., 1995], therefore attention has-been focused on disordered carbon materials. These materials could store lithium in larger quantity and have discharge capacities surpassing the theoretical capacity of the graphite based anode [Sato et al., 1994 and Yata et al., 1994]. Researchers showed that the disordered carbon materials might store lithium by a different mechanism than that is usually applied for intercalation into graphite. The reason for this difference is because of their special structure (small crystallite size and random crystallite orientation). Detail of such mechanism is given in chapter 2 (Literature review). In this chapter, the results on ball-milled graphite for the use as anode materials for lithium ion battery are discussed. The graphite powder was milled in a planetary ball mill using liquid medium to produce small particles and larger amount of defects in graphite lattice. The milling favors the cleavage of the particles and the milling in presence of liquid offers lubrication, moderates the violence of the shocks and avoids large agglomeration of the particles. The effect of disorder of graphite has been related to charge capacity of milled powder. All the results are discussed in detail in this chapter.

The graphite powder was used as starting material and the milling was carried out using planetary ball mill (PM100, Retsch) in stainless grinding medium in presence of liquid phase (Methanol), which prevents any side reaction during milling. The milling operations were done for different time durations of 8, 16, 24, 32 and 80h. The grounded powders were characterized by XRD, TGA, Raman spectra, FE-SEM, TEM and electrochemical analysis.

6.2. XRD RESULTS

All the XRD patterns for pure graphite and the graphite ball-milled for different time periods are shown in Fig. 6.1. The graphite-stacked form is called hexagonal or 2H-graphite. Most of the peaks are indexed as the hexagonal (2H) graphite and are presented in XRD patterns as shown in Fig. 6.1. The Bragg peaks (002), (100), (101), (102), (004) and (103) are indexed to hexagonal graphite. The (002) peak is sharp, indicating a higher crystallinity of graphite. It has been observed that upon increasing the milling time relative intensity of the (002) graphite Bragg peak diminishes. The

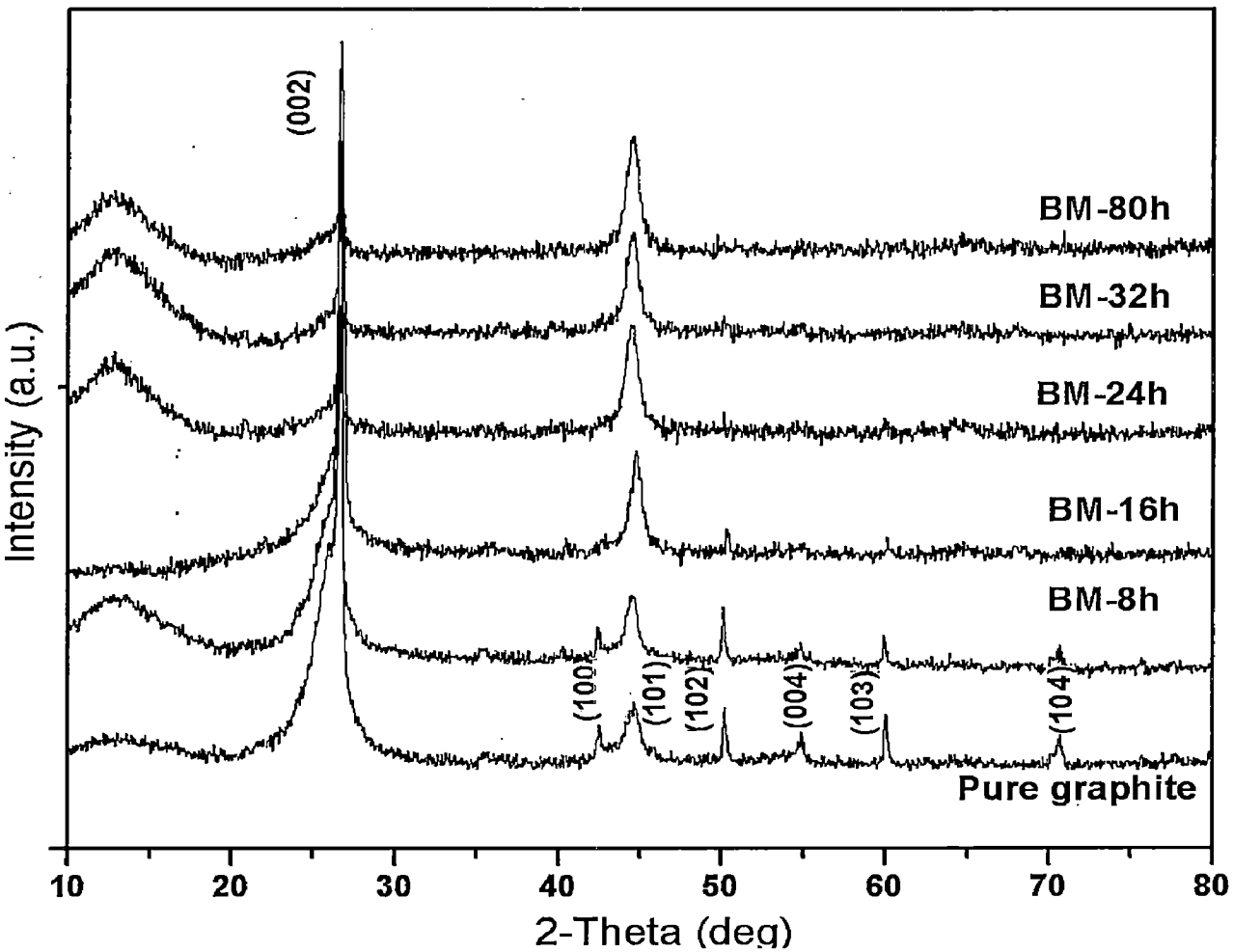

Figure 6.1: XRD pattern of ball-milled graphite for pure graphite and milled for different time 0h, 8h, 16h, 24h, 32h and 80 h.

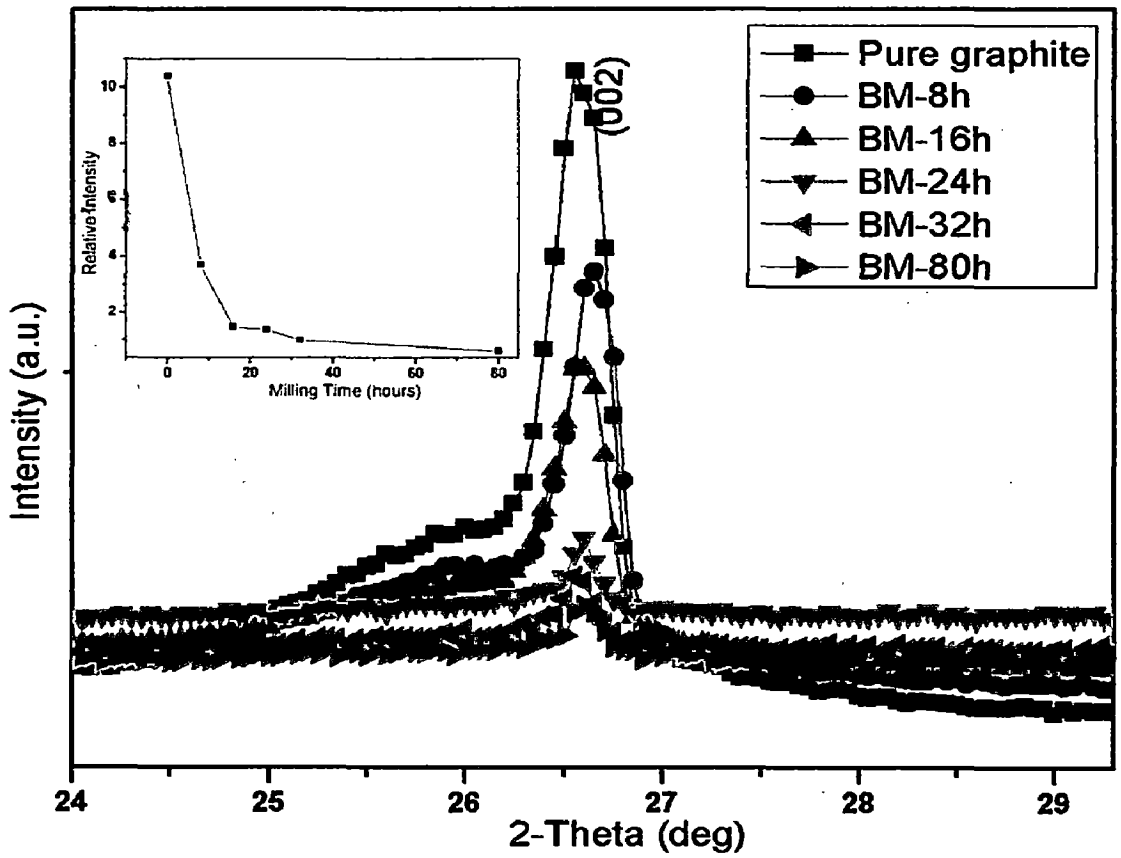

Figure 6.2: The effect of milling-time on (002) Bragg peak of graphite and inset showing the variation in intensity of same peak with milling time.

decrease in intensity of (002) Bragg peak with milling time is shown in Fig.6.2 (inset). The decrease in intensity of (002) peak implies that mechanical grinding generates an increasing amount of unorganized (disordered) carbon. The interlayer distance (d_{002}) does not change significantly even after 80 h of milling, similar results were observed by Disma et al. (1996). This phenomenon is most pronounced when powder is milled in a planetary ball-mill where the deformation forces are mainly shear in nature. In shear type of deformation, van der Waals layers shear easily without generating defects in covalently bonded basal planes. However, the intensity of (101) Bragg peak increases with milling time, which may be due to the presence of iron that increases with milling time as impurity induced by the milling tools (stainless steel). As the peak (110) position of iron is at the same angular position as that of the (101) peak for graphite. However, no other peaks for iron were observed. This is because the impurity is beyond the detectable limit of XRD. The sharpness of (002) Bragg peak indicate that the crystallinity of graphite is preserved even after 80 hours of milling. In this study,

graphite was mechanically milled in methanol. The oxygen, which is produced from air and methanol may suppresses the amorphization of powder and preserve the crystal structure of graphite during milling [Ong and Yang, 2000]. Even though the milled samples are still crystalline, they contain large amounts of defects. These interesting microstructural properties combined with a highly oxidized surface might offer enhanced lithium intercalation kinetics along with a highly favorable specific capacities and limited irreversible capacity. The XRD results of ball milled powder in liquid medium show that the medium prevents the amorphization as well as agglomeration of powder even after longer milling time.

6.3. MICROSTRUCTURAL STUDIES

6.3.1. FE-SEM Results

Figure 6.3 shows the FE-SEM micrographs for ungrounded and grounded graphite powder produced by milling in liquid medium. The ungrounded graphite particles have diameters ranging from 2-10 μm and the shape of particles is flat

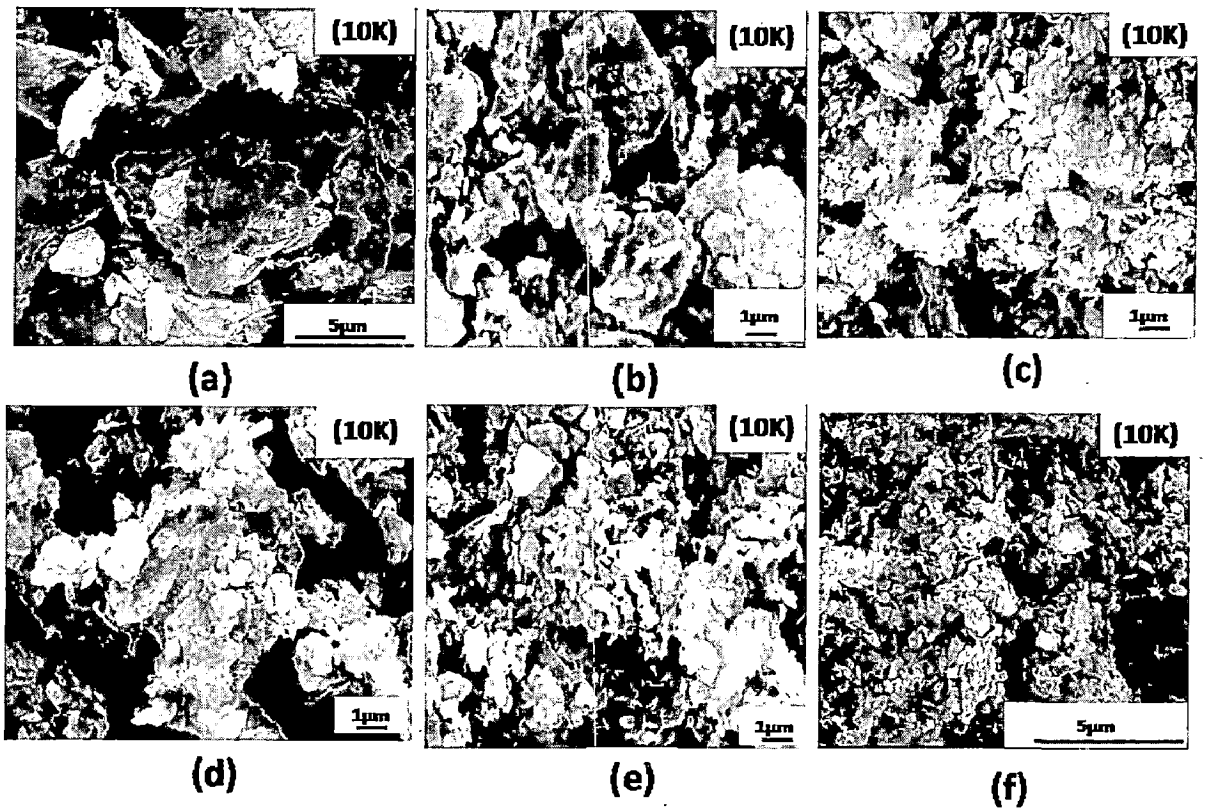

Figure 6.3: FE-SEM micrographs of ball-milled graphite for different time period of (a) 0 h (b) 8 h (c) 16 h (d) 24h (e) 32 h and (f) 80 h.

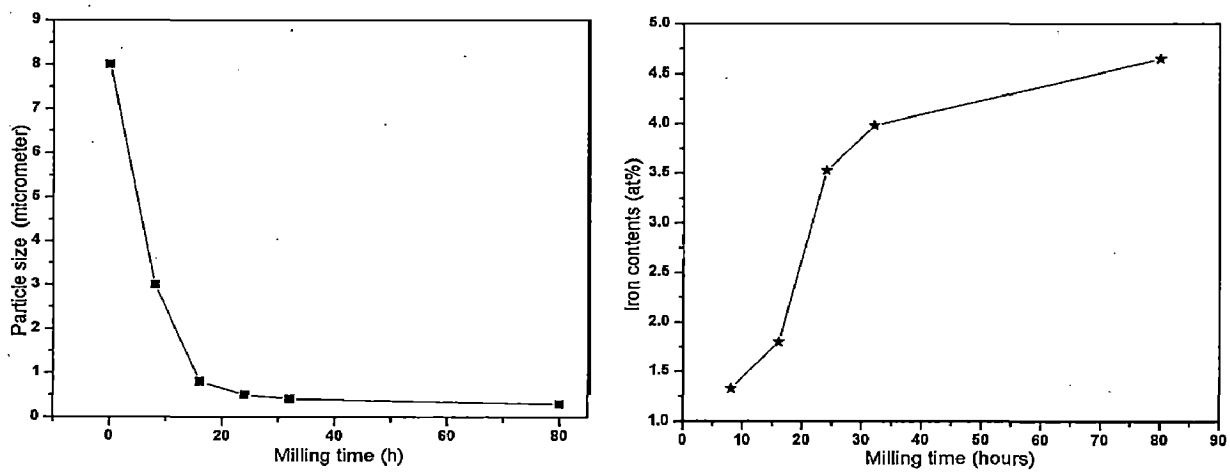

Figure 6.4: (a) Variation of particle size with milling time and (b) Increase of iron content with milling time.

lamellar and in the form of stacked layers (Fig 6.3a). After 8 hours of milling, the sharp edges of particle become rounded. It has been reported that spherical shaped particles, which were resulted in after 80 hours of milling, improves the electrode performance [Nishi et al., 1998]. The effects of milling on morphology of grounded powder for different time periods are shown in Fig 6.3 (b, c, d, e & f). The particle size decreases with milling time and the average particle size becomes 0.2 μm after 80 hours of milling. The continuous decrease of particle size with milling time is shown in Fig. 6.4a. It is observed that as the milling time increases the agglomeration of particles increases. Moreover, it is noted from FE-SEM micrographs that the agglomeration occurs on the basal plane surface as well as on the edges. The reduction in grain size and agglomeration of powder governed by two opposite phenomena during the milling process. On one hand, the particles split as a results of the internal strain created by high pressure applied to the grains and on the other hand, the highly divided particles tend to agglomerate due to high reactivity of their new surfaces, in order to minimize the surface energy. A longer milling is necessary to obtain smaller grain size or to make graphite more disordered in order to improve the charge capacity. However, the disadvantage of longer milling time is that it enhances pollution in the materials by iron metal, which adds due to abrasion of the milling tools i.e. stainless steel balls and vial used. Fig.6.4b shows that the iron content increases with milling duration. The iron content was 1.2 at % for 8 hours of milling and enhanced up to 4.5 at% after 80 hours of milling. The iron is electrochemically inactive in the voltage range in which carbon

based materials operate for charge/discharge and does not affect the electrochemical behavior of the cell.

6.3.2. TEM Results

The Fig. 6.5 shows the TEM micrographs and selected area diffraction pattern of graphite powders milled for 80 hours. The micrographs show that the particles have lamellar morphology. The agglomeration of particles in some region is also evident from the TEM image and the similar feature has been noticed in the FE-SEM micrograph of the powders milled for 80 hours (Fig. 6.5d). The Fig. 6.5d also shows an agglomerate of size about 50 nm. Pores with different sizes and curved surfaces can also be observed in agglomerate revealing the porous structure. The formation of turbostratic structure suggests fracturing of hexagonal structure of graphite into small basal planes initially. Further milling leads to breaking down the graphene layers, and eventually transforming to nano size particles. The disordered and nanoporous carbon powders produced by ball milling of graphite as shown in the TEM images provide preferable sites for lithium insertion and thereby enhancing the charge capacity of carbonaceous material when used as anode in lithium ion battery. The selected area diffraction pattern for graphite powder milled for 80 hours is shown in Fig. 6.5b. The electron diffraction pattern of nanocrystalline structure may usually exhibit more than two different diffraction rings that belong to different crystal plane (002) and (101), while that for an amorphous structure usually shows broad halo rings. Thus, the rings shown in diffraction pattern in Fig.6.5b shows that the sample is polycrystalline, which are made up of many tiny single nanocrystals. The continuous ring is formed by superposition of single crystal spot pattern. A series of concentric rings resulting from many spots, which are very close together at various rotations around the central beam spot.

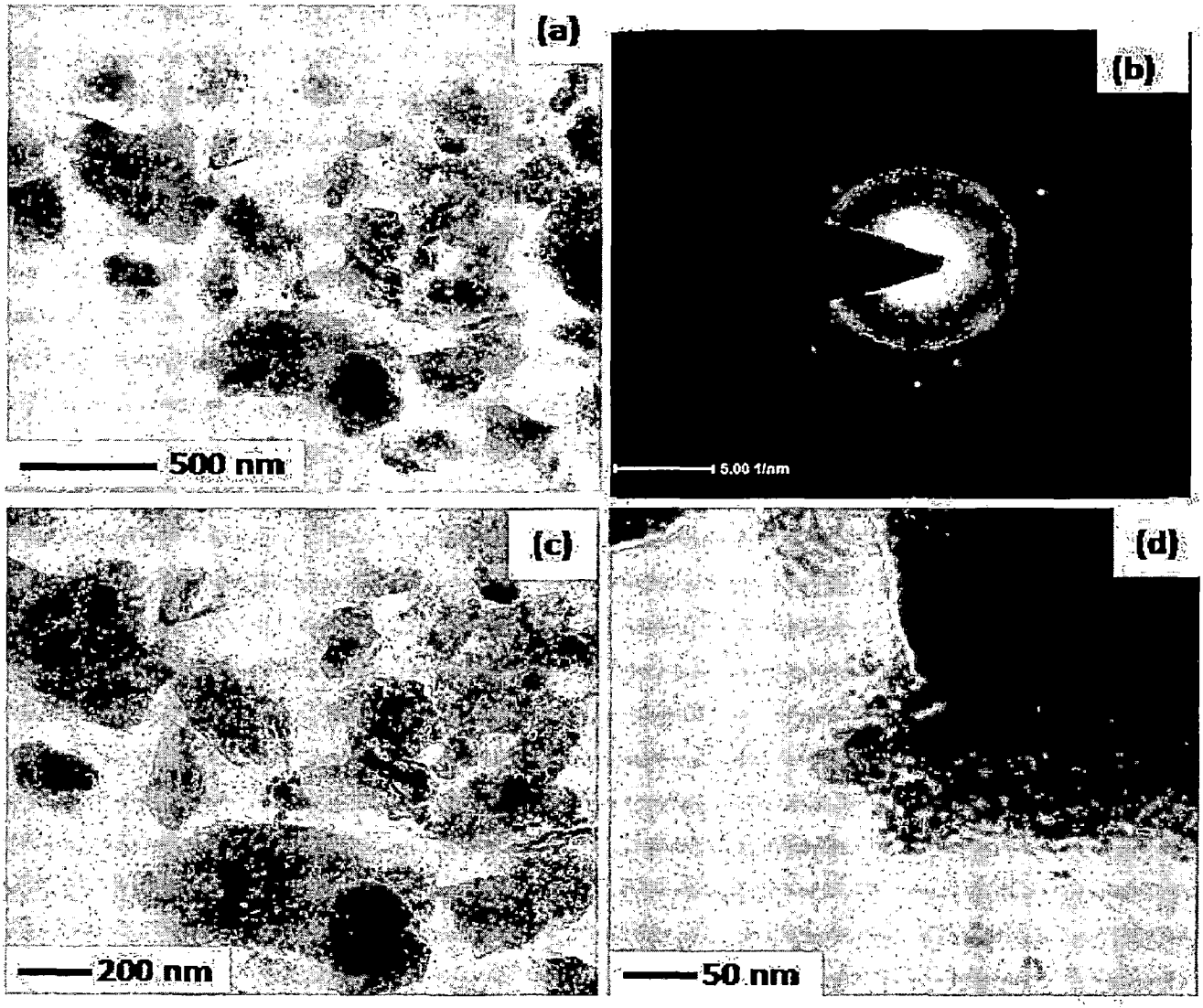

Figure 6.5: TEM micrograph of ball milled graphite for 80-hours (a) plates like structure (b) SAD pattern (C) morphology at higher magnification (d) agglomeration of milled powder.

6.4. THERMAL ANALYSIS

Figure 6.6 shows a typical TGA thermogram of weight loss as a function of temperature for milled and unmilled graphite in nitrogen atmosphere. The TGA data of the unmilled graphite shows no weight loss up to 1000 °C, after which a sharp weight loss is observed up to 1400 °C, which translates into an overall weight loss of about 10%. However, the graphite powder ball-milled for 24, 32 and 80 hours show sharp weight loss compared to unmilled graphite powder.

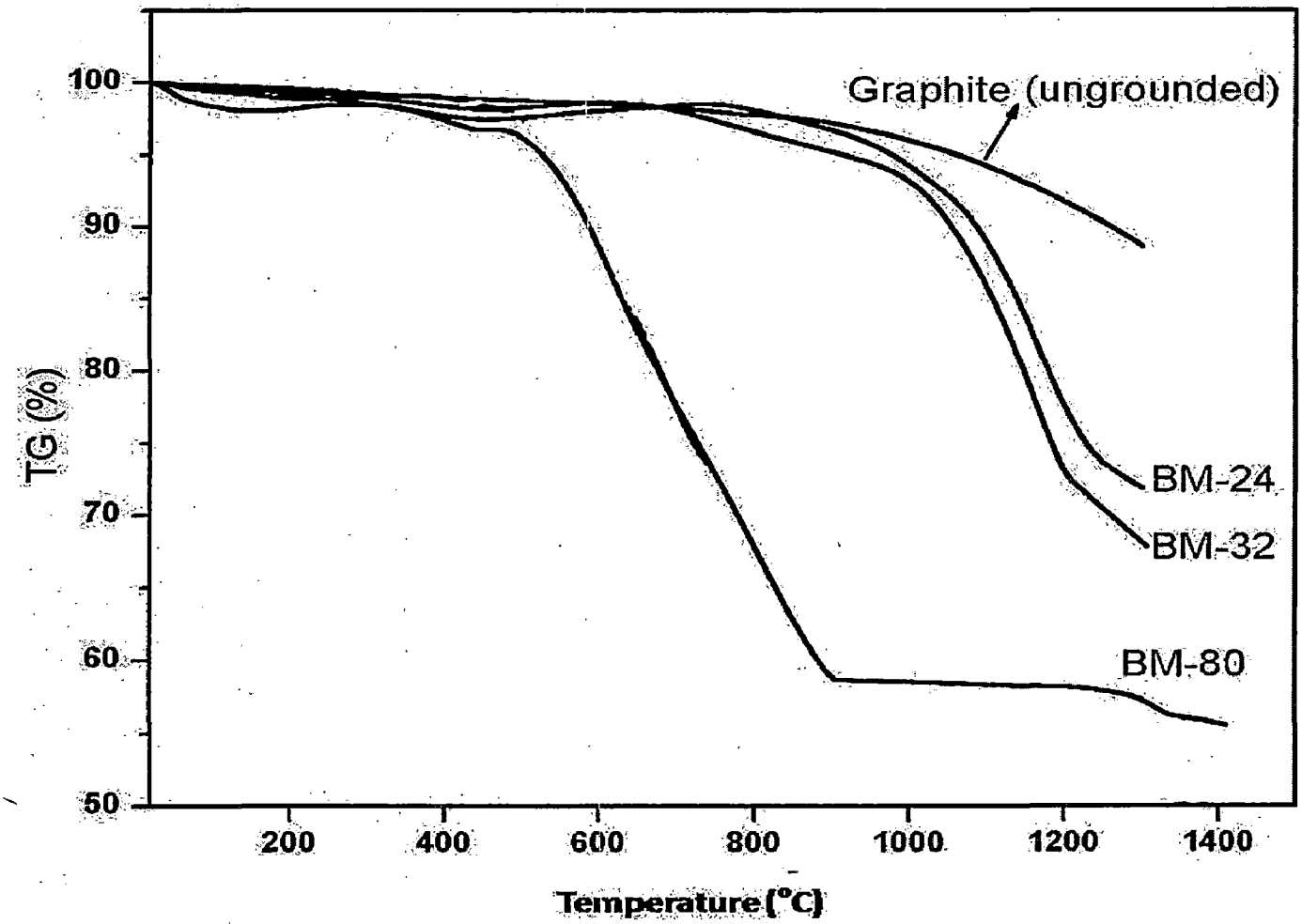

Figure 6.6: TGA analysis of unmilled and ball-milled graphite powders in liquid medium for different time periods in planetary ball-mill.

The overall weight losses due to heating up to 1400 °C are about 30, 37 and 55 % for the powders milled for 24, 32 and 80 hours respectively. The weight loss for the powders milled for 80 hours starts at about 500 °C, which shows that thermal stabilities of milled graphite powder decreases with milling time. Decomposition temperature reflects the reactivity of samples [Mathur et al., 2007 and Welham et al., 2003], the more reactive part in milled graphite powder will decompose at lower temperature and convert into carbonaceous gases. The reactivity of milled graphite powder gradually increases with increase in milling time. The weight loss in milled graphite powder below 600 °C is related to the gas emission of liquid (methanol) used as milling medium. The TGA curves confirm that the decomposition temperature decreases drastically with decrease in average particle size. Based on FE-SEM micrographs, it is

mentioned that the average particle size decreases with prolonged milling time and Raman spectra, which are discussed in next section show that the defects increase in graphite structure with increase in milling time. More the defects present at edge of basal plane more are the number of atoms containing unpaired *s* electrons. Hence, the carbon edge atoms are more reactive sites, those increases with milling time due to the formation of defects. The decrease in particle size and increased defects of milled powder reduce the decomposition temperature and hence larger mass loss has been observed for prolonged milling.

6.5. RAMAN SPECTRA

The first order Raman spectra of pure graphite, graphite ball-milled in liquid medium (methanol) for 32 and 80 hours are shown in Fig. 6.7 (a, b & c). The spectral parameters after Lorentzian fitting are tabulated in Table 6.1. The spectra were recorded in selected wave numbers ranging between 1000 and 2000 cm^{-1}. The peaks in Raman spectra were analyzed by fitting the line shapes with Lorentzian function and hence calculations of the peak integral and FWHM were done. Both experimental and fitted data are plotted as shown in Raman spectra (Fig.6.7). All the spectra show the two different bands named as G and D-bands as shown in Fig 6.7. Group theory predicts the four different modes ($2B_{2g}$, $2E_{2g}$, A_{2u} and E_{1u}) of vibration for hexagonal graphite. The A_{2u} and E_{1u} represent the translations of plane and the B_{1g} mode is an optical phonon where the carbon atoms move perpendicular to the graphene planes. Finally, E_{2g} is doubly degenerate in plane optical vibration. Only the E_{2g} represent the Raman active mode in graphite and the band at 1580 cm^{-1} has been assigned to the in-plane E_{2g} mode [Tuinstra and Koenig, 1970]. The G-band in Raman spectra at 1580 cm^{-1} is present in all types of the graphite samples. A slight frequency shift toward higher wave number was found in some samples with different crystal size. The G-band for unmilled graphite lies at about 1578 cm^{-1}, which shifts towards higher wave numbers of 1584 and 1589 cm^{-1} for the graphites milled for 32 and 80 hours respectively

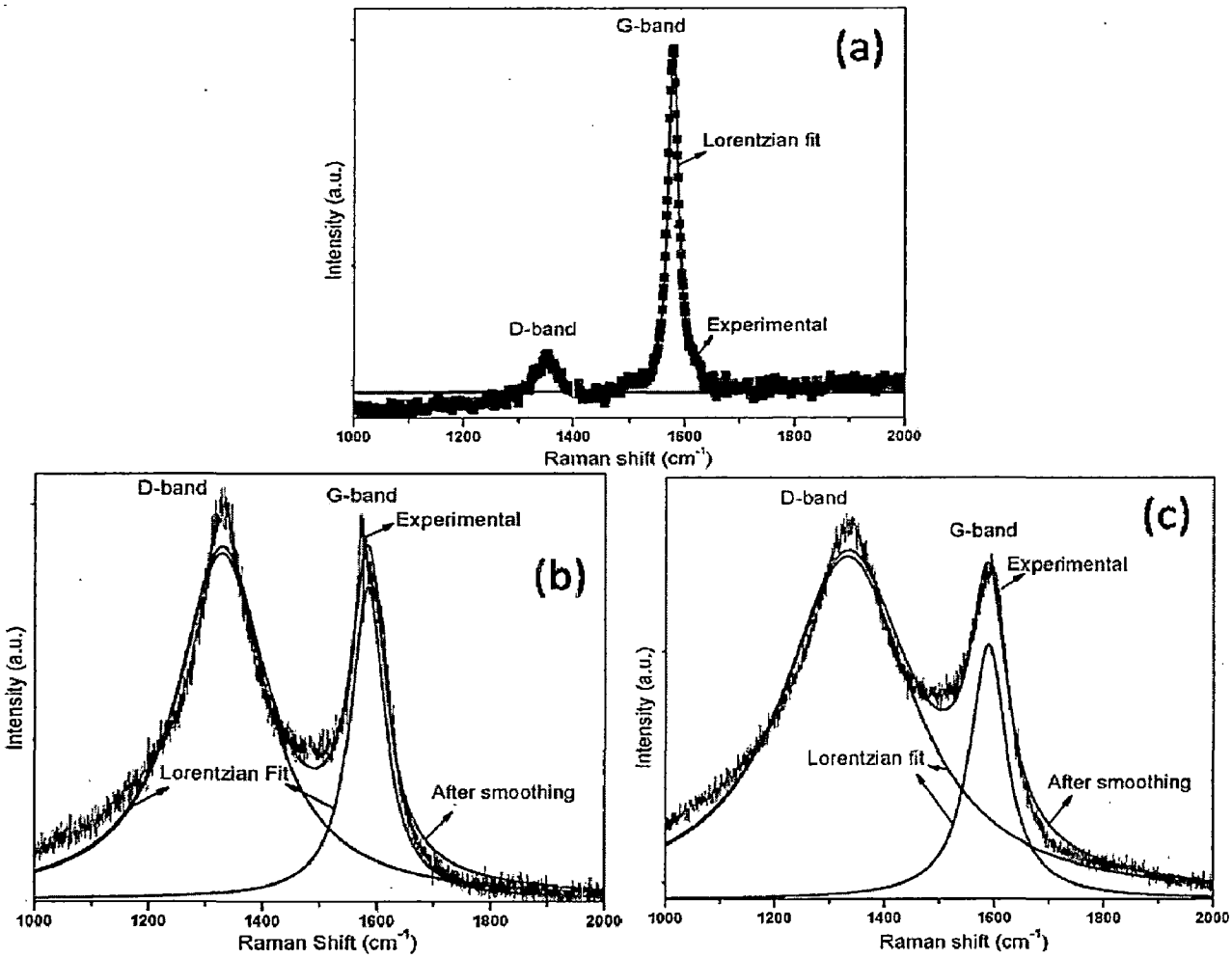

Figure 6.7: Raman spectra of (a) unmilled graphite powder (b) milled graphite powder for 32 hours and (c) milled graphite powder for 80 hours.

The D-band (1350 cm^{-1}) has been attributed to an in-plane A_{1g} zone-edge mode, which is silent for infinite layer dimension but becomes active for small and imperfect layers. The exact origin of this band is not clear but theoretical calculations [Nemanich and solin, 1977] indicate that this line arise from graphite containing disorganized regions near crystal edges and lattice defects such as edge dislocations, lattice vacancies [Tuinstra and Koenig, 1970] and interstitial carbon atoms between basal planes carbon atoms. The Raman spectra of unmilled graphite show a sharp band at about 1578 cm^{-1} (G-band) and other corresponding to D-band at about 1351 cm^{-1}. The intensity of G-band for the graphite milled for 32 and 80 hours decreases with the increase in milling time and become broader compared to the unmilled graphite.

Table 6.1. Raman spectroscopic parameters obtained after curve fitting experimental spectra using Lorentzian bands (G, D)

Sample		Peak centre (cm^{-1})	FWHM (cm^{-1})	$R=I_D/I_G$
Pure graphite	**(G-band)**	1578	23.17	0.13
	(D-band)	1351	27.62	
BM-32	**(G-band)**	1584	70	2.87
	(D-band)	1328	180	
BM-80	**(G-band)**	1589	82	4.75
	(D-band)	1332	282	

The ratio ($R=I_D/I_G$) of Raman intensity of D-band peak to G-band peak is inversely proportional to the mean crystallite size in graphite plane. The R-value as can be seen in table for unmilled graphite and graphite milled for 32 and 80 hours are 0.13, 2.87 and 4.75 respectively. The increase in R-value with milling time is indication of increased amount of disorganized region near crystal edges and the presence of the lattice defects [Shen et al., 1996] created by the ball milling. The lattice defects mainly lattice vacancies introduced due to mechanical milling and their increase with milling time is obvious from Fig 6.7. These results are consistent with thermal analysis (TGA) results discussed in section 6.4, which shows that decomposition temperature reduces with the increase in milling time as more defects are introduced with higher milling time.

6.6. ELECTRCHEMICAL MEASUREMENTS

The electrochemical measurements were carried out by using a Teflon based test cell, which was assembled inside a glove box containing Ar gas atmosphere. The working electrodes were prepared by similar way as discussed in earlier chapters. The cell was tested at 20 °C by using computer-controlled cycler (Arbin BT 200) at constant current of 100 μA in a voltage range 0.05 and 2.5 V

Figure 6.8 (a, b, c & d) shows the first discharge (lithium insertion) and charge profiles of graphite powders unmilled in one case and in another case milled for 24, 32 and 80 hours respectively. Several changes can be observed depending on the milling schedule of graphite powder. The potential profile of the milled graphite powder differs

significantly from that of unmilled graphite. A flat potential profile has been observed for unmilled graphite, however, the profiles are found to have slope for milled graphite. The curves slope without any very distinct plateaus in the discharge profile of milled graphite powder. However, in case of unmilled graphite distinguishable plateaus can be observed at two different potentials (Fig. 6.8a). This behavior is the consequence of the disorderness in the structure that forms in the graphite due to the milling. The disordered structure of milled graphite powder confirmed by XRD and Raman spectroscopy studies provides electronically and geometrically nonequivalent sites for lithium intercalation.

Table 6.2. First discharge, charge and irreversible capacity of unmilled and milled graphite powders for 24, 32 and 80 hours.

Sample	**First Discharge capacity (mAh/g)**	**First charge capacity (mAh/g)**	**Irreversible capacity (mAh/g)**
Un-milled graphite	290	155	135
BM-24	450	310	140
BM-32	510	360	150
BM-80	935	425	510

The charge capacity, discharge capacity and irreversible capacity for first cycle of anode made of both unmilled and milled powder are tabulated in Table 6.2. The reversible capacity is defined as the lithium ion deintercalation capacity and the irreversible capacity is defined as the difference between Li intercalation and deintercalation capacity. The lithium intercalation capacity increases with milling time as can be seen in Fig. 6.8 and table 6.2.

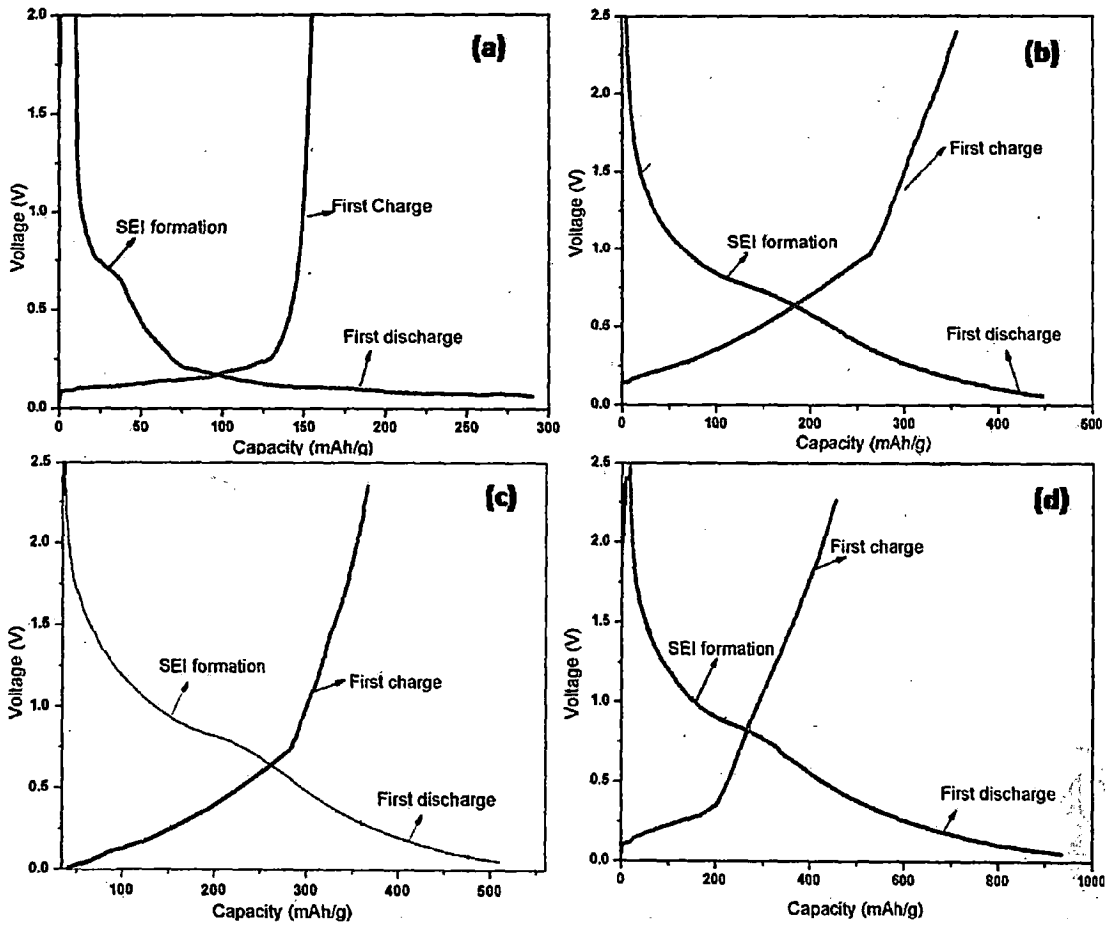

Figure 6.8: First charge and discharge capacity of (a) unmilled graphite and graphite milled in liquid medium using planetary ball-mill for (b) 24 hours (c) 32 hours (d) 80 hours.

The lithium intercalation capacity for unmilled graphite is about 290 mAh/g (corresponding 0.78 Li for 6 C), however theoretically graphite can intercalate one lithium for six carbon atoms (LiC_6) leading to a capacity of 372 mAh/g at a potential less than 0.5 V vs Li metal. This capacity is comparable with 300 mAh/g as observed by Wang et al. (1998). The first discharge capacity enhances with milling time and become 450 ($Li_{1.2}C_6$), 510 ($Li_{1.37}C_6$) and 935 ($Li_{2.52}C_6$) mAh/g for powders milled for 24, 32 and 80 hours respectively. Both reversible and irreversible capacities increase with the milling time. The reversible capacity reaches up to 425 mAh/g, which is corresponding to 1.14 Li for 6 C. The irreversible capacity during the first cycle also increases with the increase in milling time as shown in table 6.2. For higher milling time of 80 hours a large hysteresis between discharge and charge develops. The irreversible capacity increases and becomes 510 mAh/g for 80 hours of milling. However, Wang et al. [Wang et al., 1998] has observed the irreversible capacity upto

580 mAh/g for 150 hours ball-milled graphite. The increase in irreversible capacity is related to solid electrolyte interface (SEI) formation during first cycle. The lithium intercalated graphite is highly reactive which reacts with the electrolyte solution. The byproduct of the electrolyte decomposition forms a solid film on surface of electrode that occurs at 0.8 V vs Li [Naji et al., 1996]. The results are similar as reported in literature [Dishma et al., 1996]. It is believed that, a large amount of lithium is consumed in the formation of SEI on the electrode surface and contributing in irreversible capacity. The decomposition of electrolyte and formation of SEI is proportional to surface area of powder, which increases with milling time. The increase in irreversible capacity also could be due to a decrease in the electronic conductivity of electrode materials caused by grinding process as the porosity increases with milling time. The capacity of anode made of ball-milled graphite improves compared to unmilled graphite as shown in table 6.2. Due to the milling, the particle size of powder decreases, voids, and micro cavities are formed, which act as Li trapping sites in the powder. Lithium ions are doped into vacancies and microcavities [Mabuchi et al., 1995, Tokumitsu et al., 1996] or at the edge of defected edge sites [Xiang et al., 1997]. This is the reason for higher charge capacity of anode made of ball-milled graphite powder.

The cycle life of anode made of unmilled graphite and graphite milled for 24, 32 and 80 hours are shown in Fig.6.9. The discharge curves of cell using anode of unmilled graphite powder were studied up to 8th cycle whereas the cell made with milled graphite powder was tested up to 11th cycle. From the Fig. 6.9, it can be seen that the rate of capacity fading increases with milling time. Fig. 6.9a shows the discharge curves of unmilled graphite, which are all flat and have low capacity fading. However, the capacity fading increases with the increase in the milling time as can be seen in Fig. 6.9 (b, c & d). The capacity fading is maximum in the case of graphite milled for 80 hours. This capacity loss is mainly due to the SEI formation causing the consumption of large quantity of lithium [Zheng and Dahn, 1995]. The surface area of graphite powder milled for 80 hours is higher and hence more accessible for electrolyte decomposition leading to more irreversible capacity.

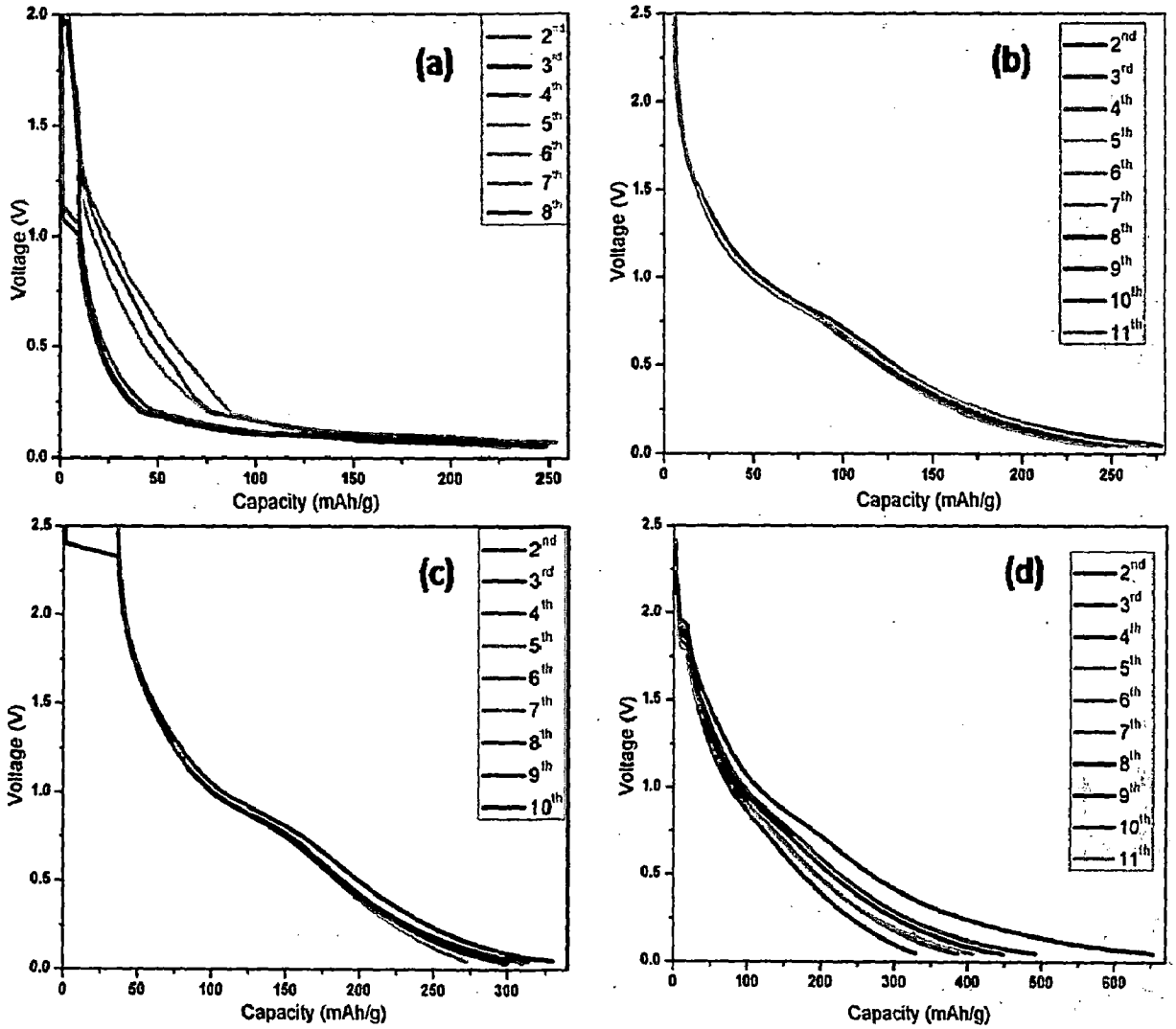

Figure 6.9: The discharge behavior from 2nd cycle onward of (a) milled graphite (b) 24 hours milled graphite (c) 32 hours milled graphite and(d) 80 hours milled graphite powder in liquid medium using planetary ball-mill.

The electrolyte decomposition is present throughout the entire cycle's process, however, this decomposition compared to the first cycle, is lower and at lower rate [Vetter et al., 2005]. There is a decrease of accessible active surface area of electrode for electrolyte decomposition with cycle number and hence fading in capacity with increase in cycle number is lesser. The results for powders milled for 24 and 32 hours are better in terms of capacity compared to pure graphite and less capacity fading compared to ball milled graphite powder for 80 hours.

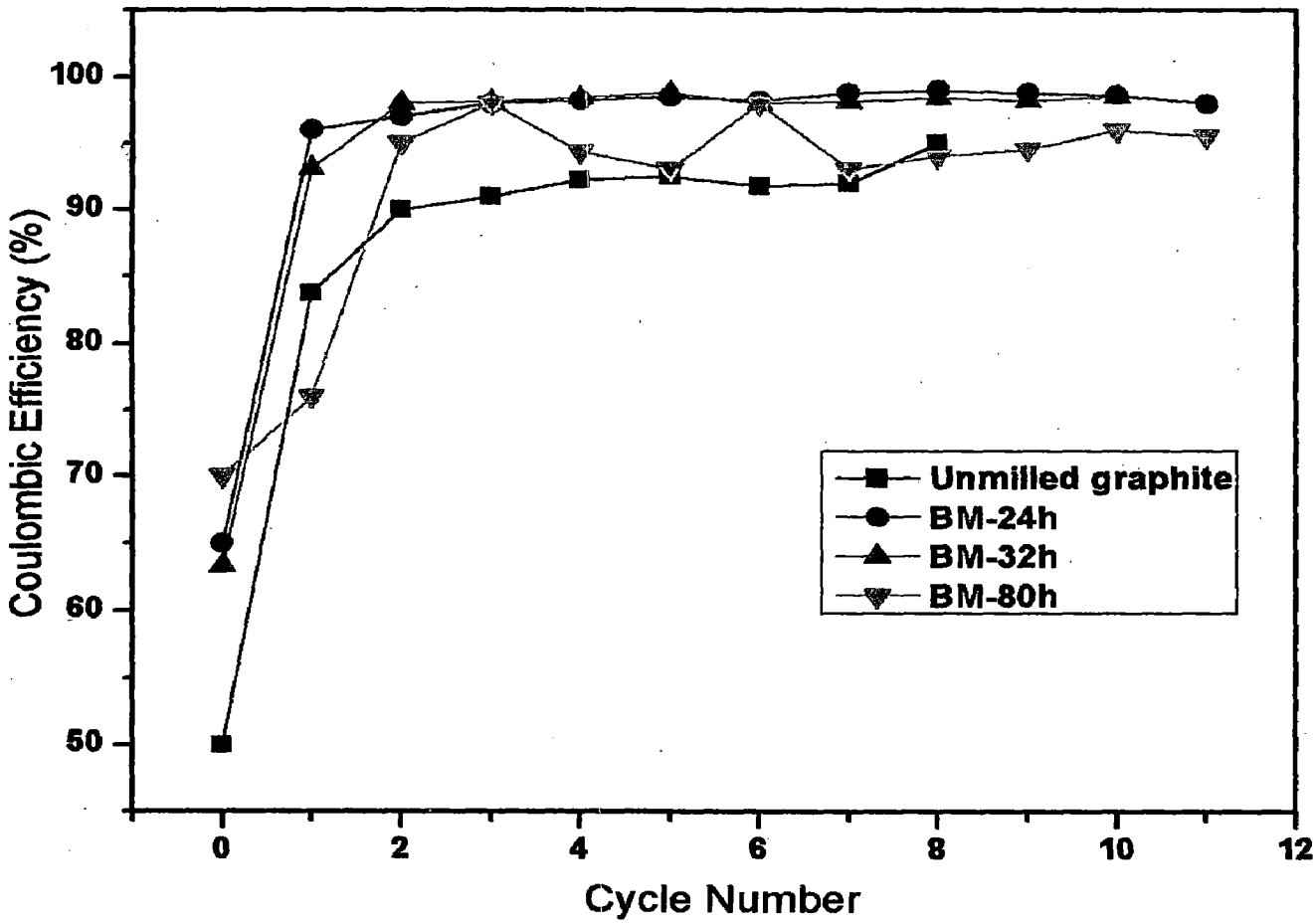

Figure 6.10: The coulombic efficiency of (a) milled graphite (b) 24 hours milled graphite (c) 32 hours milled graphite & (d) 80 hours milled graphite powder in liquid medium using planetary ball-mill.

Figure 6.10 shows the plot between coulombic efficiency vs. cycle numbers for unmilled and graphite powder milled for 24, 32 and 80 hours. The coulombic efficiency of cell is defined as the ratio of the number of charges that enter the battery during charging to the number that can be extracted from the battery during discharging. The losses that reduce coulombic efficiency are primarily due to the loss in charge due to unwanted secondary reactions. From the Fig. 6.10, it can be seen that the first cycle coulombic efficiency for pure graphite is 50 %, which enhances, in case of milled graphite powder, to and becomes 65, 63 and 70 % for powders milled for 24, 32 and 80 hours milled powder respectively. The efficiency improves in further cycles and become almost constant for unmilled graphite and the powder milled for 24, 32 and 80 hours. However, in case of powders milled for 80 hours the efficiency variation has been observed even after 10th cycle. The coulombic efficiency for graphite ball-milled for 24 and 32 h after first cycle are almost similar and higher (97 %) as compared to

that milled for 80 hours for which the efficiency is not uniform for all the cycles tested. These results indicate that for these powders, the amount of lithium inserting and deinserting is quite similar and hence the material is useful for battery cycle life.

6.7 SUMMARY

In this chapter, a systematic study has been made on the crystal structure and morphology of ball-milled graphites and their electrochemical performance during lithium insertion and de-insertion. Ball milling is not a new tool to improve the performance of anode materials of lithium battery, however a very few research reports are available about this aspect. In this study, an attempt has been made to improve anodic performance of milled graphite powder. Ball milling of graphite powder has been carried out in liquid (methanol) medium for different time periods in order to eliminate agglomeration and to avoid amorphization of the powders. The liquid medium for milling is also not reported in the literature. However, Janot and Guerard (2005) used water as liquid medium but in their study graphite and lithium were mixed together. The effect of milling time on structure and morphology of the milled powder has been observed. The thermal analysis shows the decrease in decomposition temperature, which is related to defects produce during the milling process and these results are consistent with Raman spectra of milled graphite powders. Such consistency are rarely reported in the literature. However, Welham et al. (2003) have shown the results having similar trends as obtained in the present study, although they have used different mill type. The EDX results show that impurity is induced by the balls and vial used for milling when the milling is conducted for a long time. The reversible capacity obtained up to 425 mAh/g is higher than that reported by Natarajan et al. (2001). This reversible capacity is lower than 700 mAh/g as reported by Wang et al. (1998), but their result shows that the capacity fades away to 37.8% of initial value after 20 cycles. However, in present study capacity remains almost at a constant level even after 11cycles. The higher discharge capacities obtained for milled graphite powder is related to lower particle size and defects introduced in the milling process. The capacity and coulombic efficiency (>90%) of powder milled for 24 and 30 hours are higher compared to for the powders milled up to 80 hours in the present study. The electrochemical results conclude that the powder milled for 24 and 32 hours are better-suited for anode materials in lithium ion cell compared to the powder milled for 80 hours in terms of cycle life. This result also implies the optimum milling time for

graphite powder. Thus, ball milling in liquid medium is useful tool for synthesis of carbonaceous anode materials of higher capacity.

CONCLUSIONS AND SUGGESTIONS FOR FUTURE WORK

The aim of present work is the synthesis and characterizations of different types of carbon based anode materials for application in lithium ion battery. Among the various anode materials available in the field of lithium ion batteries, the carbon-based materials are best suited for ideal battery system because of there high capacity and dimensional stability compared to other anode materials. In view of future requirements of energy storage, the anode materials having high-energy capacity and longer cycle life are required. With this perspective, attempts were made in the present work to increase the charge capacity of carbon-based materials. Detailed studies on the performance of various carbon based anode materials have been presented in chapters (Chapter 4, 5 and 6). The outcome of the entire study in the thesis is summarized in the following paragraphs. The following are the broad conclusions of the present study.

7.1 STUDIES ON THE CARBON NANOSTRUCTURES

1. The different novel catalysts particles synthesized by sol-gel process have size below 100 nm, hence suitable for use in the synthesis of carbon nanotubes.
2. The anodized alumina (AAO) prepared from pure aluminum by anodization in oxalic, H_2SO_4 and H_3PO_4 acid electrolyte baths, has been used as substrate for the synthesis of carbon nanostructures. The pore diameter of AAO ranges between 20 and 100 nm depending on the type of electrolyte bath used. The ordering of pores in AAO has also been demonstrated by FFT patterns of the surface.
3. The effect of decomposition temperature on structure of the CNTs shows that CNTs grown using novel catalysts at 650 °C have lower defect concentration and higher crystallinity compared to the CNTs grown at 580 °C as depicted by Raman spectra and XRD results.

4. The present study shows that CNTs can be grown on lithium based compound oxide catalysts, which are different from transition metals and their alloys based conventional catalysts.
5. Different morphologies of carbon nanostructures are found to develop by using different novel catalysts. The coiled and straight CNTs are synthesized using $LiNi_{0.5}Co_{0.5}O_2$ catalyst, carbon nanoribbons are grown using $LiFePO_4$ catalyst, wavy CNTs are the result of $LiCu_{0.5}Zn_{0.5}O$ catalyst use. Carbon particles joined together giving rise to a string like appearance is a result of using $LiMn_2O_4$ catalyst.
6. The most of the CNTs synthesized with $LiNi_{0.5}Co_{0.5}O_2$ catalyst are multiwall with outer diameter lying between 5 and 40 nm and length more than 5 μm.
7. The XRD results show that the interlayer spacing (d_{002}) of the MWCNTs is 3.42 Å which is 2.1 % larger than that of graphite and is marginally higher than that of MWCNTs (d_{002} = 3.40 Å) grown over other conventional catalysts. This confirms the effect of lithium based catalyst on synthesized CNTs.
8. First order Raman spectrum shows up-shift in G-band and a larger full width half maximum of the peak compared to those of graphite and MWCNTs synthesized by other (conventional) catalysts. The XRD and Raman spectra confirm the possibility of lithium insertion into CNTs during growth.
9. The first discharge capacity of CNTs grown with $LiNi_{0.5}Co_{0.5}O_2$ is 765 mAh/g, which is higher than that of CNTs grown over other (conventional) catalysts (Fe, Co, Ni etc). The electrochemical behavior of CNTs grown using this catalyst is for the first time reported in this thesis.
10. The reversible capacity of the MWCNTs grown with $LiNi_{0.5}Co_{0.5}O_2$ catalyst is 485 mAh/g, which is higher than the capacity of 100-400 mAh/g observed for MWCNTs grown over other (conventional) catalysts. This reveals the novelty of using lithium based catalyst compared to over other (conventional) catalysts.
11. The coulombic efficiency of the CNTs in the first cycle is about 65 % and from second to eleven cycles the efficiency remains constant at 96.6%, which is higher than the value reported in literature.

12. In the present thesis, it is demonstrated for the first time that carbon nanoribbons (CNRs) can be synthesized using $LiFePO_4$ as a catalyst by thermal CVD of acetylene at 650 °C.
13. The TEM and FESEM images show that CNRs have width of 50-80 nm and length more than 10μm.
14. The selected area diffraction (SAD) pattern and XRD results of the synthesized materials are consistent and indicate that CNRs are well graphitized.
15. Ratio of Raman peaks (I_D/I_G) calculated is 0.51 for CNRs, which is nearly the same as observed in the case of the pristine and heat-treated sample of CNTs.
16. The performance of the single cell using purified CNRs as the anode material has been studied and the reversible lithium intercalation capacity of the material is about 345 mAh/g,
17. A stabilized coulombic efficiency of 98% has been observed from the fifth cycle onwards. The efficiency is higher compared to other carbon nanostructures reported for the application in lithium ion batteries.

7.2 GRAPHITE MATERIALS WITH HETEROATOM (B, Si)

18. Boron doping in graphite has been done using a modified synthesis process in which elemental boron was used as the boron source. The XRD results of boron doped graphite samples show the increased crystalline size in terms of c and a lattice parameters, decrease in d-value of (002) plane and the presence of distinct (112) plane of graphite indicating that boron is doped sucessfully in graphite matrix.
19. The first order Raman spectra show the formation of new peak at about 1620 cm^{-1} in all the doped samples. The G-band (E_{2g2}) of the Raman spectra for graphite at 1578 cm^{-1} shifts to 1586 cm^{-1} due to boron doping. However the integrated intensity ratio *R* increases with increasing boron content, sugesting that boron is homogeneously distributed in graphene layers.
20. The reversible capacity of boron doped samples increases with increasing boron content. The Li-intercalation occurs at a higher voltage compared to pure graphite because boron acts as an electron acceptor in graphite lattice which results an increase in bond strength between host structure and lithium.

21. Higher reversible capacity of the boron doped samples has been observed as compared to reported in literature. Most of the cell capacity has been found below 0.2 V with a flat discharge profile in all boron doped samples.
22. The coulombic efficiency of all boron doped samples reaches up to 98% at 4th cycle which remains constant for other cycles studied. However the coulombic efficiency of pure graphite sample attains to about 92% after 2nd cycle.
23. In order to overcome the problem of capacity fading in Si/C based anode materials a new approach has been adopted in the present study. The graphite-Si powder mixtures have been milled in liquid medium followed by heat treatment at higher temperature for uniform distribution of Si in graphite matrix.
24. The XRD results show all characteristic peaks of graphite for all the compositions. The additional peaks of Si and SiC are appeared especially for the composition above 5wt% Si. Disorder in graphite structure increases with increase in Si content as indicated by the increase in FWHM and decrease in intensity of (002) peak in the XRD.
25. The results of the Raman spectra of the graphite and of 1 and 15 wt % Si mixed graphite are consistent with the XRD results of the materials. The upward shift in G-band of Raman spectra to the spectral position of 1582 and 1587 cm^{-1} are observed for Si-mixed samples.
26. The first discharge (Li insertion) and charge capacities (Li deinsertion) of Si 1 wt% sample are about 1200 and 700 mAh/g respectively amounting to the irreversible capacity of about 500 mAh/g. However, the first discharge and charge capacities estimated for Si 15 wt% are 835 and 482 mAh/g resulting to irreversible capacity of about 353 mAh/g.
27. The coulombic efficiency of Si 1 wt% sample increases from 58 to 97% in 2nd cycle and remains constant at about 97% for subsequent cycles. The anode prepared with Si 15 wt% shows a fluctuation in discharge capacity upto 4th cycle from beginning and then the capacity becomes constant (to about 83%) over the subsequent cycles starting at 4th cycle.
28. The anode of Si 15 wt % composition shows the lower discharge capacity which is perhaps due to the presence of unwanted phase (SiC) in the material. The SiC phase

acts as a buffer (electrochemically inactive phase) which increases resistance to charge transfer.

7.3 BALL-MILLED GRAPHITE AS ANODE MATERIALS FOR LITHIUM-ION BATTERY

29. The milling was done for different time periods (8, 16, 24, 32 and 80 hours). It is observed that upon increasing the milling time there is a decrease in relative intensity of the (002) graphite peak, which implies that mechanical grinding, generates an increasing amount of unorganized (disordered) carbon.
30. The thermal analysis shows the decrease in decomposition temperature of the milled powder, which implies that defects are produced during the milling process. The thermal analysis results are also consistent with Raman spectra of milled graphite powders.
31. Raman spectra of the milled graphite show that there is a decrease in intensity of G-band and increase of D-band intensity indicating disorder increases with milling.
32. Full width at half maximum (FWHM) of D-band in Raman spectra increases with increasing milling time showing the results of characterizations using Raman and XRD are consistent..
33. The microstructure and morphology of milled graphite powder analyzed by FE-SEM and TEM show the grain size of the powder decreases with milling time.
34. The electrochemical study shows that the powders undergone longer milling time have higher charge capacity. The first discharge capacity of unmilled graphite is about 280 mAh/g and increases to about 880 mAh/g for the powders milled for 80 hrs. The reversible capacity obtained up to 425 mAh/g, which is higher than reported in the literature.
35. The capacity and coulombic efficiency (>90%) of powder milled for 24 and 30 hours are higher than that of powder milled for 80 hours and of those reported in literature. Thus present study suggests an optimum time for milling.
36. The slope of discharge profile of the material increases with increasing milling time.

7.4 SUGGESTIONS FOR FUTURE WORK

1. The role of novel catalysts used in the present studies to synthesize different carbon nanostructures, by way of mechanism applicable, needs to be understood for having control on the morphology development in the carbon nanostructures.
2. Effect of chemical composition of catalyst on morphology of carbon nanostructures needs to be established.
3. In situ TEM studies can highlight the mechanism of the catalytic action of novel catalyst.
4. The different types of carbon nanostructures that have been investigated for the applications in lithium ion batteries may also be explored for other possible applications.
5. In the present study, only two types of carbon nanostructures have been demonstrated by studying their electrochemical characteristics. The electrochemical behavior of other carbon nanostructures developed needs to be studied in future.
6. The effect of the different carbon nanostructures synthesized on Raman spectra needs to be studied further to understand their structures in detail.
7. Si-graphite based anode materials have highest capacity among all known anode materials. However, these materials suffer from a problem of capacity fading. An attempt may be made to devise a novel processing route for the synthesis of such materials, which can eliminate the capacity fading problem.

REFERENCES

[1] Abraham KM and Alamgir M, Li^+-conductive solid polymer electrolytes with liquid-like conductivity, J. Electrochem. Soc., 136 (1990) 1657.

[2] Abraham KM and Alamgir M, Ambient temperature rechargeable polymer-electrolyte batteries, J. Power Source, 43 (1993) 195.

[3] Agarwal UP and Atalla RH, Raman Spectroscopy CRC Press, Inc.: Chapter 8 (1995) 152.

[4] Ajayan PM and Zhou OZ, Carbon Nanotubes, Topics Appl. Phys., Eds: M.S. Dresselhous, G. Dresselhous, Ph. Avouris, 80 (2001) 391.

[5] Ajayan PM and Ebbesen TW, Nanometer size tubes of carbon, Rep. Prog. Phys., 60 (2003) 1025.

[6] Alcuntara R, Jiminez-Mateos JM, Lavela P, Morales J, Tirado JL, Microstructure and intercalation properties of petrol cokes obtained at 1400 °C, Mater. Sci. Eng. B, 39 (1996) 216.

[7] Alvarez W, Kitiyana B, Borgna A and Resasco D, Synergism of Co and Mo in the catalytic production of single-wall carbon nanotubes by decomposition of CO, Carbon, 39 (2001) 547.

[8] Anani A, Crouch-Baker S and Huggins RA, Kinetic and thermodynamic parameters of several binary lithium alloy negative electrode materials at ambient temperature, J. Electrochem. Soc., 134 (1987) 3098.

[9] Anani A, Crouch-Baker S and Huggins RA, Investigation of a ternary lithium alloy mixed-conducting matrix electrode at ambient temperature, J. Electrochem. Soc., 135 (1988) 2103.

[10] Apetecchi GB, Croce F and Scrosatti B, High-performance electrolyte membranes for plastic lithium batteries, J. Power Sources 66 (1997) 77.

[11] Arakawa M and Yamaki J, The cathodic decomposition of propylene carbonate in lithium batteries, J. Electronal. Chem., 219 (1987) 273.

[12] Armand M, Materials for advanced batteries, eds. D.W. Murphy, J. Broadhead and Steele BCH, Plenum Press, New York (1980)145.

[13] Armand M, History of polymer electrolytes, Solid State Ionics 69 (1994) 309.

[14] Armstrong AR and Bruce PG, Synthesis of layered $LiMnO_2$ as an electrode for rechargeable lithium batteries, Nature, 381 (1996) 499.

[15] Aurbach D, Zaban A, Gofer Y, Ely YE, Weissman I, Chusid O and Abramson O, Recent studies of the lithium-liquid electrolyte interface electrochemical, morphological and spectral studies of a few important systems, J. Power Sources, 54 (1995) 76.

[16] Aurbach D, Levi MD, Gamulski K, Markovsky B, Salitra G, and Levi E, Capacity fading of $Li_xMn_2O_4$ spinel electrodes studied by XRD and electroanalytical techniques, J Power Sources, 472 (1999) 81.

[17] Bacsa WS, Ugarte D, Chatelain A and De Heer WA, High-resolution electron microscopy and inelastic light scattering of purified multishelled carbon nanotubes, Phys. Rev. B, 50 (1994) 15473.

[18] Baker RTK, Catalytic growth of carbon filaments, Carbon, 27 (1989) 315.

[19] Banerjee S, Roy S, Chen JW and Chakravorty D, Magnetic properties of oxide-coated iron nanoparticles synthesized by electrodeposition, J. of Magnetism and Magnetic Materials, 219 (2000) 45.

[20] Baranski S and Fawcett WR, The Formation of lithium-aluminum alloys at an aluminum electrode in propylene carbonate, J. Electrochem. Soc., 129 (1982) 901.

[21] Basu S, U.S. Rechargeable battery, Patent No. 4, 304, 825, Dec. 8 (1981).

[22] Baughman R H, Zakhidov A A, and De Heer W. A., Carbon nanotubes-the route toward applications, Science, 297 (2002) 787.

[23] Beaulieu LY and Dahn JR, The reaction of lithium with Sn–Mn–C intermetallics prepared by mechanical alloying, J. Electrochem. Soc., 147 (2000) 3237.

[24] Bendiab N, Anglaret E, Bantignies JL, Zahab A, Sauvajol JL, Stoichiometry dependence of the raman spectrum of alkali-doped single-wall carbon nanotubes, Phy. Rev. B, 64 (2001) 245424-1.

[25] Benjamin JS and Schelleng RD, Dispersion strengthened aluminium–magnesium alloy made by mechanical alloying, Met Trans A, 12 (1981)1827.

[26] Bernal JD, The structure of graphite, Proc. R. Soc. London Ser. A 106 (1924) 749.

[27] Besenhard JO and Fritz HP, The Electrochemistry of Black Carbons, Angew. Chem. Int. Ed. Engl. 95 (1983) 950.

[28] Besenhard JO, Yang J and Winter M, Will advanced lithium-alloy anodes have a chance in lithium-ion batteries?, J. Power Sources, 68 (1997) 87.

[29] Besenhard JO, Hess M and Komenda P, Dimensionally stable Li-alloy electrodes for secondary batteries, Solid State Ionics, 40 (1990) 525.

[30] Besenhard JO, In Soft Chemistry Routes to New Materials (Eds: J.Rouxel, M. Tournoux, R. Brec), Materials Science Vol. 152-153, Trans Tech, Aedermannsdorf, Switzerland (1994)13.

[31] Bhadeshia HKDH, Thermal analyses techniques. Differential thermal analysis, University of Cambridge, Material Science and Metallurgy. www.msm.cam.ac.uk/phase-trans/2002/Thermal1.

[32] Billaud D, McRae E and Harold A, Synthesis and electrical resistivity of lithium-pyrographite intercalation compounds (stages I, II and III), Mater. Res. Bull., 14 (1979) 857.

[33] Bittihn R, Herr R and Hoge D, Stability of lithiated carbon electrodes in organic electrolytes, J.Power sources, 43 (1993) 409.

[34] Boehm HP, Hofmann U, Rhomboedriche modification des graphits, Z. Anorg Chem., 278 (1955) 58.

[35] Boskovic BO, Stolojan V, Khan RUA and Silva SRP, Large-area synthesis of carbon nanofibres at room temperature, Nature Mater., 1 (2002) 165.

[36] Boukamp BA, Lesh GC and Huggins RA, All-solid lithium electrodes with mixed-conductor matrix, J. Electrochem. Soc., 128 (1981) 725.

[37] Bower C, Zhu W, Jin S and Zhou O, Plasma-induced alignment of carbon nanotubes, Appl. Phys. Lett., 77 (2000) 830.

[38] Brandt K, Historical development of secondary lithium batteries, Solid State Ionics, 69 (1994) 173.

[39] Britton DL., Evaluation and testing of commercially available carbon nanotubes as negative electrode for lithium ion cells., NASA/TM, 214809, 2007.

[40] Broadhead J, Disalvo FJ and Trumbore FA, Non-aqueous battery using chalcogenide electrode, US Patent 3864167.

[41] Burgess JS, Acharyab CK, Lizarazo J, Yancey N, Flowers B, Kwon G, Klein T, Weaver M, Alan M, Lane C, Turnerb H and Street S, Boron-doped carbon powders formed at 1000°C and one atmosphere, Carbon, 46 (2008) 1711.

[42] Capitaine F, Gravereau P and Delmas C, A new variety of $LiMnO_2$ with a layered structure, Solid State Ionics, 89 (1996) 197.

[43] Cassel AM, Raymake A, Kong J and Dai H., Large scale CVD synthesis of single-walled carbon nanotubes, J Phys Chem B,103 (1999) 6484.

[44] Cassel AM, McCool GC, Tee Ng H, Koehne JE,Chen B and Li J, Carbon nanotube networks by chemical vapor deposition, Appl. Phys. Lett., 82 (2003) 817.

[45] Cermignani W, Paulson TE, Onneby C and Pantano CG, Synthesis and characterization of boron-doped carbons, Carbon, 33 (1995) 367.

[46] Chang J-C, Tzeng Y-F, Chen J-M, Chiu H-T and Lee C-Y, Carbon nano beads as an anode material on high rate capability lithium ion batteries, Electrochimica Acta, 27 (2009)7066.

[47] Charlier JC and Iijima S, Carbon Nanotubes, Topics in Applied Physics", edited by Dresselhaus MS, Dresselhaus G, and Ph. Avouris, Springer-Verlag, Berlin 80(1) (2001) 55.

[48] Chen P, Zhang H-B, Lin G-D, Hong Q and Tsai KR, Growth of carbon nanotubes by catalytic decomposition of CH_4 or CO on a Ni–MgO catalyst, Carbon, 35 (1997) 1495.

[49] Chen WX, Lee JY and Liu Z, Electrochemical lithiation and de-lithiation of carbon nanotube-Sn_2Sb nanocomposites, Electrochemistry Communications 4 (2002) 260.

TO WHOM SO EVER IT MAY CONCERN

This is to certify that all the comments raised by one of the examiners have been considered by the candidate Kuldeep Singh Rana and all the revisions suggested by the examiner have been incorporated in the revised version of the Ph.D. thesis titled, "SYNTHESIS AND CHARACTERIZATIONS OF ANODE MATERIALS FOR LITHIUM ION BATTERY".

30/9/2010

ANJAN SIL
(Supervisor)
Professor
Department of Metallurgical and Materials Engineering
Indian Institute of Technology Roorkee
Roorkee – 247667
India

[50] Chen X, Yang S, Motojima S, Ichihara M, Morphology and microstructure of twisting nano-ribbons prepared using sputter-coated Fe-base alloy catalysts on glass substrates, Mater. Lett., 59 (2005) 854.

[51] Chieu TC, Dresselhaus MS and Endo M, Raman studies of benzene-derived graphite fibers, Phys. Rev. B, 26 (1982) 5867.

[52] Christian D and Vecchio K, Growth mechanism of vapor phase CVD-grown multi-walled carbon nanotubes, Carbon, 43 (2005) 2608.

[53] Claye AS, Nemes NM, Janossy A and Fischer JE, Structure and electronic properties of potassium-doped single-wall carbon nanotubes, Phys. Rev. B, 62 (2000) 4845.

[54] Claye AS, Fisher JE, Huffman CB, Rinzler AG and Smalley RE, Solid-state electrochemistry of the Li single wall carbon nanotube system, J. Electrochem. Soc., 147 (2000) 2845.

[55] Colomer JF, Bister J, Willems I, Konya Z, Fonseca A, Van Tendeloo G and Nagy JB, Synthesis of single wall carbon nanotubes by catalytic decomposition of hydrocarbons, Chem. Commun., 14 (1999)1343.

[56] Crespi A, Schmidt C, Norton J, Chen K and Skarstad PJ, Modeling and characterization of the resistance of Lithium/SVO batteries for implantable cardioverter defibrillators, J. Electrochem. Soc., 148 (2000) A30.

[57] Cullity BD and Stock SR, Elements of X-ray diffraction, Prentice Hall Publishing Comp., New Jersy (2001).

[58] Dahn JR, Phase diagram of Li_xC_6, Phys. Rev. B, 44 (1991) 9170.

[59] Dahn JR, Sleigh AK, Shi H, Reimers JN, Zhong Q and Way BM, Dependence of the electrochemical intercalation of lithium in carbons on the crystal structure of the carbon, Electrochim. Acta, 38 (1993) 1179.

[60] Dahn JR, Sleigh AK, Shi H, Way BM, Weydanz WJ, Reimers JN, Zhong Q and Sacken U. von, In lithium batteries: new materials, developments and perspectives (Ed: G. Pistoia), Elsevier, Amsterdam (1994) 1.

[61] Dahn JR, Xing W and Gao Y, The falling cards model for the structure of microporous carbons, Carbon, 35 (1997) 825.

[62] Dai H, Rinzler AG, Nikolaev P, Thess A, Colbert DT and Smalley RE, Single-wall nanotubes produced by metal-catalyzed disproportionation of carbon monoxide, Chem. Phys. Lett., 260 (1996) 471.

[63] Datta MK and Kumta PN, Annual report, Mitsubishi Chemical Corporation, 2003.

[64] Datta MK and Kumta PN, Silicon and carbon based composite anode for lithium ion batteries, Journal of Power sources, 158 (2006) 557.

[65] Davis CA, Knowles KM and Amaratunga GAJ, Cross-sectional structure of tetrahedral amorphous carbon, Surface and Coatings Technology, 76 (1995) 316.

[66] Delmas C, Alkali metal intercalation in layered oxides, Mater.Sci. Eng., B3 (1989) 97.

[67] Delmas I and Saadoune C, Electrochemical and physical properties of the $Li_xNi_{1-y}Co_yO_2$ phases, Solid State Ionics, 53 (1992) 370.

[68] Dey AN, Electrochemical alloying of lithium in organic electrolytes, J. Electrochem. Soc., 118 (1971) 1547.

[69] Disma F, Aymard L, Dupont L and Tarascon J -M, Effect of mechanical grinding on the lithium intercalation process in graphites and soft carbons, J. Electrochem. Soc., 143 (1996) 3959.

[70] Disma F, Effets du broyage mecanique sur les carbones: materiaux d'electrodes negatives pour accumulateurs au lithium. The Universite de Picardie, 1998.

[71] Dupuis A-C, The catalyst in the CCVD of carbon nanotubes—a review, Progress in Materials Science 50 (2005) 929.

[72] Eckert J, Schlutz L, Hellstern E and Urban K, Glass forming range in mechanically alloyed NiZr and the influence of the milling intensity, J. Appl. Phys., 64 (1988) 3224.

[73] Eklund PC, Holden JM and Jishi RA, Vibrational modes of carbon nanotubes; spectroscopy and theory, Carbon, 33 (1995) 959.

[74] Endo M, Kim C, Karaki T, Nishimura Y, and Matthews MJ, Brown SDM and Dresselhaus MS, Carbon, Anode performance of a Li ion battery based on graphitized and B-doped milled mesophase pitch-based carbon fibers, Carbon, 37 (1999) 561.

[75] Endo M, Kim C, Nishimura K, Fujito T and Miyashita K, Recent development of carbon materials for Li ion batteries, Carbon, 38 (2000) 183.

[76] Endo M, Kim YA, Hayashi T, Nishimura K, Matushita T, Miyashita K and Dresselhaus MS, Vapor-grown carbon fibers (VGCFs): Basic properties and their battery applications, Carbon, 39 (2001) 1287.

[77] Fan R, Buczko A, Puretzky A, Geohegan DB, Howe JY, Pantelides ST and Pennycook SJ, Nucleation of single-walled carbon nanotubes, Physics Review Letters, 90(14) (2003) 145501.

[78] Fauteux D and Koksbang R, Rechargeable lithium battery anodes: Alternatives to metallic lithium, J. Appl. electrochem., 23 (1993) 1.

[79] Fenton DE, Parker JM and Wright PV, Complexes of alkali metal ions with poly ethylene oxide, Polymer, 14 (1973) 589.

[80] Fisher E, In chemical physics of intercalation (Eds: A. P. Legrand,S. Flandrois), NATO ASI Series B 1987, Vol. 172, p. 59.

[81] Fong R, Sacken U and Dahn JR, Studies of lithium intercalated into carbons using nonaqueous electrochemical cell, J.Electrochem. Soc., 137 (1990)2009.

[82] Fonseca A, Hernadi K, Nagy JB, Bernaerts D and Lucas AA, Optimization of catalytic production and purification of bucky tubes, J Mol Catal A: Chem 107 (1996) 159.

[83] Frackowiak E, Gautier S, Gaucher H, Bonnamy S and Beguin F, Electrochemical storage of lithium multiwalled carbon nanotubes, Carbon, 37 (1999) 61.

[84] Frackowiaka E, Kierzekb K, Lotaa G and Machnikowskib J, Lithium insertion/deinsertion of boron doped graphitic carbons synthesized by different procedure, Journal of Physics and Chemistry of Solids, 69 (2008) 1179.

[85] Franklin RE, The structure of graphitic carbons, Acta Crystallographica, 4 (1951) 253.

[86] Fultz B and Howe JM, Transmission electron microscopy and diffractometry of materials, (Springer, New York) (2007).

[87] Fujimoto H, Mabuchi A, Tokumitsu K, Kasuh T and Akuzawa N, High resolution electron microscopy studies in carbonsoot, Carbon, 32 (1994) 246.

[88] Gabersces M, Bele M, Drofenic J, Dominko R and Pejovinik S, Improved carbon anode properties: pretreatment of particles in polyelectrolyte solution, J. Power sources, 97 (2001) 67.

[89] Gao B, Kleinhammes A, Tang XP, Bower C, Fleming L, Wu Y and Zhou O, Electrochemical intercalation of single-walled carbon nanotubes with lithium Chemical Physics Letters, 307, 3 (1999) 153.

[90] Gao B, Bower C, Lorentzen JD, Fleming L and Kleinhammes A, Tang XP, Mcneil LE, Wu Y and Zhou O, Enhanced saturation lithium composition in ball-milled single-walled carbon naotubes, Chem. Phys. Lett., 327 (2000) 69.

[91] Genies EM, Hany P and Santier C, A rechargeable battery of the type polyaniline/propylene carbonate-$LiClO_4$/Li-Al, J. Appl. Electrochem., 18 (1988) 751.

[92] Gholam-Abbas Nazri, Lithium batteries science and technology, General motors research & development, Kluwe academic publisher.

[93] Gilman PS and Nix WD, The structure and properties of aluminum alloys produced by mechanical alloying: powder processing and resultant powder structures, Met Trans A, 12 (1981) 813.

[94] Goldstein JI and Yakowitz H, (ed.), Practical scanning electron microscope, Plenum Press, New York (1975).

[95] Goodhew PJ, Humphreys J and Beanland R, Electron Microscopy and Analysis, Taylor and Francis, London (2001) 60.

[96] Gouveia DX, Lemos V, De Paiva JAC, Souza Filho AG, Mendes Filho J, Lala SM, Montoro LA and Rosolen JM, Spectroscopic studies of Li_xFePO_4 and $Li_xM_{0.03}Fe_{0.97}PO_4$ (M=Cr,Cu,Al,Ti), Phys. Rev. B, 72 (2005) 24105.

[97] Greskovich S C, Milling treatise on materials science and technology, Ceramic fabrication processes, (Edited by Wang F F Y, academic Press, New York) Vol. 9, (1976).

[98] Grundy PJ and Jones GA, The electron microscopy, Edward Arnold, London, (1976).

[99] Guerard D, Ball milling in presence of a fluid: results and perspectives, Rev. Adv. Mater.Sci., 18 (2008) 225.

[100] Guyomard D and Tarascon JM, Li metal-free rechargeable $LiMn_2O_4$/carbon cells: their understanding and optimization, J Electrochem Soc, 139 (1992) 937.

[101] Haverkamp J, Mayo RM, Bourham MA, Narayan J, Jin C and Duscher G, Plasma plume characteristics and properties of pulsed laser deposited diamond-like carbon films, J. Appl. Phys., 93 (2003) 3627.

[102] Heal JW, Sparrow JT and Cross PM, Use of the scanning electron microscope, Pergamon Press, Oxford (1972).

[103] Hernadi A, Fonseca K, Nagy JB, Bernaerts D and Lucas AA, Fe-catalyzed carbon nanotubes, Carbon, 34 (1996) 1249.

[104] Hever KO, Ion mobility in crystals of a mixed-alkali ferrite: $K_xNa_{1-x}Fe_7O_{11}$, J. Elctrochem. Soc., 115 (1968) 826.

[105] Hiura H., Ebbesen TW, Tanigaki K and Takahashi H, Raman studies of carbon nanotubes, Chem. Phys. Lett., 202 (1993) 509.

[106] Hooley JG, Physical chemistry and mechanism of intercalation in graphite, Mater Sci Eng., 31 (1977) 17.

[107] Hsoeh HM, Tai NH, Lee CY, Chen JM and Wang FT, Electrochemical properties of multiwall carbon nanotubes electrode for secondary lithium-ion battery, Rev. Adv. Mater. Sci., 5 (2003) 61.

[108] Huang H, Liu W, Huang X, Chen L, Kelder EM and Schoonman J, Effect of rhombohedral phase on lithium intercalation capacity in graphite, Solid State Ionics, 110 (1998) 173.

[109] Huang HT, Subba Rao GV and Chowdari BVR, $LiAl_xCo_{1-x}O_2$ as 4 V cathodes for lithium ion batteries, J. Power Sources, 81-82 (1999) 690.

[110] Huggins A, Materials science principles related to alloys of potential use in rechargeable lithium cells, J. Power Sources, 26 (1989) 109.

[111] Idota Y, Kabuto T, Matsufuji A, Maekawa Y and Miyasaki T, Tin-based amorphous oxides: a high-capacity lithium-ion storage material, Science, 276 (1997) 1395.

[112] Ihara S, Itoh S and Kitakami JI, Helically coiled cage forms of graphitic carbon, Phys. Rev. B, 48 (1993) 5643.

[113] Iijima S, Helical microtubules of graphitic carbon, Nature, 354 (1991) 56.

[114] Imanishi N, Ohashi S, Ichikawa T, Takeda Y, Yamamoto O and Kanno R, Carbon-lithium anodes for lithium secondary batteries, J. Power Sources, 39 (1992) 185.

[115] Inaba M, Yoshida H, Ogumi Z, Abe T, Mizutani Y and Asano M, *In Situ* Raman Study on Electrochemical Li Intercalation into GraphiteJ. Electrochem. Soc., 142 (1995) 20.

[116] Ivanov V, Nagy JB, Lambin P, Lucas A, Zhang XF and Bernaerts D, The study of carbon nanotubules produced by catalytic method, Chem. Phys. Lett., 223 (1994) 329.

[117] Jang Y-II, Huang BY, Chiang Y–M and Sadoway DR, Electrochem. stabilization of $LiMnO_2$ in the α-$NaFeO_2$ structure type by $LiAlO_2$ Addition, Solid State Lett., 1 (1998) 13.

[118] Janot R and Guerard D, Ball-milling in liquid media applications to the preparation of anodic materials for lithium-ion batteries, Progress in Materials Science 50 (2005) 1.

[119] Jeong SH, Lee JO and Lee JH, Preparation of aligned carbon nanotubes with prescribed dimensions: template synthesis and sonication cutting approach, Chem. Mater, 14 (2002) 1859.

[120] Jessensky O, Muller F and Gosele U, Self-Organized Formation of Hexagonal Pore Structures in Anodic Alumina, J. Electrochem. Soc., 145(11) (1998(a) 3735.

[121] Kanamura K, Toriyama S, Shiraishi S and Takehara Z, electrochemical Oxidation Processes on Ni Electrodes in Propylene Carbonate Containing Various Electrolyte Salts, J. Electrochem. Soc., 143 (1996) 2548.

[122] Kanno R, Kawamoto Y, Takeda Y, Ohashi S, Imanishi N and Yamamotto O, Carbon Fiber as a Negative Electrode in Lithium Secondary Cells, J. Electrochem. Soc., 139 (1992) 3397.

[123] Kanzow H and Ding A, Formation mechanism of single-wall carbon nanotubes on liquid–metalparticles, Phys. Rev. B, 60 (1999) 11180.

[124] Kasavajjula U, Wang C and Appleby AJ, Nano- and bulk-silicon-based insertion anodes for lithium-ion secondary cells, J. Power Sources 163 (2007) 1003.

[125] Kastner J, Pichler T, Kuzmany H, Curran S, Blau W, Weldon DN, Delamesiere M, Draper S and Zandbergen H, Resonance raman and infrared spectroscopy of carbon nanotubes, Chem. Phys. Lett., 221 (1994) 53.

[126] Kasuh T, Mabuchi A, Tokumitsu K and Fujimoto H, Recent trends in carbon negative electrode materials, J. Power Sources, 68 (1997) 99.

[127] Kawaguchi M, Nozaki K, Motojima S and Wagana HI, A growth mechanism of regularly coiled carbon fibers through acetylene pyrolysis, J. Cryst. Growth, 118 (1992) 309.

[128] Kim MS, Rodriguez NM and Baker RTK, The role of interfacial phenomena in the structure of carbon deposits, J. Catal., 134 (1992) 253.

[129] Kim Il-seok, Blomgren GE and Kumta PN, Si–SiC nanocomposite anodes synthesized using high-energy mechanical milling, J. Power Sources, 130 (2004) 275.

[130] Klinke C, Bonard J-M and Kern K, Comparative study of the catalytic growth of patterned carbon nanotube films, Surf Sci., 492 (2001)195.

[131] Koizol K, Shaffer M and Windle A, Three-dimensional internal order in multiwalled carbon nanotubes grown by chemical vapor decomposition, Adv. Mater, 6 (2005) 760.

[132] Kong J, Cassel AM and Dai H, Chemical vapor deposition of methane for single – walled carbon nanotubes, Chem. Phys. Lett., 292 (1998) 567.

[133] Larcher D, Mudalige C, George AE, Porter V, Gharghouri M and Dahn JR, Electrochemical insertion of Li and irreversibility in disordered carbons prepared from oxygen and sulfur-containing pitches, Electrochem. Acta., 44 (1999) 4069.

[134] Lazzari M and Scrosati B and cyclable A, Lithium organic electrolyte cell based on two intercalation electrodes, J. Electrochem. Soc., 127 (1980) 773.

[135] Lee CJ, Park J, Kim JM, Huh Y, Lee JY and No KS, Low-temperature growth of carbon nanotubes by thermal chemical vapor deposition using Pd, Cr, and Pt as co-catalyst, Chem. Phys. Lett., 327 (2000) 277.

[136] Lemos V, Guerini S, Lala SM, Montoro LA and Rosolen JM, Li-inserted carbon nanotube raman scattering, Microelectronics Journal, 36 (2005) 1020.

[137] Leroux F, Metenier K, Gautier S, Frackowiak E, Bonnamy S and Beguin F, Electrochemical insertion of lithium in catalytic multi-walled carbon nanotubes, J. Power Sources, 81 (1999) 317.

[138] Li W, Reimers JN and Dahn JR, In situ X-ray diffraction and electrochemical studies of $Li_{1-x}NiO_2$, Solid State Ionincs, 67 (1993) 123.

[139] Li Y, Kim W, Zhang Y, Rolandi M, Wang D and Dai H, Growth of single-walled carbon nanotubes from discrete catalytic nanoparticles of various sizes, J. Phys. Chem. B, 105 (2001) 11424.

[140] Li Y, Liu J, Wang Y and Wang ZL, Preparation of monodispersed Fe–Mo nanoparticles as the catalyst for CVD synthesis of carbon nanotubes, Chem. Mater., 13 (2001) 1008.

[141] Liao XZ, Serquis A and Jia QX, Peterson DE and Zhu YT, Effect of catalyst composition on carbon nanotube growth, Appl. Phys. Lett., 82 (2003) 2694.

[142] Lipson H and Stokes AR, A new structure of carbon, Nature, 149 (1942) 328.

[143] Liu WR, Wang J-H, Wu H-C, Shieh DT, Yang MH and Wu NL, Electrochemical Characterizations on Si and C-Coated Si Particle Electrodes for Lithium-Ion Batteries, J. Electrochem. Soc. 152 (2005) A1598.

[144] Livage J, The gel route to transition metal oxides, J. Solid State Chem., 64 (1986) 322.

[145] Lopez N, Illas F and Pacchioni G, Electronic effects in the activation of supported metal clusters: density functional theory study of H_2 dissociation on Cu/SiO_2, J. Phys. Chem. B, 103 (1999) 8552.

[146] Lowell CE, Solid solution of boron in graphite, J. Am Ceram Soc., 50 (1967) 142.

[147] Lu W and Chung DDL. Anodic performance of vapor-derived carbon filaments in lithium-ion secondary battery, Carbon 39 (2001) 493.

[148] Lueking A and Yang RT, Hydrogen spillover from a metal oxide catalyst onto carbon nanotubes—implications for hydrogen storage, J. Catal., 206 (2002) 165.

[149] Mabuchi A, Fujimoto H, Tokumitsu K and Kasuh T, Charge-discharge mechanism of graphitized mesocarbon microbeads, J. Electrochem. Soc., 142 (1995) 3049.

[150] Machnikowski J, Frackowiak E, Kierzek K, Waszak D, Benoit R and Be guin F, Lithium insertion into boron containing carbons prepared by co-pyrolysis of coal-tar pitch and borane–pyridine complex, J. Phys. Chem. Solids, 65 (2004) 153.

[151] Mahanandia P, Nanda KK, Prasad V and Subramanyam SV, Synthesis and characterization of carbon nanoribbons and single crystal iron filled carbon nanotubes, Mater. Res. Bull., 23 (2008) 3252.

[152] Mao O and Dahn JR, Mechanically alloyed Sn–Fe(–C) powders as anode materials for Li ion batteries. III. Sn_2Fe:$SnFe_3C$ active/inactive composites, J. Electrochem. Soc., 146 (1999) 423.

[153] Maruyama S, Kojima R, Miyauchi Y, Chiashi S and Kohno M, Low-temperature synthesis of high-purity single-walled carbon nanotubes from alcohol, Chem. Phys. Lett., 360 (2002) 229.

[154] Masuda H and Fukuda K, Ordered metal nanohole arrays made by a two-step replication of honeycomb structures of anodic alumina, Science, 268 (1995) 1466.

[155] Mathur RB, Dhami TL, Maheshari P, Gupta A K, Rangarajan J, Sharma RK and Sharma CP, A process for making porous conducting carbon composite electrode suitable for fuel cell application, 14-12-2006 (Patent 0395 DEL 2007).

[156] Matsuda M, Morita M and Tachihara F, Conductivity of lithium salts in the mixed systems of high permittivity solvents and low viscosity solvents, Bull. Chem. Soc. Jpn., 59 (1986) 1967.

[157] Maurin G, Bousqueta C, Henna F, Bernier P, Almairac R and Simon B, Electrochemical lithium intercalation into multiwall carbon nanotubes: a micro-Raman study, Solis State Ionics, 136/137 (2000) 1295.

[158] Maxfield M, Jow TR, Gould S, Sewchock MG and Shacklette LW, Composite Electrodes Containing Conducting Polymers and Li Alloys, J. Electrochem. Soc., 135 (1988) 299.

[159] Mishra A, Saha M, Bhatia G, Rajendra, Aggarwal K, Raman V and Yadav HS, A comparative study on the development of pitch precursor for general-purpose carbon fibres, Journal of Materials Processing Technology, 168 (2005) 316.

[160] Mizushima K, Jones PC, Wiswman PJ and Goodenough JB, Li_xCoO_2 ($0<x<-1$): A new cathode material for batteries of high energy density, Mat.Res. Bull., 15 (1980)783.

[161] Moret R, in Intercalation in Layered Materials, NATO Advanced Study Institute Series B: Physics Vol. 148 (Plenum, New York, 1986) 185.

[162] Moshtev RV, Zlatilova P, Manev V and Saito A, The $LiNiO_2$ solid solution as a cathode material for rechargeable lithium batteries, J. Power Sources 54 (1995) 329.

[163] Mukhopadhyay K, Koshio K, Tanaka N, and Shinohara H, A simple and novel way to synthesize aligned nanotube bundles at low temperature, Jpn. J. Appl. Phys., 37 (1998) L1257.

[164] Mukhopadhyay I, Hoshino N, Kawasaki S, Okino F, Hsu WK and Touhara H, J. Electrochemical Li insertion in B-doped multiwall carbon nanotubes, Electrochem. Soc., 149 (2002) A 39.

[165] Murphy DW., Christian PA and Carides JN, Vanadium Oxide Cathode Materials for Secondary Lithium Cells, J. Electrochem. Soc., 126 (1979) 497.

[166] Murphy DW and Vanadium C, Oxide cathode materials for secondary lithium cells, Science, 205 (1979) 651.

[167] Nagaura T and Tozawa K, Lithium ion rechargeable battery, Prog. Batteries Sol. Cells 9 (1990) 209.

[168] Naji J, Ghanbaja B, Humbert P and Willmann DB, Electroreduction of graphite in $LiClO_4$-ethylene carbonate electrolyte. Characterization of the passivating layer by transmission electron microscopy and Fourier-transform infrared spectroscopy, J. Power Sources, 63 (1996) 33.

[169] Nalimova VA, Bindra C and Fisher JE, Enhanced metastability of high-density Li intercalation in boron-doped graphite, Solid State comm., 97 (1996) 583.

[170] Natarajan C, Fujimoto H, Mabuchi A, Tokumitsu K and Kasuh T, Effect of mechanical milling of graphite powder on lithium intercalation properties, Journal of Power Sources 92 (2001) 187.

[171] Nemanich RJ and Solin SA, First- and second-order raman scattering from finite-size crystals of graphite, Phys. Rev. B, 20 (1979) 392.

[172] Nesper R, Structure and chemical bonding in zintl-phases containing lithium, Solid State Chem., 20 (1990) 1.

[173] Nimon ES and Churikov AV, Electrochemical behaviour of Li-Sn, Li-Cd and Li-Sn-Cd alloys in propylene carbonate solution, Electrochim. Acta, 41(1996) 1455.

[174] Nohma T, Yoshimura, Nishio K, Yamamoto Y, Fukuoka S and Hara M, Development of coin-type lithium secondary batteries containing manganese dioxide/Li-Al, J. Power Sources ,1996, 58, 205.

[175] Novak P, Int. Meeting Li Batteries IMLB12 Nara, Japan Abstract 9 (2004).

[176] Ohzuku T and Ueda A, Solid-state redox reactions of $LiCoO_2$ ($R\bar{3}m$) for 4 Volt secondary lithium cells, J. Electrochem. Soc., 141 (1994) 2972.

[177] Öncel Ç and Yürüm Y, Carbon nanotube synthesis via the catalytic CVD method: a review on the effect of reaction parameters. fullerenes, Nanotubes and Carbon Nanostructures, 14(1) (2006) 17.

[178] Ong TS and Yang H, Effect of atmosphere on the mechanical milling of natural graphite, Carbon, 38 (2000) 2077.

[179] Padhi AK, Nanjundaswamy KS and Goodenough JB., Phospho-olivines as positive-electrode materials for rechargeable lithium batteries, J. Electrochem. Soc., 144 (1997) 1188.

[180] Padhi AK, Nanjundaswamy KS, Masquelier C, Okada S and Goodeenough JB, Effect of Structure on the Fe^{3+}/Fe^{2+} redox couple in iron phosphates, J. Electrochem. Soc., 144 (1997)1609.

[181] Pan H, Lin J, Feng Y and Gao H, Electrical-bridge model on the self-organized growth of nanopores in anodized aluminum oxide, IEEE Transactions on Nanotechnology 3 (2004) 462.

[182] Pan ZW, Xie ZW, Chang BH, Sun LF, Zhou WY and Wang G, Direct growth of aligned open carbon nanotubes by chemical vapor deposition, Chem. Phys. Lett., 299 (1999) 97.

[183] Pannala S and Wood RF, Multiscale simulations of carbon nanotube nucleation and growth: Mesoscopic continuum calculations, J. Nanosci. Nanotech., 4(1) (2004) 463.

[184] Peled E, Menachem C and melman A, Improved graphite anode for lithium-ion batteries chemically, J. Electrochem. Soc., 143 (1996) L4.

[185] Perez-Cabero M, Rodriguez-Ramos I, Guerrero-Ruiz A, Characterization of carbon nanotubes and carbon nanofibers prepared by catalytic decomposition of acetylene in a fluidized bed reactor, J. Catal., 215 (2003) 305.

[186] Pierre AC, Sol-gel processing of ceramic powders, Ceramic Bulletin, 70 (1991)1281.

[187] Pierson HO, Handbook of chemical vapor deposition (CVD), Noyes publications, U.S.A. (1999).

[188] Placzek G. "Rayleigh Streeung und Raman Effekt", In: Hdb. der Radiologie, 2 (1934). 209.

[189] Rao BML, Francis RW and Christopher HA, Lithium-aluminum electrode, J. Electrochem. Soc., 124 (1997) 1490.

[190] Raton FL, Hand book of chemistry and physics, 68th edition, R.C Weast, Ed., CRC Press, Boca 1987.

[191] Ren ZF, Huang ZP, Wang DZ, Wen JG, Xu JW, Wang JH, Calvet LE, Chen J, Klemic JF and Reed MA, Growth of a single freestanding multiwall carbon nanotube on each nanonickel dot, Appl. Phys. Lett., 75 (1999) 1086.

[192] Richard C, Charles B, Evans A and Wilson S, Encyclopedia of materials characterization, by Butterworth-Heinemann, a division of Reed Publishing CUSA) Inc, (1992) 421.

[193] Rossat Mignod J, Fruchart D, Moran MJ and Milliken JW, Neutron scattering study of lithium-graphite intercalation compounds, Synth.Met.,2 (1980)143.

[194] Rossen E, Jones CDW and Dahn JR, Electrochem. structure and electrochemistry of $Li_xMn_yNi_{1-y}O_2$, Solid State Ionics, 57 (1992) 311.

[195] Saadoune C and Delmas I, Electrochemical and physical properties of the $Li_xNi_{1-y}Co_yO_2$ phases, Solid State Ionics, 53-56 (1992) 370.

[196] Sanchez P, Belin C, Crepy C and De Guibert A, Electrochemical studies of lithium-boron alloys in non-aqueous media-comparison with pure, J. Appl. Electrochem.19 (1989) 421.

[197] Sanyal M K, Agrawal VV, Bera MK, Kalyanikutty KP, Daillant J, Blot C, Kubowicz S, Konovalov O and Rao CNR, Formation and ordering of gold nanoparticles at the toluene-water interface, J. Phys. Chem. C, 112 (2008) 1739.

[198] Satishkumar BC, Govindaraj A, Sen R and Rao CNR, Single-walled nanotubes by the pyrolysis of acetylene–organometallic mixtures, J. Chem. Phys. Lett., 293 (1998) 47.

[199] Sato K, Noguchi M, Demachi A, Oki N and Endo M, A mechanism of lithium storage in disordered carbons, Science, 264 (1994) 556.

[200] Satoh A, Takami N and Ohsaki T, Electrochemical intercalation of lithium into graphitized carbons, Solid State Ionics, 80 (1995) 291.

[201] Schaffer GB and Mc Cormick PG, On the kinetics of mechanical alloying. Met Trans A 23 (1992) 1285.

[202] Schaffer GB and Forrester JS, The influence of collision energy and strain accumulation on the kinetics of mechanical alloying, J. Mater. Sci., 32 (1997) 3157.

[203] Schönfelder HH, Kitoh K and Nemoto H, Nanostructure criteria for lithium intercalation in non-doped and phosphorus-doped hard carbons, J. Power Sources, 68 (1997) 258.

[204] Seidel R, Duesberg GS, Unger E, Graham AP, Liebau M and Kreupl F, Chemical vapor deposition growth of single-walled carbon nanotubes at 600°C and a simple growth model, J. Phys. Chem. B, 108 (2004) 1888.

[205] Seth RBS, Lal C, Rao R, Singh BP and Dhami TL, Co-synthesis, purification and characterization of single- and multi-walled carbon nanotubes using the electric arc method, Carbon, 45 (2007) 132.

[206] Shen TD, Ge WQ, Wang KY, Quan MX, Wang JT, Wei WD and Koch CC, Structural disorder and phase transformation in graphite by ballmilling, Nanostructured Materials, 7 (1996) 393.

[207] Shimoda H, Gao B, Tang XP, Kleinhammes A, Fleming L, Wu Y and Zhou O, Lithium Intercalation into opened single-wall carbon nanotubes: storage capacity and electronic properties, Phys. Rev. Lett., 88(2002) 015502-1.

[208] Shingubara S, Morimoto K, Sakaue H and Takahagi T, Self-Organization of a Porous Alumina Nanohole Array Using a Sulfuric/Oxalic Acid Mixture as Electrolyte, Electrochem. Solid-State Lett., 7 (2004) E15.

[209] Shiraishi S, Kurihara H, Okabe K, Hulicova D and Oya A, Electric double layer capacitance of highly pure single-walled carbon nanotubes (HiPco™ Buckytubes™) in propylene carbonate electrolytes, Electrochem. Commun., 4 (2002) 593.

[210] Silva SRP, Knowles KM, Amaratunga GAJ and Putnis A, The microstructure of inclusions in nanocrystalline carbon films deposited at low temperature, Diamond and Related Materials, 3 (1994) 1048.

[211] Sinnott SB, Andrews R, Qian D, Rao AM, Mao Z, Dickey EC,et al. Model of carbon nanotube growth through chemical vapor deposition, Chem. Phys. Lett., 315 (1999) 25.

[212] Singh KA, Pathak LC and Roy SK, Effect of citric acid on the synthesis of nanocrystalline yttria stabilizized zirconia powders by nitrate-citrate process, Ceramics International, 33 (2007) 1463.

[213] Smith RC and Silva SRP, "Maximizing the electron field emission performance of carbon nanotube arrays." Appl. Phys. Lett., 94 (2009)13.

[214] Sogabe T, Nakajima K and Inagaki M, Effect of boron doping on structure and some properties of carbon-carbon composite, J. Mater Sci. 31 (1996) 6469.

[215] Song IK, Yu WJ., Cho YS, Choi GS and Kim D, The determining factors for the growth mode of carbon nanotubes in the chemical vapor deposition process, Nanotechnology, 15 (2004) S590.

[216] Song MK, Hong SD and No KT, The Structure of Lithium Intercalated Graphite Using an Effective Atomic Charge of Lithium, J. Elctrochem. Soc., 148 (2001) A1159.

[217] Song XY, Kinoshita K and Tran TD, Microstructural characterization of lithiated graphite, J.Electrochem. Soc. 143 (1996) L120.

[218] Spahr M., Novak P, Schnyder B, Haas O and Nesper RJ, Characterization of layered lithium nickel manganese oxides synthesized by a novel oxidative coprecipitation

method and their electrochemical performance as lithium insertion electrode materials, J. Electrochem. Soc., 145 (1998) 1113.

[219] Takei K, Terada N, Kumai K, Iwahori T, Uwai T and Miura T, Effects of the macroscopic structure of carbon black on its behavior as the anode in a lithium secondary cell, J. Power Sources, 55 (1995) 191.

[220] Takeuchi ES and Thiebolt WC, The reduction of silver vanadium oxide in lithium/silver vanadium oxide cells, J. Electrochem. Soc., 135 (1988) 2691.

[221] Tanaka U, Sogabe T, Sakagoshi H, Ito M and Tojo T, Anode property of boron-doped graphite materials for rechargeable lithium-ion batteries, Carbon, 39 (2001) 931.

[222] Tarascon JM and Armand M, Issues and challenges facing rechargeable lithium batteries, Nature, 414 (2001) 359.

[223] Tatsumi K, Akai T, Imamura T, Zaghib K, Iwashita N, Higuchi S and Sawda YJ. Electrochem. Soc., 143 (1996) 1923.

[224] Thackery MM, Structural considerations of layered and spinel lithiated oxides for lithium ion batteries, J. Electrochem. Soc., 142 (1995) 2558.

[225] Thackeray MM, David WIF, Bruce PG and Goodenough JB, Lithium insertion into manganese spinels, Mat.Res. Bull., 18 (1983) 461.

[226] Tibbetts GG, Why are carbon filaments tubular?, J Cryst Growth, 66 (1984) 632.

[227] Tuinstra F and Koenig JL, Raman spectrum of graphite, J. Chem. Phys., 53 (1970) 1126.

[228] Veeraghavan B, Paul J, Haran B and Popov B, Study of polypyrrole graphite composite as anode material for secondary lithium-ion batteries, J.Power Sources, 109 (2002) 377.

[229] Vetter J, Novak P, Wagner MR, Veit C, Moller KC, Besenhar JO, Winter M, Wohlfahrt-Mehrens M, Vogler C and Hammouche A, Ageing mechanisms in lithium-ion batteries, Journal of Power Sources, 147 (2005) 269.

[230] Virk RS, Study of Voltage, Acid Concentration, and temperature on nanopore attributes of anodized aluminum (San Jose State Univ. San Jose, (2005) pp.3-4.

[231] Vitins G and West KJ, Lithium intercalation into layered $LiMNO_2$, Electrochem. Soc., 144 (1997) 2587.

[232] Wagner RS and Ellis WC. Vapor–liquid–solid mechanism of single crystal growth. Appl. Phys. Lett. 4 (1964) 89.

[233] Wakihara M, Recent developments in lithium ion batteries, Materials Science and Engineering, R33 (2001) 109.

[234] Walt A. de Heer, Liquid carbon, carbon-glass beads, and the crystallization of carbon nanotubes, Science, 307 (2005) 907

[235] Wang S, Matsumura Y and Maeda T, A model of the interactions between disordered carbon and lithium, Synth. Met. 71 (1995) 1759.

[236] Wang S, Zhang Y, Yang L and Liu Q, The effect of carbonizing conditions on the capacity of carbon anodes derived from poly(p-phenylene), Solid State Ionics, 919 (1996) 86.

[237] Wang GX, Zhong S, Bradhurst DH, Dou SX and Liu HK, Synthesis and characterization of $LiNiO_2$ compounds as cathodes for rechargeable lithium batteries, J. Power Sources, 76 (1998) 141.

[238] Wang CS, Wu GT, Zhang XB, Qi ZF, Li WZ, J. Lithium insertion in carbon-silicon composite materials produced by mechanical milling, Electrochem. Soc., 145 (1998) 275.

[239] Wang CS, Wu GT and Li WZ, Lithium insertion in ball-milled graphite, Journal of Power Sources, 76 (1998) 1.

[240] Wang GX, Yao J and Liu HK, Characterization of nanocrystalline Si-MCMB composite anode materials, Electrochem. Solid-State Lett., 7 (2004) A250.

[241] Warren BE, x-ray diffraction study of carbon black, J. Chem. Phys. 9 (1934) 551.

[242] Watson M, Chan H, Harmer M and Caram H, Effects of milling liquid on the reaction bonded aluminum oxide process, J Am Ceram Soc., 81 (1998)2053.

[243] Way BM and Dahn JR, The Effect of boron substitution in carbon on the intercalation of lithium in $Li_x(B_zC_{1-z})_6$, J. Electrochem. Soc., 141 (1994) 907.

[273] Zhong DY, Liu S and Wang G, Patterned growth of coiled carbon nanotubes by a template-assisted technique, Appl. Phys. Lett., 83 (2003) 4423.

[274] Zhong J, Chu H, Wang J, Hong J, Tan W and Li Y, Ultralow feeding gas flow guiding growth of large-scale horizontally aligned single-walled carbon nanotube arrays, Nano Lett., 7 (2007) 2073.

[275] Zhou G-T, Palchik O, Pol VG, Sominski E, Koltypina Y and Gedanken A, Microwave-assisted solid-state synthesis and characterization of intermetallic compounds of Li3Bi and Li3Sb. J. Mater. Chem., 13 (2003) 2607.

[276] Zlatilova P, Balkanov I, and Geronov Y, J. Thin foil lithium-aluminium electrode, The effect of thermal treatment on its electrochemical behaviour in nonaqueous media, Power Sources, 24 (1988) 71.

[277] Zelinski BJJ and Uhlmann DR, Gel technology in ceramics, J. Phys. Chem. Solids, 45 (1984) 1069.

[244] Wei Wang, Datta MK and Kumta PN, Silicon-based composite anodes for Li-ion rechargeable batteries, J. Mater. Chem., 17 (2007) 3229.

[245] Welham NJ. Berbenni V and Chapman PG, Effect of extended ball milling on graphite, Journal of Alloys and Compounds 349 (2003) 255.

[246] Weydanz WJ, Way BM, Buuren T and Dahn JR, Behavior of nitrogen-substituted carbon (N_zC_{1-z}) in Li/Li(N_zC_{1-z})$_6$ cells, J. Electrochem. Soc., 141 (1994) 900.

[247] Whittingham MS, Electrical energy storage and intercalation chemistry, Science, 192 (1976) 1226.

[248] Whittingham MS, Chalcogenide battery, US Patent 4009052.

[249] Whittingham MS, Chemistry of intercalation compounds: Metal guests in chalcogenide hosts, Prog. Solid State Chem., 12 (1978) 41.

[250]Wilson AJC, Variance as a measure of line broadening, Nature, 193(1962) 568.

[251] Wilson AJC, On variance as a measure of line broadening in diffractometry, general theory and small particle size, Proc. Phys. Soc., (London), 80 (1962) 286.

[252] Wilson AM, Zank G, Eguchi K, Xing W and Dahn JR, Pyrolysed silicon-containing polymers as high capacity anodes for lithium-ion batteries, J. Power Sources, 68 (1997) 195.

[253] Wilson AM and Dahn JR, Lithium insertion in carbons containing nanodispersed silicon, J. Electrochem Soc., 142 (1995) 326.

[254] Winter M, Jürgen O, Besenhard JO, Michael E. Spahr, and Petr Novμk, Insertion electrode materials for rechargeable lithium batteries, Adv. Mater., 10, (1998) 10.

[255] Winter M and Besenhard JO, Electrochemical lithiation of tin and tin-based intermetallic and composites, Electrochim. Acta 45 (1999) 31.

[256] Wu YP, Rahm E and Holze R, Carbon anode materials for lithium ion batteries, J. Power Sources, 114 (2003) 228.

[257] Wu GT, Wang CS, Zhang XB, Yang HS, Qi Z, He P and Li W, J., Structure and lithium insertion properties of carbon nanotubes., Electrochem. Soc., 146 (1999) 1696.

[258] Wu YP, Rahm E and Holze R, Effects of heteroatoms on electrochemical performance of electrode materials for lithium ion batteries, Electrochim Acta, 47 (2002) 3491.

[259] Wu YP, Rahm E and Holze R, Applications of nano-technologies in lithium secondary batteries, Chin J, Batteries (Dianchi) 32 (2003) 356.

[260] Wyckoff RWG, 1964, Crystal Structures, Vol. 1 (New York: Interscience).

[261] Yang Z, Wu H and Simard B, Charge–discharge characteristics of raw acid-oxidized carbon nanotubes, Electrochem. Commun., 4 (2002) 574.

[262] Yang ZH and Wu HQ, The electrochemical impedance measurements of carbon nanotubes, Chem. Phys. Lett., 343 (2001) 235.

[263]Yang ZH, Zhou YH, Sang SB, Feng Y and Wu HQ., Lithium insertion into multi-walled carbon nanotubes predoped with lithium, Matter. Chem. Phys., 89 (2005) 295.

[264] Yang J, Winter M and Besenhard JO, Small particle size multiphase Li-alloy anodes for lithium-ionbatteries, Solid State Ionics, 90 (1996) 281.

[265] Yang J, Wang BF, Wang K, Liu Y, Xie JY and Wen ZS, Si/C Composites for high capacity lithium storage materials, Electrochem. Solid-State Lett., 6 (2003) A154.

[266] Yata S, Kinoshita H, Komori M, Ando N, Kashiwamura T, Harada T, Tanaka K and Yamabe T, Structure and properties of deeply Li-doped polyacenic semiconductor materials beyond C_6Li stage, Synth. Met., 62 (1994) 153.

[267] Yata S, in Proc. of the Int. Workshop on Advanced Batteries (Lithium Batteries), Osaka (1995) 204

[268] Yazami R and Reynier Y, Thermodynamics and crystal structure anomalies in lithium-intercalated graphite, Journal of Power Sources, 153 (2006) 312.

[269] Yoon YJ, Bae JC, Baik HK, Cho SJ, Lee SJ, Song KM, et al., Growth control of single and multiwalled carbon nanotubes by thin film catalyst, J. Chem Phys Lett., 366 (2002) 109.

[270] Zheng T, Xue JS and Dahn JR, Lithium insertion in hydrogen-containing carbonaceous materials, Chem. Mater, 8 (1996) 383.

[271] Zheng T and Dahn JR, The effect of turbostratic disorder on the staging transitions in lithium intercalated graphite, Synth. Met., 73 (1995)1.

[272] Zheng T, Liu Y, Fuller EW, Tseng S, Sacken U Von and Dahn JR, Lithium insertion in high capacity carbonaceous materials, J. Electrochem. Soc., 142 (1995) 2581.

ANSWERS TO THE QUERIES OF EXAMINER

.	Comments and Reference	Answer to comments	Present Reference
ıter 2			
	Page 7. Gupta et al.(2007) is not in the list of references.	The reference Gupta et al. (2007) is replaced by another reference Mathur et al. (2007) which was already present in the list of references.	**Page 7, Line 7** **Page 185, Reference [155]**
	Page 8. Whittingham (1976) is out of sequence in the list of references-it is before the Wang et al. papers for example.	The reference has been placed in order of sequence.	**Page 8, Line 10 of section 2.** **Page 193, Reference [247]**
	Page 8. Raw et al. (1997) is not in the list of references.	The reference is actually Rao et al.(1997) which is present in the list of references in the original version of the thesis. The typing mistake has been corrected (i.e. from Raw to Rao) in Page 8.	**Page 8, Line 19 of section 2.** **Page 188, Reference [189]**
	Page 8. Dey et al. (1971) is not in the list of references. There is a single author paper in the references, so if it is this one, it should be referred to as Dey (1971) in the text.	The reference is actually Dey (1971) which is in the list of references. Correction has been made in the text.	**Page 8, Lines 19 and 20 section 2.2** **Page 178, Reference [68]**
	Page 9. Yazami et al. (1983) is not in the list of references. Is it perhaps the Yazami and Reynier (2006) paper ?	It is Yazami and Reynier (2006) paper and the correction has been made in the text.	**Page 9, Line 2** **Page 194, Reference [268]**
	Page 9. Goodenough et al. (1980) and (1983) are not in the list of references.	The references are Mizushima et al., 1980 and Thackeray et al., 1983 which are present in the list of references. Corrections have been made in the text.	**Page 9, Line 8** **Page 185, Reference [16** **Page 191, Reference [225]**
	Page 9. Line 13. It should be Lazzari, not Lazzami.	Correction has been made.	**Page 9, Line 12**

Page 9. Line 13. Nagaura et al. (1990) is not in the list of reference	The reference is Nagaura and Tozawa 1990, which has been included in the list of references.	**Page 9, Line 12** **Page 186, Reference [167]**
Page 9. Anode and cathode should be explained here in the context of positive and negative electrodes. The candidate's explanation does not rival that on Wikipedia !	The required explanation has been incorporated in the text.	**Page 9, Lines 8 to 15 section 2.3:** A lithium i battery consists of ..... when cell is being discharged
Page 13. Goodenough et al. (1997) is not in the list of references.	The reference is actually Padhi et al. (1997), which is in the list of references.	**Page 13, Line 2 of secti 2.4.5** **Page 187, Reference [180]**
Page 15: It should be 'disintegration' at the start of the line six lines after equation (2.3).	The spelling mistake has been corrected in the text.	**Page 15, Line 6 aft equation (2.3)**
Page 18. Datta et al. is in fact Datta and Kumta.	Datta et al. has been corrected as Datta and Kumta in the text.	**Page 18, Line 21**
Page 19. Wakinhara et al. is in fact a single authored publication by Wakihara, as I found when looking up this paper. Warren et al. (1934) is not in the list of references, nor is Franklin et al. (1951) referred to in the caption to Figure 2.4.	Wakinhara et al. has been corrected as Wakihara (2001) in the text. Warren (1934) and Franklin (1951) both are single authored publications and are added to the list of references.	**Page 19, Line 13** **Page 19, Line 15 and capti of Fig. 2.4** **Page 179, Reference [85]** **Page 192, Reference [241]**
Page 20. Wyckoff (1964) is not in the list of references (Fig.2.5).	The reference Wyckoff (1964) is included in the list of references.	**Page 20, caption of Fig. 2.5** **Page 194, Reference [260]**
Page 21. There is no Eq.2.6 (referred to six lines after Equation 2.4).	The equation referred is Eq. 2.4. The correction has been made in the text.	**Page 21, Line 6 after the E (2.4)**
Page 22: Song et al.(1996) is not in the list of references (Figure 2.7)	The reference Song et al. (1996) has been included in the list of references.	**Page 22, caption of Fig. 2.7** **Page 190, Reference [217]**

Page 23: Besenhard et al. (1983) is not in the list of references (Figure 2.8). After the caption to this figure it should be "plateau indicates' in the first line.	The reference is Besenhard and Fritz (1983), which has been included in the list of references. The correction has been made in the text. The spelling mistake has been corrected in the text.	**Page 23, caption of Fig. 2.8** **Page 175, Reference [27]** **Page 24: Line 1**
Page 24: Figure 2.9 is not from the Dahn 1991 paper- I checked !	Actually, the reference is Winter et al., 1998; the correction has been made in the text.	**Page 24, caption of Fig. 2.9**
Page 27. Dahn et al. (1996) is not in the list of references.	The reference is Zheng et al. 1996, which has been included in the list of references and accordingly correction has been made in the text.	**Page 27, Line 16** **Page 194, Reference [270]**
By this point in this thesis I had made the comment in my handwritten notes: 'Clearly the content is of Ph.D. standard, but the attention to detail of the candidate is sloppy.'	----------	----------
Page 29. Section 2.5.5.3, first sentence. Words such as 'are possible' seem to be lacking at the end of the sentence.	First sentence in the section 2.5.5.3 has been corrected in the text.	**Page 29, Line 4 of secti 2.5.5.3**
Page 30. Line 6: after insertion words such as 'can be expected' seem to have been omitted. Burgers et al. (2008) is not in the list of references. Perhaps this is Burgess et al. ?	The sentence has been corrected. It is Burgess et al. (2008), the correction has been made in the text.	**Page 30, Line 10.** **Page 30, Line 11.**

Page 33. Silva et al. (2009) is not in the list of references. Should it not be transistor ? I could not find any evidence that Davis et al. (1995) discussed CNTs.	The reference is actually Smith and Silva (2009), which is in the list of references. The correction has been made in the text. The word is "transistor". The correction has been made in the text. The reference is actually Wu et al., 2003, which is in the list of references. The correction has been made in the text.	**Page 33: Line 10 of sectic 2.5.7** **Page 190, Reference [213]** **Page 33, Line 11 of 2.5.7** **Page 34, Line 3** **Page 193, Reference [256]**
Page 35: PAAO is undefined. ..... I'm not sure CNFs are defined either when they first appear, e.g., page 35. 'Nowadays' is one word, not three (line 6 of 2.5.7.2).	CNFs and PAAO have been defined in the text. "Now a days" has been corrected to "Nowadays"	**Page 35, Line7 of 2.5.7.1 ar Line 9 of 2.5.7.2** **Page 35, Line 5 and 6 2.5.7.2**
Page 40. Duuris et al. (2005) is not in the list of references.	Actually, the reference is Dupuis (2005), which is in the list of references. The correction has been made in the text.	**Page 40, Line 4**
Page 42. 2.5.7.7, 'SWCNTs are consists' is not English !	The sentence has been corrected as well as first para of the section 2.5.7.7 has been modified.	**Page 42, Lines 1 to 5 section 2.5.7.7**
Page 43. The reference is Shimoda et al. (2002). Penultimate line: 'an aqueous electrolyte are not useful' is not English !	The correction has been made. The part of the line has been corrected as "an aqueous electrolyte is not useful"	**Page 43, Line 8** **Page 44, Line 3**
Page 44. Neither Kanamura et al. (2002) nor Feuillard et al. (1957) are in the list of references. I wrote as a general comment the the English on page 44 is poor. I also wrote in my notes that Chapter 2 just finishes – it needs a concluding paragraph or two to set the scene for the later chapters.	Actually the reference is Kanamura et al., 1996, which has been included in the list of references. The reference is Armand (1994), and included in the list of references. A concluding paragraph (Based on extensive literature survey..... in following chapters.) has been added at the end of the Chapter 2.	**Page 44, Line 16** **Page 182, Reference [121]** **Page 44, Line 27** **Page 174, Reference [13]** **Pages 44 to 45**

ɔter 3

Page 47. Calcination seems a concept poorly appreciated by the candidate. Literally this refers to the loss of carbon dioxide by calcium carbonate to form calcium oxide (lime), but there are more general definitions – see the Wikipedia entry for a start !	The part describing the calcination process has been modified in the text.	**Page 49, Lines 2 to 6 after Fig.3.2**
Page 48. Zhou et al. (2003) is not in list of references.	Zhou et al., 2003 has been included in the list of references.	**Page 50, Line 6** **Page 195, Reference [275]**
Page 50. Is the candidate sure that he meant to use the word 'nonporous' in line 4 of 3.2.3 ?	The word has been corrected to 'nanoporous'.	**Page 52, Line 4 of secti 3.2.3**
Page 51. Virk et al. (2005) is not in the list of references. Table 3.1 is clearly reproduced from a source which the candidate has failed to acknowledge in the table.	The reference is Virk 2005, which has been added in the list of references. Reference Shingubara et al., 2004 has been incorporated in the caption to the table 3.1.	**Page 53, Line 9** **Page 191, Reference [230]** **Page 53, Table 3.1** **Page 190, Reference [208]**
Page 52: third paragraph, first sentence is not English. I'm not convinced about the last sentence on this page either.	The sentence has been modified. The last sentence has been removed from the text.	**Page 54, first sentence of t third paragraph**
Page 52. Schaffer et al. (1992) in not in the list of references. Is it possible that it might be Schaffer and Forrester (1997) ?	The reference is Schaffer and Mc Cormick (1992), which has been added in list of references.	**Page 54, Last line** **Page 189, Reference [201]**
Page 56. Should it not be 'thermogravimetry' and 'differential' in section 3.3? In 3.3.1, I would have thought it was 'lose' not 'loose'	'Thermogravimitry' and 'differntial' have been corrected as 'thermogravimetry' and 'differential'. 'Loose' has been corrected as 'lose'.	**Page 58, Lines 4 and 6 section 3.3** **Page 58, Line 2 of secti 3.3.1**

Page 61. Placzek et al. (1934) is not in the list of references. In 3.5.1 it should be Stokes not Stockes.	The reference is Placzek (1934), which has been added to list of references. 'Stockes' has been corrected to 'Stokes'.	**Page 63, Line 3 of section 3.** **Page 188, Reference [188]** **Page 63, Line 7 of secti 3.5.1**
Page 62 and 63. These figures have not been acknowledged. Figure 3.15 has also not been acknowledged. The source of Figs. 3.10 and 3.11 are not mentioned.	Reference (Agarwal and Atalla, 1995) has been provided in both the figures 3.10 and 3.11. Reference (Goodhew et al., 2001) has been mentioned in Figure 3.15 caption.	**Pages 64 and 65, captions Fig. 3.10 and Fig. 3.11** **Page 173, Reference [3]** **Page 73, Fig. 3.15** **Page 180, Reference [95]**
I am not convinced what is to be gained from Fig.3.18 other than showing the proof of existence of the glove box used !	Fig.3.18 has been eliminated.	**Page 76**

ıter 4

Page 77. Che et al. (1998), Shimoda et al. (2000) and Chung et al. (2001) are all omitted from the list of references. The sentence beginning 'The electrochemical studies …' does not make sense. I could not find a reference to CNTs in Endo et al. (2001).	In the text the references have been corrected as Chen et al., 2002, Shimoda et al., 2002 and Lu and Chung, 2001. These references are added in the list of references. The sentence has been modified. The reference Endo et al., 2001 is related to CNFs not specifically for CNTs. The reference is in the list of references.	**Page 77, Lines 13 and 14 of section 4.1** **Page 176, Reference [49]** **Page 189, Reference [207]** **Page 184, Reference [147]** **Page 77, Lines 14 and 15 section 4.1** **Page 77, Line 17** **Page 179, Reference [76]**
Page 80. There is repetition here of parts of page 78.	The repeatation part has been eliminated from page 80, (this is not indicated in the text).	**Page 80**

Page 87. I am not convinced that the arrangement in Figure 4.6c is that of a regular hexagonal array.	Discussion of the Fig.4.6 (c) has been modified to show the hexagonal porous structures in localized regions.	**Page 87, Lines 4 and 5**
Page 89. The marker in the Figure 4.7c is difficult to read. Baker et al. (1989) is actually a single author paper by Baker (1989).	The marker has been made readable. Baker et al. (1989) has been corrected as Baker (1989).	**Page 89, Fig. 4.7c.** **Page 89, Line 3 of section 4**
Page 92. The increase in d-values…' seems a particularly vague statement.	The sentence 'The increase in d-value……..' has been modified.	**Page 92, Lines 5 to 8**
Page 94. (v) is $LiMn_{1.8}Fe_{0.2}O_4$. Again, I note repetition here.	$LiMn_{1.2}Fe_{0.2}O_4$ has been corrected as $LiMn_{1.8}Fe_{0.2}O_4$. To eliminate the repetition, the penultimate sentence in the Para just before Section 4.6.2 has been deleted from text.	**Page 94, Line 8 of secti 4.6.2**
Page 96. The sentences at the top of this page are in essence a repeat of sentences on page 91.	The repeat sentence in page 96 has been removed from text.	**Page 96**
Page 100. Line 1-7 are yet more vague comments. The inset to Figure 4.16(b) is elliptical. Is 3.396Å significant to four significant figures ? If so, it seems remarkable for an interplanar spacing obtained from electron diffraction patterns.	This part of the text has been modified. The inset to Figure 4.16(b) appears elliptical due to image processing problem. This has been rectified. The 3.396 Å has been expressed figure as 3.40 Å.	**Pages 99-100, Lines 1-10, after Fig.4.15** **Page 100, Fig. 4.16 (b)** **Page 101, Line 4.**
Page 104. I'm not sure I follow the logic here in the first paragraph. Perhaps the candidate can enlighten his oral defence committee here.	The candidate will explain at the time of oral defence.	----------

Page 108. Yet more repetition in 4.6.4 – simply refer to Chapter 3!	The first paragraph in the section 4.6.4 has been removed to avoid the repetition.	**Page 108, Section 4.6.4**
Page 109. If the material, the XRD of which is in Figure 4.22(d), is amorphous, then why is a 101 peak seen in the XRD ? I would have thought this indicates a small crystalline size material, not an amorphous material.	The first sentence after the Figure 4.22 has been modified.	**Page 109, Line 1 after the Fig. 4.22**
Page 111. Yet more repetition-this time about the interpretation of Raman spectra.	The first paragraph of 4.6.5 has been removed to avoid the repetition.	**Page 110**
Page 119. I do not see a voltage plateau at 0.9 V in Figure 4.27 ! It should be 'discharge' in this figure.	The sentence containing 'The voltage plateau around 0.9 V.....interface (SEI)' has been removed.	**Page 118, First para after tl Fig. 4.27**
Page 121. It is not clear from the summary what new work has been presented in Chapter 4 and what merely confirms prior work elsewhere.	The novelty statement of the Chapter 4 has been added in the summary. The summary has been modified stating clearly about the new work and idea that have been presented in this Chapter 4. (New types of catalysts have been introduced first time and idea behind using lithium-based catalyst was to insert lithium into CNTs during the growth process and hence improve electrochemical behavior. The successful attempt has been made to change morphologies of carbon nanostructures by changing novel catalysts. CNRs are used as anode material for lithium ion battery for the first time.	**Pages 120 to 121**

pter 5

Page 124. Sogabe (1996) is not in the list of references.	The reference Sogabe et al., 1996 has been added to the list of references.	**Page 124, Lines 9 and 11 ol section 5.2.1** **Page 190, Reference [214]**

Page 127. Yet more repetition, and all seems hand-waving and qualitative.	The repetition has been removed from the text in the page 127.	**Page 127, Section 5.2.3, Firs paragraph**
Pages 132-133. The results here seem to confirm those of Way and Dahn (1994) and their interpretation. What is new here?	The reference Way et al., 1994 in the text has been corrected as Way and Dahn, 1994. The discussion has been modified by giving an explanation on what is new about this part of the work. (The synthesis process is different, the results are better in terms of flat voltage profiles and most of the charge capacity appeared at lower voltage, which are requirements for better anode materials).	**Page 132, Line 1** **Page 132, Lines 4 to 9** (However, in..... performance of battery.)
Page 138. The four EDX maps should be labelled with the chemical element being analysed.	All the four EDX maps have been labelled with the corresponding chemical elements. The labeling with (C) and (Si) in the EDX maps implies the elements carbon and silicon respectively.	**Page 138, Fig. 5.10**
Page 140. In the right-hand diagram, it should be Si-content on the horizontal axis.	The spelling mistake has been corrected.	**Page 140, Fig. 5.12 right hand diagram**
Page 141. Why (yet again) are the D and G bands explained?	The explanation on D and G bands has been removed from this page.	**Page 141, First paragraph after the Fig. 5.13**
Page 143. Figure 5.14(c) : it should be 'Charging profile'.	In Figures 5.14(b) and (c) 'Charge profile' is written.	**Page 143, Fig. 5.14 (b) and (c)**
Page 144. Kasavajjula et al. (2007) and Liu et al. (2005) are not in the list of references.	The references Kasavajjula et al., 2007 and Liu et al., 2005 have been included in the list of references.	**Page 144, Line 19** **Page 182, Reference [124];** **Page 184, Reference [143]**
As with Chapter 4, I found it difficult to draw from the summery to Chapter 5 what new work has been presented in Chapter 5 and what merely confirms prior work elsewhere.	In Chapter 5, an improved synthesis process was adopted and the effect of this process on electrochemical behavior of the materials synthesized has been discussed. The summary of this Chapter 5 has been modified.	**Pages 146 to 147.**

	Pages 139 and 150. Why are the two XRDs of graphite different ? Both are 'pure graphite.'	The XRD patterns in two Fig. 5.11 (page 139) and Fig. 6.11 (page 150) are presented in the angular ranges (2θ) of 20-90° and 10-80° respectively. Though both are pure graphite, the graphite powders used for studying graphite-Si composites (Fig. 5.11) and ball milling effects (Fig. 6.1) are from two different sources. Although the characteristic peaks (002), (100), (101), (102), (004), (103) of graphite 2H are present in both the XRD patterns. The pattern in Fig. 5.11 has a peak at 2θ = 43.45° corresponding to graphite 3R phase. The pattern in Fig.6.1 has got relatively higher noise figures. Moreover, the pattern in the Fig. 5.11 is of the powdered sample heat treated at 1200°C. Whereas the pattern in the Fig.6.1 is of the sample without having undergone any heat treatment.	**Page 139, Fig. 5.11 and Pag 150, Fig. 6.1**
	Page 151.'generating too defects' (line 8). What does it mean ? Where does the iron go ? I'm not sure. Is the candidate ?	The sentence has been modified. Iron remains as an impurity in milled graphite powder, which was later removed by acid treatment. However, the impurity content (i.e. iron %) is very low (approximately 5 at%) in the ball milled graphite powder, therefore the impurity is less than the detectable limit of XRD analysis.	**Page 151, Lines 6 to 8**
	Page 152. Ong et al. seems to be Ong and Yang (2000).	'Ong et al.' has been corrected as Ong and Yang (2000).	**Page 152, Line 3**
	Page 155. The diffraction in (b) is not circular.	This defect was due to image processing. This has been corrected in Figure 6.5 (b).	**Page 155, Fig. 6.5 (b)**
	Page 156. Temperature is spelt incorrectly on the horizontal axis of Fig. 6.6.	The spelling mistake has been corrected . Other reference 'Welham et al., 2003' has	**Page 156, Fig. 6.6**

Presumably others have looked at the effects of ball milling. E.g., Mathur et al. (2007). It seems odd that the candidate makes no reference to prior work to back the comments he makes here in 6.4. I note 6.4 occurs twice – page 155 and page 157.	been added to this section 6.4. The subsection 6.4. Raman Spectra has been corrected as 6.5. Raman Spectra.	**Page 156, Line 5, after Fig.6.6** **Page 157**
Page 158. Figure 6.7(b) has 'smooting' instead of 'smoothing'. Presumably the interpretation here is consistent with the thermal analysis, but there is no comment to this effect.	"smooting" has been corrected as "smoothing". A comment (last sentence in the section 6.5) as suggested by the examiner has been added.	**Page 158, Fig. 6.7 (b)** **Page 159, Lines 8 to 10**
Page 161. It should be 'formation' in Figure 6.8 (c).	The spelling mistake has been corrected.	**Page 161, Fig. 6.8 (b) and (**
Page 165. Yet again, I've no feeling from the summary about how much of this work is new and what merely confirms prior work elsewhere.	Ball milling of graphite powder has been carried out in liquid (methanol) medium for different time periods in order to avoid agglomeration and amorphization of powder. The medium used for milling is not reported in literature. The summary has been modified by giving a comparison of the results with those of others.	**Pages 165 and 166**
Page 167. The conclusions follow the pattern elsewhere in the thesis. I've little feeling apart from point 11 about what new work the candidate has undertaken, although it is evident from Page ix that the candidate has papers either published or in press. I am mystified about why the candidate has not clearly flagged up new work (as he has done with point 11 for example)	The conclusions at the following serial numbers 1, 3, 4, 5, 7, 8, 9, 10, 11, 17, 18, 21, 23, 30 31, 35 and 36 have been suitably modified to state clearly about the new work.	**Pages 167 to 171**

References : Specific comments

S. No.	Comments & Reference	Answer to comments	Present Reference
1.	[4]. This article does not seem to have a title.	The title has been included.	Page 173, Reference [5
2.	[154]. This article does not seem to have a title either.	The title has been included.	Page 186, Reference [1
3.	[181]. It is 'Butterworth'.	Correction has been made	Page 188, Reference [1
4.	[211]. It should be 'filaments' in the title !	Correction has been made	Page 191, Reference [2
5.	[216]. This article does not seem to have a title either.	The reference has been corrected.	Page 192, Reference [2
6.	The 'W' subgroup of references are not in alphabetical order, nor is the 'S' subgroup in so far as the reference to Schaffer and Forrester is out of sequence. Look at [198] and [199] – they should be swopped.	The 'W' and 'S' subgroups of references have been arranged in alphabetical order.	Pages 188 – 190, F [195] – [218] Pages 192 – 194, References [232] – [26